Special Issue "Mineral Surface Science and Nanogeoscience"

A special issue of *Minerals* (ISSN 2075-163X).

Guest Editor
Dr. Athanasios Godelitsas

Special Issue Information

In the last decades technological developments have revitalized a new area of research in Mineralogy with respect of the structure and reactivity of mineral surfaces. Mineral Surface Science is closely associated to the fields of Molecular Geochemistry and Biogeochemistry, concerning the investigation of geochemical processes at the molecular level. The expansion of both scientific subjects is based on the combined utilization of advanced microscopic and - surface- spectroscopic techniques, such as AFM, STM, TEM, SIMS, LIBS, and XPS. Nowadays, it is possible to study, by means of *in situ* AFM, crystal growth and dissolution processes occurring at mineral-fluid interfaces, in real time, also on a molecular scale (nanoscale). Moreover, accelerator-/Synchrotron-based techniques, including PIXE, NRRA, RBS, SR-(μ)XRF, SR-(μ)XRD and (μ)XANES/EXAFS, present new opportunities for Nanogeoscience and, in general, to Earth and Environmental Sciences. Mineral Surface Science and molecular Geochemistry have contributed to the establishment of Nanogeoscience with regard to the study of nanoparticles in nature and the investigation of geological processes in the nanoscale (1 nm– 100 nm). As an example, a part of the research currently elaborated concerns the surface chemical behavior of calcite. This common carbonate mineral plays a major role in the global CO_2 cycle, participates in key biomineralization processes, and shows high reactivity in fluids controlling the geoavailability and bioavailability of certain contaminants. On the other hand, nanoporous minerals, such as zeolites, clays, and Fe-Mn-oxides/oxyhydroxides, are important natural materials when studying the Earth and developing relevant Environmental Technology. Additionally, Mineral Surface Science and Nanogeoscience are crucial in ore systems research. This Special Issue will focus on recent advances in Mineral Surface Science and Nanogeoscience, including, but not limited to, topics such as crystal growth; mineral dissolution; nanominerals; mineral nanoparticles; nanoporous minerals; nanoscale ore mineralogy; environmental mineralogy; environmental nanoparticles; atmospheric particles; biominerals; medical mineralogy; nanofossils; and nanoscopic methods.

Dissolution and Sorption Processes on the Surface of Calcite in the Presence of High Co^{2+} Concentration

Jorge González-López [1],*, Ángeles Fernández-González [1], Amalia Jiménez [1], Athanasios Godelitsas [2], Spyridon Ladas [3], Georgios Provatas [4], Anastasios Lagogiannis [4], Ioannis N. Pasias [5], Nikolaos S. Thomaidis [5] and Manuel Prieto [1]

[1]   Department of Geology, University of Oviedo, Calle Arias de Velasco s/n, Oviedo 33005, Spain; mafernan@geol.uniovi.es (Á.F.-G.); amalia@geol.uniovi.es (A.J.); mprieto@geol.uniovi.es (M.P.)

[2]   Department of Geology & Geoenvironment, National and Kapodistrian University of Athens, Zographou Campus, 15784 Athens, Greece; agodel@geol.uoa.gr

[3]   Surface Science Laboratory, Department of Chemical Engineering, University of Patras, 26504 Patras, Greece; ladas@chemeng.upatras.gr

[4]   Tandem Accelerator Laboratory, Institute of Nuclear Physics, NCSR "DEMOKRITOS", GR-15310 Attiki, Greece; gprovatas@inp.demokritos.gr (G.P.); lagoya@inp.demokritos.gr (A.L.)

[5]   Department of Chemistry, National and Kapodistrian University of Athens, Zografou Campus, 15771 Athens, Greece; iopas@chem.uoa.gr (I.N.P.); ntho@chem.uoa.gr (N.S.T.)

*   Correspondence: jgonzalez@geol.uniovi.es; Tel.: +34-985-105-774

Abstract: The interaction of the calcite surface with Co^{2+}-rich aqueous solutions ([Co$^{2+}_{aq}$]$_{initial}$ = 1000 ppm, i.e., ca. 17 mM) was investigated by means of macroscopic experiments and surface spectroscopic techniques.   In the case of the macroscopic experiments, calcite powder and monocrystals were immersed into solutions for different time periods (from 1 min to one month).   The Ca concentrations in the filtrates was measured by means of atomic absorption spectrometry (AAS) while the interacted solids were studied using a combination of X-ray photoelectron spectroscopy (XPS) and ^{12}C-rutherford backscattering spectrometry (^{12}C-RBS). The macroscopic data showed a characteristic surface dissolution process, in parallel to the surface sorption processes. Adsorption and co-precipitation were seen for almost the entire immersion period for both calcite powder and monocrystals. The surface study by XPS (analyzed at a depth of approximately 12 nm) suggested that adsorption takes place in the first hour of the interaction, followed by incorporation of Co^{2+} into calcite surface layers, leading to the formation of a Co^{2+}-bearing surface (co)precipitate, which occurs over a period of hours and days. The ^{12}C-RBS measurements on calcite {10$\bar{1}$4} indicated that the thickness of this surface co-precipitate was 270 nm after one day and then stabilized at 320 nm after more than a week.

Keywords: calcite; surface; cobalt; dissolution; adsorption; surface co-precipitation; photoelectron spectroscopy; Rutherford backscattering

1. Introduction

Cobalt makes up only about 0.0025 wt % of the Earth's crust [1], but is essential for our health as it forms the active center of cobalamins. Cobalamins are a group of coenzymes, the most important of which is vitamin B$_{12}$. Cobalt can also be toxic at high concentrations. The presence of cobalt in the environment is related mainly to anthropogenic activity resulting from mining, the pigment industry and the dumping of Co-Li batteries. The maximum recommended exposure is 1×10^{-4} mg·cobalt/m^3 and 1×10^{-2} mg/Kg·day for inhalation and oral exposure, respectively [2]. The agency for toxic

substances and disease registry (ATSDR) report also takes into account the hazards involved with the artificial radioactive ^{60}Co isotope, which is used in many applications (e.g., medicine, sterilization and industrial radiography). The release of this radiogenic isotope into the environment is harmful to humans, animals and marine life. It is also the most stable artificial isotope with a half-life of 5.27 years, leading to its accumulation in the environment. Since Co^{2+} is soluble, its mobility in water is high which can lead to the contamination of soils and groundwater and the incorporation of the metal into the trophic chain [3].

Certain mineral structures can remove heavy metals from the environment. Sorption processes onto mineral phases, and particularly onto carbonates [4], frequently control the immobilization of contaminants and govern their dispersion and accumulation. The main mechanisms involved in metal sorption processes are absorption (including ion exchange), adsorption and co-precipitation, finally leading to surface crystal growth [5] (Figure 1). The adsorption only involves the formation of chemical bonds onto the mineral surface sites. Absorption implies the incorporation of dissolved metal ions onto mineral surface layers. On the other hand, co-precipitation fundamentally leads to the formation of a new phase, which is not necessarily related to the bulk mineral composition and structure. Many studies have focused on remediation technologies with natural minerals such as zeolites, sulphates and carbonates in the last two decades [6–8]. Among these minerals, carbonates are the most widely used, particularly calcite, which has been employed due to its widespread availability and reactivity [9].
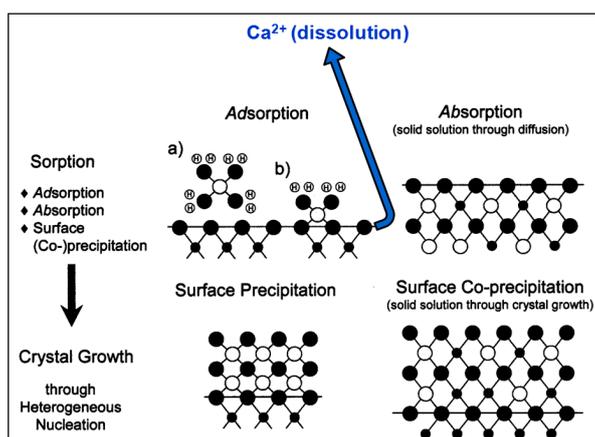
Figure 1. Metal (e.g., Co) sorption and dissolution processes on carbonate mineral surfaces (modified after [5]).

Kornicker et al. [10] measured the sorption process of an aqueous solution of Co^{2+} ($[Co^{2+}_{aq}]_{initial}$ < 60 ppm) onto calcite and concluded that only adsorption occurs. No $CoCO_3$ was found to be precipitated onto the calcite or aragonite surfaces. Xu et al. [11] investigated the interaction of Co^{2+} ($[Co^{2+}_{aq}]_{initial}$ < 6 ppm) with both calcite-cleaved monocrystals and powder by means of X-ray photoelectron spectroscopy (XPS). They reported that initially the incorporation of Co into calcite occurred at a fast rate (up to 7.2 nmol/min·mg) and is attributed to adsorption. This was followed by a co-precipitation mechanism and the formation of a $(Co,Ca)CO_3$ solid solution with the Co content related to the initial pH and the calcite saturation index. They also indicated that no oxidation of Co^{2+} takes place during the interaction. Furthemore, Cheng et al. [12] studied the interaction of the calcite surface with Co ($[Co^{2+}_{aq}]_{initial}$ = 29.47 ppm) using surface-extended X-ray absorption fine structure (SEXAFS) and X-ray standing wave (XSW). Their results indicated that Co replaces Ca atoms in the M–O octahedron at the surface and also that at the top of the surface, the Co^{2+} ions are bounded to OH groups in order to maintain the octahedral coordination observed in XSW. In addition, Braybrook et al. [13] carried out both experimental and computational work based on calcite growth in the presence of aqueous Co^{2+}. Both their simulations and experiments provided support for the conclusion that synthetic calcite growth occurs. Their simulations showed interference between the {10$\bar{1}$4} and {01$\bar{1}$1}

planes, thus suggesting Co incorporation on the <44$\overline{8}$1> acute steps. However, they claimed that both experimental and computational results indicated that Co accumulation only occurs on the calcite mineral surface. Freij et al. [14] performed a series of experiments ($[Co^{2+}_{aq}]_{initial} < 600$ ppm) using atomic force microscopy (AFM) and concluded that a $Co_xCa_{1-x}CO_3$ micro-layer is formed, covering the entire calcite surface. Further, Katsikopoulos et al. [15] studied the crystal growth from a (Co,Ca)CO$_3$ solid solution using silica gel double diffusion and direct precipitation experiments. They demonstrated that a large amount of Co (up to 33 mol % of Co) entered the CaCO$_3$ structure, but experiments were conducted far from equilibrium due to supersaturation; thus, the Co incorporation into calcite could occur in a metastable state. Moreover, Lee et al. [16], in a paper significant for medical applications, investigated the influence of citrate and phthalate on the growth of calcite in the presence of Co^{2+} and found that citrate and phthalate inhibit the precipitation of calcite. Recently, González-López et al. [17] reported the thermochemistry of (Ca,Co)CO$_3$ solid solutions from density functional theory simulations and concluded that many $Ca_{1-x}Co_xCO_3$ mineral solid solutions (with observed compositions of up to $x = 0.027$, and above $x = 0.93$) are metastable with respect to phase separation. Finally, Xu et al. [18] studied the interaction of calcite with solutions with a very low Co^{2+} concentration ($[Co_{aq}]_{initial} = 1$–10 ppm) using AFM and XPS. They suggested that that the lattice misfit between CoCO$_3$ and CaCO$_3$ is too large to allow heteroepitaxial growth of a pure cobalt carbonate phase in ambient conditions.

This present work attempts to understand the interaction between the calcite surface and aqueous solutions with a high Co^{2+} concentration ($[Co^{2+}_{aq}]_{initial} = 1000$ ppm, ~17 mM). For this purpose, different sets of experiments were designed. Macroscopic experiments of calcite powder and monocrystals were immersed into solutions for varying time periods (from 1 min to one month), with the aim of observing surface dissolution processes (analysis of the filtrates for Ca by atomic absorption spectrometry (AAS)). Surface spectroscopic experiments were conducted to obtain a novel spectroscopic "3D image" of the interactions using a combination of surface-sensitive techniques (XPS and ^{12}C-rutherford backscattering spectrometry (^{12}C-RBS)) and also to analyze the distribution of Co onto the calcite surface and resolve the potential sorption mechanisms.

2. Materials and Methods

2.1. Macroscopic Experiments

Natural pure calcite (transparent Iceland spar) was held in solution with the salt Co(NO$_3$)$_2$·6H$_2$O at room temperature. The initial concentration of aqueous cobalt was kept high at 1000 ppm ($[Co^{2+}_{aq}]_{initial} = 1000$ ppm). The calcite mineral was tested in two different forms: as a fine powder obtained using an agate mortar, and as freshly cleaved {10$\overline{1}$4} monocrystals with a base size of ~0.5 × 0.5 and a height of 0.1 cm. In the powder experiments, 50 mg of calcite were mixed with 50 mL (Solid/Liquid ratio = 1 mg/mL) of the initial Co solution ($[Co^{2+}_{aq}]_{initial} = 1000$ ppm, ~17 mM) and placed into 30 mm × 115 mm polypropylene (PPN) tubes with a screw tap (Greiner Bio-One). The mixture was stirred vigorously at the start. The solutions were keep stable for different reaction times (1 and 12 h, and 1, 7, 14, 21, 30 and 60 days). The solids were separated from the aqueous solution by filtration using a Nalgene® dispositive filter (Thermo Fisher Scientific, Cambridge, UK) and Millipore® 0.45 μm filter (Millipore Corp., Bedford, MA, USA) which were carefully rinsed with distilled water. The filtrates from each experiment were analyzed for their Ca content using AAS (Perkin-Elmer 2380 Ca lamp with a wavelength of 422.7 nm, Perkin Elmer, Wellesley, MA, USA). For the monocrystals 20 mL of the initial solution ($[Co^{2+}_{aq}]_{initial} = 1000$ ppm, ~17 mM) was added to a 50 mL glass beaker where the single crystals were immersed. As the crystals were immersed into the solution, they were agitated for a few seconds using Teflon® tweezers to ensure the interaction between crystals and solution. Then, the vessels were covered to prevent contamination from external sources. Experiments with monocrystals were carried out for shorter interaction times, compared to powder experiments. They were immersed for 1, 5, 15 and 30 min, 1 and 12 h, one and two days,

one week, and one month (Table 1). The surface area was obtained geometrically, by measuring the height and width of each rhombohedron. After the interaction the crystals were carefully removed and rinsed with distilled water before being dried in air and then characterized by XPS (Leybold-SPECS, Berlin/Cologne, Germany) and ^{12}C-RBS.

Table 1. Data of the macroscopic experiments of the immersed calcite monocrystals.

Monocrystal Experiments			
Interaction Time	Surface Area (cm^2)	Weigh (g)	Geometric Specific Surface Area (cm^2/g)
1 min	75.90	0.085	897.15
5 min	45.47	0.040	1142.44
15min	81.33	0.105	774.58
30 min	67.62	0.068	1000.22
1 h	73.93	0.106	697.44
12 h	78.92	0.115	668.06
1 day	85.53	0.099	861.34
2 days	111.13	0.181	613.64
1 week	56.23	0.064	878.66
1 month	66.56	0.050	1344.63

2.2. Surface Spectroscopic Characterization of the Interacted Solids (XPS and ^{12}C-RBS)

XPS measurements were carried out on monocrystals interacted for 1 h, one day and one week. They were placed into the chamber of a MAX200 system (Leybold, Cologne, Germany), at room temperature and ~10^{-8} mbar pressure. Non-monochromatic Mg K$_\alpha$ X-rays and a Hemispherical Electron Energy Analyser (EA200 detector, SPECS, Berlin, Germany) with Multi-Channel Detection and were calibration certified (ISO15472 and ISO24237 [19,20]). The analyser operated under conditions optimized for the optimal signal intensity (constant pass energy of 100 eV, maximum lens aperture, analysis along the specimen surface normal). The analysed depth of the sample, was about 12 nm and signal intensity decreased roughly exponentially with increasing depth. A surface of 10 mm × 10 mm which was to be analyzed was first subjected to light argon-ion sputtering (1.5 keV ion beam energy, ~0.9 μA sample current and x-y rastering), with the aim to remove some of the superficial 'carbon' contamination layer. The ^{12}C-RBS measurements were carried out, in the case of monocrystals which had been immersed for 1 h, one day, one week and one month, using the 5.5 MV Tandem Accelerator at NCSR "DEMOKRITOS" located in Athens (Greece) with an 8 MeV ^{12}C-beam (Figure 2). RBS can be used to obtain composition profiles of the lower surface layers of the calcite crystals. The use of heavier ions (^{12}C), rather than typical protons, enhances the analytical depth resolution.


Figure 2. Experimental set-up of the ^{12}C-rutherford backscattering spectrometry (^{12}C-RBS) measurements.

3. Results and Discussion

3.1. Macroscopic Data—Dissolution of Calcite in the Presence of Co^{2+}

The release of Ca^{2+} (ppm of Ca per g of the solid), when powdered calcite was immersed in the initial Co^{2+} aquous solution as a function of time, is shown in Figure 3. The results clearly indicate a

progressive surface dissolution process [21,22], running in parallel with the metal sorption processes (which were confirmed by XPS and ^{12}C-RBS and are described in the next section). It is obvious that the dissolution of calcite depends on the S/L ratio (1 mg/mL in our case). The process starts from the surface, where Co^{2+} also interacts, and theoretically may alter the entire crystal structure. In the case of the experiments with calcite monocrystals it was feasible to correlate—in the presence of $[Co^{2+}_{aq}]_{initial}$ = 1000 ppm in the solution—the release of Ca^{2+} per geometric specific surface area as a function of time.
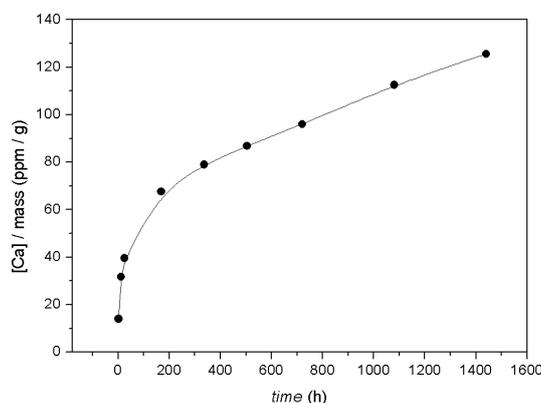

Figure 3. Release of Ca^{2+} (ppm of Ca per g of the solid) upon interaction of the powdered calcite with $[Co^{2+}_{aq}]_{initial}$ = 1000 ppm as a function of time.

It is also evident that dissolution depends significantly on the specific surface area of the carbonate mineral particles. The smaller the crystal size, the higher the dissolution rate. This is clearly seen when the high dissolution rates for the powdered experiments are compared with the single-crystal experiments. There was a rapid increase of the Ca concentration in the solution in short time steps after immersion. This was eventually stabilized after one week, reaching a value of 3.8×10^{-3} ppm/g·cm^{-2}. The equivalent total Ca^{2+} release in ppm for the monocrystals after one week of interaction was 3.2 ppm. Ca^{2+} release in the powder experiments differed greatly from the monocrystal experiments due to the differences in the surface reactivity. In the powder experiments, Ca^{2+} liberation never reached an asymptotic maximum value (see Figure 3). This suggests that calcite powder is dissolved during the entire interaction time, together with surface replacement of Ca^{2+} by Co^{2+}. The cause of this behavior is the fact that not only one monocristal is in place, but there is an accumulation of microcrystals which significantly increase the global surface reactivity. In this way, the total Ca^{2+} released after immersion for one week with approximately 0.5 g of calcite powder was 33.8 ppm, and assuming the average mass of all monocrystal experiments, the calculated calcium concentration was 6.6 ppm, rather higher than the previous Ca^{2+} total. Therefore, for the same mass of calcite powder, dissolution was faster. Indeed, it is suggested that the initial fast increase of Ca^{2+} in the aqueous solution was driven by the coupled dissolution and sorption process; this is supported by the modeling experiments using the PHREEQC code [23] (the total Ca^{2+} released into the solution was only 23.21 ppm, and thus the approximately 35 ppm of Ca^{2+} at the end of the first rise exceeded the calcite dissolution equilibrium). On the contrary, the last linear trend in Ca^{2+} release was only presumably caused by sorption which involves the surface replacement of Ca^{2+} by Co^{2+} towards the formation of a Cobalt-bearing co-precipitate.

3.2. Spectroscopic Data—Sorption of Co^{2+} on the Surface of Calcite

The XPS spectra for interacted calcite monocrystals (after 1 h, one day and one week of interaction) are shown in Figure 4. The Co 2p3/2 and 2p1/2 photoelectron peaks correspond to binding energies (BE) of 781.4 and 796.9 eV, respectively. These are characteristic of many Co compounds [11]. However, Co^{3+} or mixed Co^{2+} and Co^{3+} compounds seem not to be present due to the strong satellites of both

Co 2*p* peaks. It is well known that these satellites are characteristic for octahedrally coordinated Co^{2+} phases [24]. Moreover, the intensity of the peaks reveals that, for the samples immersed for one day and one week, there was evidence of Co incorporation into the calcite near-surface layers. The peaks indicate that there was a correlation between the intensity and the interaction time. Although the peak for 1 h is small, we cannot ignore the possibility that almost all adsorption of Co on the calcite surface was reached. In fact, since the O 1*s* photoelectron peak (531.6 eV) was assigned to both CaCO$_3$ and surface OH groups, and furthermore there was an excess of oxygen over the 1:3 stoichiometry for CaCO$_3$ (1:3.3), the existence of Co–OH bonds has been suggested as cobalt is adsorbed onto the surface after 1 h of interaction. O 1*s* peaks show a large tail because of the presence of some organic oxygen together with carbon. Given that XPS is a highly sensitive surface technique, organic carbon and oxygen, ubiquitous at any conditions, were detected. In addition, the decrease of the intensity of the O 1*s* peaks with time suggests that fewer Co–OH bonds are formed at the calcite surface and, instead, a surface layer of a mixed Co^{2+} compound could been have been precipitated after one day of interaction. However, the analyzed depth was ~12 nm and therefore deeper incorporation of Co cannot be excluded (for this purpose ^{12}C-RBS was conducted, as discussed below). The C 1*s* photoelectron peak at 289.6 eV has a distinct hydrocarbon signal (284.8 eV), and is recognized as characteristic of CaCO$_3$ for all samples. The peak's intensity decreases with time, similar to that of O 1*s*, revealing again a Co-bearing surface layer replacing the calcite surface. On the other hand, the one week sample which had been slightly sputtered with light argon ions allowed the removal of the first atomic layers, and we found that, in addition to hydrocarbon surface reduction, the Co/Ca ratio was reduced considerably (from 0.33 to 0.09). This is in agreement with the over-layer formation proposed for interaction times longer than 1 h.
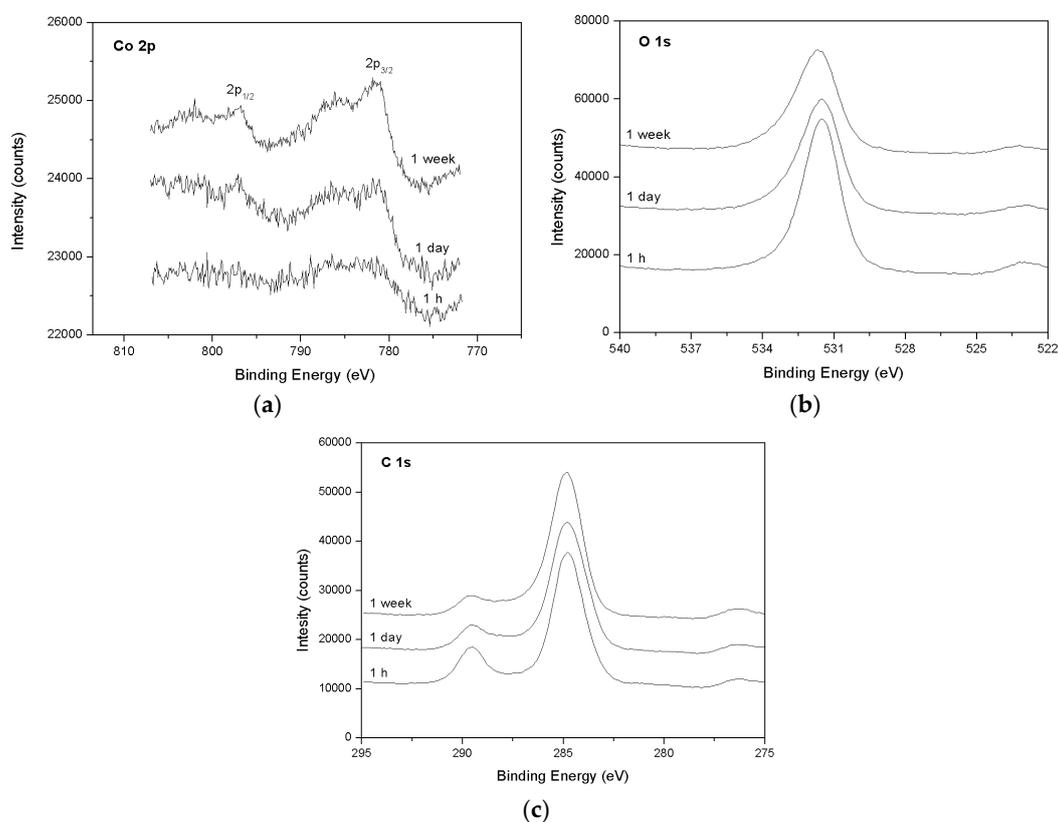

Figure 4. X-ray photoelectron spectra (XPS) spectra of calcite surfaces immersed in an aqueous solutions with a high Co^{2+} concentration ([Co$_{aq}$]$_{initial}$ = 1000 ppm) for 1 h, one day and one week. (**a**) Co 2*p* (**b**) O 1*s* (**c**) C 1*s*.

As mentioned above, XPS gives information about Co speciation and distribution at near-surface layers (up to 12 nm) of the immersed calcite crystals. It is unclear whether Co^{2+} ions, except for adsorption, have been incorporated into deeper layers of the dissolved calcite surface structure, forming a real co-precipitate. The complementary use of RBS (e.g., [25]), particularly of ^{12}C-RBS having a higher resolution, may yield a surface spectroscopic "3D image" of the metal. The same methodology has been previously applied in the case of the interaction of calcite with Pb in aqueous solutions [26]. It is known that the shapes of the RBS peaks are related to the metal distribution at varying depths. Sharp peaks reveal the formation of a metal-rich thin layer on the calcite surface (i.e., adsorption), while asymmetrical peaks and plateaus indicate metal incorporation onto calcite bulk (i.e., absorption) [25]. The ^{12}C-RBS spectra, showing Co distributions on surfaces at varying depths for the samples immersed for one day and one week, are shown in Figures 5 and 6, respectively. The RBS from calcite $\{10\bar{1}4\}$ interacted for 1 h, and gave no evidence of Co due to detection limits, in contrast to XPS which is more sensitive for near-surface layers.

According to the ^{12}C-RBS data, the surface layer of calcite was affected by Co^{2+} after an interaction of one day, reaching a depth of 270 nm. That proves that after the initial adsorption, which occurs on a short timescale as indicated by XPS, metal incorporation takes place and a true co-precipitate is formed. Furthermore, after one week of interaction, the depth of this co-precipitate was apparently stabilized, reaching a thickness of 320 nm (almost the same thickness was recorded in the case of calcite immersed for one month). It is therefore argued that Co is removed from the aqueous medium, in the beginning via adsorption onto the dissolving surface, and later on by co-precipitation. A similar behavior has been observed in the case of the interaction of Co^{2+} with the surface of dolomitic marble, also studied by XPS and RBS [27].
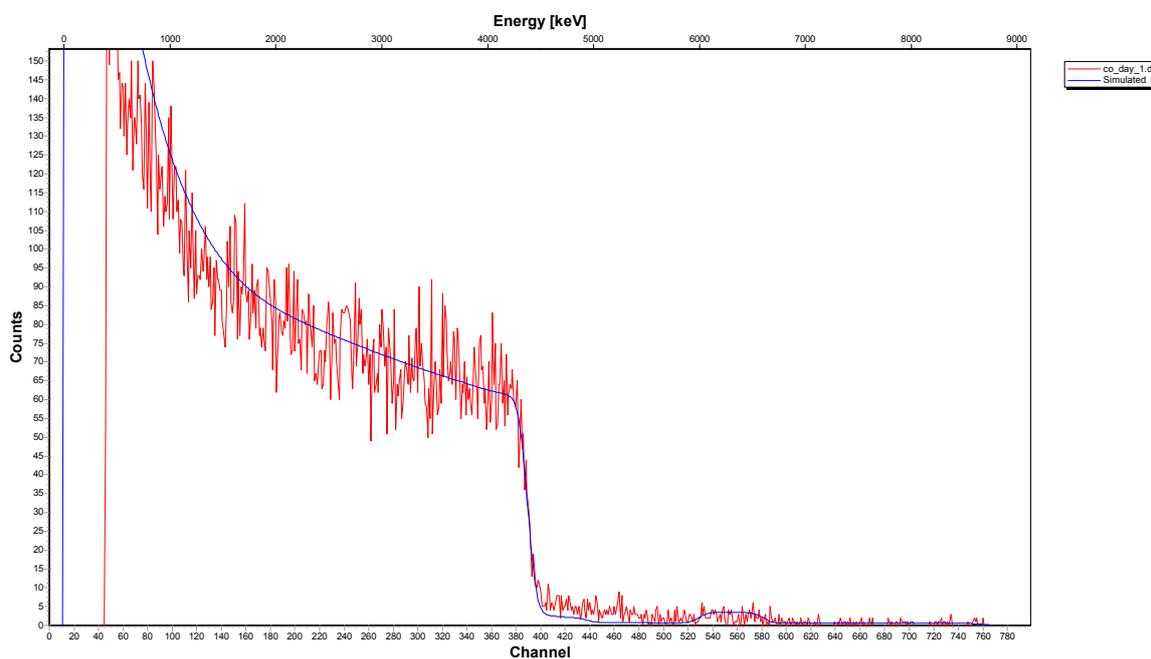
Figure 5. ^{12}C-RBS spectrum of calcite $\{10\bar{1}4\}$ interacted in an aqueous solution with a high Co^{2+} concentration ($[Co_{aq}]_{initial}$ = 1000 ppm) over one day.
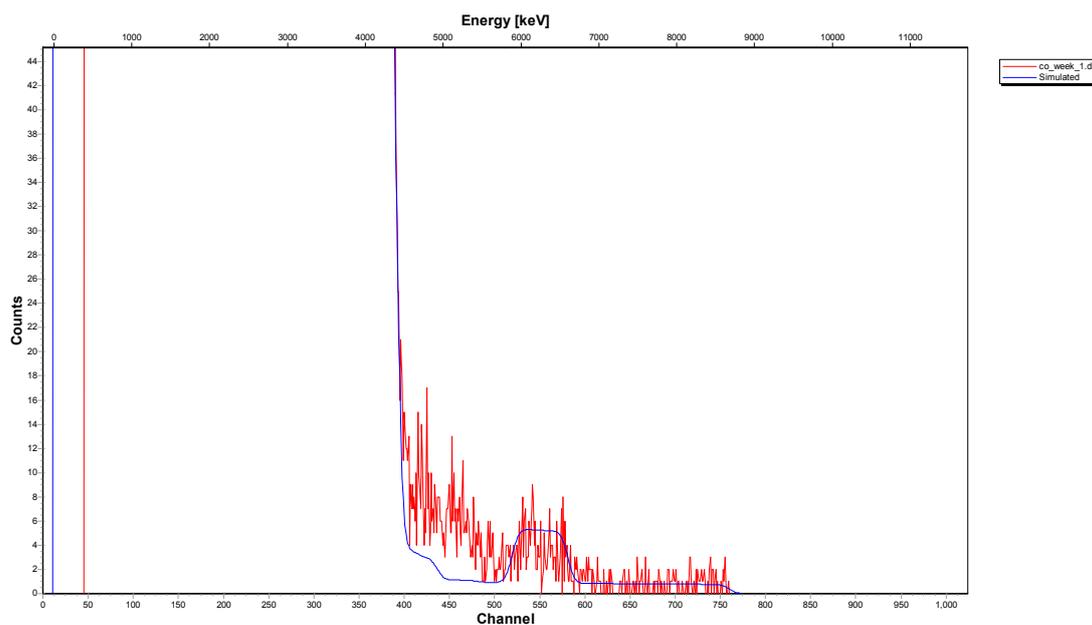
Figure 6. ^{12}C-RBS spectrum of calcite {10$\bar{1}$4} interacted in an aqueous solution with a high Co^{2+} concentration ([Co_{aq}]$_{initial}$ = 1000 ppm) over one week.

4. Conclusions

The main findings of this work can be summarized in the following points:

- According to macroscopic results, for both calcite powder and monocrystals interacted in an aqueous solution with a high Co^{2+} concentration ([Co_{aq}]$_{initial}$ = 1000 ppm, ~17 mM), dissolution occurs on the surface, causing systematic release of Ca^{2+} into solution. This runs in parallel to surface Co^{2+} sorption processes.
- The XPS surface study (analyzed at a depth of around 12 nm) confirmed that, indeed, sorption occurs at near-surface layers of calcite, initially by adsorption of Co–OH units and later by surface (co-)precipitation.
- The ^{12}C-RBS measurements on calcite {10$\bar{1}$4} indicated that co-precipitation is related to a Co^{2+}-bearing surface layer under the calcite surface, showing a thickness of 270 nm after one day of interaction and reaching 320 nm after one week and/or month.

Author Contributions: Jorge González-López, Ángeles Fernández-González, Amalia Jiménez, Athanasios Godelitsas and Manuel Prieto designed the research; Ioannis N. Pasias and Nikolaos S. Thomaidis contributed to the AAS measurements; Spyridon Ladas contributed to the XPS study; Georgios Provatas and Anastasios Lagogiannis contributed to the ^{12}C-RBS study; Jorge González-López and Athanasios Godelitsas wrote the paper.

Conflicts of Interest: The authors declare no conflict of interest.

Abbreviations

The following abbreviations are used in this manuscript:

AAS	Atomic absorption spectrometry
XPS	X-ray photoelectron spectroscopy
RBS	Rutherford backscattering spectrometry
SEXAFS	Surface-extended X-ray absorption fine structure
XSW	X-ray standing wave
AFM	Atomic force microscopy

References

1. Smith, I.; Carson, B.L. *Trace Metals in the Environment Vol 6. Cobalt an Apraisal of Environmental Exposure*; Ann Arbor Science Publishers Inc.: Ann Arbor, MI, USA, 1981; p. 1202.

2. Agency for Toxic Substances and Disease Registry. *Toxicological Profile for Cobalt*; U.S. Department of Health and Human Services, Public Health Service: Atlanta, GA, USA, 2004.

3. Kim, J.H.; Gibb, H.J.; Howe, P.D.; Sheffer, M. *Cobalt and Inorganic Cobalt Compounds*; Concise International Chemical Assessment Document; World Health Organization: Geneva, Switzerland, 2006; Volume 69.

4. Stipp, S.L.; Hochella, M.F.; Parks, G.A.; Leckie, J.O. Cd^{2+} uptake by calcite, solid-state diffusion, and the formation of solid-solution: Interface processes observed with near-surface sensitive techniques (XPS, LEED, and AES). *Geochim. Cosmochim. Acta* **1992**, *56*, 1941–1954. [CrossRef]

5. Godelitsas, A.; Astilleros, J.M. Dissolution, sorption/(re)precipitation, formation of solid solutions and crystal growth phenomena on mineral surfaces: implications for the removal of toxic metals from the environment. In *EMU Notes in Mineralogy—Volume 10: Ion Partitioning in Ambient-Temperature Aqueous Systems*; Prieto, M., Stoll, H., Eds.; European Mineralogical Union: Chantilly, VA, USA, 2010.

6. Godelitsas, A.; Charistos, D.; Dwyer, J.; Tsipis, C.; Filippidis, A.; Hatzidimitriou, A.; Pavlidou, E. Copper (II)-loaded heu-type zeolite crystals: Characterization and evidence of surface complexation with *N,N*-diethyldithiocarbamate anions. *Microporous Mesoporous Mater.* **1999**, *33*, 77–87. [CrossRef]

7. Morales, J.; Astilleros, J.M.; Jiménez, A.; Göttlicher, J.; Steininger, R.; Fernández-Díaz, L. Uptake of dissolved lead by anhydrite surfaces. *Appl. Geochem.* **2014**, *40*, 89–96. [CrossRef]

8. Prieto, M.; Cubillas, P.; Fernández-González, Á. Uptake of dissolved Cd by biogenic and abiogenic aragonite: A comparison with sorption onto calcite. *Geochim. Cosmochim. Acta* **2003**, *67*, 3859–3869. [CrossRef]

9. Astilleros, J.M.; Fernandez-Diaz, L.; Putnis, A. The role of magnesium in the growth of calcite: An AFM study. *Chem. Geol.* **2010**, *271*, 52–58. [CrossRef]

10. Kornicker, W.A.; Morse, J.W.; Damasceno, R.N. The chemistry of Co^{2+} interaction with calcite and aragonite surfaces. *Chem. Geol.* **1985**, *53*, 229–236. [CrossRef]

11. Xu, N.; Hochella, M.F.; Brown, G.E., Jr.; Parks, G.A. Co(II) sorption at the calcite-water interface: I. X-ray photoelectron spectroscopic study. *Geochim. Cosmochim. Acta* **1996**, *60*, 2801–2815. [CrossRef]

12. Cheng, L.; Sturchio, N.C.; Bedzyk, M.J. Local structure of Co^{2+} incorporated at the calcite surface: An X-ray standing wave and sexafs study. *Phys. Rev. B* **2000**, *61*, 4877–4883. [CrossRef]

13. Braybrook, A.L.; Heywood, B.R.; Jackson, R.A.; Pitt, K. Parallel computational and experimental studies of the morphological modification of calcium carbonate by cobalt. *J. Cryst. Growth* **2002**, *243*, 336–344. [CrossRef]

14. Freij, S.J.; Putnis, A.; Astilleros, J. Nanoscale observations of the effect of cobalt on calcite growth and dissolution. *J. Cryst. Growth* **2004**, *267*, 288–300. [CrossRef]

15. Katsikopoulos, D.; Fernández-González, Á.; Prieto, A.C.; Prieto, M. Co-crystallization of Co (II) with calcite: Implications for the mobility of cobalt in aqueous environments. *Chem. Geol.* **2008**, *254*, 87–100. [CrossRef]

16. Lee, Y.J.; Reeder, R.J. The role of citrate and phthalate during Co (II) coprecipitation with calcite. *Geochim. Cosmochim. Acta* **2006**, *70*, 2253–2263. [CrossRef]

17. González-López, J.; Ruiz-Hernández, S.; Fernández-González, Á.; Jiménez, A.; de Leeuw, N.; Grau-Crespo, R. Cobalt incorporation in calcite: Thermochemistry of $(Ca,Co)CO_3$ solid solutions from density functional theory simulations. *Geochim. Cosmochim. Acta* **2014**, *142*, 205–216. [CrossRef]

18. Xu, M.; Ilton, E.; Engelhard, M.; Qafokua, O.; Felmy, A.R.; Rosso, K.M.; Kerisit, S. Heterogeneous growth of cadmium and cobalt carbonate phases at the ($10\bar{1}4$) calcite surface. *Chem. Geol.* **2015**, *397*, 24–36. [CrossRef]

19. International Organization for Standardization. *Surface Chemical Analysis—X-ray Photoelectron Spectrometers—Calibration of Energy Scales*; ISO 15472:2001; International Organization for Standardization: Geneva, Switzerland, 2001.

20. International Organization for Standardization. *Surface Chemical Analysis—X-ray Photoelectron Spectrometers—Repeatability and Constancy of Intensity Scale*; ISO 24237:2005; International Organization for Standardization: Geneva, Switzerland, 2005.

21. Cubillas, P.; Kohler, S.; Prieto, M.; Chairat, C.; Oelkers, E.H. Experimental determination of the dissolution rates of calcite, aragonite, and bivalves. *Chem. Geol.* **2005**, *216*, 59–77. [CrossRef]

22. Morse, J.W. The kinetics of calcium carbonate dissolution and precipitation. *Rev. Mineral. Geochem.* **1983**, *11*, 227–264.

23. Parkhurst, D.L.; Appelo, C. *User's Guide to PHREEQC (Version 2): A Computer Program for Speciation, Batch-Reaction, One-Dimensional Transport, and Inverse Geochemical Calculations*; U.S. Geological Survey: Reston, VA, USA, 1999.

24. Petitto, S.C.; Marsh, E.M.; Carson, G.A.; Langell, M.A. Cobalt oxide surface chemistry: The interaction of CoO(100), Co_3O_4(110) and Co_3O_4(111) with oxygen and water. *J. Mol. Catal. A Chem.* **2008**, *281*, 49–58. [CrossRef]

25. Carroll, S.A.; Bruno, J.; Petit, J.-C.; Dran, J.-C. Interactions of U (VI), Nd, and Th (IV) at the calcite-solution interface. *Radiochim. Acta* **1992**, *58*, 245–252. [CrossRef]

26. Godelitsas, A.; Astilleros, J.M.; Hallam, K.; Harissopoulos, S.; Putnis, A. Interaction of calcium carbonates with lead in aqueous solutions. *Environ. Sci. Technol.* **2003**, *37*, 3351–3360. [CrossRef] [PubMed]

27. Godelitsas, A.; Kokkoris, M.; Misaelides, P. Investigation of the interaction of Greek dolomitic marble with metal aqueous solutions using Rutherford backscattering and X-ray photoelectron spectroscopy. *J. Radioanal. Nucl. Chem.* **2007**, *272*, 339–344. [CrossRef]

The Effect of Ca^{2+} and Mg^{2+} on the Dispersion and Flocculation Behaviors of Muscovite Particles

Jiayan Tang [1], Yimin Zhang [1,2,3,*] and Shenxu Bao [1,2]

[1]   School of Resources and Environmental Engineering, Wuhan University of Technology, Wuhan 430070, China; tangjiayan1205@126.com (J.T.); sxbao@whut.edu.cn (S.B.)

[2]   College of Resources and Environmental Engineering, Wuhan University of Science and Technology, Wuhan 430081, China

[3]   Hubei Provincial Engineering Technology Research Center of High Efficient Cleaning Utilization for Shale Vanadium Resource, Wuhan 430081, China

*   Correspondence: zym126135@126.com; Tel.: +86-27-6886-2876

Abstract: The dispersion and flocculation behavior of muscovite suspensions in the presence of Ca^{2+} and Mg^{2+} are relevant for industrial processing of pre-concentrated muscovite from stone coal, a primary source of vanadium. In this study, the dispersion and flocculation behavior were investigated by means of sedimentation, zeta potential, and ion absorption experiments, as well as the force between particles and ion speciation calculations. The results indicated that the dispersion and flocculation behavior of muscovite particles without excess ions were in qualitative agreement with the classical DLVO theory. The muscovite particles aggregated mainly due to basal surface-edge interactions in acidic suspensions but were dispersed in alkaline suspension by electrostatic repulsion of the total particle surface. In acidic suspensions, the ability of muscovite to form dispersions of muscovite was increased with the decrease in the electrostatic attraction between the basal surface and the edge caused by the compression of the electric double layers withCa^{2+} and Mg^{2+}. In alkaline suspension, the main adsorption form of Ca^{2+} and Mg^{2+} on muscovite surface was the ion-hydroxy complexes. The flocculation behavior of muscovite was affected by the static bridge effect of the ion-hydroxy complexes.

Keywords: muscovite; calcium and magnesium ions; zeta potential; DLVO; dispersion and flocculation

1. Introduction

Muscovite is the primary vanadium-bearing mineral in stone coal [1], which is an important resource of vanadium making up more than 87% of the domestic reserves of vanadium in China [2]. Hence, efficient processing methods of the vanadium-bearing stone coal has become increasingly important, and it has been confirmed that the pre-concentration of muscovite from the stone coal by roasting-flotation was an effective method [3]. Previous studies have found that the suspension produced by the roasted stone coal and water contain large quantities of metal ions and micro-fine particles. Metal ions and micro-fine particles can seriously reduce the separation efficiency of the pre-concentration of muscovite by flotation [3,4]. Hence, the removal of micro-fine particles has an important role in the pre-concentration steps of muscovite. Meanwhile, the effect of their removal depends on the dispersion and flocculation behavior of the specific minerals, so the study of the dispersion and flocculation behavior of muscovite is important.

The simplest framework to address the dispersion and flocculation behavior of minerals is the classical DLVO theory presented by Derjaguin, Landau, Verwey, and Overbeek [5]. The application of DLVO theory for fine particles and colloid has long been considered to be credible. This theory suggests

that the total potential energy between charged interfaces is described as the sum of the Van der Waals attraction potential and the electrostatic potential. The strength of the Van der Waals attraction potential is related to the material itself and the distance between particles, but the roughness of the particle surface may also contribute [6,7]. The electrostatic potential is principally influenced by the surface charge density and the composition of ions in solution [8–11]. The surface charge determined the magnitude of this force, while multivalent metal ions may adsorb strongly to negatively charged interfaces, thereby reducing the magnitude of the potential [12–14].

Such interactions of metal ions adsorbed on the mineral surface have broad implications in mineral processing. The flotation of spodumene with fatty acid anionic collector can be implemented by adding Ca^{2+} and Fe^{3+} [15]. Ca^{2+} can render the positive charge of the surface of magnetite in the pH range from 3 to 10 and reduce the dispersion ability of silicates [16,17]. It was also evidenced that Ca^{2+} and Mg^{2+} can affect the surface properties of apatite, which can reduce the recovery of flotation [18,19]. Chlorite and lizardite, but also quartz, can be floated with xanthate in the pH range from 7 to 10 by adding Cu^{2+} and Ni^{2+} [20]. Cu^{2+} and Ca^{2+} can enhance the adsorption density of carboxymethyl cellulose (CMC) on the surface of chlorite [21]. It has been shown that Ca^{2+} and Mg^{2+} adsorbed on the surface of diaspore could cause the compression of the electric double layer, and result in the decrease of the repulsion force between diaspore particles [22,23]. Previous studies have found that the valence of cation plays a major role in the ability of dispersion of diaspore, kaolinite, illite, and pyrophyllite with sodium carbonate and sodium hexametaphosphate suspensions [24]. The mechanism of metal ion adsorption on the mineral surface has also been studied, relying mainly on a hydroxy complex hypothesis and surface precipitation theory. James and Hu et al. [25,26] suggest that the key form was the precipitate of metal hydroxide. Others studies have shown that the dominant species was the hydrolyzed metal ions. For high valence and small radius ions, like Fe^{3+}, the dominant species would be in the form of hydroxide precipitate, i.e., $Fe(OH)_3$. While for the low valence and large radius ions, like Ca^{2+}, the effective species would mainly be hydroxy complexes of the metal ions, i.e., $Ca(OH)^+$ [27].

Previous studies have been based on the effect of metal ions on the flotation behavior of minerals, but very few studies have focused on the actual dispersion and flocculation properties. In this study, the dispersion and flocculation behavior of muscovite influenced by Ca^{2+} and Mg^{2+} were investigated. The objective was to improve understanding of the dispersion and flocculation behavior of muscovite and thus improve the effect of pre-concentration of vanadium-bearing muscovite.

2. Experimental Section

2.1. Materials

Natural pure muscovite was obtained from the town of Lingshou in Hebei province, China. The chemical composition of the sample is listed in Table 1, which is similar to the theoretical chemical composition of muscovite (SiO_2 45.2%, Al_2O_3 38.5%, K_2O 11.8%, H_2O 4.5%). The sample was hand-picked and ground to $-25~\mu m$ in an agitating mill with a zirconia ball. The particle size of the sample was measured by BT-9300H laser particle size analyzer (Bettersize instruments Ltd., Dandong, China), and the result is given in Figure 1. The D90 is 21.69 μm and the average particle diameter is 10.75 μm. One fraction of the sample was further ground to about $-5~\mu m$ by an agate mortar for zeta potential measurements. The Ca^{2+} and Mg^{2+} solutions were obtained from analytical reagents of $CaCl_2$ and $MgSO_4$ purchased from Sinopharm Chemical Reagent Co., Ltd. (Wuhan, China). HCl and NaOH were used for the pH adjustment of the suspension. The pH of the suspension was monitored using a digital pH meter. All experiments were carried out at room temperature of $22 \pm 2~^{\circ}C$ with deionized water.

Table 1. Chemical composition of pure minerals (wt %).

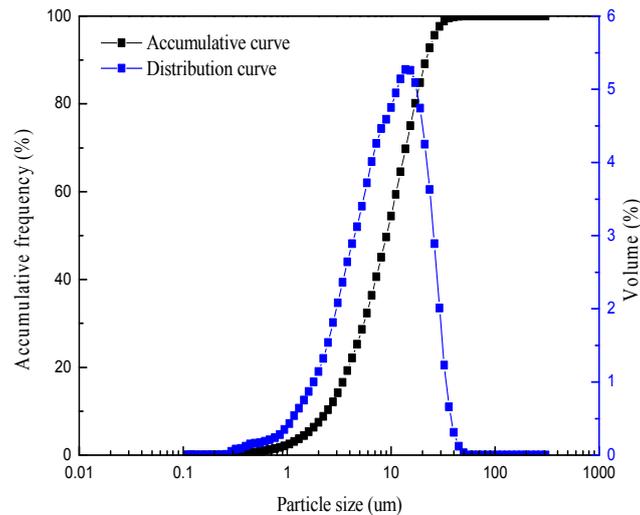| Chemical Composition	Na$_2$O	MgO	Al$_2$O$_3$	SiO$_2$	K$_2$O	Fe$_2$O$_3$
Content	0.50	0.92	30.64	46.95	10.57	5.12

Figure 1. Particle size of the sample.

2.2. Methods

2.2.1. Sedimentation Test

To evaluate the dispersion properties, 2 g of muscovite was placed into a beaker with 50 mL of deionized water, agitated for 10 min in UP500HE ultrasonic oscillators (Leijunda Ultrasonic Electronic Equipment Ltd., Nanjing, China), and transferred into a 100-mL glass measuring cylinder. Metal ions and HCl or NaOH were added into the measuring cylinder with water up to 100 mL. The cylinder was turned upside down three times and was set aside for 10 min. The upper part, approximately 50% of the total volume, was siphoned out to a beaker for pH measurement. The sediment and the upper part were collected, dried, and weighed. The degree of dispersion (D) was calculated as

$$D = m_{sed}/(m_{susp} + m_{sed}) \times 100\%, \tag{1}$$

where m_{susp} is the mass of the upper part, and m_{sed} is the mass of the sediment.

2.2.2. Zeta Potentials Measurement

The zeta potentials of the sample in the different suspension were measured by Zetasizer Nano ZS90 (Malvern Instrument Co., Malvern, UK). The sample (2 mg) was placed in 100 mL of deionized water, and the suspension was conditioned with Ca^{2+} or Mg^{2+} ions over the pH range from 2 to 12. An average zeta potential value of at least six individual measurements was recorded.

2.2.3. Calculation of Interfacial Energy between Particles

Based on the classical DLVO theory, the total potential energy is described as the sum of the Vander Waals attraction potential and the electrostatic potential [22].

$$V_T = V_W + V_S, \tag{2}$$

where V_W is the Van der Waals attraction potential and V_S is the electrostatic potential.

The DLVO theory can be used to model perfectly smooth surfaces of certain geometries (i.e., flat surfaces spheres, or cylinders). Here, the muscovite was assumed as spherical particle.

The Van der Waals attraction potential was calculated as

$$V_W = -\frac{A_{131}}{6H} \times \frac{R_1 R_2}{R_1 + R_2}, \tag{3}$$

where A_{131} is the Hamaker constant, H is the distance between the particles, and R is the particle radius.

Meanwhile, the electrostatic potential was calculated as

$$V_S = \frac{\pi \varepsilon R_1 R_2}{R_1 + R_2} \left(\phi_{01}^2 + \phi_{02}^2 \right) \left(\frac{2\phi_{01}\phi_{02}}{\phi_{01}^2 + \phi_{02}^2} p + q \right);$$ (4)

$$p = \ln \left[\frac{1 + \exp(-\kappa H)}{1 - \exp(-\kappa H)} \right]; \text{ and}$$ (5)

$$q = \ln \left[1 - \exp(-2\kappa H) \right],$$ (6)

where ϕ_0 is approximatively replaced the measured value of zeta potential, R is the particle radius, and the Debye length κ^{-1} represents the thickness of the double layer. ε is the dielectric constant [28,29].

2.2.4. Adsorption Capacity Measurement

The concentration of Ca^{2+} and Mg^{2+} ions was measured by a Prodigy 7 inductively coupled plasma-optical emission spectrometer (Leeman Labs Inc., Hudson, NH, USA). Again, 2 g of muscovite was mixed with Ca^{2+} or Mg^{2+} ions (1×10^{-3} mol/L) in a suspension of 100 mL in a glass measuring cylinder, and HCl and NaOH were used for pH adjustment. The cylinder was turned upside down three times and set aside for 10 min. The solid particles were separated by centrifugation for 12 min with 2000 r/min, and the concentration of the Ca^{2+} or Mg^{2+} ions in the supernatant was measured. The amount adsorbed was calculated as

$$\Gamma = \frac{(C_0 - C_{eq.})}{m} V$$ (7)

where Γ is the unit mass mineral adsorption quantity, C_0 is the initial concentration of the ions, $C_{eq.}$ is the ion concentration in the supernatant, V is volume (100 mL), and m is the quality of muscovite.

3. Results and Discussion

3.1. Sedimentation Behavior of Muscovite

The sedimentation behavior of muscovite in deionized water, with and without the Ca^{2+} and Mg^{2+} ions, were investigated at different pH levels.

It can be seen from Figures 2 and 3 that, in the absence of excess Ca^{2+} and Mg^{2+} ions, the sedimentation yield of the sample decreased with increasing pH, within a range from 1 to 6, after the yield was around 50% in a pH range from 6 to 12, indicating that the muscovite particles aggregated in an acidic solution and dispersed in alkaline suspension.

In the presence of Ca^{2+} (Figure 2), the sedimentation yield decreased with increasing pH to a certain point and then increased again, with an inflexion point near pH = 4. The sedimentation yield decreased in pH range from 2 to 4 compared with no ions, which indicated that the flocculation behavior of muscovite was hindered by Ca^{2+}. With pH being > 4, sedimentation yield increased as a function of pH, indicating that the flocculation of muscovite particles was caused by the addition of Ca^{2+}. Increasing the concentration of Ca^{2+}, the sedimentation yield basically remained unchanged in acidic suspension, but increased in alkaline suspension. With the presence of Mg^{2+} (Figure 3), the trend of sedimentation was basically similar to that with Ca^{2+}. The difference was that the sedimentation yield increased first and decreased later at around pH = 9 with 1×10^{-3} mol/L Mg^{2+} and at around pH = 10 with 5×10^{-3} mol/L Mg^{2+}.

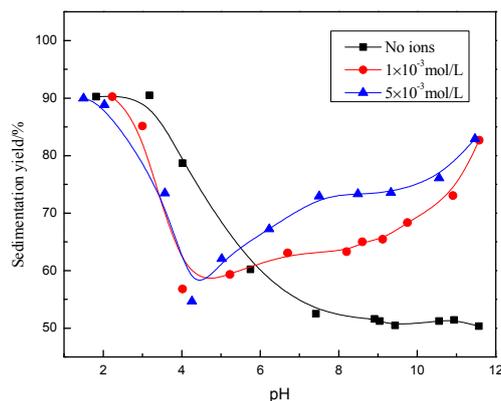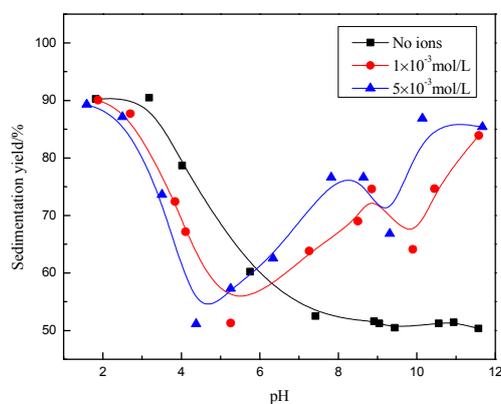**Figure 2.** The effect of pH value on dispersion and flocculation of mineral with the presence of Ca^{2+}.

Figure 3. Effect of pH value on dispersion and flocculation of mineral with the presence of Mg^{2+}.

3.2. Zeta Potential Analysis

Changes in the pH of suspensions can influence the surface properties of minerals [30]. Zeta potentials of muscovite as a function of pH in deionized water with and without Ca^{2+} and Mg^{2+} is presented in Figure 4. It can be seen that the zeta potentials of muscovite were negative over a wide range of pH from 2 to 14 and decreased with the increase in pH, which is consistent with previous studies [31–33]. The trend of the decreasing zeta potential with an increase in pH is similar to the presence of Ca^{2+} and Mg^{2+}, but the absolute value of the potential was lower and found to decrease with increasing ion concentration. Surprisingly, in high alkaline suspension containing Mg^{2+}, namely, when the pH range from 10 to 12, the negatively charged surface became positively charged.

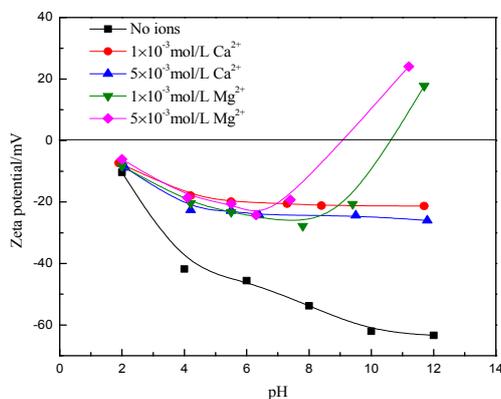**Figure 4.** Zeta potentials of muscovite as a function of pH in deionized water with Ca^{2+} and Mg^{2+}.

3.3. Calculation of Surface Energy of Particles Using Classic DLVO Theory

Assuming spherical particle geometry, the interaction energy values of the particles in the presence or absence of Ca^{2+} and Mg^{2+} was calculated according to the classical DLVO theory, with the results from the zeta potential measurements, and the Hamaker constant of $A_{131} = 2.2 \times 10^{-20}$ J, the dielectric constant of $\varepsilon = 6.95 \times 10^{-10}$ $C^2 \cdot J^{-1} \cdot m^{-1}$, $\kappa = 0.104$ nm^{-1} [28,29], and $R_1 = R_2 = 10.75/2$ μm. As can be seen from the results in Figure 5, the energy barrier increased with increasing pH, so the ability to from a dispersion was improved with increasing pH, which was found to be consistent with the settling experiments. However, the presence of Ca^{2+} and Mg^{2+} can reduce the surface potential and thus reduce the interaction energy values of the particles. This should increase flocculation, but it is in contrast to the experimental results presented earlier.
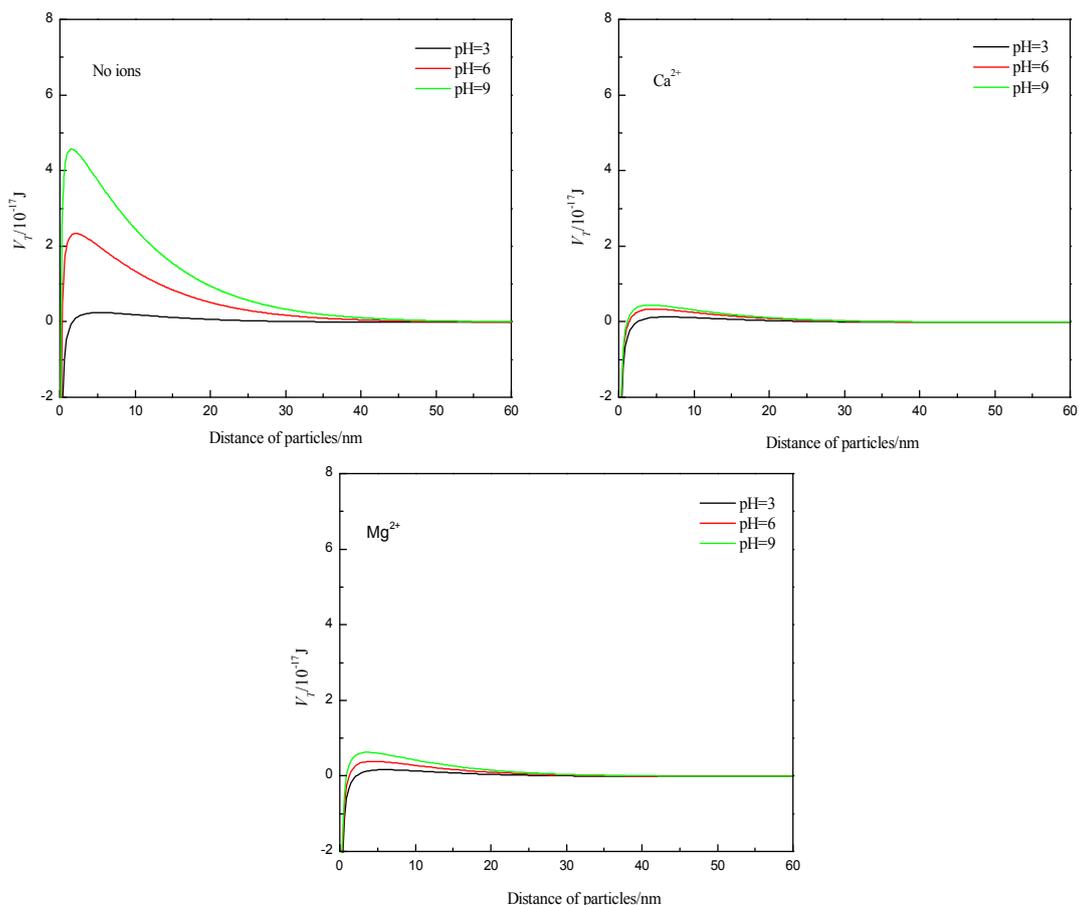
Figure 5. Total interaction energy of particles at different pH values without and with Ca^{2+}, Mg^{2+}.

Muscovite is a kind of layered crystal structure of mineral, which is formed from an octahedral layer sandwiched between two identical tetrahedral (SiO_4) layers. So particle–particle flocculation may occur through three types of structural interaction: basal surface (001)—basal surface, basal surface-edge, and edge-edge. In general, the measurement of zeta potential can represent the mineral surface electrical property; however, considering the crystal anisotropy of muscovite, the zeta potential of muscovite is the overall electrical properties of the basal surface and the edge. The basal surface of muscovite has a negative charge, which is not affected by pH [31]. As a result, its value can be approximated to the zeta potential when the pH value of the suspension is equal to the point of zero charge of the edge (PZC_{edge}). When the net charge of the surface is zero, the PZC is defined as a point on the pH-scale, and the PZC_{edge} of muscovite in theory is 6.84 [34]. The potential computation formula of the edge is as follows: $\varphi_{edge} = 0.059 \left(PZC_{edge} - pH \right)$. Considering the smaller edge area

compared to the basal surface area, the R_{edge} was assumed to be one tenth of the $R_{basal \cdot surface}$(10.75/2 μm). The interaction energy values of the particles were re-calculated, and the results are shown in Figure 6. The results show that the interaction energies of the form of basal surface-edge were negative at pH values of 3 and 6, which means that the particles can undergo flocculation, consistent with the experimental phenomenon, testifying that the particles were aggregated in acidic suspension mainly by the form of the basal surface-edge. Adding the 1×10^{-3} mol/L Ca^{2+} and Mg^{2+}, the surface potential was reduced, and the electrostatic attraction between the basal surface and the edge was then also reduced, so the dispersion increased, which was also consistent with the experimental phenomenon.
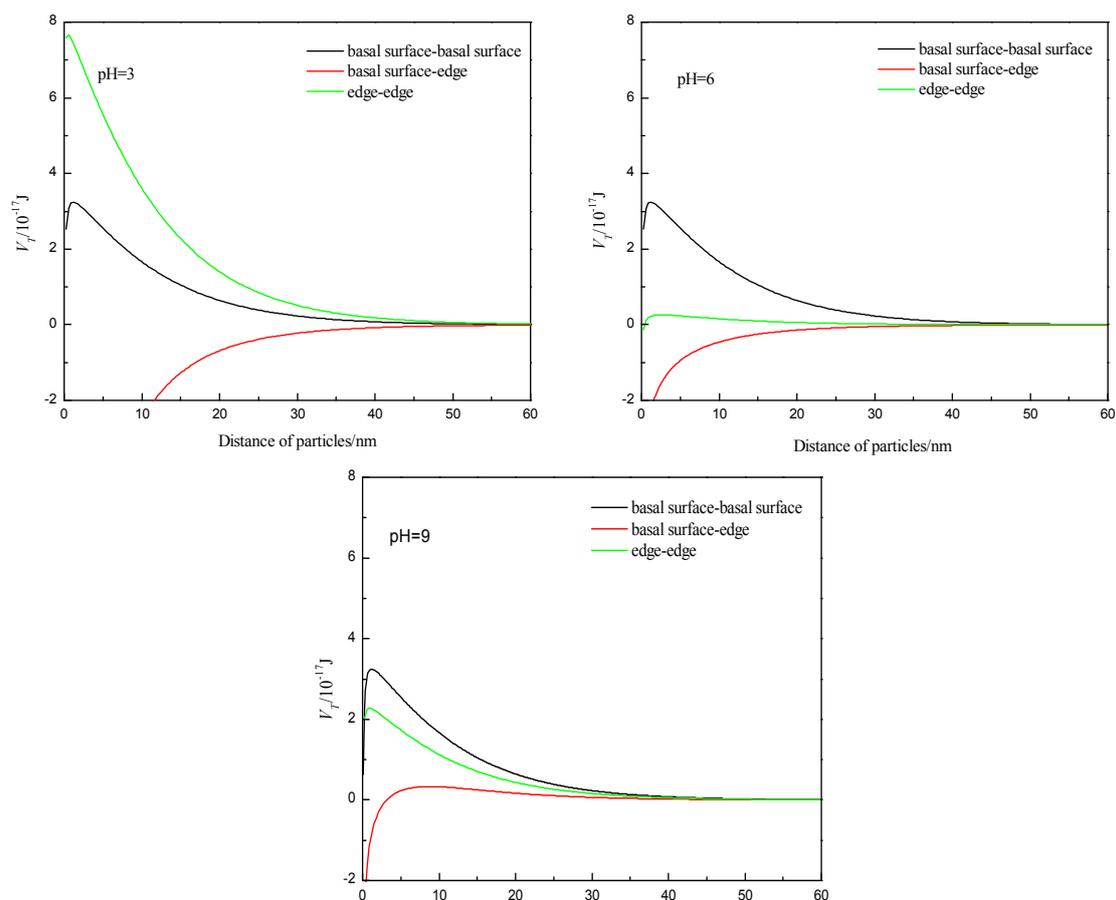
Figure 6. Total interaction energy of three kinds of form at different pH values.

3.4. Metal Species in Different Solution

In the solution with different pH values, the species and the content of the species in the presence of 1×10^{-3} mol/L Ca^{2+} or Mg^{2+} ions were analyzed and calculated using the stability constants for hydroxide formation, and the results are shown in Figures 7 and 8, respectively. When pH < 12, the dissociative Ca^{2+} and $Ca(OH)^+$ are the key species in the solution. Ca^{2+} and $Ca(OH)^+$ lowered the absolute value of zeta potential of muscovite by compressing electric double layer [22,23], which was consistent with the zeta potential analysis. Mg^{2+} and $Mg(OH)^+$ are the key species in the solution at pH < 9.92, and they had a similar effect to that of Ca^{2+} and $Ca(OH)^+$. However, $Mg(OH)_2(s)$ is the main species at pH > 9.92. At a pH range from 10 to 12, the zeta potential was zero, caused by $Mg(OH)_2(s)$, and this phenomenon agrees with the results researched by Krishnan and Iwasaki [35].
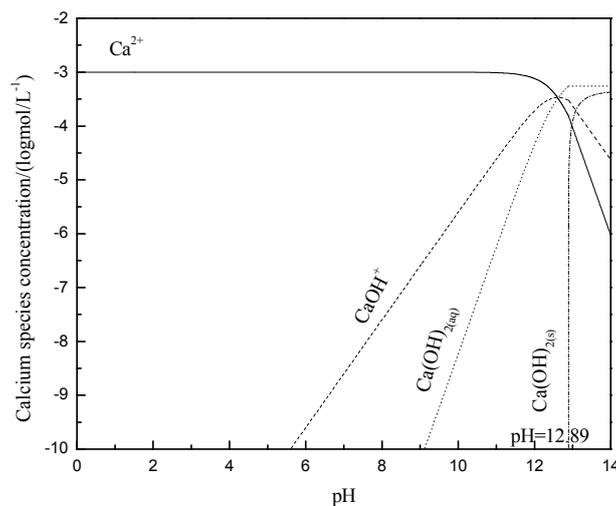
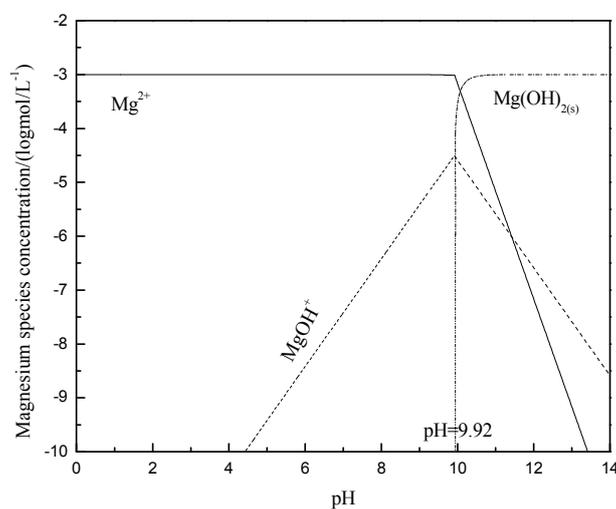**Figure 7.** Calculated concentration of calcium species in solution with 1×10^{-3} mol/L Ca^{2+}.

**Figure 8.** Calculated concentration of magnesium species in solution with 1×10^{-3} mol/L Mg^{2+}.

The adsorption capacity of Ca^{2+} and Mg^{2+} on muscovite is shown in Figure 9. When pH < 4, there was less adsorption capacity of Ca^{2+} and Mg^{2+} ions on muscovite. When pH > 4, the adsorption capacity of calcium and magnesium ions began to increase, which was consistent with the sedimentation experiment, namely, the agglomeration increased when pH > 4. Combined with Figures 7 and 8, it can be found that the ion and the hydroxyl complexes were the key species in the solution; the concentration of the hydroxyl compounds and the adsorption quantity all increased with the increase in the pH. Thus, it was confirmed that the hydroxy complex was the key form adsorbed on the muscovite, which may make the partial surface of muscovite with a positive charge. The flocculation of muscovite was caused by a bridging effect of the hydroxy complex, as shown in Figure 10. With the increase of pH and the concentration of Ca^{2+} and Mg^{2+}, the hydroxy complex increased, and the bridging effect increased, so the sedimentation rate increased. $Mg(OH)_2(s)$ was the main form when pH > 9.92, which led to the changing property of the suspension system, thus making the anomalous changes of sedimentation rate when the pH neared 9.92.
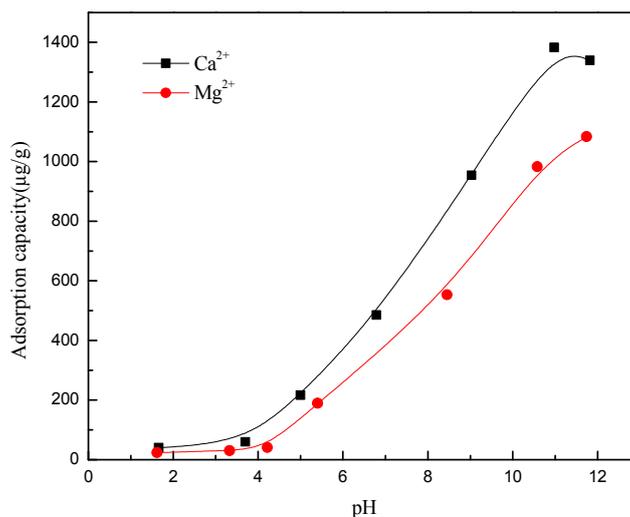
Figure 9. Adsorption capacity of Ca^{2+} and Mg^{2+} at different pH levels.
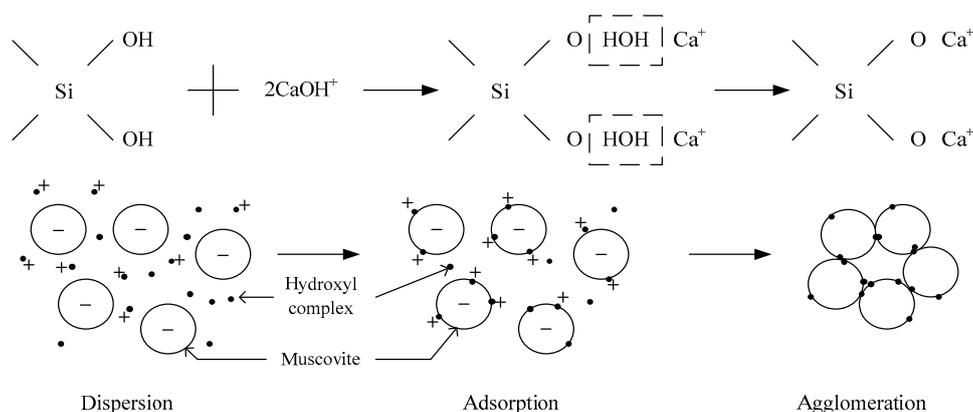
Figure 10. Bridging effect of hydroxy complex.

4. Conclusions

The conclusions from this research can be summarized as follows:

1. The dispersion and flocculation behavior of muscovite in the absence of excess Ca^{2+} and Mg^{2+} agree with the classic DLVO theory based on the crystal anisotropy. The muscovite particles were aggregated in acidic suspension mainly by the form of basal surface-edge.
2. The hydroxy complex of Ca^{2+} and Mg^{2+} was the main adsorption form on the mineral surface. The flocculation of muscovite was caused by a bridging effect of the hydroxy complex, which destroyed the excellent dispersion stability in alkaline suspension.

Author Contributions: Jiayan Tang conceived and designed the experiments, Jiayan Tang performed the experiments; Jiayan Tang analyzed the data; Yimin Zhang contributed reagents, materials, and analysis tools; Jiayan Tang and Shenxu Bao wrote the paper.

Conflicts of Interest: The authors declare no conflict of interest.

References

1. Zhang, Y.M.; Hu, Y.J.; Bao, S.X. Vanadium emission during roasting of vanadium-bearing stone coal in chlorine. *Miner. Eng.* **2012**, *30*, 95–98. [CrossRef]

2. Zhu, X.B.; Zhang, Y.M.; Huang, J.; Liu, T.; Wang, Y. A kinetics study of multi-stage counter-current circulation acid leaching of vanadium from stone coal. *Int. J. Miner. Process.* **2012**, *114–117*, 1–6. [CrossRef]

3. Zhao, Y.L.; Zhang, Y.M.; Liu, T.; Chen, T.J.; Bian, Y.; Bao, S.X. Pre-concentration of vanadium from stone coal by gravity separation. *Int. J. Miner. Process.* **2013**, *121*, 1–5. [CrossRef]

4. Zhao, Y.L.; Zhang, Y.M.; Song, S.X.; Chen, T.J.; Bao, S.X. Behaviors of impurity elements Ca and Fe in vanadium-bearing stone coal during roasting and its control measure. *Int. J. Miner. Process.* **2016**, *148*, 100–104. [CrossRef]

5. Valmacco, V.; Elzbieciak-Wodka, M.; Herman, D.; Trefalt, G.; Maroni, P.; Borkovec, M. Forces between silica particles in the presence of multivalent cations. *J. Colloid Interface Sci.* **2016**, *472*, 108–115. [CrossRef] [PubMed]

6. Ackler, H.D.; French, R.H.; Chiang, Y.M. Comparisons of Hamaker constants for ceramic systems with intervening vacuum or water: From force laws and physical properties. *J. Colloid Interface Sci.* **1996**, *179*, 460–469. [CrossRef]

7. Elzbieciak-Wodka, M.; Popescu, M.N.; Ruiz-Cabello, F.J.M.; Trefalt, G.; Maroni, P.; Borkovec, M. Measurements of dispersion forces between colloidal latex particles with the atomic force microscope and comparison with Lifshitz theory. *J. Chem. Phys.* **2014**, *140*, 104906. [CrossRef] [PubMed]

8. Morag, J.; Dishon, M.; Sivan, U. The governing role of surface hydration in ion specific adsorption to silica: An AFM-based account of the Hofmeister universality and its reversal. *Langmuir* **2013**, *29*, 6317–6322. [CrossRef] [PubMed]

9. Popa, I.; Sinha, P.; Finessi, M.; Maroni, P.; Papastavrou, G.; Borkovec, M. Importance of charge regulation in attractive double-layer forces between dissimilar surfaces. *Phys. Rev. Lett.* **2010**, *104*, 228301. [CrossRef] [PubMed]

10. Trefalt, G.; Behrens, S.H.; Borkovec, M. Charge Regulation in the Electrical Double Layer: Ion Adsorption and Surface Interactions. *Langmuir* **2015**, *32*, 380–400. [CrossRef] [PubMed]

11. Dishon, M.; Zohar, O.; Sivan, U. From repulsion to attraction and back to repulsion: The effect of NaCl, KCl, and CsCl on the force between silica surfaces in aqueous solution. *Langmuir* **2009**, *25*, 2831–2836. [CrossRef] [PubMed]

12. Pashley, R.M.; Israelachvili, J.N. DLVO and hydration forces between mica surfaces in Mg^{2+}, Ca^{2+}, Sr^{2+}, and Ba^{2+} chloride solutions. *J. Colloid Interface Sci.* **1984**, *97*, 446–455. [CrossRef]

13. Ruiz-Cabello, F.J.M.; Trefalt, G.; Csendes, Z.; Sinha, P.; Oncsik, T.; Szilagyi, I.; Maroni, P.; Borkovec, M. Predicting aggregation rates of colloidal particles from direct force measurements. *J. Phys. Chem. B* **2013**, *117*, 11853–11862. [CrossRef] [PubMed]

14. Zohar, O.; Leizerson, I.; Sivan, U. Short range attraction between two similarly charged silica surfaces. *Phys. Rev. Lett.* **2006**, *96*, 177802. [CrossRef] [PubMed]

15. Yu, F.; Wang, Y.; Wang, J.; Xie, Z. Investigation on different behavior and mechanism of Ca(II) and Fe(III) adsorption on spodumene surface. *Physicochem. Probl. Miner.* **2014**, *50*, 535–550.

16. Potapova, E.; Grahn, M.; Holmgren, A.; Hedlund, J. The effect of calcium ions and sodium silicate on the adsorption of a model anionic flotation collector on magnetite studied by ATR-FTIR spectroscopy. *J. Colloid Interface Sci.* **2010**, *345*, 96–102. [CrossRef] [PubMed]

17. Potapova, E.; Yang, X.; Grahn, M.; Holmgren, A.; Forsmo, S.P.E.; Fredriksson, A.; Hedlund, J. The effect of calcium ions, sodium silicate and surfactant on charge and wettability of magnetite. *Colloids Surf. A Physicochem. Eng. Asp.* **2011**, *386*, 79–86. [CrossRef]

18. Dos Santos, M.A.; Santana, R.C.; Capponi, F.; Ataíde, C.H.; Barrozo, M.A. Effect of ionic species on the performance of apatite flotation. *Sep. Purif. Technol.* **2010**, *76*, 15–20. [CrossRef]

19. Dos Santos, M.A.; Santana, R.C.; Capponi, F.; Ataíde, C.H.; Barrozo, M.A. Influence of the water composition on the selectivity of apatite flotation. *Sep. Purif. Technol.* **2012**, *47*, 606–612. [CrossRef]

20. Fornasiero, D.; Ralston, J. Cu(II) and Ni(II) activation in the flotation of quartz, lizardite and chlorite. *Int. J. Miner. Process.* **2005**, *76*, 75–81. [CrossRef]

21. Feng, Q.M.; Feng, B.; Lu, Y.P. Influence of copper ions and calcium ions on adsorption of CMC on chlorite. *Trans. Nonferr. Met. Soc. China* **2013**, *23*, 237–242. [CrossRef]

22. Zhou, Y.L.; Hu, Y.H.; Wang, Y.H. Effect of metallic ions on dispersibility of fine diaspore. *Trans. Nonferr. Met. Soc. China* **2011**, *21*, 1166–1171. [CrossRef]

23. Zhou, Y.L.; Wang, Y.H.; Hu, Y.H.; Sun, D.X.; Yu, M.J. Influence of metal ions on floatability of diaspore and kaolinite. *J. Cent. South Univ.* **2009**, *40*, 268–274.

24. Wang, Y.H.; Chen, X.H.; Zhou, Y.L. Effect of metal ions on dispersity of fine aluminum silicate minerals. *Met. Mine* **2007**, *5*, 38–43.

25. James, R.O.; Healy, T.W. Adsorption of hydrolyzable metal ions at the oxide—Water interface. III. A thermodynamic model of adsorption. *J. Colloid Interface Sci.* **1972**, *40*, 65–81. [CrossRef]

26. Hu, Y.H.; Wang, D.Z. Mechanism of adsorption and activation flotation of metallic ion on oxide mineral-water interface. *J. Cent. South Inst. Min. Metall.* **1987**, *5*, 501–508.

27. Yu, F.S.; Wang, Y.H.; Wang, J.M.; Xie, Z.F.; Zhang, L. First-principle investigation on mechanism of Ca ion activating flotation of spodumene. *Rare Met.* **2014**, *33*, 358–362. [CrossRef]

28. Luo, Z.J.; Hu, Y.H.; Wang, Y.H.; Qiu, G.Z. Mechanism of dispersion and aggregation in reverse flotation for bauxite. *Chin. J. Nonferr. Met.* **2001**, *11*, 683–686.

29. Qiu, G.Z.; Hu, Y.H.; Wang, D.Z. *Interactions between Particles and Flotation of Fine Particles*; Central South University: Changsha, China, 1993.

30. Fuerstenau, D.W. Zeta potentials in the flotation of oxide and silicate minerals. *Adv. Colloid Interface Sci.* **2005**, *114*, 9–26. [CrossRef] [PubMed]

31. Nishimura, S.; Tateyama, H.; Tsunematsu, K.; Jinnai, K. Zeta potential measurement of muscovite mica basal plane-aqueous solution interface by means of plane interface technique. *J. Colloid Interface Sci.* **1992**, *152*, 359–367. [CrossRef]

32. Nosrati, A.; Addai-Mensah, J.; Skinner, W. Muscovite clay mineral particle interactions in aqueous media. *Powder Technol.* **2012**, *219*, 228–238. [CrossRef]

33. Xu, L.; Wu, H.; Dong, F.; Wang, L.; Wang, Z.; Xiao, J. Flotation and adsorption of mixed cationic/anionic collectors on muscovite mica. *Miner. Eng.* **2013**, *41*, 41–45. [CrossRef]

34. Liu, X.W. Crystal Structure and Surface Property of Diaspore and Phyllosilicate Minerals. Ph.D. Thesis, Central South University, Changsha, China, 2003.

35. Krishnan, S.V.; Iwasaki, I. Floc formation in quartz—$Mg(OH)_2$ system. *Colloids Surf.* **1985**, *15*, 89–100. [CrossRef]

The Effect of Chloride Ions on the Activity of Cerussite Surfaces

Qicheng Feng [1], Shuming Wen [1,*], Qinbo Cao [1,*], Jiushuai Deng [1] and Wenjuan Zhao [2]

[1] State Key Laboratory of Complex Nonferrous Metal Resources Clean Utilization,
Faculty of Land Resource Engineering, Kunming University of Science and Technology,
Kunming 650093, China; fqckmust@126.com (Q.F.); dengshuai689@126.com (J.D.)

[2] Kunming Metallurgical Research Institute, Kunming 650031, China; wenjuan19880718@163.com

* Correspondence: shmwen@126.com (S.W.); cabdxx@163.com (Q.C.); Tel.: +86-871-515-3445 (S.W.)

Abstract: Chloride ions were found to potentially increase activity of cerussite surfaces. Dissolution experiments, zeta potential measurements, X-ray photoelectron spectroscopy (XPS) studies, and density functional theory (DFT) computation were conducted in this study. Dissolution experiments showed that the lead ion concentrations in the NaCl solution system were lower than those in the deionized water system and that the lead ion concentrations in NaCl + Na$_2$S aqueous systems decreased by approximately one order of magnitude compared with that in the Na$_2$S system alone. Results of zeta potential measurements revealed that the pretreatment with chloride ions of cerussite caused a more positive zeta potential than that without chloride ions. XPS analysis results indicated that the number of lead ions on the mineral surface increased after cerussite was treated with chloride ions. Results of DFT computation implied that the number of lead atoms on the mineral surface increased and that the activity improved after PbCl$^+$ was adsorbed onto the cerussite surface. The contribution of chloride ions to the activity on the mineral surface is attributed to the increase in the number of active sites and enhancement in the activity of these sites, resulting in improved sulfidization and flotation performance.

Keywords: cerussite; active sites; chloride ions; adsorption; DFT

1. Introduction

Lead oxide minerals are an important lead resource, and cerussite is a typical lead oxide mineral. With increasing lead consumption, lead sulfide ores cannot meet the requirements of lead smelting; lead oxide resources must be efficiently utilized to address the imbalance between metal lead supply and demand [1–3]. Sulfidization flotation has been the most commonly and commercially used method for concentration and pretreatment of lead oxide minerals, and the most critical stage in this process is sulfidization [4–6]. Numerous sulfidization techniques including mechanochemical sulfidization [7,8], hydrothermal sulfidization [2,9], and sulfidization roasting [1,10] have been attempted to sulfidize lead oxide materials. However, only the surface sulfidization method is available because of technical and economic conditions. Nevertheless, this method continues to exhibit deficiencies, such as low sulfidization efficiency, weak sulfidization products, abundant dosage of sulfidization agents and collectors, as well as low lead recovery. Thus, surface sulfidization reinforcement is crucial to concentrate lead oxide minerals by flotation.

Flotation reagents cannot be adsorbed onto mineral surfaces with a homogeneous distribution, and they initially interact with the active sites on the mineral surface. Therefore, the number and activity of active sites on the mineral surface are vital to the surface sulfidization method. Adding chloride ions prior to sulfidization can greatly enhance the flotation recovery of cerussite [11].

This excellent flotation performance of cerussite treated with chloride ions was ascribed to the strong coordination of chloride ions to lead ions. The chloride ion concentrations determine the distributions of various lead chloride complexes in solutions, and $PbCl^+$ is the dominant species in solutions at low concentrations of chloride ions. In this case, it attaches more readily to the surface of cerussite through ligands than Pb^{2+}, thereby increasing the number of active sites on the mineral surface and improving the subsequent sulfidization. Chloride ions also possess a small ionic radius, strong penetrability, and strong adsorption capacity onto metals; thus, chloride ions can combine with lead on the cerussite surface to form lead chloride complexes and even pass through the mineral surface to exchange carbonate ions (CO_3^{2-}) with the inner cerussite, which can further increase the activity on the cerussite surface [11–13]. Adding chloride ions prior to sulfidization can activate the cerussite surface and reinforce the sulfidization of cerussite.

The contribution of chloride ions to the sulfidization flotation of cerussite has been reported in detail through various experiments and measurements as well as theoretical analysis in our previous publication [11], but the surface properties of cerussite treated with chloride ions remain unclear. In the present study, dissolution experiments, zeta potential measurements, X-ray photoelectron spectroscopy (XPS) studies, and density functional theory (DFT) computation were conducted to investigate the effect of chloride ions on activity of cerussite surface and to further reveal the nature of their contribution to surface sulfidization reinforcement.

2. Materials and Methods

2.1. Materials and Reagents

The cerussite mineral samples obtained from the Lanping lead–zinc mine (Lanping, Yunnan, China) were crushed and handpicked to remove various impurities such as calcite and quartz. The purified minerals were dry ground in an agate mortar and screened to −74 + 45 μm and −5 μm sized fractions. The −74 + 45 μm mineral particles were used in the dissolution experiments and XPS analysis, and the −5 μm particles were used for zeta potential measurements. The chemical analysis and X-ray diffraction analysis results showed that the samples were of high purity with only minor impurities. All of the reagents used in this study were of analytical grade. Pure deionized water was used throughout the experiment.

2.2. Dissolution Experiments

Dissolution experiments were conducted after dispersing 5 g of the cerussite samples into 500 mL of aqueous phase, which was placed in a thermostatically controlled water bath. The suspensions were magnetically stirred at 650 rpm, and the solution was maintained at 298 K. Five milliliters of the resultant solution was accurately withdrawn at specific time intervals for each dissolution system, and the solid–liquid separation was performed using a centrifuge. The separated liquid was collected to analyze the total lead concentrations by means of inductively coupled plasma-atomic emission spectrometry (ICPS-1000II, Shimadzu, Kyoto, Japan), and the maximum standard deviation for measurement of each liquid sample was within ±2%. Four sets of dissolution experiments including the pretreatment of cerussite samples with and without chloride ions were conducted in the absence or presence of $Na_2S \cdot 9H_2O$ in this study.

2.3. Zeta Potential Measurements

Zeta potentials of the samples were obtained by using a zeta potential analyzer instrument (ZetaPlus, Brookhaven, New York, NY, USA). The mineral suspension (0.01% mass fraction) was dispersed in a beaker magnetically stirred for a determined time in the presence of the desired concentrations of sodium chloride at a determined pH value, which was regulated through $0.10 \ mol \cdot L^{-1}$ NaOH or $0.10 \ mol \cdot L^{-1}$ HNO_3 solutions. After 10 min of settling of the resultant suspensions, the pH value was measured and recorded, and the fine mineral particles were transferred

to the measurement vessel for zeta potential measurements at room temperature. The zeta potential of each sample was measured three times with the maximum standard deviation of ± 2.0 mV, and the average was reported as the final value in the present study.

2.4. XPS Analysis

The measured samples were obtained at the desired conditions described in Section 2.2 for XPS analysis. The XPS measurements were carried out by using a PHI5000 Versa Probe II (PHI5000, ULVAC-PHI, Chigasaki, Japan) equipped with a monochromatic Al K$_\alpha$ X-ray source. The survey scan of the analyzed sample was conducted to identify the chemical components, and a high-resolution scan on a specific element was then performed. Subsequently, the MultiPak Spectrum software was used to calculate and analyze the spectra and surface atomic ratios of measured samples, and the carbon 1s spectral peak was used to calibrate all of the measured spectra.

2.5. Computational Methods

All computations were based on the cerussite crystal structure reported by Antao and Hassan [14]. The cerussite (110) surface was used for surface structure and property calculation. Figure 1 illustrates the slab model of perfect cerussite (110) surface, which contained 20 Å atomic and 20 Å vacuum layers. The computations were conducted through first-principle calculations based on DFT as implemented in Cambridge Serial Total Energy Package (CASTEP) developed by Payne et al. [15]. The valence electron configurations involved in the present calculation included C $2s^2 2p^2$, O $2s^2 2p^4$, Pb $5d^{10} 6s^2 6p^2$, and Cl $3s^2 3p^5$. The exchange-correlation functional used was the generalized gradient approximation developed by Perdew et al. [16] for solids. The kinetic energy cutoff of 340 eV for the plane-wave basis was employed throughout this study. The Brillouin zone was sampled with Monkhorst–Pack special k-points of a $4 \times 3 \times 1$ grid for all the structure calculations. Pulay density mixing method was employed for self-consistent electronic minimization. The energy, force, and displacement tolerance was 1.0×10^{-5} eV/atom, 3.0×10^{-2} eV/Å, and 1.0×10^{-3} Å, respectively.
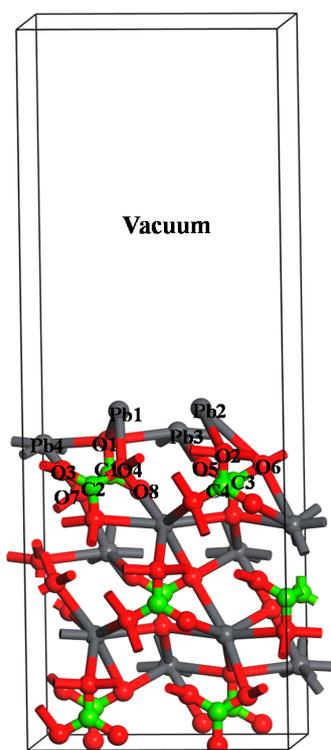

Figure 1. Slab model of perfect cerussite (110) surface.

3. Results and Discussion

3.1. Dissolution Experiments

As a semi-soluble salt mineral with a standard solubility product constant of 7.40×10^{-14} [17–19], there are a great number of dissolved lead ions in the pulp solution released from the cerussite mineral lattice, which will significantly affect the lead species balance in the mineral/solution interface. Meanwhile, such a dissolution process will render the adsorbed species of flotation reagents away from the mineral surface in the subsequent process, and it is also associated with the large consumption of flotation reagents. Thus, the dissolution properties of cerussite become evident in analyzing its subsequent sulfidization and flotation behavior. To investigate the effect of chloride ions on the dissolution properties of cerussite, we discussed the dissolved lead ion concentrations of cerussite in various systems as a function of time. The results are shown in Table 1.

Table 1. Dissolved lead ion concentrations of cerussite in various systems as a function of time.

| Time, min	Concentrations of Pb in Various Systems, mg/L			
	Deionized Water	NaCl	Na_2S	$NaCl + Na_2S$
1	1.5166	1.4208	0.2579	0.0382
3	1.9698	1.7309	0.2356	0.0289
6	2.2364	2.0611	0.2033	0.0297
10	2.6481	2.7033	0.3154	0.0187
15	3.1456	2.9109	0.1197	0.0384
20	3.2942	3.1346	0.1245	0.0456
30	3.3803	3.2844	0.2336	0.0353
45	3.6342	3.1327	0.1355	0.0322
60	3.8023	3.0532	0.1639	0.0246

The solubility of cerussite differed in various solution systems (see Table 1). The lead ion concentrations gradually increased with the dissolution time in deionized water system, which followed the dissolution behavior of carbonate minerals [20]. For the NaCl solution system, the lead ion concentration was similar in magnitude to that presented in deionized water, and the lead ion concentration also increased with the dissolution time within 30 min of dissolution. It began to decrease after 30 min, which indicated that the dissolution rate of lead ions was higher than their adsorption rate on the mineral surface within 30 min, whereas it reversed after 30 min of dissolution. Combined with the result shown in our previous publication [11], the dominant species of lead chloride complexes presented in the solution is $PbCl^+$ when the concentration of chloride ions was low, and $PbCl^+$ has better affinity for attaching to the cerussite surface than Pb^{2+}. Thus, the adsorption capacity of Pb species onto the mineral surface in the NaCl solution system is stronger than that in deionized water. The lead ion concentrations in the NaCl solution system were lower than those in the deionized water system (see Table 1), implying that more lead ions existed on the mineral surface in the NaCl solution system according to the mass balance of lead. The active sites on the cerussite surface were lead ions during the sulfidization flotation of the surface; thus, the number of active sites increased on the cerussite surface after pretreatment with chloride ions, and this increase increased the likelihood of subsequent sulfidization and flotation. This finding further confirms the result of our previous study [11].

The change in lead ion concentrations as a function of time in Na_2S and $NaCl + Na_2S$ aqueous systems were exhibited to further verify the increased activity on the mineral surface. The lead ion concentrations drastically dropped in the Na_2S system compared with the deionized water system (see Table 1). This decrease is attributed to the formation of lead sulfide species on the mineral surface through the interaction of sulfide ions with dissolved lead ions in pulp solutions. The formed lead sulfide films would screen or reduce the dissolution of cerussite, but it could not be uniformly

distributed onto the mineral surface. Thus, some lead ions were dissolved into the pulp solution. After the cerussite was pretreated with chloride ions, the lead ion concentrations in the aqueous phase decreased by approximately one order of magnitude compared with that in the Na_2S system alone. This result is attributed to the favorable condition created by chloride ions. The increased number of active sites on the mineral surface provided more binding sites to subsequent sulfide ions; thus, more sulfide ions were adsorbed onto the mineral surface to form a greater number of lead sulfide species, and these species were probably distributed onto the mineral surface evenly and densely. The dissolution of the cerussite surface coated with the formed lead sulfide species through chloride ions pretreatment significantly decreased. Thus, the occurrence of hydrophobic lead xanthate species formed on the cerussite surface through mineral dissolution could be prevented or reduced.

3.2. Zeta Potential Measurements

The zeta potential, as an in situ surface-sensitive technique, is frequently used to describe the interaction of flotation reagents and mineral surface [21,22]. Electrokinetic potential measurements were used to further characterize the effect of chloride ions on activity of cerussite surface. Figure 2 presents the zeta potential of cerussite in the absence or presence of chloride ions as a function of pH values.
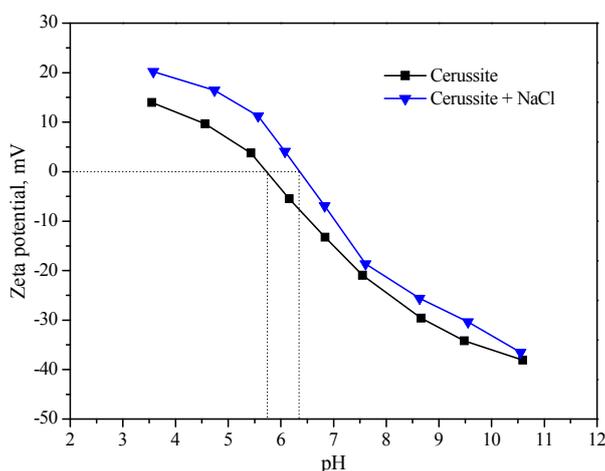

Figure 2. Zeta potential of cerussite as a function of pH.

The isoelectric point (IEP) value of cerussite without pretreatment of chloride ions was obtained as about pH 5.7 (see Figure 2), which was located at the values of pH 4.0 and 6.5 according to previous research [23–25]. The zeta potential decreased with the increase in pH values. The zeta potential was positive for pH values lower than pH 5.7 but negative for pH values higher than pH 5.7. After cerussite was added into the NaCl solution, the zeta potential became more positive within the entire pH range, and the IEP value increased from pH 5.7 to 6.4 (see Figure 2). This finding indicated that the number of positively charged species increased on the mineral surface, and the increased species may be lead species that resulted from migration between the mineral lattice and aqueous solutions. This deduction was attributed to the following reasons. First, chloride ions added in pulp solutions can combine with lead on the cerussite surface to form $PbCl^+$, which acts as the dominant species of lead chloride complexes in the pulp solution, and adsorbed onto the mineral surface and formed a lead-rich surface. Second, even the carbonate ions (CO_3^{2-}) with the inner cerussite can be exchanged by chloride ions [11–13]. All of these pathways result in increased lead concentrations on the mineral surface (i.e., increased number of active sites), which was revealed by the change of zeta potential. This result corresponded well with the dissolution experiments.

3.3. XPS Studies

XPS, as a sensitive surface technique, can identify the valence state and chemical composition of targeted elements on the measured mineral surface according to the difference in the binding energy of inner electrons from each element. In this study, XPS analysis was employed to further illustrate the increased activity on the cerussite surface induced by chloride ions. The peak fitting and separation was applied to analyze the collected XPS spectra, and the MultiPak Spectrum software was used to determine the relative contents of different compositions in the targeted elements through removal of the contaminated component. The C 1s, O 1s, and Pb 4f XPS spectra for the mineral surface before and after being treated with chloride ions were analyzed in the present study.

Figures 3a and 4a illustrate the C 1s and O 1s spectra for the mineral surface treated without chloride ions, respectively. The C 1s spectrum presented three well-separated XPS peaks positioned at 284.80, 286.30, and 289.28 eV (see Figure 3a). Combined with previous research [26–28], for C 1s spectrum, the chemical state at 284.80 and 286.30 eV XPS peaks were attributed to the contaminated carbon (i.e., hydrocarbon and carbon–oxygen species), and the other XPS peak at 289.28 eV was assigned to the carbon in the carbonate group. The two XPS peaks at 531.42 and 533.16 eV fit the O 1s spectrum (see Figure 4a), which were assigned to the oxygen in the carbonate group and contaminated carbon–oxygen species on the cerussite surface treated without chloride ions. Thus, the authentic contributors to the C and O components of the measured sample were positioned at 289.28 and 531.42 eV, respectively. This analysis result was also for other samples treated with chloride ions.
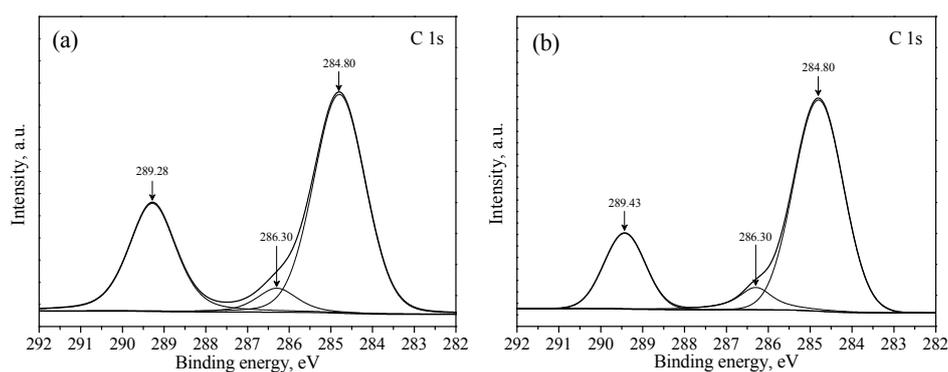
Figure 3. C 1s spectra for the mineral surface treated with chloride ions: (**a**) before; (**b**) after.
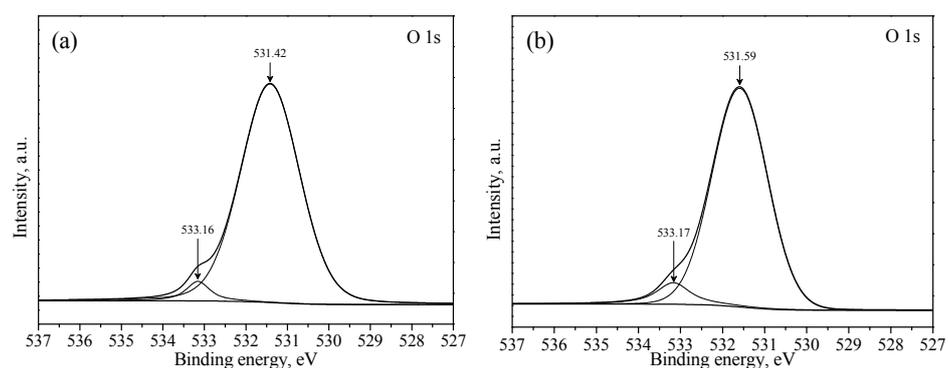
Figure 4. O 1s spectra for the mineral surface treated with chloride ions: (**a**) before; (**b**) after.

Table 2 presents the atomic concentrations of cerussite samples before and after being treated with chloride ions. The data revealed that the atomic concentrations of C and O in untreated samples were 19.31% and 60.45%, respectively. The atomic concentrations of C and O on the mineral surface treated with chloride ions decreased to 18.11% and 58.93%, respectively. Table 3 shows the binding energy of each element from cerussite samples before and after being treated with chloride ions.

As shown in Figures 3b and 4b and Tables 2 and 3, the binding energy of C 1s and O 1s XPS peaks in the carbonate group were 289.43 and 531.59 eV, respectively, in mineral surfaces treated with chloride ions. Compared with the result of cerussite treated without chloride ions, the binding energy of C 1s and O 1s peaks shifted from 289.28 to 289.43 and from 531.42 to 531.59 eV, respectively. These results indicated that the concentration decrease in the carbonate group on the mineral surface occurred when cerussite was pretreated with chloride ions.

Table 2. Atomic concentration of cerussite samples treated with chloride ions: (**a**) before; (**b**) after.

Samples	Atomic Concentration, %			Atomic Concentration Ratio	
	C 1s	O 1s	Pb 4f	Pb/C	Pb/O
a	19.31	60.45	20.23	1.05	0.33
b	18.11	58.93	22.96	1.27	0.39

Table 3. Binding energy of each element from various cerussite samples treated with chloride ions: (**a**) before; (**b**) after.

Samples	Binding Energy, eV			Chemical Shift, eV		
	C 1s	O 1s	Pb 4f	C 1s	O 1s	Pb 4f
a	289.28	531.42	138.81	-	-	-
b	289.43	531.59	138.95	0.15	0.17	0.14

Figure 5a,b illustrates the Pb 4f spectra for the mineral surface before and after being treated with chloride ions, respectively. A single and symmetric Pb $4f_{7/2}$ and Pb $4f_{5/2}$ doublet appeared in the Pb 4f spectrum, and the property of the Pb $4f_{5/2}$ and Pb $4f_{7/2}$ peaks was identical (see Figure 5a). The Pb $4f_{7/2}$ XPS peak at a binding energy of 138.81 eV was assigned to $PbCO_3$ [26,29,30]. Combined with the data in Table 3, the binding energy of Pb $4f_{7/2}$ XPS peak had a shift of 0.14 eV after cerussite was pretreated with chloride ions. The atomic concentrations of Pb on the mineral surface were 20.23% and 22.96%, respectively, before and after cerussite was treated with chloride ions (see Table 2), indicating an increase in the atomic concentrations of Pb on the chloride ion-treated cerussite surface. The Pb sites on the mineral surface, as active sites, interact with sulfide ions in the pulp solution in the subsequent sulfidization process. Thus, the increase in active sites on the mineral surface provides a favorable condition for the subsequent sulfidization and flotation of cerussite.
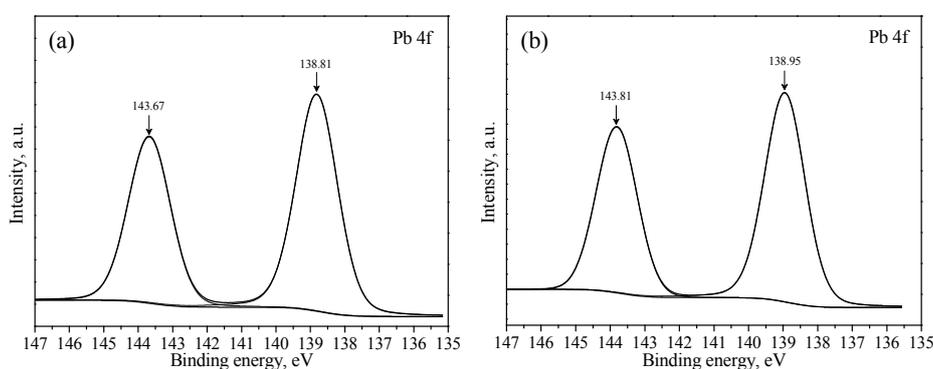

Figure 5. Pb 4f spectra for the mineral surface treated with chloride ions: (**a**) before; (**b**) after.

3.4. DFT Computation

It has been reported in our previous publication [11] that the distributions of different lead chloride complexes depend on the chloride ion concentration in the solution, and the dominant species

of lead chloride complexes is PbCl$^+$ at low concentrations of chloride ions. In the present study, the adsorption of PbCl$^+$ on the cerussite (110) surface was investigated and its adsorption configuration is shown in Figure 6. After PbCl$^+$ was adsorbed onto the mineral surface, Cl atoms bonded to Pb2 atom on the mineral surface; meanwhile, the Pb atoms in PbCl$^+$ can be stably adsorbed to the mineral surface, thereby increasing the number of Pb atoms on the mineral surface (i.e., the number of active sites on the cerussite surface increased), which corresponded well with the experimental results.
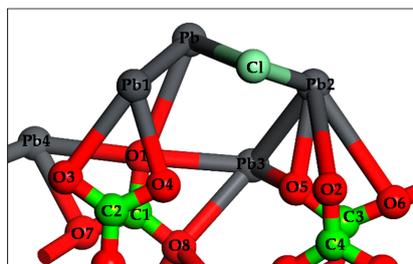

Figure 6. Adsorption configurations of PbCl$^+$ on perfect cerussite (110) surface.

The density of states of Cl atom and its bonded Pb atom after PbCl$^+$ was adsorbed onto the cerussite surface were analyzed to investigate the adsorption behavior of PbCl$^+$ and its effects on electronic structure and properties on the cerussite surface. The results are shown in Figure 7. The density of states near the Fermi level was attributed to the Pb 6p and Cl 3p orbital, and the Pb 6p and Cl 3p orbital were overlapped between −2.0 and 3.5 eV (see Figure 7), indicating the formation of a strong bond between them (i.e., a stable adsorption of PbCl$^+$ occurred on the mineral surface), increasing the number of Pb atoms on the cerussite surface. The density of states of Pb atoms for perfect cerussite (110) surface before and after PbCl$^+$ adsorption was compared and discussed to further illustrate the change of electronic structure and properties on the mineral surface. A pronounced change occurred in the shape of the density of states for Pb atoms after PbCl$^+$ was adsorbed onto the mineral surface and the peak intensity of the density of states for Pb atoms improved (see Figure 8). Moreover, the peaks shifted to the Fermi level, revealing that the activity of Pb atoms on the mineral surface was enhanced after PbCl$^+$ was adsorbed onto the mineral surface. This result provided another reason for the contribution of chloride ions to the surface properties of cerussite.
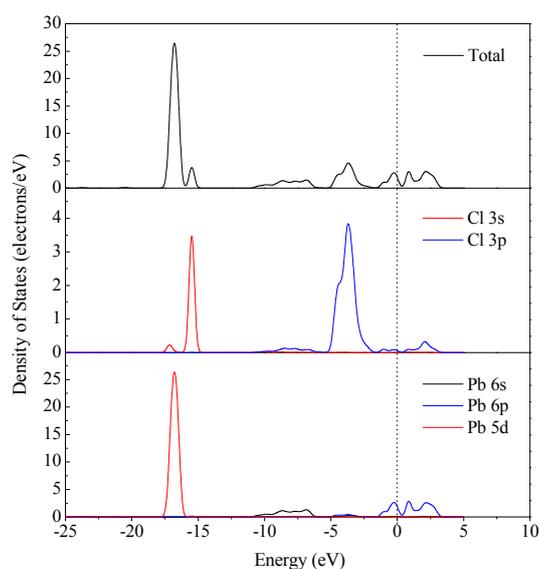
Figure 7. Density of state of atoms for cerussite surface after PbCl$^+$ adsorption.
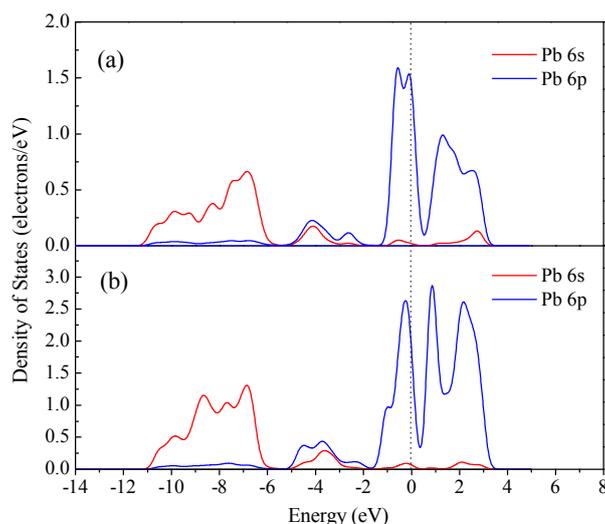
Figure 8. Density of state of Pb atoms for perfect cerussite surface: (**a**) before; (**b**) after PbCl$^+$ adsorption.

4. Conclusions

The mechanisms of increased activity on the cerussite surface induced by chloride ions were investigated through dissolution experiments, zeta potential measurements, XPS analysis, and DFT computation. The results of dissolution experiments indicated that the number of active sites on the mineral surface increased after cerussite was pretreated with chloride ions based on the changes of the lead ion concentrations in various solution systems. The increase in zeta potential on the mineral surface implied that the numbers of lead ion species increased through the migration of lead ion species from aqueous solutions to the mineral surface. The XPS analysis results visually attest that the atomic concentrations of C and O decreased and the atomic concentration of Pb increased on the cerussite surface treated with chloride ions compared with the results without chloride ions. These complementary surface analysis techniques consistently revealed that the pretreatment of the cerussite surface with chloride ions resulted in an increase in the number of active sites. The DFT results indicated that both the number of active sites and the activity of active sites on the mineral surface increased and improved, which was beneficial to the subsequent sulfidization and flotation of cerussite. These analysis results provided an integrated and comprehensive theoretical foundation for the contribution of chloride ions to the sulfidization flotation of cerussite.

Author Contributions: Qicheng Feng and Shuming Wen conceived and designed the experiments; Qicheng Feng and Wenjuan Zhao performed the experiments; Qicheng Feng and Qinbo Cao analyzed the data; Jiushuai Deng contributed DFT computation; Qicheng Feng wrote the paper.

Conflicts of Interest: The authors declare no conflict of interest.

References

1. Li, Y.; Wang, J.K.; Wei, C.; Liu, C.X.; Jiang, J.B.; Wang, F. Sulfidation roasting of low grade lead-zinc oxide ore with elemental sulfur. *Miner. Eng.* **2010**, *23*, 563–566. [CrossRef]
2. Li, C.X.; Wei, C.; Deng, Z.G.; Li, X.B.; Li, M.T.; Xu, H.S. Hydrothermal sulfidation and flotation of oxidized zinc-lead ore. *Metall. Mater. Trans. B* **2014**, *45*, 833–838. [CrossRef]
3. Feng, Q.C.; Wen, S.M.; Wang, Y.J.; Zhao, W.J.; Deng, J.S. Investigation of leaching kinetics of cerussite in sodium hydroxide solutions. *Physicochem. Probl. Miner. Process.* **2015**, *51*, 491–500.
4. Fa, K.Q.; Miller, J.D.; Jiang, T.; Li, G.H. Sulphidization flotation for recovery of lead and zinc from oxide-sulfide ores. *Trans. Nonferr. Met. Soc. China* **2005**, *15*, 1138–1144.

5. Gush, J.C.D. Flotation of oxide minerals by sulphidization—The development of a sulphidization control system for laboratory testwork. *J. S. Afr. Inst. Min. Metall.* **2005**, *105*, 193–197.

6. Feng, Q.C.; Wen, S.M.; Zhao, W.J.; Liu, J.; Liu, D. Effect of pH on surface characteristics and flotation of sulfidized cerussite. *Physicochem. Probl. Miner. Process.* **2016**, *52*, 676–689.

7. Yuan, W.Y.; Li, J.H.; Zhang, Q.W.; Saito, F. Mechanochemical sulfidization of lead oxides by grinding with sulfur. *Powder Technol.* **2012**, *230*, 63–66. [CrossRef]

8. Ke, Y.; Chai, L.Y.; Liang, Y.J.; Min, X.B.; Yang, Z.H.; Chen, J.; Yuan, S. Sulfidation of heavy-metal-containing metallurgical residue in wet-milling processing. *Miner. Eng.* **2013**, *53*, 136–143. [CrossRef]

9. Ke, Y.; Chai, L.Y.; Min, X.B.; Tang, C.J.; Zhou, B.S.; Chen, J.; Yuan, C.Y. Behavior and effect of calcium during hydrothermal sulfidation and flotation of zinc-calcium-based neutralization sludge. *Miner. Eng.* **2015**, *74*, 68–78. [CrossRef]

10. Han, H.S.; Sun, W.; Hu, Y.H.; Jia, B.L.; Tang, H.H. Anglesite and silver recovery from jarosite residues through roasting and sulfidization-flotation in zinc hydrometallurgy. *J. Hazard. Mater.* **2014**, *278*, 49–54. [CrossRef] [PubMed]

11. Feng, Q.C.; Wen, S.M.; Zhao, W.J.; Wang, Y.J.; Cui, C.F. Contribution of chloride ions to the sulfidization flotation of cerussite. *Miner. Eng.* **2015**, *83*, 128–135. [CrossRef]

12. Bargar, J.R.; Brown, G.E.; Parks, G.A. Surface complexation of Pb(II) at oxide-water interfaces: III. XAFS determination of Pb(II) and Pb(II)-chloro adsorption complexes on goethite and alumina. *Geochim. Cosmochim. Acta* **1998**, *62*, 193–207. [CrossRef]

13. Guo, Y.B.; Li, C.; Liu, Y.C.; Yu, L.M.; Ma, Z.Q.; Liu, C.X.; Li, H.J. Effect of microstructure variation on the corrosion behavior of high-strength low-alloy steel in 3.5 wt % NaCl solution. *Int. J. Miner. Metall. Mater.* **2015**, *22*, 604–612. [CrossRef]

14. Antao, S.M.; Hassan, I. The orthorhombic structure of $CaCO_3$, $SrCO_3$, $PbCO_3$ and $BaCO_3$: Linear structural trends. *Can. Mineral.* **2009**, *47*, 1245–1255. [CrossRef]

15. Payne, M.C.; Teter, M.P.; Allan, D.C.; Arias, T.A.; Joannopoulos, J.D. Iterative minimization techniques for ab initio total-energy calculations: Molecular dynamics and conjugate gradients. *Rev. Mod. Phys.* **1992**, *64*, 1045–1097. [CrossRef]

16. Perdew, J.P.; Ruzsinszky, A.; Csonka, G.I.; Vydrov, O.A.; Scuseria, G.E.; Constantin, L.A.; Zhou, X.L.; Burke, K. Restoring the density-gradient expansion for exchange in solids and surfaces. *Phys. Rev. Lett.* **2008**, *100*, 136406. [CrossRef] [PubMed]

17. Powell, K.J.; Brown, P.L.; Byrne, R.H.; Gajda, T.; Hefter, G.; Leuz, A.K.; Sjöberg, S.; Wanner, H. Chemical speciation of environmentally significant metals with inorganic ligands. Part 3: The Pb^{2+} + OH^-, Cl^-, CO_3^{2-}, SO_4^{2-}, and PO_4^{3-} systems (IUPAC Technical Report). *Pure Appl. Chem.* **2009**, *81*, 2425–2476. [CrossRef]

18. Shirota, Y.; Niki, K.; Shindo, H. Stabilities of crystal faces of aragonite-type strontianite ($SrCO_3$) and cerussite ($PbCO_3$) compared by AFM observation of facet formation in acid. *J. Cryst. Growth* **2011**, *324*, 190–195. [CrossRef]

19. Feng, Q.C.; Wen, S.M.; Zhao, W.J.; Deng, J.S.; Xian, Y.J. Adsorption of sulfide ions on cerussite surfaces and implications for flotation. *Appl. Surf. Sci.* **2016**, *360*, 365–372. [CrossRef]

20. Shi, Q.; Zhang, G.F.; Feng, Q.M.; Deng, H. Effect of solution chemistry on the flotation system of smithsonite and calcite. *Int. J. Miner. Process.* **2013**, *119*, 34–39. [CrossRef]

21. Feng, B.; Feng, Q.M.; Lu, Y.P. The effect of lizardite surface characteristics on pyrite flotation. *Appl. Surf. Sci.* **2012**, *259*, 153–158. [CrossRef]

22. Li, F.X.; Zhong, H.; Xu, H.F.; Jia, H.; Liu, G.Y. Flotation behavior and adsorption mechanism of α-hydroxyoctyl phosphinic acid to malachite. *Miner. Eng.* **2015**, *71*, 188–193. [CrossRef]

23. Fuerstenau, M.C.; Olivas, S.A.; Herrera-Urbina, R.; Han, K.N. The surface characteristics and flotation behavior of anglesite and cerussite. *Int. J. Miner. Process.* **1987**, *20*, 73–85. [CrossRef]

24. Popov, S.R.; Vučinić, D.R. The effect of prolonged agitation in lead ion solution on ethylxanthate adsorption and surface characteristics of cerussite. *Int. J. Miner. Process.* **1992**, *35*, 85–100. [CrossRef]

25. Popov, S.R.; Vučinić, D.R. Kinetics of ethylxanthate adsorption on cerussite in alkaline media in presence or absence of dissolved lead ions. *Int. J. Miner. Process.* **1994**, *41*, 115–128. [CrossRef]

26. Grano, S.R.; Prestidge, C.A.; Ralston, J. Sulphite modification of galena surfaces and its effect on flotation and xanthate adsorption. *Int. J. Miner. Process.* **1997**, *52*, 1–29. [CrossRef]

27. Buckley, A.N.; Goh, S.W.; Lamb, R.N.; Woods, R. Interaction of thiol collectors with pre-oxidised sulfide minerals. *Int. J. Miner. Process.* **2003**, *72*, 163–174. [CrossRef]

28. Nowak, P.; Laajalehto, K. On the interpretation of the XPS spectra of adsorbed layers of flotation collectors-ethyl xanthate on metallic lead. *Physicochem. Probl. Miner. Pross.* **2007**, *41*, 107–116.

29. Cozza, C.; Castro, V.D.; Polzonetti, G.; Marabini, A.M. An X-ray photoelectron spectroscopy (XPS) study of the interaction of mercapto-benzo-thiazole with cerussite. *Int. J. Miner. Process.* **1992**, *34*, 23–32. [CrossRef]

30. Chanturia, V.A.; Bunin, I.Z.; Ryazantseva, M.V.; Khabarova, I.A.; Koporulina, E.V.; Anashkina, N.E. Surface activation and induced change of physicochemical and process properties of galena by nanosecond electromagnetic pulses. *J. Min. Sci.* **2014**, *50*, 573–586. [CrossRef]

The Influence of Impurity Monovalent Cations Adsorption on Reconstructed Chalcopyrite (001)-S Surface in Leaching Process

Zhenlun Wei [1], Yubiao Li [1,2,*], Qing Xiao [2] and Shaoxian Song [1]

[1] School of Resources and Environmental Engineering, Wuhan University of Technology, Wuhan 430070, China; erebus@whut.edu.cn (Z.W.); ssx851215@whut.edu.cn (S.S.)

[2] School of Natural and Built Environments, University of South Australia, Mawson Lakes, SA 5095, Australia; qing.xiao@mymail.unisa.edu.au

* Correspondence: Yubiao.Li@whut.edu.cn

Abstract: Hydrometallurgical processing of chalcopyrite is hindered predominantly due to the passivation layers formed on the chalcopyrite surface. However, the effects of impurity cations released from the gangue are not yet well understood. Density functional theory (DFT) calculations were carried out to investigate monovalent cations of Na^+ and K^+ on chalcopyrite (001)-S surface using Materials Studio. The results show that the $3d$ orbital of Fe and $3p$ orbital of S predominantly contribute to their activities during chalcopyrite oxidation and dissolution processes. In addition, SO_4^{2-} is more likely to be adsorbed on one Fe site in the presence of Na^+, while it is preferentially adsorbed on two Fe sites in the presence of K^+. However, the adsorption of both Na_2SO_4 and K_2SO_4 on the chalcopyrite (001)-S surface contributes to the breakage of S–S bonds, indicating that the impurity cations of Na^+ and K^+ are beneficial to chalcopyrite leaching in a sulfuric environment. The adsorption energy and partial density of states (PDOS) analyses further indicate that the adsorption of Na_2SO_4 on chalcopyrite (001)-S surface is favored in both -BB (bidentate binuclear) and -BM (bidentate mononuclear) modes, compared to the adsorption of K_2SO_4.

Keywords: chalcopyrite; surface; adsorption; DFT

1. Introduction

Chalcopyrite ($CuFeS_2$), as one of the most abundant copper-bearing sulfide minerals, accounts for approximately 70% of the copper reserve on Earth [1]. Chalcopyrite is not only an economic mineral for copper production in both pyrometallurgical and hydrometallurgical processes, but is also related to many environmental problems such as acid mine drainage (AMD) [2]. With stricter environmental requirements being raised, pyrometallurgical processing of chalcopyrite is decreasingly important. In contrast, hydrometallurgical strategy has been realized to be more promising, although industrial implementation is still limited to date, predominantly due to slow leaching kinetics [3–5].

Most studies show that the slow kinetics of chalcopyrite are not only due to its crystal structure requiring high energy to be broken, but also due to the passivation layers formed on the chalcopyrite surface during the leaching process, with the latter being considered to be rate controlling [2,6–14]. In order to develop proper alternatives to avoid surface passivation and enhance the hydrometallurgical efficiency, various strategies, including surface-sensitive X-ray photoelectron spectroscopy (XPS) synchrotron-based techniques [15–18] have been attempted to investigate the surface products.

However, chalcopyrite is normally not present in a pure state in the natural environment; instead, it co-exists with other minerals, including pyrite, galena, silicates, and some salts. Recently,

Qian et al. [19] investigated the effects of some aqueous impurities, such as Na^+, K^+, Ca^{2+}, Al^{3+}, and Si^{4+} on chalcopyrite leaching, under controlled conditions (pH 1.0, 750 mV, and 75 °C), indicating that different impurity cations play various roles in chalcopyrite leaching. However, they only discussed the effects of these cations in a specific leaching condition; no further theoretical interpretation at the molecular level was available.

As chalcopyrite displays poor cleavage, its fracture presents various oriented surfaces [20]. Although differing surfaces, including (100), (101), (110), (111), and (112) have been investigated [21], the reconstructed (001)-S surface has been recommended as the most representative surface for chalcopyrite [22]. Therefore, in order to better understand reactions occurring on the chalcopyrite surface, this study aims to reveal the interaction between monovalent cations (i.e., Na^+ and K^+) and reconstructed chalcopyrite (001)-S surface in sulfuric solution using molecular modelling strategy.

2. Methodology

The calculations in this study were performed using the CASTEP module in Materials Studio 6.0, based on density functional theory (DFT), with the exchange and correlation potential (XC) and generalized gradient approximation (GGA) proposed by Perdew and Wang [23]. The core electrons were described by ultrasoft pseudopotentials considering the following valence configuration: Fe $3s^2\ 3p^6\ 3d^6\ 4s^2\ 4p^0$, Cu $3d^{10}\ 4s^1\ 4p^0$, S $3s^2\ 3p^4\ 3d^0$, Na $2p^6\ 3s^1$, K $3s^2\ 3p^6\ 3d^1$. The valence states were expanded in plane waves, with a kinetic energy cutoff of 351 eV. The integration over the Brillouin zone was performed using the Monkhorst−Pack scheme, with a $3 \times 3 \times 3$ k-point mesh for structure optimization and a $3 \times 3 \times 1$ k-point mesh for electronic structure calculation.

In order to simulate the reconstruction of the S-terminated (001) surface, a unit cell containing eight atomic layers in the c direction was used. In addition, a vacuum with a thickness of 10 Å along the c direction was established to avoid interactions between the top and bottom surfaces in the slab.

3. Results and Discussion

3.1. Optimization of Bulk Chalcopyrite

Figure 1 shows the optimized unit of chalcopyrite used, which contains four Cu, four Fe, and eight S atoms, while the lattice parameters are presented in Table 1.
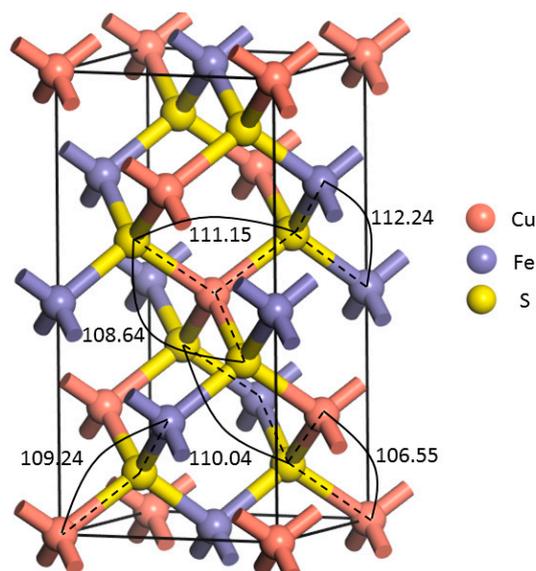

Figure 1. The optimized unit of chalcopyrite.

**Table 1.** Geometrical parameters of the chalcopyrite bulk (values in Å).

Parameters	Experimental [24]	PWscf [11]	PWscf [25]	Siesta [25]	This Work
a	5.289	5.263	5.263	5.277	5.237
c	10.423	10.362	10.418	10.447	10.424
u	0.2574	0.2585	-	-	0.2632
Fe–S	2.257	2.241	2.248	2.250	2.225
Cu–S	2.302	2.293	2.300	2.300	2.303
Fe–Fe	3.713	3.693	-	-	3.694
Cu–Cu	3.713	3.693	-	-	3.694
Fe–Cu	3.740	3.721	-	-	3.703
S–S	3.685	3.607	-	-	3.607

The lattice parameters of the bulk chalcopyrite after geometric optimization agree highly with the experimental values obtained by Hall and Stewart [24]—i.e., an *a* value of 5.237 vs. 5.289 Å and a *c* value of 10.424 vs. 10.423 Å, indicating that the computational setting of this study is highly reliable. In addition, the distances of Fe–S and Cu–S bonds in this work are 2.225 and 2.303 Å, respectively, which are within a very minor difference as compared to that experimentally identified—i.e., a 0.032 and 0.001 Å difference from the related experimental values [24]. The bond lengths of Fe–Fe, Cu–Cu, and Fe–Cu are calculated as 3.694, 3.694 and 3.703 Å, respectively, consistent with that both measured and calculated using other software, such as PWscf Quantum Espresso package and Siesta [25], as shown in Table 1. Moreover, the S–S bond is calculated as 3.607 Å, which is within a 3% variation compared to the experimental result of 3.685 Å. These calculations indicate that the optimization process is well performed. As shown in Figure 1, the angle of S–Cu(Fe)–S varies from 108.64° to 111.15°, while those of Cu(Fe)–S–Cu(Fe) varies from 106.55° to 112.24°.

The optimization performed using Materials Studio indicates that the developed pseudopotential and numerical basis sets are capable of simulating bulk chalcopyrite.

3.2. (001)-S Surface Reconstruction

In order to simulate the reconstructed (001)-S surface, a unit cell containing eight atomic layers in the *c* direction was applied. In addition, a vacuum with a thickness of 10 Å along the *c* direction was established to avoid interactions between the slabs. Figure 2 shows the unrelaxed and relaxed (001)-S surface.
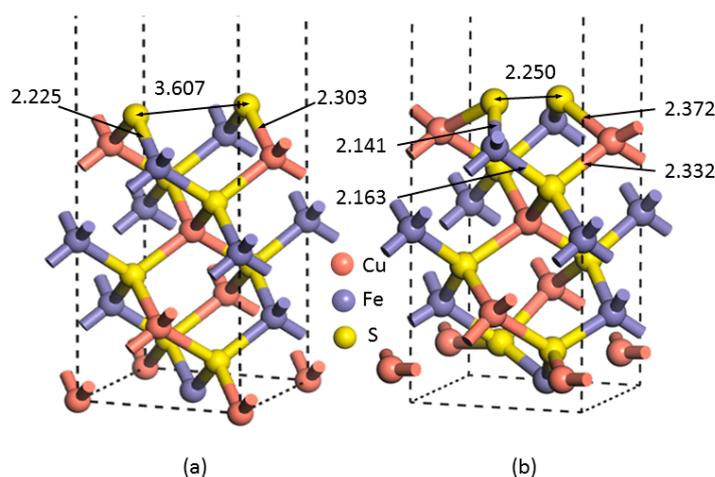
Figure 2. The chalcopyrite (001)-S surface: (**a**) unrelaxed and (**b**) relaxed. Distances in Angstroms.

The most significant change observed is the distance between the two uppermost sulfur atoms; i.e., reduced from 3.607 Å at the unrelaxed lattice surface to 2.250 Å when reconstruction occurred, indicating that the (001)-S surface rearranged. In addition, the distance between the uppermost and

the bottommost atomic layer (along the *c* axis) of the relaxed unit is significantly reduced due to reconstruction. The distance of the reconstructed S–S bond is very close to that obtained elsewhere using differing approaches [25,26]. Moreover, this value is consistent with that of the ideal disulfide (S_2^{2-}); i.e., 2.276 Å, calculated at the PBE/6-311G (d, p) level of theory [11]. The slight decrease of the bond distance by a small value of 0.026 Å is probably due to the antibonding-occupied π^* orbitals of the S_2^{2-} that were involved in bonding with the metal centers on the surface. The bond length of the upper S–Fe decreased from 2.225 to 2.141Å, while the upper S–Cu increased from 2.303 to 2.372 Å (Table 2).

Table 2. Reconstructed (001)-S surface.

Parameters	PWscf [11]	Siesta [25]	This Work
S–S	2.158	2.23	2.250
S-Fe	2.319	2.24	2.141
S-Cu	2.326	2.30	2.372

Furthermore, the electron densities of the unrelaxed and relaxed chalcopyrite (001)-S surfaces shown in Figure 3 assist in verifying that a bond was clearly formed between two sulfur atoms at the first atomic layer after relaxation, as the electron density of the uppermost S atoms at the relaxed (001)-S surface (Figure 3b) overlapped, definitely different from the unrelaxed (001)-S surface shown in Figure 3a. All these pieces of evidence, in addition to that observed in the experiment using synchrotron- or lab-based XPS techniques [20,27,28], support the formation of disulfides on the reconstructed (001)-S surface.
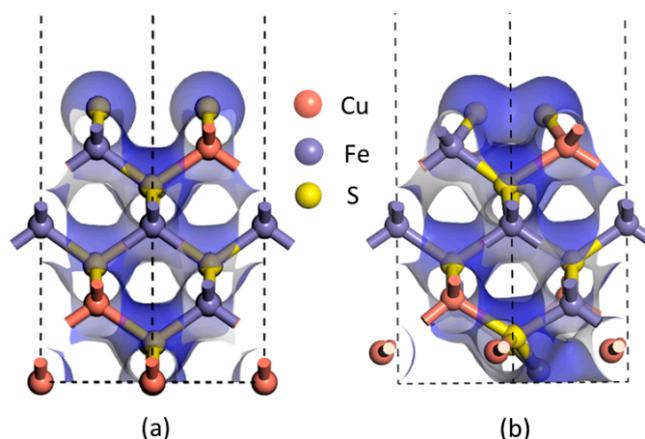
**Figure 3.** The electron density of chalcopyrite (001)-S surfaces: (**a**) unrelaxed and (**b**) relaxed.

3.3. Adsorption Sites

A (2 × 2 × 1) supercell was used to simulate the adsorption process. As some previous research works regarding chalcopyrite leaching were conducted in a sulfuric acid system [19,29,30], the adsorption sites of the SO_4^{2-} and cations would play a role in chalcopyrite dissolution.
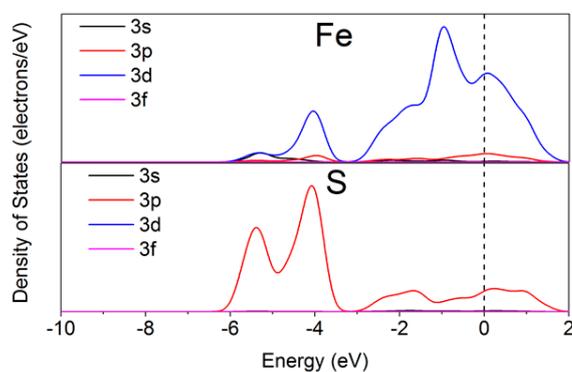
The density of states (DOS) of chalcopyrite (001)-S is shown in Figure 4, which indicates that the total energy band near Fermi level is predominantly contributed from Fe and S atoms, while the Cu atom does not play a significant role.

The partial density of states (PDOS) of the chalcopyrite shown in Figure 5 further indicates that the energy bond of the Fe atom near the Fermi level is mainly due to its 3*d* orbital, with other orbitals being less active. However, the 3*p* orbital is observed to contribute to that of the S atom. As electrons are very active at around the Fermi level, both Fe and S are expected to be involved in physical and/or chemical reactions on the chalcopyrite (001)-S surface. Studies have revealed that Fe sites are the

most electrophilic and the most active on the chalcopyrite surfaces, while the nearby S sites are more nucleophilic [25,28,29]. In contrast, both experimental and theoretical calculations indicate that the oxidation state of Cu on fresh and moderately oxidized chalcopyrite surface remains unchanged as +1 unless significant oxidation occurs [28].
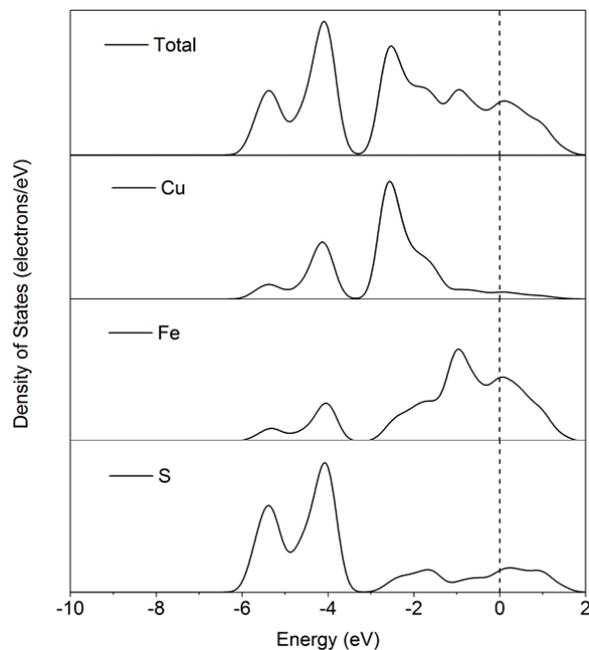

Figure 4. Density of states of chalcopyrite (001)-S surface.

Figure 5. Partial density of states of chalcopyrite (001)-S surface.

Therefore, the Fe atom on the (001)-S surface is highly likely to be the most stable site for the SO_4^{2-} adsorption (as shown in Figure 6), which is consistent with that found in [25,28]. However, as indicated in [22], there are two possible coordination modes for the adsorption of SO_4^{2-}; i.e., BB and BM, with the SO_4^{2-} being coordinated to two iron atoms in the former mode while being coordinated to one of the iron atoms in the latter mode. The adsorption sites for metal cations, however, are more likely to be adsorbed at electron-depleted S sites [28].
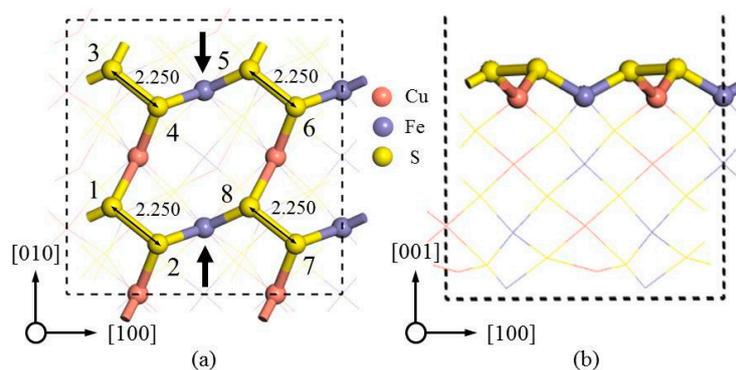
Figure 6. The adsorption sites of SO_4^{2-} on the chalcopyrite (001)-S surface: (**a**) top view; (**b**) side view. Distances are in angstroms.

As the adsorption of metal cation and sulfate were only considered to be adsorbed on the (001)-S chalcopyrite surface, the bottom five layers of chalcopyrite were kept fixed to make sure that they do not have an impact on the surface properties. The adsorption energy was then calculated according to Equation (1)

$$\Delta E_{ads} = E_{surf + met} - E_{surf} - E_{met} \tag{1}$$

where $E_{surf + met}$ is the total energy of the surface with the metal sulfate adsorbed, E_{surf} corresponds to the total energy of the reconstructed surface, and E_{met} is the total energy of the metal sulfate. All these values were calculated in a box with the same volume to calculate the surfaces at the Γ-point.
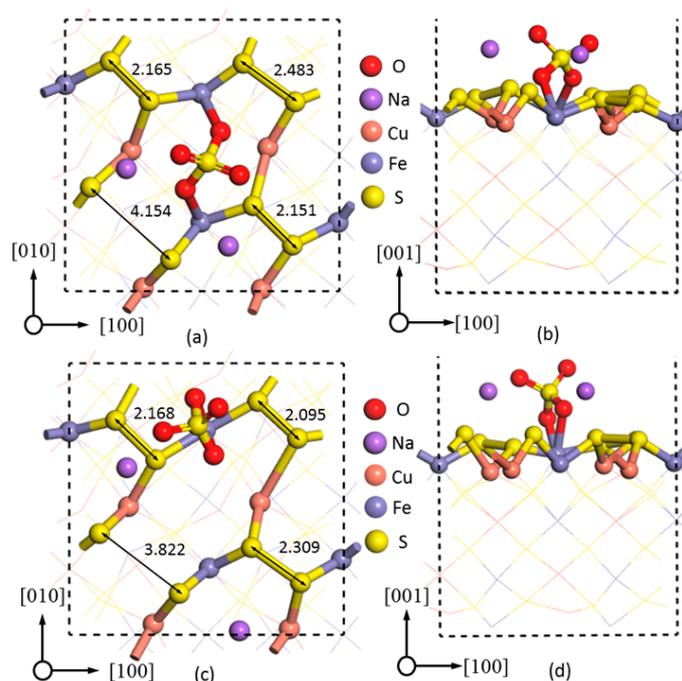
3.4. Na$_2$SO$_4$ Adsorption

Table 3 shows the adsorption energy for the metal ions adsorbed at different sites on the (001)-S chalcopyrite surface. It is observed that the adsorption of Na$^+$ on sites 1 and 2 was most preferential, with an adsorption energy of -68.96 kcal·mol^{-1} when at -BB mode—significantly greater than that adsorbed at sites 3 and 4, 5 and 6, and 7 and 8 at same mode (Table 3). Therefore, the adsorption on sites 1 and 2 was regarded as the most likely adsorption sites.

Table 3. Adsorption energies for metal sulfates adsorption at different sites on the (001)-S chalcopyrite surface. BB: bidentate binuclear; BM: bidentate mononuclear.

Co-ordination Mode	Adsorption Site	ΔE (kcal·mol^{-1})	d_{Fe-O} (Å)	d_{S-S} (Å)
Na$_2$SO$_4$-BB	1 and 2	-68.96	2.252, 2.276	4.154
Na$_2$SO$_4$-BB	3 and 4	-63.42	2.155, 2.303	3.161
Na$_2$SO$_4$-BB	5 and 6	-60.62	2.106, 2.090	4.442
Na$_2$SO$_4$-BB	7 and 8	-62.49	-, 2.154	3.075
Na$_2$SO$_4$-BM	1 and 2	-77.7	2.059, 2.274	3.822
K$_2$SO$_4$-BB	1 and 2	-35.78	2.249, 2.335	3.765
K$_2$SO$_4$-BB	3 and 4	-16.64	2.029, 2.045	2.908
K$_2$SO$_4$-BB	5 and 6	-34.70	-, 2.193	3.389
K$_2$SO$_4$-BB	7 and 8	-19.10	-, 2.220	2.429
K$_2$SO$_4$-BM	1 and 2	6.52	-	-

In addition, Figure 7a,b showed the adsorption of two Na$^+$ ions at sites 1 and 2 in -BB mode. Upon the adsorption of Na$^+$ and SO_4^{2-}, the S–S bond length between S sites 1 and 2 was increased from 2.250 to 4.154 Å, with the latter being significantly greater than the reasonable S_2^{2-} bond length of 2.276 Å [11], indicating the breakage of the S–S bond between sites 1 and 2 after Na$_2$SO$_4$ adsorption. As S_2^{2-} was one of the passivation layers described [8,29,31], the breakage of S–S was therefore beneficial to chalcopyrite leaching. In contrast, the two disulfide bonds were compressed from 2.250 (Figure 6a) to 2.165 (sites 3 and 4) and 2.151 Å (sites 7 and 8) (Figure 7a), respectively. The S_2^{2-} bond

between the sulfur atoms 5 and 6, however, increased from 2.250 to 2.483 Å, just slightly greater than ideal S_2^{2-} bond length.
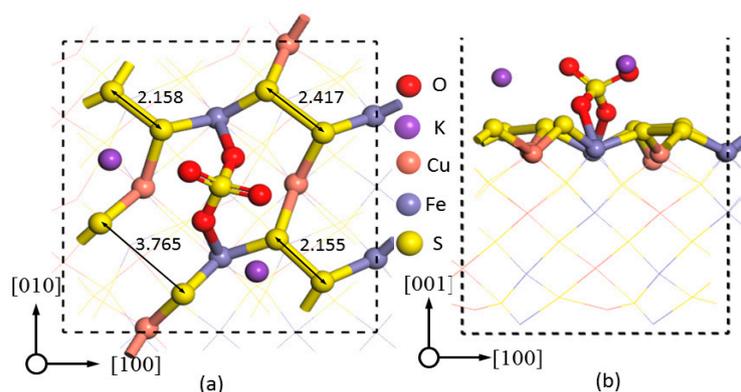

Figure 7. The most stable configuration of Na_2SO_4 adsorbed on the (001)-S chalcopyrite surface: (**a**) top view and (**b**) side view in -BB mode; (**c**) top view and (**d**) side view in -BM mode. Distances are in angstroms.

Figure 7c,d showed the most stable configuration for Na_2SO_4 adsorption on the chalcopyrite (001)-S surface; i.e., Na^+ at sites 1 and 2, and SO_4^{2-} at one Fe site forming two Fe–O bonds of 2.059 and 2.274 Å in -BM adsorption mode. Compared to SO_4^{2-} adsorbed on two Fe sites in -BB configuration, the adsorption energy was -77.7 kcal·mol^{-1} when SO_4^{2-} was adsorbed on one Fe site in -BM mode—8.74 kcal·mol^{-1} lower, although two Na^+ atoms were adsorbed at the same sites of 1 and 2, indicating that -BM mode is more preferential for the adsorption of Na_2SO_4, although the S–S bond (3.822 Å, Figure 7b) was 0.332 Å shorter than that in BB configuration. The S–S bonds between sites 3 and 4 and 5 and 6 were decreased from 2.250 to 2.168 and 2.095 Å, respectively, with the S–S bond between 7 and 8 being slightly increased to 2.309 Å in -BB mode.

3.5. K_2SO_4 Adsorption

Table 3 showed that the lowest adsorption energy for K_2SO_4 adsorbed on the chalcopyrite (001)-S surface was -35.78 kcal·mol^{-1}, at sites 1 and 2 in -BB mode, indicating that the most stable adsorption sites for K_2SO_4 was similar to that of Na_2SO_4; i.e., breaking the S–S bond (3.765 Å). The two Fe–O bonds were found as 2.249 and 2.335 Å, respectively, significantly greater than those when K^+ was adsorbed at other sites (Table 3).

However, the adsorption energy for K_2SO_4 on the chalcopyrite (001)-S surface in BM mode was 6.52 kcal·mol^{-1}, indicating that the adsorption of K_2SO_4 in BM configuration was unlikely to occur. Figure 8 showed that the adjacent two disulfide bonds of Fe atoms were compressed from 2.250 to 2.158 (sites 3 and 4) and 2.155 Å (sites 7 and 8), respectively. The bond distance of another disulfide bond connecting S atoms 5 and 6 was increased from 2.250 to 2.417 Å, although S–S breakage was not observed.

Figure 8. The most stable configuration of K_2SO_4 adsorbed on the chalcopyrite (001)-S surface: (**a**) top and (**b**) side view in -BB mode. Distances are in angstroms.

4. Conclusions

The reconstructed chalcopyrite (001)-S surface shows the formation of disulfide based on both the bond length and electron density. The DOS calculation indicates that Fe and S atoms are more active for the adsorption of anion and cation ions, respectively. However, Cu atom on the chalcopyrite surface is considered to be in a relatively stable state. In addition, the PDOS studies reveal that the 3*d* orbital of Fe and 3*p* orbital of S predominantly contribute to their activities during the oxidation and dissolution processes.

When SO_4^{2-} was adsorbed in -BB mode, the adsorption of Na^+ and K^+ on the chalcopyrite (001)-S surface is most likely at S sites 1 and 2, with the lowest adsorption energies being as -68.96 and -35.78 kcal·mol^{-1}, respectively. However, the -BM mode was more likely for the adsorption of Na_2SO_4 as compared to -BB mode, while it is unlikely to occur for K_2SO_4 in -BM mode. It should be noted that the adsorption of both Na_2SO_4 and K_2SO_4 contributes to the breakage of the S–S bond between sites 1 and 2, indicating that the presence of the impurity cations Na^+ and K^+ in sulfuric solution is beneficial to chalcopyrite leaching.

These findings are of significance to better understand chalcopyrite leaching in the presence of some common cations in the sulfuric acid leaching system, at the molecular scale. Further investigations should also be made simulating the real leaching conditions with more ions present for chalcopyrite leaching.

Author Contributions: Yubiao Li and Zhenlun Wei conceived and designed the modelling experiments; Yubiao Li, Zhenlun Wei and Qing Xiao analyzed data, Yubiao Li and Shaoxian Song contributed to all the discussion. All authors have contributed to the writing of the paper.

Conflicts of Interest: The authors declare no conflict of interest.

References

1. Wang, S. Copper leaching from chalcopyrite concentrates. *JOM* **2005**, *57*, 48–51. [CrossRef]
2. Harmer, S.L.; Thomas, J.E.; Fornasiero, D.; Gerson, A.R. The evolution of surface layers formed during chalcopyrite leaching. *Geochim. Cosmochim. Acta* **2006**, *70*, 4392–4402. [CrossRef]
3. Watling, H.R. Chalcopyrite hydrometallurgy at atmospheric pressure: 1. Review of acidic sulfate, sulfate–chloride and sulfate–nitrate process options. *Hydrometallurgy* **2013**, *140*, 163–180. [CrossRef]
4. Nazari, G.; Dixon, D.G.; Dreisinger, D.B. The mechanism of chalcopyrite leaching in the presence of silver-enhanced pyrite in the Galvanox™ process. *Hydrometallurgy* **2012**, *113–114*, 122–130. [CrossRef]

5. Pan, H.D.; Yang, H.Y.; Tong, L.L.; Zhong, C.B.; Zhao, Y.Z. Control method of chalcopyrite passivation in bioleaching. *Trans. Nonferr. Met. Soc. China* **2012**, *22*, 2255–2260. [CrossRef]

6. Stott, M.B.; Watling, H.R.; Franzmann, P.D.; Sutton, D. The role of iron-hydroxy precipitates in the passivation of chalcopyrite during bioleaching. *Miner. Eng.* **2000**, *13*, 1117–1127. [CrossRef]

7. Hiroyoshi, N.; Miki, H.; Hirajima, T.; Tsunekawa, M. Enhancement of chalcopyrite leaching by ferrous ions in acidic ferric sulfate solutions. *Hydrometallurgy* **2001**, *60*, 185–197. [CrossRef]

8. Klauber, C.; Parker, A.; van Bronswijk, W.; Watling, H. Sulphur speciation of leached chalcopyrite surfaces as determined by X-ray photoelectron spectroscopy. *Int. J. Miner. Process.* **2001**, *62*, 65–94. [CrossRef]

9. Parker, A.; Klauber, C.; Kougianos, A.; Watling, H.R.; van Bronswijk, W. An X-ray photoelectron spectroscopy study of the mechanism of oxidative dissolution of chalcopyrite. *Hydrometallurgy* **2003**, *71*, 265–276. [CrossRef]

10. Antonijevic, M.M.; Bogdanovic, G.D. Investigation of the leaching of chalcopyritic ore in acidic solutions. *Hydrometallurgy* **2004**, *73*, 245–256. [CrossRef]

11. De Oliveira, C.; Duarte, H.A. Disulphide and metal sulphide formation on the reconstructed surface of chalcopyrite: A DFT study. *Appl. Surf. Sci.* **2010**, *257*, 1319–1324. [CrossRef]

12. Ghahremaninezhad, A.; Asselin, E.; Dixon, D.G. Electrochemical evaluation of the surface of chalcopyrite during dissolution in sulfuric acid solution. *Electrochim. Acta* **2010**, *55*, 5041–5056. [CrossRef]

13. Viramontes-Gamboa, G.; Peña-Gomar, M.M.; Dixon, D.G. Electrochemical hysteresis and bistability in chalcopyrite passivation. *Hydrometallurgy* **2010**, *105*, 140–147. [CrossRef]

14. He, H.; Xia, J.L.; Hong, F.F.; Tao, X.X.; Leng, Y.W.; Zhao, Y.D. Analysis of sulfur speciation on chalcopyrite surface bioleached with acidithiobacillus ferrooxidans. *Miner. Eng.* **2012**, *27–28*, 60–64. [CrossRef]

15. Acres, R.G.; Harmer, S.L.; Beattie, D.A. Synchrotron XPS studies of solution exposed chalcopyrite, bornite, and heterogeneous chalcopyrite with bornite. *Int. J. Miner. Process.* **2010**, *94*, 43–51. [CrossRef]

16. Acres, R.G.; Harmer, S.L.; Beattie, D.A. Synchrotron XPS, NEXAFS, and ToF-SIMS studies of solution exposed chalcopyrite and heterogeneous chalcopyrite with pyrite. *Miner. Eng.* **2010**, *23*, 928–936. [CrossRef]

17. Acres, R.G.; Harmer, S.L.; Beattie, D.A. Synchrotron PEEM and ToF-SIMS study of oxidized heterogeneous pentlandite, pyrrhotite and chalcopyrite. *J. Synchrotron Radiat.* **2010**, *17*, 606–615. [CrossRef] [PubMed]

18. Acres, R.G.; Harmer, S.L.; Shui, H.W.; Chen, C.H.; Beattie, D.A. Synchrotron scanning photoemission microscopy of homogeneous and heterogeneous metal sulfide minerals. *J. Synchrotron Radiat.* **2011**, *18*, 649–657. [CrossRef] [PubMed]

19. Qian, G.J.; Li, J.; Li, Y.B.; Gerson, A.R. Probing the effect of aqueous impurities on the leaching of chalcopyrite under controlled conditions. *Hydrometallurgy* **2014**, *149*, 195–209. [CrossRef]

20. Harmer, S.L.; Pratt, A.R.; Nesbitt, W.H.; Fleet, M.E. Sulfur species at chalcopyrite ($CuFeS_2$) fracture surfaces. *Am. Mineral.* **2004**, *89*, 1026–1032. [CrossRef]

21. De Oliveira, C.; de Lima, G.F.; de Abreu, H.A.; Duarte, H.A. Reconstruction of the chalcopyrite surfaces—A DFT study. *J. Phys. Chem. C* **2012**, *116*, 6357–6366. [CrossRef]

22. De Lima, G.F.; de Oliveira, C.; de Abreu, H.A.; Duarte, H.A. Sulfuric and hydrochloric acid adsorption on the reconstructed sulfur terminated (001) chalcopyrite surface. *Int. J. Quantum Chem.* **2012**, *112*, 3216–3222. [CrossRef]

23. Perdew, J.P.; Wang, Y. Accurate and simple analytic representation of the electron-gas correlation energy. *Phys. Rev. B* **1992**, *45*, 13244. [CrossRef]

24. Hall, S.R.; Stewart, J.M. The crystal structure refinement of chalcopyrite, $CuFeS_2$. *Acta Crystallogr. Section B* **1973**, *29*, 579–585. [CrossRef]

25. De Lima, G.F.; de Oliveira, C.; de Abreu, H.A.; Duarte, H.L.A. Water adsorption on the reconstructed (001) chalcopyrite surfaces. *J. Phys. Chem. C* **2011**, *115*, 10709–10717. [CrossRef]

26. Mielczarski, J.A.; Cases, J.M.; Alnot, M.; Ehrhardt, J.J. XPS characterization of chalcopyrite, tetrahedrite, and tennantite surface products after different conditioning. 1. Aqueous solution at pH 10. *Langmuir* **1996**, *12*, 2519–2530. [CrossRef]

27. Klauber, C. Fracture-induced reconstruction of a chalcopyrite ($CuFeS_2$) surface. *Surf. Interface Anal.* **2003**, *35*, 415–428. [CrossRef]

28. Li, Y.; Chandra, A.P.; Gerson, A.R. Scanning photoelectron microscopy studies of freshly fractured chalcopyrite exposed to O_2 and H_2O. *Geochim. Cosmochim. Acta* **2014**, *133*, 372–386. [CrossRef]

29. Li, Y.; Kawashima, N.; Li, J.; Chandra, A.P.; Gerson, A.R. A review of the structure, and fundamental mechanisms and kinetics of the leaching of chalcopyrite. *Adv. Colloid Interface Sci.* **2013**, *197–198*, 1–32. [CrossRef] [PubMed]

30. Li, Y.B.; Qian, G.J.; Li, J.; Gerson, A.R. Kinetics and roles of solution and surface species of chalcopyrite dissolution at 650 mV. *Geochim. Cosmochim. Acta* **2015**, *161*, 188–202. [CrossRef]

31. Yin, Q.; Kelsall, G.H.; Vaughan, D.J.; England, K.E.R. Atmospheric and electrochemical oxidation of the surface of chalcopyrite ($CuFeS_2$). *Geochim. Cosmochim. Acta* **1995**, *59*, 1091–1100. [CrossRef]

Restraining Na-Montmorillonite Delamination in Water by Adsorption of Sodium Dodecyl Sulfate or Octadecyl Trimethyl Ammonium Chloride on the Edges

Hongliang Li [1,2], Yunliang Zhao [3], Tianxing Chen [1], Yuri Nahmad [2] and Shaoxian Song [1,*]

[1]   School of Resources and Environmental Engineering, Wuhan University of Technology, Luoshi Road 122, Wuhan 430070, China; lihongliang222@126.com (H.L.); chentian2728@163.com (T.C.)
[2]   Doctorado Institucional de Ingeniería y Ciencia de Materiales, Universidad Autonoma de San Luis Potosi, Av. Sierra Leona 530, San Luis Potosi, C.P. 78210, Mexico; yuri@ifisica.uaslp.mx
[3]   Hubei Key Laboratory of Mineral Resources Processing and Environment, Wuhan University of Technology, Luoshi Road 122, Wuhan 430070, China; yunliang286@163.com
*   Correspondence: shaoxian@uaslp.mx

Abstract: The delamination of montmorillonite in water leads to sliming in ore slurry, which is detrimental to mineral flotation and solid/water separation. In this work, the delamination of Na-montmorillonite (Na-MMT) has been restrained by sodium dodecyl sulfate (SDS) or octadecyl trimethyl ammonium chloride (1831) through the adsorption on the edge of the mineral. The experimental results have shown that the pretreatment by adding SDS and 1831 could greatly reduce the Stokes size percentage of -1.1 µm particles in the aqueous Na-MMT suspension. From the X-ray diffractometer (XRD) results, the interlayer spacing of the MMT pre-treated by SDS and 1831 is smaller than that of original MMT particles. Adsorption position of SDS and 1831 on MMT surfaces was analyzed by the measurements of adsorption capacity of SDS and 1831, inductively-coupled plasma spectra, and zeta potential before and after the plane surface of MMT was covered with tetraethylenepentaminecopper ($[Cu(tetren)]^{2+}$). The results indicated that SDS and 1831 are adsorbed on the edge and the whole surface of Na-MMT, respectively. Delamination of MMT could be well restrained by the adsorption of SDS and 1831 on the edges of MMT.

Keywords: montmorillonite; restraining delamination; mechanical chemical adsorption; surfactants

1. Introduction

Na-montmorillonite (Na-MMT) is one kind of 2:1 phyllosilicates with the exchangeable Na^+ cation adsorbed in the interlayer space close to the tetrahedral basal oxygen atoms [1]. When the Na-MMT particle is immersed in water, the interlayer of MMT will be hydrated. The interlayer hydration includes (i) hydration of interlayer cations; (ii) interaction of clay mineral surfaces with water molecules and interlayer cations; and (iii) water activity in the clay mineral–water system [2]. Vibrational studies have shown that they are less hydrogen-bonded to each other and the water molecules are strongly polarized by the interlayer cation extending to about 12 H_2O molecules per interlayer cation. These findings are in good agreement with quasi-elastic neutron scattering (QENS) studies which reveal that water diffusion in the interlayer space is about an order of magnitude slower relative to bulk water [3]. Generally, the water molecules forms hydration shells around the interlayer cations which offer the energy for expanding the interlayer space, while the other water molecules get adsorbed into the expanded interlayer space [4,5]. After the interlayer is intercalated with water

molecules and the interlayer space is expanded, the Na-MMT can be easily exfoliated and delaminated into fine nanosheets [6].

The delamination of MMT appears in many separation processes, such as hydrometallurgy, magnetic separation and solid-water separation [7,8]. For example, the presence of colloidal MMT in copper leachate would lead to an extreme difficulty for the purification of the leachate [9]. The delamination of MMT would result in the declining of the settling rate of the MMT particles and, thus, poor sedimentation [10]. Furthermore, it would reduce the efficiency of filtering. Thus, it is vital to create a new method to reduce the content of fine particle from tailings slurries which are caused by delamination of Na-MMT in leaching process.

Güven [2] has found that the non-ionic polar organic molecules can replace the adsorbed water on external surfaces of MMT. As a result, the surface of MMT particles can become hydrophobic, losing their tendency to attract water molecules. Sodium dodecyl sulfate (SDS) is an anionic surfactant with the formula $CH_3(CH_2)_{11}SO_4Na$. Octadecyl trimethyl ammonium chloride (1831) is a cationic surfactant with the formula $C_{21}H_{46}NCl$. In this work, SDS and 1831 was pre-adsorbed onto the edge surface before immersion of Na-MMT in water, in order to reverse the hydrophilic edge surface to hydrophobic, thereby, preventing water adsorption in the interlayer space and to prevent Na-MMT from delaminating to super fine particles in water. In the processes, surfactant adsorption on MMT would not bring any problem for separation in hydrometallurgy, magnetic separation, and solid-water separation. Therefore, there are significant applications of our finding in this study to the above-mentioned processes. The adsorption position of the surfactant is determined by the adsorption relation between the surfactant and tetraethylenepentaminecopper ($[Cu(tetren)]^{2+}$), by which ($[Cu(tetren)]^{2+}$) can pre-block the structural charges of MMT.

2. Experimental

2.1. Sample Preparation

The Na-MMT powder sample was obtained from Chifeng Ningcheng Montmorillonite Co., Inner Mongolia, China. The composition of the sample was characterized using a Bruker D8 Advance X-ray diffractometer (XRD) at a voltage of 40 kV and a current of 30 mA with Cu K radiation (λ = 0.15418 nm). Figure 1 gives the XRD pattern, showing that the purity of the sample is very high grade and only contains negligible impurities.
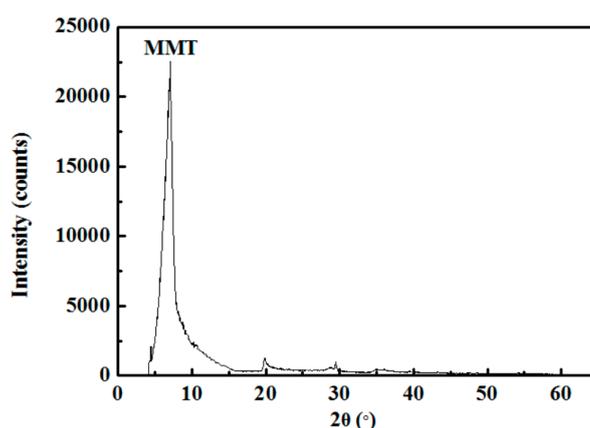
Figure 1. XRD pattern of MMT sample.

The analytical grade $Cu(NO_3)_2 \cdot 3H_2O$, tetraethylenepentamine, methyl orange solutions, ethanol, cetylpyridinium bromide, dichloromethane, methylene blue, thymol blue, Na_2SO_4, 95% sulfuric acid, SDS and 1831 are obtained from Sigma-Aldrich Co, Shanghai, China. The water was produced using a Millipore Milli-Q Direct 8/16 water purification system (Billerica, MA, USA) with 18.2 MΩ.

2.2. Pre-Adsorption of SDS and 1831 on the MMT Surface

0.5 mL liquid agent and 1 g MMT are added into a grinding tank (diameter 4.5 cm and height 5 cm with seven zirconia balls). The mass ratio of ore to agent was 50:1. The MMT and agent were mixed in a QM-3SP04 planetary mill (Shanghai Longtuo Co. Ltd, Shanghai, China) mechanically for 60 min at 150 rev/min. The MMT paste was dispersed in 80 mL water by stirring for 3 min at 450 rev/min. The prepared suspension was used for the measurements of Stokes size. The Stokes size was measured by centrifugal classification using a Thermo Fisher Sorvall ST16 centrifuge (Waltham, MA, USA). The solid in suspension was separated by centrifugation and the solid component was dried in an electro-thermostatic blast oven for 8 h at 60 °C. The interlayer spacing of the dried powder was detected using a Bruker D8 Advance X-ray diffractometer (XRD) (Karlsruhe, Germany).

2.3. Detection of Adsorption Position of SDS and 1831 on MMT Surface

2.3.1. Adsorption of $[Cu(tetren)]^{2+}$ on the Plant Surface of MMT

The delaminated MMT sample named MMT 1 was prepared as follows: 15 g MMT powder was poured into 500 mL deionized water and then delaminated for 8 min using an intermittent sonication at the strength of 60% by a Vernon Hills Illinois Cp505 ultrasound dispersion (Hielscher, Ringwood, NJ, USA). The ultrasound-treated MMT was separated by centrifuge for 4 min at 10,000 rev/min and 3 min at 11,000 rev/min, in order to get the delaminated supernatant of MMT. Then, the MMT 1 supernatant was obtained by diluted the delaminated supernatant to 0.01 g/L. Zeta potential of the dilute suspension was measured using a Malvern Zetasizer Zeta-Nano (Malvern, UK).

An analogous procedure was followed to obtain the $[Cu(tetren)]^{2+}$ solutions in deionized water. A 0.01M $[Cu(tetren)]^{2+}$ solution was prepared by mixing equal volumes of 0.02 mol/L $Cu(NO_3)_2 \cdot 3H_2O$ and 0.02 mol/L tetraethylenepentamine. 50 mL of the MMT 1 suspension and 150 μL of the $[Cu(tetren)]^{2+}$ solution were added to a centrifuge tube. After 24 h equilibration with shaking, $[Cu(tetren)]^{2+}$ was adsorbed onto the plane surface of MMT until saturation to obtain MMT 2 sample. The zeta potential of MMT 2 suspension was measured using a Malvern Zetasizer Zeta-Nano.

2.3.2. Concentration Measurement of SDS and 1831

Concentration of SDS can be measured by spectrophotometric quantification method. The colorimetric reaction of the SDS was carried out as follows: 1 mL desired concentration (from 0–9 mmol/L) of SDS was poured into a 25 mL volumetric flask. 24 mL coloring solution was poured into the volumetric flask and allowed to react for 2 h. The SDS solution was colored and the absorbance of the solutions was measured using a Thermo Genesys spectrophotometer (Waltham, MA, USA). The coloring solution was obtained as follows: 20 mL methyl orange solutions, 100 mL ethanol, 20 mL cetylpyridinium bromide solutions, 100 mL ethanol, and 760 mL deionized water were poured into a 1000 mL volumetric flask in order. Both the concentrations of the methyl orange solutions and the cetylpyridinium bromide solutions are 2.5 mmol/L. The mixed solution was reacted for 3 h in the volumetric flask.

The concentration of 1831 in aqueous solutions was determined by titration. Octadecyl trimethyl ammonium chloride (1831) is one kind of cationic surfactant with the formula $C_{21}H_{46}NCl$. The titration solution was 1831. The titrate solutions was prepared as follows: 20 mL SDS solutions, 5 mL mixed indicator, 5 mL acidity Na_2SO_4 solutions, 10 mL deionized water, and 15 mL dichloromethane was poured into a beaker in order. The concentration of SDS was 3 mmol/L. The 1831 solution was dropped into the titrate solutions until the pink phase turned colorless. The amount of the 1831 was equals to the dropped SDS. The standard curve of 1831 is shown in Figure 2b.

The mixed indicator was obtained by mixing 225 mL thymol blue solutions with 30 mL methylene blue solutions. The thymol blue solutions was prepared as follows: 0.05 g thymol blue was dissolved in 50 mL 20% ethanol water solutions. The supernatant was separated by filtration and then diluted to 500 mL. The concentration of methylene blue solutions was 0.036 g/L. The acidity Na_2SO_4 solutions

was obtained as follows: 100 g Na_2SO_4 was poured in 12.6 mL 95% sulfuric acid solutions and then dissolved and diluted to 1 L.

(**a**)

(**b**)
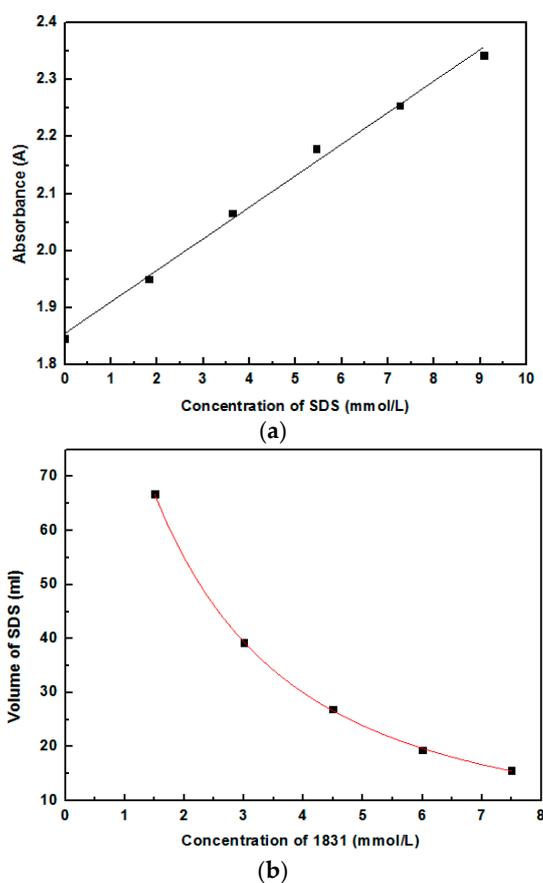
Figure 2. Standard curve of SDS and 1831. (**a**) SDS; and (**b**) 1831.

### 2.3.3. Adsorption Position of SDS and 1831 on the MMT Surface

Adsorption position of SDS and 1831 was determined by the adsorption isotherms results, zeta potential result, and exchange of Cu content on the surface of MMT 1/MMT 2. Firstly, 0.5 mL SDS/1831 with certain concentration was added into 5 mL MMT 1/MMT 2 suspensions. After that, suspensions were diluted to 50 mL with deionized water and reacted for 12 h. The concentration of SDS and 1831 in liquid phase was determined by spectrophotometric quantification and titration methods, respectively. The zeta potential of the prepared suspension was measured by using a Malvern Zetasizer Zeta-Nano (Malvern, UK). To measure the Cu content of the samples and the concentration of surfactants, suspension was centrifuged for 2 min at 4000 rev/min in order to separate the solid and liquid. After that, the solid sample was dried in an electro-thermostatic blast oven for 8 h at 60 °C in order to detect the Cu content. Then, Cu content of the prepared sample was detected by a Perkin Elmer Optima 4300DV inductively-coupled plasma spectrometer (ICP) (Waltham, MA, USA).

3. Results and Discussion

3.1. Restraining Montmorillonite Delamination

The Stokes size of the MMT in water after adsorbed SDS and 1831 are presented in Figure 3. The Stokes size percentage of −1.1 μm particles of MMT pre-treated by SDS and 1831 was 10.1% and 9.2%, respectively. These two values are much larger than those of original MMT (32.2%), indicating that the Stokes size of the original MMT was finer than that which was pre-treated by SDS and 1831.

It means that the delamination was restrained by pre-adsorption of SDS and 1831. The delamination of Na-MMT in water is often caused by the interlayer hydration [6,11–20]. However, after 1 h mixing in planetary mill, the agent and MMT particles mixed with each other sufficiently. The SDS and 1831 were adsorbed onto the MMT surface and the surface was changed to hydrophobic before the MMT was immersed in water. Then, the water molecule was block out of the interlayer and the interlayer hydration was restrained. In this case, the effect of delamination was weakened by pre-adsorption of SDS and 1831.
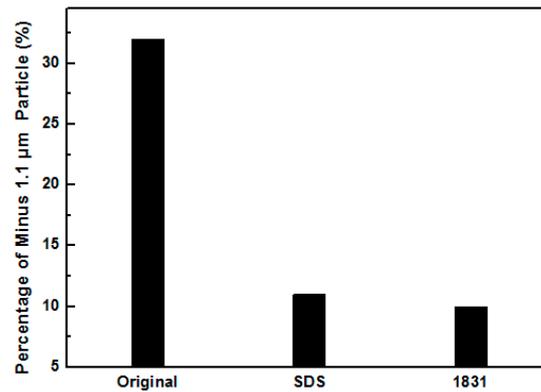
Figure 3. Stokes percentage of minus 1.1 μm particle in aqueous solutions pre-treated by of SDS and 1831.

Figure 4 shows the XRD pattern of MMT pre-treated by SDS and 1831. The interlayer spacing of the original MMT and MMT treated by the agent was measured by XRD. The results show that the interlayer spacing of the original MMT is mainly including two different kinds: 1.24 and 1.34 nm. It can be known that the MMT with the interlayer spacing of 1.34 nm was interlayer hydrated and can be delaminated in water. After MMT particles was dried in an electro-thermostatic blast oven at 60 °C, some of the hydrated water molecules of Na^+ still remained around [21] and the interlayer spacing was turned to 1.34 nm. It can be inferred that the interlayer counter ions offers the hydration energy for these MMT particles adsorbing water molecules and expanding the interlayer spacing in water. Then, leading to these MMT particles delaminated to fine particles [6,19–21]. Figure 4 also shows that the interlayer spacing of MMTs adsorbed with SDS and 1831 are both 1.24 nm, which was less than that of original MMT (1.34 nm). The smaller interlayer spacing can be attributed to the hydrophobization of MMT which can prevent the intercalation of water into the interlayer space. In this case, XRD results confirmed that the interlayer hydration of MMT was restrained by the adsorption of SDS and 1831.
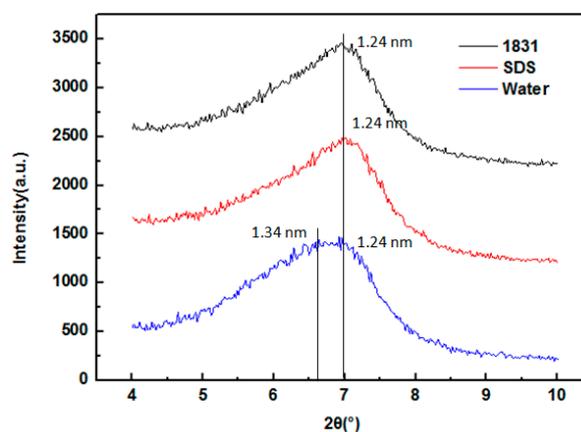
Figure 4. XRD pattern of MMT particles pre-treated by mechanical chemical adsorption of SDS and 1831.

3.2. Adsorption Position of SDS and 1831 on the Surface of MMT

Adsorption position of SDS and 1831 was measured by the adsorption capacity on the different surface of MMT. Firstly, the plane surface of MMT 1 was covered with $[Cu(tetren)]^{2+}$ to prepare MMT 2. The zeta potential of MMT 1 and MMT 2 are shown in Figure 5. The zeta potential of MMT 2 was around 0 mV, meaning that the plant surface was fully covered with $[Cu(tetren)]^{2+}$. After that, the adsorption capacity of SDS and 1831 on the surface of MMT 1 and MMT 2 was measured. The adsorption capacity is shown in Figures 6 and 7, respectively, and, the content of Cu adsorbed on MMT 2 surface after being treated by SDS and 1831 are shown in Figure 8. The results show that the adsorption capacity of SDS and 1831 was similar before and after the MMT adsorbed $[Cu(tetren)]^{2+}$. However, the content of Cu on MMT 2 treated by SDS was much higher than that of treated by 1831. These results indicated that the $[Cu(tetren)]^{2+}$ adsorbed on the plant surface can be replaced by 1831, but cannot be replaced by SDS. Because the SDS adsorption capacity was similar before and after the MMT was adsorbed with $[Cu(tetren)]^{2+}$, it can be known that SDS cannot be adsorbed on the plant surface of MMT. Thus, the adsorption capacity of SDS on the MMT surface can be attributed to the adsorption on edge surface. Since the $[Cu(tetren)]^{2+}$ adsorbed on the plant surface can be replaced by 1831, it means that 1831 was adsorbed on the whole surface of MMT. Since the MMT cannot be delaminated in water after being treated with SDS, then, the delamination of MMT can be restrained as long as the surfactant was adsorbed on the edge surface of MMT.
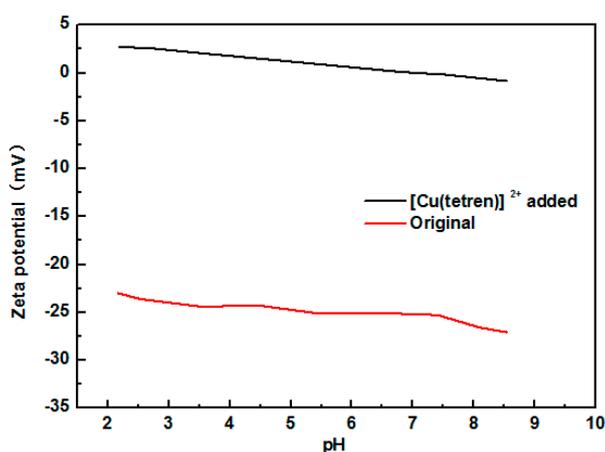

Figure 5. Zeta potential of MMT treated with $[Cu(tetren)]^{2+}$.

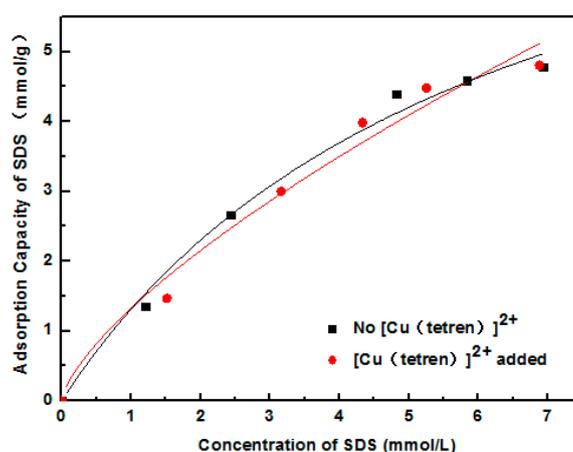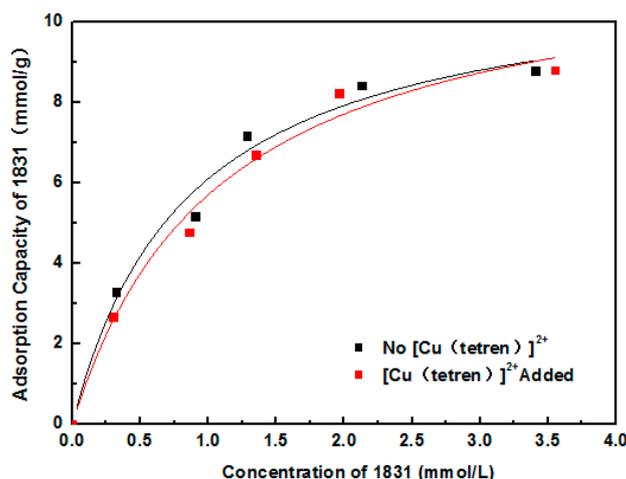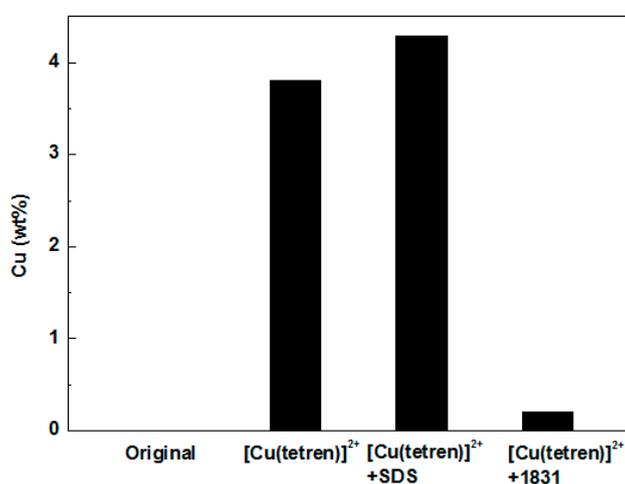**Figure 6.** Adsorption capacity of SDS on the surface of original MMT sample and the MMT sample adsorbed with $[Cu(tetren)]^{2+}$.

Figure 7. Adsorption capacity of 1831 on the surface of the original MMT sample and the MMT sample adsorbed with $[Cu(tetren)]^{2+}$.


Figure 8. Content of Cu in MMT samples treated by different methods.

Figure 9 shows the zeta potential of MMT 2 in different concentration of SDS solutions. The zeta potential of MMT 2 decreased as the concentration of SDS increased. This result reconfirmed that the SDS was adsorbed onto the edge surface of MMT. SDS was one kind of anion surfactant, meanwhile, the plane surface of the MMT has a permanent negative charge [22], it can be inferred that the SDS cannot adsorbed onto the plane surface of MMT. Then, the decreasing of zeta potential of MMT 2 would attribute to the adsorption of SDS on the edge surface of MMT.

Figure 10 shows the zeta potential of MMT 2 in different concentrations of 1831 solutions. The results show that the zeta potential of MMT 2 will decrease with the increase of 1831 concentration when the 1831 concentration lower than 0.30 mmol/L. When the concentration of 1831 is higher than 0.30 mmol/L, the zeta potential will increase with the increase of 1831 concentration. This result reconfirmed that the 1831 can adsorbed onto the whole surface of MMT. At the beginning, the $[Cu(tetren)]^{2+}$ was adsorbed on the plane surface of MMT 2. As one kind of cationic surfactant, the 1831 will adsorb onto the plane surface of MMT and the $[Cu(tetren)]^{2+}$ will be replaced when the concentration of 1831 is lower than 0.30 mmol/L. The valence of 1831 is +1, which is smaller than that of $[Cu(tetren)]^{2+}$, leading to the decrease of positive charge on the plane surface of MMT. After the concentration of 1831 is raised higher than 0.30 mmol/L, the zeta potential of the 1831 increased as more of the 1831 molecule was adsorbed onto the whole surface of the MMT 2. Thus, the 1831 was adsorbed on the whole surface of MMT.
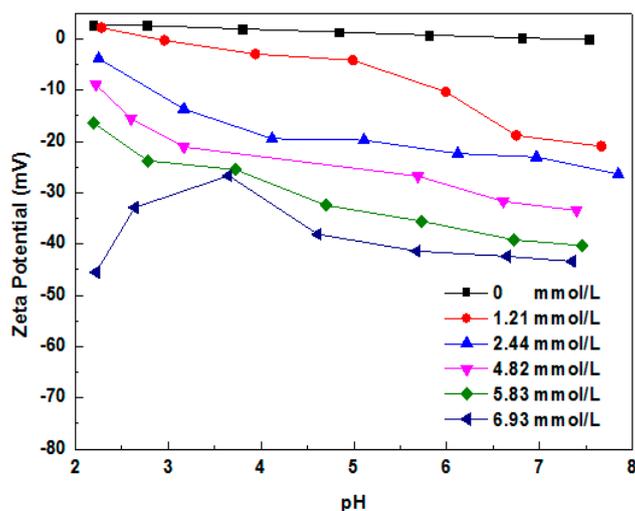
Figure 9. Zeta potential of MMT samples immersed in different concentration of SDS solutions with various pH values.
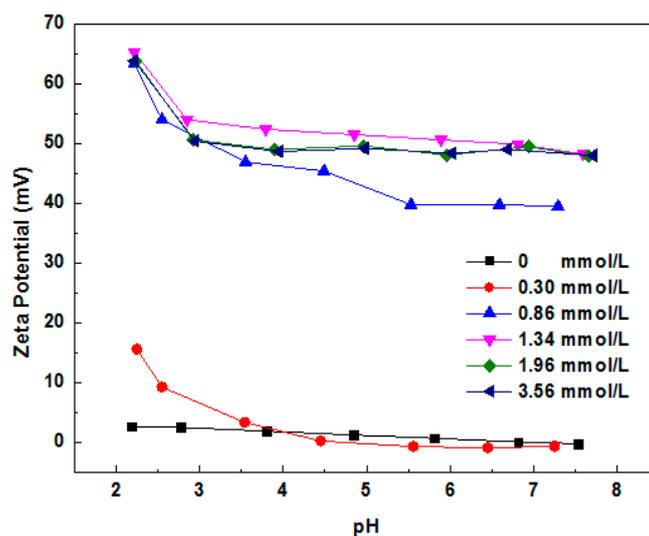
Figure 10. Zeta potential of MMT samples immersed in different concentrations of 1831 solutions with various pH values.

In summary, the adsorption position of SDS and 1831 on the surface of MMT are show in Figure 11. Figure 11 shows the original MMT particles, the adsorption position of [Cu(tetren)]$^{2+}$, the co-relationship of adsorption of SDS and [Cu(tetren)]$^{2+}$, the adsorption position of 1831 on the surface of MMT, the adsorption position of SDS, respectively. The experiential results in Figure 11d,c indicate that the [Cu(tetren)]$^{2+}$ adsorbed on the plant surface can be replaced by 1831 but cannot be replaced by SDS, and the [Cu(tetren)]$^{2+}$ can be adsorbed onto the edge surface of MMT caused by the adsorption of SDS on the edge surface, as shown by Figure 11c. Therefore, SDS was only adsorbed on the edge surface of MMT and 1831 was adsorbed both on the edge surface and plant surface of MMT, meanwhile, as shown in Figure 11e,d, respectively.
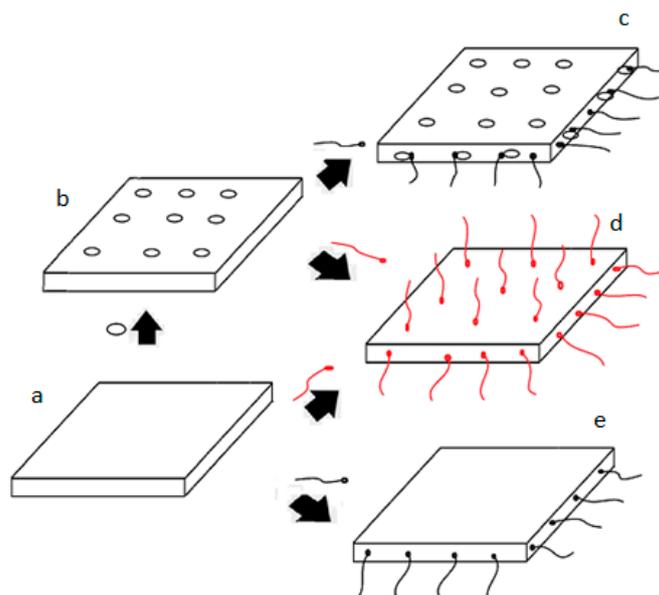
Figure 11. Schematic representation of the adsorption position of SDS and 1831 on the surface of MMT particles. (⬯: [Cu(tetren)]$^{2+}$; ⌇●: SDS; ⌇: 1831).

4. Conclusions

(1) The SDS and 1831 can be pre-adsorbed onto the edge surface of MMT mixed by grinding. The edge surface of MMT was turned hydrophobic before the MMT was immersed into water. The water molecule was block out of the interlayer space and the interlayer hydration was avoided when the MMT was immersed in water. Delamination of montmorillonite in water can be restrained by pre-adsorption of SDS and 1831.

(2) SDS is only adsorbed on the edge surface of MMT, while 1831 is adsorbed on both of the edge and plane of MMT. The hydrophobization of edge surface of MMT is useful in restraining delamination of MMT.

Author Contributions: Hongliang Li and Shaoxian Song conceived and designed the experiments; Hongliang Li and Yunliang Zhao performed the experiments; Hongliang Li, Shaoxian Song and Yuri Nahmad analyzed the data; Tianxing Chen and Yunliang Zhao contributed reagents/materials/analysis tools; Hongliang Li and Shaoxian Song wrote the paper.

Conflicts of Interest: The authors declare no conflict of interest.

References

1. Skipper, N.T.; Sposito, L.G.; Chou Chang, F.R. Monte Carlo simulation of interlayer molecular structure in swelling clay minerals. 2. Monolayer hydrates. *Clays Clay Miner.* **1995**, *43*, 294–303. [CrossRef]
2. Güven, N. Molecular aspects of clay-water interactions. In *Clay-Water Interface and Its Rheological Implications*; Güven, N., Pollastro, R.M., Eds.; CMS Workshop Lectures; The Clay Minerals Society: Chantilly, VA, USA, 1992; Volume 4, pp. 1–80.
3. Malikova, N.; Cadene, A.; Dubois, E.; Marry, V.; Durand-Vidal, S.; Turq, P.; Breu, J.; Longeville, S.; Zanotti, J.M. Water diffusion in a synthetic hectorite clay studied by quasi-elastic neutron scattering. *J. Phys. Chem. C* **2007**, *111*, 17603–17611. [CrossRef]
4. Johnston, C.T.; Sposito, G.; Erickson, C. Vibrational probe studies of water interactions with montmorillonite. *Clays Clay Miner.* **1992**, *40*, 722–730. [CrossRef]

5. Swenson, J.; Bergman, R.; Longeville, S. A neutron spin-echo study of confined water. *J. Chem. Phys.* **2001**, *115*, 11299–11305. [CrossRef]

6. Sposito, G.; Grasso, D. Electrical double layer structure, forces, and fields at the clay water interface. In *Interfacial Forces and Fields: Theory and Applications*; Hsu, J.P., Ed.; Marcel Dekker: New York, NY, USA, 1999; pp. 207–249.

7. Bussière, B. Hydrogeotechnical properties of hard rock tailings from metal mines and emerging geoenvironmental disposal approaches. *Can. Geotech. J.* **2007**, *44*, 7–40. [CrossRef]

8. Biggs, S. Aggregate structures and solid-liquid separation processes. *KONA Powder Part. J.* **2006**, *24*, 41–53. [CrossRef]

9. Jergensen, G.V. *Copper Leaching, Solvent Extraction, and Electrowinning Technology*; SME: Littleton, CO, USA, 1999.

10. Gorakhki, M.H.; Bareither, C.A. Salinity effects on sedimentation behavior of kaolin, bentonite, and soda ash mine tailings. *Appl. Clay Sci.* **2015**, *114*, 593–602. [CrossRef]

11. Norrish, K. The swelling of montmorillonite. *Discuss. Faraday Soc.* **1954**, *18*, 120–134. [CrossRef]

12. Norrish, K.; Rausell-Colom, J.A. Low-angle X-ray diffraction studies of the swelling of montmorillonite and vermiculite. In Proceedings of the 10th National Conference on Clays and Clay Minerals, Austin, TX, USA, 14–18 October 1961; Shineford, A., Franks, P.C., Eds.; Pergamon Press: New York, NY, USA, 1963; pp. 123–149.

13. Cebula, J.D.; Thomas, R.K.; White, J.W. Small angle neutron scattering from dilute aqueous dispersions of clay. *J. Chem. Soc. Faraday Trans. 1 Phys. Chem. Condens. Phases* **1980**, *76*, 314–321. [CrossRef]

14. Schramm, L.L.; Kwak, J.C.T. Influence of exchangeable cation composition on the size and shape of montmorillonite particles in dilute suspension. *Clays Clay Miner.* **1982**, *30*, 40–48. [CrossRef]

15. Nadeau, P. The physical dimensions of fundamental particles. *Clay Miner.* **1985**, *20*, 499–514. [CrossRef]

16. Avery, R.G.; Ramsay, J.D.F. Colloidal properties of synthetic hectorite clay dispersions. III. Light and small angle neutron scattering. *J. Colloid Interface Sci.* **1986**, *109*, 448–454. [CrossRef]

17. Sposito, G. The diffuse-ion swarm near smectitic particles suspended in 1:1 electrolyte solutions: Modified Gouy-Chapman theory and quasicrystal formation. In *Clay-Water Interface and Its Rheological Implications*; Güven, N., Pollastro, R.M., Eds.; CMS Workshop Lectures; The Clay Minerals Society: Chantilly, VA, USA, 1992; Volume 4, pp. 128–155.

18. Jasmund, K.; Lagaly, G. *Tonminerale und Tone. Struktur, Eigenschaften, Anwen-Dung und Einsatz in Industrie und Umwelt*; Steinkopff: Darmstadt, Germany, 1993; pp. 10–20. (In German)

19. Lagaly, G. From clay mineral crystals to colloidal clay mineral dispersions. In *Coagulation and Flocculation. Theory and Applications*; Dobias, B., Ed.; Marcel Dekker: New York, NY, USA, 1993; pp. 427–494.

20. Lagaly, G. From clay minerals to clay mineral dispersions. In *Coagulation and Flocculation*, 2nd ed.; Stechemesser, H., Dobias, B., Eds.; Taylor and Francis: Boca Raton, FL, USA, 2005; pp. 519–600.

21. Morodome, S.; Kawamura, K. In situ X-ray diffraction study of the swelling of montmorillonite as affected by exchangeable cations and temperature. *Clays Clay Miner.* **2011**, *59*, 165–175. [CrossRef]

22. Brigatti, M.F.; Galan, E.; Theng, B.K.G. Chapter 2: Structure and minerlaogy of clay minerals. In *Hand Book of Clay Science*; Elsevier: Amsterdam, The Netherlands, 2012; p. 42.

Molecularly-Limited Fractal Surface Area of Mineral Powders

Petr Jandacka [1,2,*], Jaromir Pistora [1,3], Jan Valicek [2,4] and Vilem Madr [5]

[1] IT4Innovations Centre and Nanotechnology Centre, VSB—Technical University of Ostrava,
    17. listopadu 15/2172, 70833 Ostrava, Czech Republic; jaromir.pistora@vsb.cz
[2] Institute of Physics, Faculty of Mining and Geology, VSB—Technical University of Ostrava,
    17. listopadu 15/2172, 70833 Ostrava, Czech Republic; jan.valicek@vsb.cz
[3] Department 606, VSB—Technical University of Ostrava, 17. listopadu 15/2172, 70833 Ostrava,
    Czech Republic
[4] Institute of Clean Technologies, VSB—Technical University of Ostrava, 17. listopadu 15/2172, 70833 Ostrava,
    Czech Republic
[5] Department of Natural Sciences and Humanities, College of Logistics, Palackeho 1381/25, 75002 Prerov,
    Czech Republic; vilem.madr@vslg.cz
* Correspondence: petr.jandacka@vsb.cz; Tel.: +420-597-323-365

Abstract: The topic of the specific surface area (SSA) of powders is not sufficiently described in the literature in spite of its nontrivial contribution to adsorption and dissolution processes. Fractal geometry provides a way to determine this parameter via relation SSA $\sim x^{(D-3)}s^{(2-D)}$, where x (m) is the particle size and s (m) is a scale. Such a relation respects nano-, micro-, or macro-topography on the surface. Within this theory, the fractal dimension $2 \leqslant D < 3$ and scale parameter s plays a significant role. The parameter D may be determined from BET or dissolution measurements on several samples, changing the powder particle sizes or sizes of adsorbate molecules. If the fractality of the surface is high, the SSA does not depend on the particle size distribution and *vice versa*. In this paper, the SSA parameter is analyzed from the point of view of adsorption and dissolution processes. In the case of adsorption, a new equation for the SSA, depending on the term $(2-D)\cdot(s_2 - s_{BET})/s_{BET}$, is derived, where s_{BET} and s_2 are effective cross-sectional diameters for BET and new adsorbates. Determination of the SSA for the dissolution process appears to be very complicated, since the fractality of the surface may change in the process. Nevertheless, the presented equations have good application potential.

Keywords: specific surface area; fractal dimension; adsorption; mineral powder; dissolution

1. Introduction

Specific surface area (SSA) is an important parameter influencing many physical and chemical processes, but there is no useful general equation for this quantity available in literature. This paper focuses on the surfaces of natural mineral powders (particular or granular materials, porous media), but the presented theory could be applied to all types and forms of materials. Surface energy, mechanical fragmentation processes, dissolution processes, chemical reactivity among liquid and solid powder particles, and adsorption are all strongly determined by the surface area of interacting powders [1–4].

The well-known measurement method for direct determination of the SSA is the BET (*Brunauer*, *Emmett*, *Teller*) method [5], which is based on gas adsorption. Alternatively, a dissolution process allows the SSA determination [6,7]. The "geometric" SSA can be derived from sieve or laser measurements of particle size distribution [8,9] or from capillary elevation of liquid through powder [10,11]. A correct equation for the determination of SSA must take into account the size

distribution of particles and surface topography. Theoretical relations for computation of the specific surface area of powder materials are presented in [9] for smooth particles or in reviews for fractal (rough-surface, irregular-surface) particles in [12–14], which also dealing with principal problems of the surface topography.

The goal of this paper is to offer relationships for practical evaluation of the real surface area of powders. Such an approach offers the possibility of evaluation of large sample sets if the fractal dimension *D* of a surface is well known, for example from several BET measurements. The end of the paper mentions errors committed by other authors expressing SSA through fractal geometry.

1.1. Powders

In general, the powders may be prepared via two processes: (i) by a mechanical fragmentation of large pieces of material through sequential fragmentation to powder form and (ii) by a crystallization pathway, where crystals are created within a solution. In case of mechanically fragmented materials, particle shapes are relatively independent of crystallographic parameters [15]. In cases of crystals that grew within the solution, their shapes are determined by the types of crystal lattices. Their SSA depends on particle size (grain or crystal sizes), particle shapes, and level of surface topography. The differences between surface topography may be very significant, as presented for several materials in Figures 1 and 2.
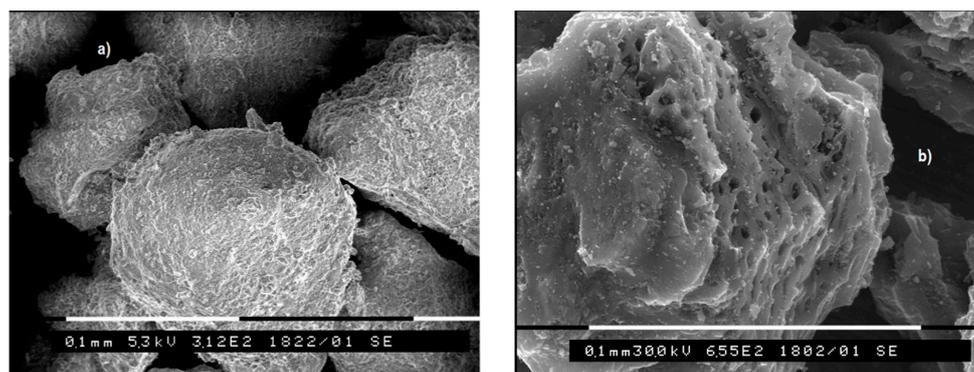
Figure 1. Examples of powder particles with high SSA: fractal-like topography of montmorillonite (**a**) with SSA $\approx$ 1000 $m^2 \cdot g^{-1}$ (nanometric pores) and activate black coal (**b**) with surface area around 1100 $m^2 \cdot g^{-1}$ and pore size of approximately 5 μm (maximum)—its surface seems to be non-homogenous, *i.e.*, non-fractal. Scale bars 0.1 mm.
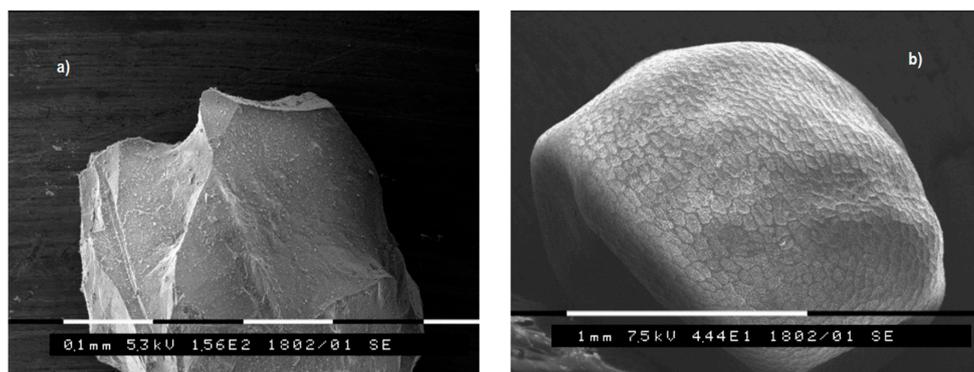
Figure 2. Relatively smooth surface topography of olivine, SSA $\approx$ 1 $m^2 \cdot g^{-1}$ (**a**) and bio-sample of rapeseed oil having bio-topography (**b**)—where the surface area was not measured. Scale bars: (**a**) 0.1 mm, (**b**) 1 mm.

1.2. Particle Size Distribution

Particle sizes in poly-disperse samples typically follow two-parametric distribution, most often log-normal (or Gaussian normal), power function GGS (*Gates*, *Gaudin*, *Schuhmann*), or exponential function RRSB (*Rosin*, *Rammler*, *Sperling*, *Bennet*) [16]. Evaluation of their surface area is not simple, in contrast to samples with very narrow size ranges, often considered and denoted as monodisperse. The most frequent type of distribution is log-normal, which was observed in both mechanically fragmented and crystallized powders [16,17]. The SSA of monodispersional, smooth, spheric particles is equal to SSA = $6/(\rho \cdot x)$, where ρ is particle density (true density) and x (m) the particle size (effective diameter). The SSA of the smooth-spheric particles following the log-normal size distribution is SSA = $6\rho^{-1} \cdot \exp[-(\mu + 2.5w^2)]$, where μ and w are the arithmetic mean and standard deviation of $\ln(x_i)$ values, respectively, and x_i is the diameter of an individual particle [8,9].

1.3. Surface Fractal Topography

A very useful mathematical tool for describing surface topography seems to be Mandelbrot´s fractal geometry [18]. This theory was successfully used for description of the topography of mineral powder surfaces [19–21]. The conclusions of such an analysis are:

(I) surface topography may have a fractal character, as found for more than 75% of materials [19]; (II) the surface fractal dimension D typically ranges between 2 and 3 and $D = 2$ denotes a smooth surface; (III) the surface topography is self-similar; (IV) the fractal dimension D can be determined from the linear dependence of log(SSA) on log(x), the slope is equal to ($D - 3$), or can alternatively be calculated from the dependence of log(SSA) on log(s), where the slope is equal to ($2 - D$), where x is the powder particle parameter (radius or diameter) and s (m) is the measurement scale (most often the size of adsorbate's molecule); (V) the SSA of particular materials can be expressed as $C \cdot s^{2-D} \cdot x^{D-3}$, where C (m^3/kg) is a constant related to the shape and density of the particles, s (m) is the size of adsorption molecule, x (m) is the size of the particles, and D is the surface fractal dimension [21].

The s parameter may even reach a lattice dimension of crystals, *i.e.*, 10^{-10} m. Because of an experimentally found paradox that D variables depend on the type of adsorbate (size of s), the researchers [7] introduced a new parameter, the "reaction fractal dimension" D_R (see Table 1). It means that the same powder may have different fractal dimensions according to the type of adsorbate molecules interacting with the powder surface. In several works dealing with the fractal dimension of surfaces, the scale parameter was omitted in spite of the fact that it is not possible to perform fractal analysis without it (see Discussion).

Table 1. Surface fractal dimensions and their standard deviations of natural powders in a shortened table taken from [7]. The D_R is the reaction fractal dimension and D is the true fractal dimension.

Powder Material	Process for D_R Determination	Particle Size Range (μm)	D_R	D [a]
Upper Columbus dolomite ($CaCO_3$-$MgCO_3$)	Acidic dissolution in NH_4Cl	163–2605	2.15 ± 0.10	2.91 ± 0.02
Upper Columbus dolomite ($CaCO_3$-$MgCO_3$)	Acidic dissolution in oxalate buffer	163–2605	2.34 ± 0.04	2.91 ± 0.02
Niagara dolomite ($CaCO_3$-$MgCO_3$)	Acidic dissolution in NH_4Cl	163–2605	2.07 ± 0.06	2.58 ± 0.01
Niagara dolomite ($CaCO_3$-$MgCO_3$)	Acidic dissolution in oxalate buffer	163–2605	2.19 ± 0.05	2.58 ± 0.01
Halimeda skeletal carbonate (green algae)	Acidic dissolution in seawater	81–513	2.05 ± 0.08	3.02 ± 0.07

[a] determined from BET or dissolution methods using small adsorbate molecules.

Table 1. *Cont.*

Powder Material	Process for D_R Determination	Particle Size Range (μm)	D_R	D [a]
Hybla alkali feldspar (potassium aluminosilicate)	Dissolution in HCl (pH 5)	56–400	2.95 ± 0.16	2.36 ± 0.02
Hybla alkali feldspar (potassium aluminosilicate)	Dissolution in boric acid buffer (pH 9)	56–400	3.06 ± 0.06	2.36 ± 0.02
Quartz	Dissolution in HF (3.66 M)	45–1000	2.14 ± 0.06	2.08 ± 0.08
Ottawa sand (quartz)	Dissolution in HF (3.66 M)	89–711	2.15 ± 0.06	2.08 ± 0.08
Madagascar quartz	Dissolution in HF (0.1 M)	0.4–6	1.59 ± 0.05	1.99 ± 0.06
Madagascar quartz	Dissolution in dilute NaOH	0.4–6	1.78 ± 0.07	1.99 ± 0.06
Vitreous silica	Dissolution in HF (0.1 M)	0.4–12.6	1.95 ± 0.04	2.03 ± 0.04
Iceland spar calcite ($CaCO_3$)	Reaction with $Fe(ClO_4)_3$ in presence of 2% CO_2	100–631	2.11 ± 0.03	2.16 ± 0.04
Iceland spar calcite ($CaCO_3$)	Reaction with $Fe(ClO_4)_3$ in presence of 20% CO_2	64–631	2.45 ± 0.04	2.16 ± 0.04
Iceland spar calcite ($CaCO_3$)	Dissolution in HCl (pH 3)	137–631	1.80 ± 0.06	2.16 ± 0.04

[a] determined from BET or dissolution methods using small adsorbate molecules.

2. Methods

This paper presents a theoretical framework to describe the SSA. Focusing on provision of applicable relations for the SSA of powder mineral materials, which are greatly spread in chemical processes, and currently play a significant role in nanotechnology, we used the basic findings of the Mandelbrot fractal theory [14]. This theory was completed using parameters related to the size distribution of powder particles. To support the theory, data from previous measurements are presented in Tables 1 and 2. Theoretical simulations were performed using Matlab 7.0 and Microsoft Excel codes.

The photos of the mineral particles were obtained from SEM Philips 515 (Philips, Amsterdam, The Netherlands). The presented SSA values (for Figures 1 and 2) were acquired from BET measurements on a Sorptomatic 1990 device (Thermo Fisher Scientific, Waltham, MA, USA).

Terminology: There is a problem in deciding whether specific surface area (SSA) is an appropriate name for the quantity that is the subject of the article. We could rename it chemical specific surface area, reaction specific surface area, or reactive specific surface area. Whatever the most appropriate name may be, what is known for certain is that real SSA does not exist since it depends on the *s* scale parameter, *i.e.*, on the size of adsorbate (dissolvent). In our opinion, it is better to keep the traditional name SSA, which is used in the main experimental technique (BET), to have the possibility of comparison, and simultaneously add the term reactive specific surface area (RSSA) as a more appropriate value for real surface processes. In the RSSA, which is defined in the discussion section, diffusion time of adsorbate (dissolvent) to fractal-porous media plays an important role.

3. Results and Discussion

In this section, the SSA is derived for pure powder materials using fractal theory. This approach provides a possibility for a recomputation of the SSA results from BET measurements to the SSA for a new adsorbate. The SSA value is then transformed to the RSSA in the discussion section below. Simple models for time-development of reaction fractal dimension D_R during surface interaction processes are simulated.

3.1. Shape Factor and Particle Shape Approximation

In this paper, the simplest spheric approximation of particle shapes, a sphere with diameter *x*, is used. Then, the surface area of the smooth spheric particles is $A = \pi x^2$ and its volume is $V = \pi x^3/6$, in which π and $\pi/6$ are shape factors. Real particles and crystals have various shapes and their shape factors cannot easily be derived.

3.2. Size Distribution of the Powder Particles

In laboratory work, it is experimentally very difficult to prepare a powder monodispersion, the particle size distribution of which can be described by a Dirac delta function. The powders are actually prepared as pseudo-monodispersions (narrow polydispersions) with $x_{\min}$ and $x_{\max}$ parameters. If the $x_{\max} - x_{\min}$ size interval is narrow, the particle size distribution can simply be considered as uniform, but the size uniformity as well as the uniformity of other quantities (surface area or volume of particles) is not guaranteed. The parameters of this type of distribution are presented in Appendix A, including x_A and x_V, the particle sizes with average surface area and volume, respectively, which are needed for the determination of the SSA. If the powders follow a linear distribution (see Figure 3), the related parameters, presented in Appendix B, can be used. It seems to be most practical to use the parameters for experimental distribution (see Appendix C). If, as is often observed, powder particles follow log-normal distribution, the mentioned parameters are presented in Appendix D. The particle size distribution of a powder can be determined most precisely by laser analyzers.
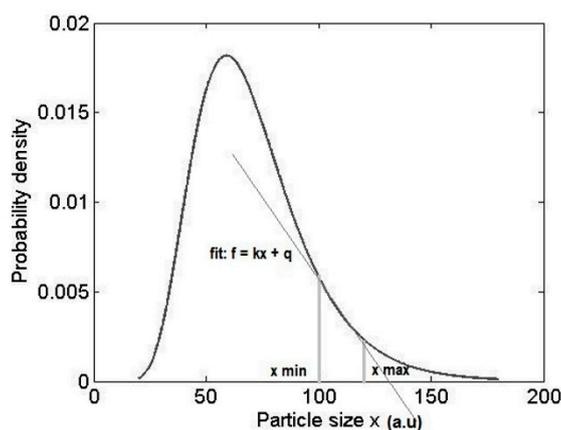
Figure 3. Linear approximation of particle size distribution within a narrow interval of log-normal particle size distribution.

3.3. Determination of the Specific Surface Area (SSA)

Considering the main results of fractal theory [18], a practical equation can be derived for computation of the SSA of powders with fractal (non-smooth) surfaces.

The maximal amount of molecules covering the spheric particle in a single layer is

$$N = \left(\frac{\pi x_A^2}{s^2}\right)^{D_A} = \pi^{D_A} \left(\frac{x_A}{s}\right)^{2D_A} = \pi^{D/2} \left(\frac{x_A}{s}\right)^D, \tag{1}$$

where x_A (m) is the particle size with average surface area, *s* (m) is the effective cross sectional diameter of a liquid molecule, *D* (-) is the true fractal dimension of the surface, and $D_A = D/2$ fractal dimension of the surface related to the area scale. For similar considerations see [22,23]. Approximation of the adsorbate molecular cross-sectional area by square seems to be theoretically more valid than approximation by circle. Equation (1) corresponds with Mandelbrot´s fractal geometry, where the fractal dimension for unit area (length) is expressed by the well-known equation $D = \log(N)/\log(1/\varepsilon)$,

where $\varepsilon \leqslant 1$ is a dimensionless equivalent to the scale parameter s. A total area of the single particle (granule, grain, crystal) is

$$A = Ns^2 = \pi^{D/2} x_A^D s^{(2-D)} (\text{m}^2). \tag{2}$$

The SSA is generally defined as SSA $= A/(\rho V) = n A_{\text{ave}}/(\rho n V_{\text{ave}})$, where A and V are the surface area and volume of all powder particles with density ρ, A_{ave} and V_{ave} are average values for a set of particles, and n is their count. Respecting the fractal character of a surface, the SSA is

$$\text{SSA} = 6\pi^{(D/2-1)} \frac{x_A^D \cdot s^{(2-D)}}{\rho x_V^3} (\text{m}^2/\text{kg}) \tag{3a}$$

In case of true mono-dispersion,

$$\text{SSA} = 6\pi^{(D/2-1)} \frac{x^{(D-3)} \cdot s^{(2-D)}}{\rho} (\text{m}^2/\text{kg}), \tag{3b}$$

where x is the particle size (effective diameter).

The limits of Equation (3b) are SSA $= 6/(\rho \cdot x)$ for $D = 2$ and SSA $= 6\pi^{0.5}/(\rho \cdot s)$ for $\lim_{D \to 3}$SSA. An equation similar to Equation (3b) is presented in [21] and in a simpler form also in the book by Adamson [12], page 564. The importance of the x_A and x_V parameters significantly decreases if the value of D approaches 3.

The form of Equation (3b) confirms the validity of the mutual experimentally observed linear relation between log(SSA) and log(x) or the linear relation between log(SSA) and log(s), with slopes equal to $(D - 3)$ and $(2 - D)$ respectively [7,19], as mentioned in the introduction. It seems that such experimentally determined dependences with a significant linear theoretical fit imply a fractal (or self-similar) character of measured surfaces. Also, several authors note the multifractality of the surface [24,25]. It is contentious whether the dependences presented in [24] express "multifractality" or non-fractality of surface. Multifractality of surface seems to be hard to explain since the basis of the fractal theory is a dimensional replication of the same surface motive.

Considering alternative evaluation of the external surface area by SSA$_{\text{ext}} = \lambda 6/(\rho \cdot x)$ relation in [26], where λ is the surface roughness, the slope of linear relation between log(SSA) and log(x) is equal to -1. Such an equation is not applicable to fractal surfaces and may be fully recovered by Equation (3a) or (3b).

3.4. Useful Equations

Logarithmic transformation of Equation (3a,b) gives

$$\log(\text{SSA}) = b + m_1 \log(x_A) - 3\log(x_V) \tag{4a}$$

$$\log(\text{SSA}) = b + m_2 \log(x), \tag{4b}$$

where $b = \log[6\pi^{(D/2-1)} \rho^{-1} s^{(2-D)}]$ and $m_1 = D$ and $m_2 = (D - 3)$. Equation (4b) corresponds with the relation generally used for evaluation of SSA of mineral powders [26]. The slope in the log(SSA) *vs.* log(x) dependence is presented for several minerals in Table 2 (original slopes recomputed for fractal dimensions). In several cases, the fractal dimension D does not fall into the interval $2 \leqslant D < 3$, similarly as in the case of Table 1. Such results were not explained in the original paper [7], but theoretically, using Equation (4a), the paradox can be explained.

Brantley and Mellott [26] used the mentioned dependence (Equation (4b)); however, they worked with narrow polydispersions. As a particle size parameter, they introduced the "mean particle diameter" $d = 10^n = (x_{\max} \cdot x_{\min})^{0.5}$, where $n = (\log x_{\max} + \log x_{\min})/2$, considering the particle size distribution as log-normal. For example, for Amelia albite, the presented size limits amount to $x_{\max} = 840$ μm and $x_{\min} = 500$ μm and the mean particle diameter amounts to $d = 648$ μm.

Their approach is not correct, because considering the particle size distribution as log-normal in all powder size intervals is not correct (the log-normal distribution cannot be expected within the individual size intervals, see Figure 3). As a result, the expressions for *d* do not represent the effective particle dimension.

Table 2. Evaluation of fractal dimensions of natural mineral powders—table transferred from [26]. The values of the fractal dimension *D* were computed on the basis of the above derived relation *D* = *m* + 3, see Equation (5c).

Powder Material	*m*	*D*
Quartz	−1.0	2.0
Microcline (Keystone)	−0.8 ± 0.2	2.2 ± 0.2
Microcline (Keystone)	−0.8 ± 0.1	2.2 ± 0.1
Albite glass	−1.4 ± 0.1	1.6 ± 0.1
Albite (Amelia)	−1.0 ± 0.1	2.0 ± 0.1
Albite (Evje)	−0.7 ± 0.1	2.3 ± 0.1
Oligoclase (Madawaska)	−0.6 ± 0.2	2.4 ± 0.2
Labradorite (Labrador)	−0.5 ± 0.1	2.5 ± 0.1
Bytownite (Duluth)	−0.5 ± 0.1	2.5 ± 0.1
Bytownite (Crystal Bay)	−0.6 ± 0.2	2.4 ± 0.2
Anorthite (Miyake Jima)	−1.2 ± 0.2	1.8 ± 0.2
Anorthite (Grass Valley)	−0.20 ± 0.05	2.80 ± 0.05
Olivine (San Carlos)	−1.1 ± 0.2	1.9 ± 0.2
Olivine (Twin Sisters)	−0.3 ± 0.2	2.7 ± 0.2
Diopside (Herschel)	−0.6 ± 0.2	2.4 ± 0.2
Hornblende (Gore Mtn.)	−0.6 ± 0.1	2.4 ± 0.1

3.5. Determination of the Surface Fractal Dimension D

Equation (4a,b) offer the possibility of regression determination of the true surface fractal dimension *D* or reaction fractal dimension D_R. In the case of real powders having dispersion of particle sizes, valid relations are

$$\log(\text{SSA} \cdot x_V{}^3) \sim D \cdot \log(x_A) \tag{5a}$$

$$\log(\text{SSA}) \sim (2 - D) \cdot \log(s). \tag{5b}$$

Fractal dimension of mono-dispersion can be determined using the relation

$$\log(\text{SSA}) \sim (D - 3) \cdot \log(x) \tag{5c}$$

or through the relation presented in Equation (5b). In this sense, the values and uncertainties of the *D* and D_R fractal dimensions, presented in Tables 1 and 2 should be revised according to Equation (5a). The parameters x_A and x_V can be most simply computed from experimental distribution (see Appendix C), which is determined based on the particle size measurement using a laser analyzer. Vandamme *et al.* deal with the theoretical limits of such an approach by simulating single-layer molecular coverage of the hypothetical nano-, micro- and millimetric irregularities on the material surface [23].

3.6. Uncertainty Computation

We usually need to express the results in the form of (SSA ± u_{SSA}) m^2/kg. The practicality of the main presented results (Equation (3a,b)) is significantly dependent on the $u_{\text{SSA}} = [\Sigma(u_{q_i} \cdot \partial \text{SSA}/\partial q_i)^2]^{0.5}$ uncertainty, where q_i is the *q*-th quantity. The most significant contribution to u_{SSA}, which is the total uncertainty, probably really induces uncertainty of the u_D surface fractal dimension. The u_D should be determined as exactly as possible.

3.7. Incorrect Use of Fractal Theory for the SSA Evaluation

In several papers, the fractal theory is incorrectly used for the SSA evaluation. Authors usually ignore the significance of the s scale parameter, which is one of the most important parameters within the fractal theory. For example, in [26] an equation is presented for geometric SSA in the form of $a\rho^{-1}x^{(D-3)}$, where a is the shape coefficient. The s parameter is missing and if D is not equal to 2, SSA does not have the $m^2 \cdot kg^{-1}$ unit. Similar incorrect equations were previously presented, for which see [27]. Working with fractal theory, the authors again ignored the s scale parameter, and presented an incorrect equation SSA = $kd_{ave}^{(D-3)}$ for spheric monodispersion, where a is the shape coefficient and d_{ave} is the average size of particles.

3.8. Transformation of the SSA Value after the BET Measurement for a New Adsorbate

The SSA_{BET} acquired through BET measurement can be determined using several types of adsorbate molecules (N_2, Kr, or Ar and others). If use of powder for interaction with another adsorbate (for example water) is desirable after the BET measurement, the new SSA_2 can be estimated by the general equation $SSA_2 = SSA_{BET} + \Delta SSA = SSA_{BET} + \Delta s \cdot dSSA_{BET}/ds_{BET}$ and $\Delta s = (s_2 - s_{BET})$, where s_2 is the size of the molecule of the new adsorbate and s_{BET} the size of the molecule used in the BET measurement. Now, the SSA_{BET} is considered as an experimental value, but derivation is applied to Equation (3a), $SSA_{BET} = 6\pi^{(D/2-1)}\rho^{-1}x_A{}^D x_V{}^{-3} s_{BET}{}^{(2-D)}$. The derived surface area related to the new adsorbate is:

$$SSA_2 = SSA_{BET} \cdot [1 + (2-D) \cdot (s_2 - s_{BET})/s_{BET}]\ (m^2/kg). \tag{6}$$

The s values are constants and represent the cross-sectional diameters of adsorbate molecules and are not dependent on the type of adsorbent. The tabulated values of a b constant ($m^3 \cdot mol^{-1}$) from the van der Waals equation should be used for their estimations (see Table 3). The s effective diameter equals $(b/N_A)^{1/3}$, where N_A is Avogadro's number. The standard uncertainty of such a transformation should be estimated from u_{BET} and uncertainties of D, s_{BET} and s_2. The validity of Equation 6 should be tested in BET measurements, but is probably restricted by variation of fractal dimension, as subsequently presented.

Table 3. Estimations of the effective cross-sectional diameters $s = (b/N_A)^{1/3}$ of selected adsorbate molecules according to the tabulated b values [28] contained in van der Waals's equation. The standard uncertainty of s is estimated from $u_b = 10^{-8}$ $m^3 \cdot mol^{-1}$ value.

Adsorbate	$b \cdot 10^6$ ($m^3 \cdot mol^{-1}$)	$s \cdot 10^{10}$ (m)	Adsorbate	$b \cdot 10^6$ ($m^3 \cdot mol^{-1}$)	$s \cdot 10^{10}$ (m)	Adsorbate	$b \cdot 10^6$ ($m^3 \cdot mol^{-1}$)	$s \cdot 10^{10}$ (m)
N_2	38.70	4.09 ± 0.03	HCl	40.60	4.16 ± 0.03	C_3H_8	90.30	5.43 ± 0.02
Ar	32.00	3.84 ± 0.04	$C_2H_4O_2$	107.00	5.74 ± 0.02	C_3H_8O	98.30	5.58 ± 0.02
Kr	39.60	4.12 ± 0.03	SO_2	56.70	4.65 ± 0.03	Rn	62.00	4.79 ± 0.02
H_2	26.62	3.61 ± 0.04	CO	39.54	4.12 ± 0.03	Hg	16.96	3.11 ± 0.06
He	23.50	3.47 ± 0.05	CO_2	42.81	4.23 ± 0.03	CS_2	72.50	5.04 ± 0.02
H_2O	30.40	3.78 ± 0.04	O_2	31.70	3.83 ± 0.04	H_2S	43.00	4.24 ± 0.03
C_2H_6O	83.95	5.30 ± 0.02	CH_4	42.75	4.23 ± 0.03	C_7H_8	146.00	6.37 ± 0.01
C_6H_6	119.0	5.95 ± 0.02	CH_4O	67.00	4.91 ± 0.02	C_8H_{10}	176.00	6.78 ± 0.01
HF	73.85	5.08 ± 0.02	O_3	49.10	4.43 ± 0.03	Br	44.40	4.28 ± 0.03

## 3.9. Discussion on Variability of Fractal Dimension

The existence of different fractal dimension D for various adsorbates (or dissolvents, on the same mineral powder) is an empirical finding and does not seem to have any theoretical substantiation. The fractal dimension is likely to be an invariant surface constant (according to fractal theory), independent on the size of the adsorbate molecule. On the other hand, the existence of the abovementioned phenomenon is strongly supported by experiments (see Table 1). Taking into account the two different surface processes, adsorption and dissolution, the explanation could be based on a

consideration of the time-dependent creation of the molecular layer on the powder surface connected with the different intensity of molecular diffusion into the pores as well as on the change of surface topography during the dissolution [29–31]. Other surface interaction processes like precipitation, crystal growth, and corrosion can be analyzed, while their description is probably very similar [30,32].

In the case of adsorption/sorption processes that are based on van der Waals forces on the interface, the connection between true fractal dimension D and the reaction fractal dimension D_R could be most simply estimated via an asymptotic function:

$$D_R = 2 + w(1 - e^{-kt}),\qquad(7)$$

where $D = 2 + w$, $w = \langle 0, 1 \rangle$ and $k > 0\,\text{s}^{-1}$ are constants and t (s) is the time (for simulations see Figure 4). The k constant represents the intensity of adsorbate diffusion to pores. The boundary conditions of the presented equation are $D_R = 2$ at the time $t = 0$ s and the opposite condition is $\lim_{t \to \infty} D_R = D$. More complicated derivations for this process could be made from advanced models of penetration of liquid to fractal porous media [31].
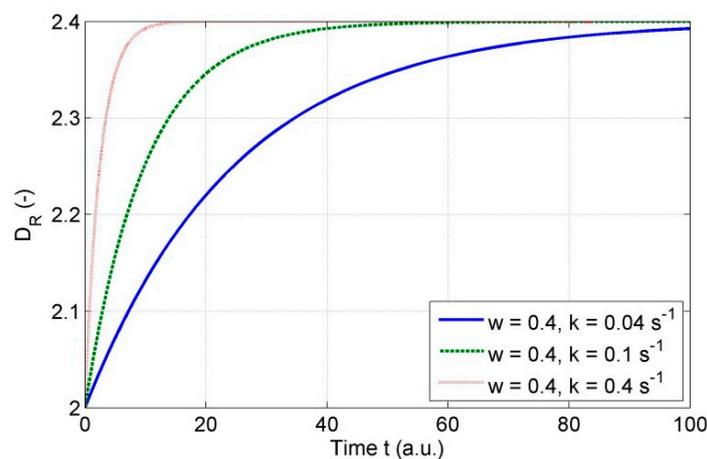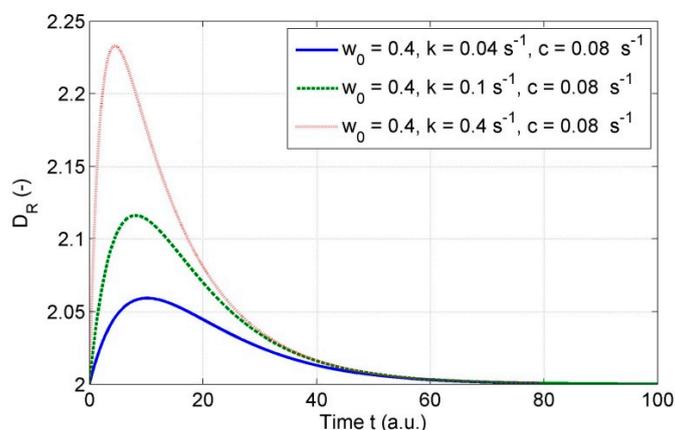

Figure 4. Simulation of hypothetic time-dependence of D_R on the time in the case of adsorption processes—influence of diffusion of adsorbate on fractal surface topography.

In the case of dissolution processes that are based on surface chemical interactions reducing the amount of solid material, the variability of fractal dimension probably depends on time, too. This seems to be a more complicated issue than adsorption, which poses many specific problems [33]. The reaction surface area A is one of the parameters in dissolution rate r, which is presented in the form of $r = kA\lambda \cdot \exp[-E/(RT)]$ in unit mol/(m$^2 \cdot$ s), where k and λ are constants, E is the specific activation energy, and RT is specific heat [30]. It is apparent that the SSA has to change during the dissolution and the dissolution rate changes during the process according to the change of fractal dimension. For the development of reaction fractal dimension, a simple function that could be valid for an ideal dissolution process can be estimated as follows:

$$D_R = 2 + w(1 - e^{-kt}), \quad w = w_0 \cdot e^{-ct},\qquad(8)$$

where $k > 0$ s^{-1} is a constant and $2 + w_0 \cdot e^{-ct} = D$ is the true surface fractal dimension, $c > 0$ s^{-1} represents the intensity at which smoothness is achieved, $w_0 = \langle 0, 1 \rangle$ is a constant related to initial fractal dimension. This relation is deduced from the condition that at the beginning of interaction, the process is similar to adsorption and fractal dimension $D_R = 2$, because the adsorbate molecules start to diffuse to pores and inner irregularities at that moment. Simultaneously, the dissolution is active on the external cover of particles and the fractality (or roughness) is reduced. Adding these two processes results in time-dependence, as presented in Figure 5. In reality, however, the fractality (roughness) can

increase with time in some dissolution processes, making this idealized model invalid provided that any inhomogeneities and non-reactive surface points appear on the surface [30,33,34].

Figure 5. Simulation of hypothetic time-dependence of D_R on the time in the case of specific dissolution process—influence of diffusion and "dissolution of fractality."

The reaction fractal dimension D_R appears to be a time-dependent quantity during adsorption or dissolution. From this point of view, it is more practical to write the reaction fractal dimension in the form of $D_{R,t}$, where t (s) is the measurement time. For example, $D_{R,6h}$ denotes the value of the reaction fractal dimension after six hours of adsorption/dissolution. A more precise designation would be $D_{R,He,6h}$ with the specification of a He-like adsorbate/dissolvent. A single value of SSA for a specific powder does not exist, and surface area quantity must be related to the adsorbate size and time. This approach could explain the paradox of a different cross-sectional area of the same gas on a different material, as presented in many papers e.g., [35], and perhaps also the paradox $D < 2$ in Tables 1 and 2.

Thus, we have two basic equations. The first one is the equation for the SSA, the idealized Equation (3a), which is valid only for long reaction times and is appropriate for adsorption or sorption. The equation can be rewritten to find a more practical relation for general time-dependent surface interaction processes. Consequently, reactive specific surface area can be expressed as follows:

$$\text{RSSA}_{X,t} = 6\pi^{(0.5D_{R,t} - 1)}\frac{x_A^D \cdot s^{(2 - D_{R,t})}}{\rho \cdot x_V^3}\,(\text{m}^2/\text{kg}) \tag{9}$$

where X is the designation of a liquid or gas substance (H_2O, N_2, He, *i.e.*, adsorbate, dissolvent), t (s) is the reaction time and s (m) is the size of adsorbate or dissolvent. Therefore, whereas the SSA does not depend on time, the RSSA does. The Equation (9) is appropriate for a description of dissolution processes. The SSA seems to be a constant quantity for long-standing adsorption processes, but not for dissolution processes, because there the true fractal surface dimension D changes with time. The dissolution rate expressed as mass/time is proportional to the $\text{RSSA}_{X,t}$ by the relation

$$\frac{\text{d}m}{\text{d}t} \sim \text{RSSA}_{X,t} \tag{10}$$

but the total amount Δm (kg) of solute is

$$\triangle m \sim \overline{\text{RSSA}_{X,t}} = \frac{1}{\Delta t}\int_{t1}^{t2} \text{RSSA}_{X,t}\text{d}t \tag{11}$$

and depends on the mean of $\text{RSSA}_{X,t}$, where $\Delta t = t_2 - t_1$ is the dissolution time interval.

4. Conclusions

It is possible to determine the SSA of the powder particles using fractal theory by means of Equation (3a), or in the case of time-dependent surface processes by Equation (9) via the RSSA. For the exact evaluation of the SSA or RSSA for a set of the same type of samples, first the reaction fractal dimension of surface D_R should be determined using dependence $\log(\text{RSSA}_{X,t} \cdot x_V{}^3) \sim D_{R,t} \cdot \log(x_A)$ or $\log(\text{RSSA}_{X,t}) \sim (2 - D_{R,t}) \cdot \log(s)$, by several BET or dissolution measurements. The value of the SSA depends on the size of the interacting molecule. The size of this molecule is equal to s scale, a significant parameter within fractal geometry. The value of the reaction fractal dimension D_R seems to be a function of the time and the true fractal dimension D.

A new equation $\text{SSA}_X = \text{SSA}_{\text{BET}} \cdot [1 + (2 - D) \cdot (s_X - s_{\text{BET}})/s_{\text{BET}}]$, where s_{BET} and s_X are effective cross-sectional diameters for the BET and for new adsorbate molecules, was derived. After the BET measurement, this equation can be used for estimation of the SSA of the same powder potentially interacting with a new adsorbate.

Author Contributions: Petr Jandacka designed and performed the measurements; Petr Jandacka and Jan Valicek analyzed the data; Jaromir Pistora and Vilem Madr provided materials and measurement devices—they controlled of activities; Petr Jandacka formulated the theory, derived the equations and wrote the paper.

Conflicts of Interest: The authors declare no conflict of interest.

Appendix A. *Estimation of the x_A and x_V Effective Particle Dimensions for the Uniform Particle Size Distribution*

If spheric particle size x (diameter) has a uniform distribution $f_x(x) = 1/(x_{\max} - x_{\min})$, then the surface area $A = h(x) = \pi x^2$ has a distribution

$$f_A(A) = f_x\left[h^{-1}(A)\right]\frac{\mathrm{d}x}{\mathrm{d}A}, \tag{A1}$$

where $h^{-1}(A) = x = (A/\pi)^{0.5}$. Consequently, probability densities for surface area, depending on A and x, are

$$f_A(A) = \frac{1}{2\pi(x_{\max} - x_{\min})}\left(\frac{\pi}{A}\right)^{0.5}, \tag{A2}$$

and

$$f_A(x) = \frac{1}{2\pi x(x_{\max} - x_{\min})}. \tag{A3}$$

Average surface area can be computed according to the following equation:

$$A_{\text{ave}}(A) = \int_{A\min}^{A\max} A \cdot f_A(A)\,\mathrm{d}A, \tag{A4}$$

and because $\mathrm{d}A = 2\pi x\mathrm{d}x$, dependence on x equals

$$A_{\text{ave}}(x) = \int_{x\min}^{x\max} \frac{\pi x^2}{(x_{\max} - x_{\min})}\mathrm{d}x = \frac{\pi\left(x_{\max}^3 - x_{\min}^3\right)}{3(x_{\max} - x_{\min})}. \tag{A5}$$

Analogically, using the same algorithm, the average volume is

$$V_{\text{ave}}(x) = \frac{\pi\left(x_{\max}^4 - x_{\min}^4\right)}{24(x_{\max} - x_{\min})}. \tag{A6}$$

The size of a particle with average surface area has a diameter of

$$x_A = (A_{ave}/\pi)^{0.5}, \tag{A7}$$

and the size of a particle with average volume has a diameter of

$$x_V = (6V_{ave}/\pi)^{1/3}. \tag{A8}$$

Appendix B. *Estimation of the Effective Particle Dimensions x_A and x_V for the Linear particle Size Distribution*

Considering the linear particle size distribution $f_x(x) = kx + q$, the following condition can be stated:

$$1 = \int_{xmin}^{xmax} (kx + q)\mathrm{d}x = \frac{k}{2}\left(x_{max}^2 - x_{min}^2\right) + q\left(x_{max} - x_{min}\right), \tag{B1}$$

where the intercept q equals

$$q = \frac{2 - k\left(x_{max}^2 - x_{min}^2\right)}{2\left(x_{max} - x_{min}\right)}. \tag{B2}$$

Using the same algorithm as in Appendix A, the average surface area is

$$A_{ave}(x) = \frac{\pi k}{4}\left(x_{max}^4 - x_{min}^4\right) + \frac{\pi q}{3}\left(x_{max}^3 - x_{min}^3\right), \tag{B3}$$

and the average volume is

$$V_{ave}(x) = \frac{\pi k}{30}\left(x_{max}^5 - x_{min}^5\right) + \frac{\pi q}{24}\left(x_{max}^4 - x_{min}^4\right). \tag{B4}$$

The k and q parameters should be determined based on a linear fit of the experimental distribution in a selected size interval (see Figure 3). The spheric particle with average surface area has a diameter of

$$x_A = (A_{ave}/\pi)^{0.5}, \tag{B5}$$

and the diameter of spheric particle having average volume is

$$x_V = (6V_{ave}/\pi)^{1/3}. \tag{B6}$$

Appendix C. *Estimation of the x_A and x_V Effective Particle Dimensions for the Experimental Particle Size Distribution*

The probability density of experimental distribution is

$$f = n_i/[n(x_b - x_a)], \tag{C1}$$

where $(x_b - x_a)$ is the particle size interval of a bin.

The spheric particle sizes with average surface area and average volume are

$$x_A = \left(\frac{1}{n}\sum_{i=1}^{n} n_i x_i^2\right)^{0.5}, \tag{C2}$$

$$x_V = \left(\frac{1}{n} \sum_{i=1}^{n} n_i x_i^3 \right)^{1/3},$$
(C3)

where n is the total number of particles and n_i are the frequencies of particle sizes x_i.

Appendix D. *Estimation of the x_A and x_V Effective Particle Dimensions for the Log-Normal Particle Size Distribution*

The probability density of the log-normal distribution is

$$f(x) = \frac{1}{\omega x \sqrt{2\pi}} \exp \left(-\frac{\ln x - \mu}{2\omega^2} \right).$$
(D1)

The average surface area and the average volume are

$$A_{\mathrm{ave}} = \pi \cdot \exp(2\mu + 2\omega^2),$$
(D2)

$$V_{\mathrm{ave}} = \pi \cdot \exp(3\mu + 4.5\omega^2)/6,$$
(D3)

where μ is the arithmetic mean and w standard deviation of the $\ln(x_i)$ values [8,9]. In the particle size distribution, the diameter of a spheric particle with average surface area is

$$x_A = (A_{\mathrm{ave}}/\pi)^{0.5}$$
(D4)

and the diameter of a spheric particle with average volume is

$$x_V = (6V_{\mathrm{ave}}/\pi)^{1/3}.$$
(D5)

References

1. Greathouse, J.; Johnson, K.; Greenwell, H. Interaction of natural organic matter with layered minerals: Recent developments in computational methods at the nanoscale. *Minerals* **2014**, *4*, 519–540. [CrossRef]
2. Li, J.; Hitch, M. Carbon dioxide sorption isotherm study on pristine and acid-treated olivine and its application in the vacuum swing adsorption process. *Minerals* **2015**, *5*, 259–275. [CrossRef]
3. Ozkanlar, A.; Kelley, M.; Clark, A. Water organization and dynamics on mineral surfaces interrogated by graph theoretical analyses of intermolecular chemical networks. *Minerals* **2014**, *4*, 118–129. [CrossRef]
4. Ghanbarian-Alavijeh, B.; Millán, H. The relationship between surface fractal dimension and soil water content at permanent wilting point. *Geoderma* **2009**, *151*, 224–232. [CrossRef]
5. Brunauer, S.; Emmett, P.H.; Teller, E. Adsorption of gases in multimolecular layers. *J. Am. Chem. Soc.* **1938**, *60*, 309–319. [CrossRef]
6. Dokoumetzidis, A.; Macheras, P. A century of dissolution research: From Noyes and Whitney to the biopharmaceutics classification system. *Int. J. Pharm.* **2006**, *321*, 1–11. [CrossRef] [PubMed]
7. Farin, D.; Avnir, D. Reactive fractal surfaces. *J. Phys. Chem.* **1987**, *91*, 5517–5521. [CrossRef]
8. Jandacka, P.; Hlavac, L.M.; Madr, V.; Sancer, J.; Stanek, F. Measurement of specific fracture energy and surface tension of brittle materials in powder form. *Int. J. Fract.* **2009**, *159*, 103–110. [CrossRef]
9. Jandacka, P.; Sancer, J.; Vojtkova, H.; Besta, P.; Brazda, R.; Kolicova, P.; Simkova, L. Fracture energy of selected brittle silicates. *Ceram. Silik.* **2011**, *55*, 355–361.
10. Carman, P.C. Capillary rise and capillary movement of moisture in fine sands. *Soil Sci.* **1941**, *52*, 1–14. [CrossRef]
11. Jandacka, P.; Dvorsky, R.; Lunacek, J. Measurement of powder surface area using capillary elevation method. *Inzynieria Miner.* **2015**, *16*, 171–179.
12. Adamson, W.A. *Physical Chemistry of Surfaces*; John Wiley & Sons, Inc.: New York, NY, USA, 1990.

13. Lüttge, A.; Arvidson, S.R. The mineral-water interface. In *Kinetics of Water-Rock Interaction*; Brantley, L.S., Kubicki, D.J., White, F.A., Eds.; Springer: New York, NY, USA, 2008; pp. 73–107.

14. Lüttge, A.; Arvidson, R.S.; Fischer, C. Fundamental controls of dissolution rate spectra: Comparisons of model and experimental results. *Procedia Earth Planet. Sci.* **2013**, *7*, 537–540. [CrossRef]

15. Jandacka, P.; Uhlar, R.; Kolenova, I.; Duskova, V.; Mahdalova, V.; Filipkova, K.; Zeman, D. *Charakteristika Tvarů Částic Minerálních Partikulárních Látek*; Recyklace odpadů XIII, Ostrava, Czech Republic; VSB-TU Ostrava: Ostrava, Czech Republic, 2009. (In Czech)

16. Zisselmar, R.; Kellerwessel, H. Approximate mathematical description of particle-size distributions—Possibilities and limitations as to the assessment of comminution and classification processes. *Part. Part. Syst. Character.* **1985**, *2*, 49–55. [CrossRef]

17. Eberl, D.D.; Drits, V.A.; Srodon, J. Deducing growth mechanisms for minerals from the shapes of crystal size distributions. *Am. J. Sci.* **1998**, *298*, 499–533. [CrossRef]

18. Mandelbrot, B. *The Fractal Geometry of Nature*; W. H. Freeman and Company: San Francisco, CA, USA, 1982.

19. Avnir, D.; Farin, D.; Pfeifer, P. Molecular fractal surfaces. *Nature* **1984**, *308*, 261–263. [CrossRef]

20. Avnir, D.; Farin, D.; Pfeifer, P. Surface geometric irregularity of particulate materials—The fractal approach. *J. Colloid Interface Sci.* **1985**, *103*, 112–123. [CrossRef]

21. Borkovec, M.; Wu, Q.; Degovics, G.; Laggner, P.; Sticher, H. Surface area and size distributions of soil particles. *Colloids Surfaces A Physicochem. Eng. Asp.* **1993**, *73*, 65–76. [CrossRef]

22. Ficker, T. Fractal strength of cement gels and universal dimension of fracture surfaces. *Theor. Appl. Fract. Mech.* **2008**, *50*, 167–171. [CrossRef]

23. Vandamme, H.; Levitz, P.; Bergaya, F.; Alcover, J.F.; Gatineau, L.; Fripiat, J.J. Monolayer adsorption on fractal surfaces—A simple two-dimensional simulation. *J. Chem. Phys.* **1986**, *85*, 616–625. [CrossRef]

24. Stach, S.; Cybo, J.; Chmiela, J. Fracture surface—Fractal or multifractal? *Mater. Character.* **2001**, *46*, 163–167. [CrossRef]

25. Stach, S.; Roskosz, S.; Cybo, J.; Cwajna, J. Multifractal description of fracture morphology: Investigation of the fractures of sintered carbides. *Mater. Character.* **2003**, *51*, 87–93. [CrossRef]

26. Brantley, S.L.; Mellott, N.P. Surface area and porosity of primary silicate minerals. *Am. Miner.* **2000**, *85*, 1767–1783. [CrossRef]

27. Piscitelle, L.; Segars, R. Effect of the particle size distribution in determining a powder´s fractal dimension by single gas BET: A mathematical model. *J. Colloid Interface Sci.* **1992**, *149*, 226–232. [CrossRef]

28. Brož, J.; Roskovec, V.; Valouch, M. *Fyzikální a Matematické Tabulky*; SNTL: Prague, Czech Republic, 1980. (In Czech)

29. El-Safty, S.A. Sorption and diffusion of phenols onto well-defined ordered nanoporous monolithic silicas. *J. Colloid Interface Sci.* **2003**, *260*, 184–194. [CrossRef]

30. Fischer, C.; Kurganskaya, I.; Schäfer, T.; Lüttge, A. Variability of crystal surface reactivity: What do we know? *Appl. Geochem.* **2014**, *43*, 132–157. [CrossRef]

31. Ghanbarian, B.; Hunt, A.G. Universal scaling of gas diffusion in porous media. *Water Resour. Res.* **2014**, *50*, 2242–2256. [CrossRef]

32. Fischer, C.; Karius, V.; Weidler, P.G.; Lüttge, A. Relationship between micrometer to submicrometer surface roughness and topography variations of natural iron oxides and trace element concentrations. *Langmuir* **2008**, *24*, 3250–3266. [CrossRef] [PubMed]

33. Arvidson, R.S.; Ertan, I.E.; Amonette, J.E.; Luttge, A. Variation in calcite dissolution rates: A fundamental problem? *Geochim. Cosmochim. Acta* **2003**, *67*, 1623–1634. [CrossRef]

34. Fischer, C.; Arvidson, R.S.; Lüttge, A. How predictable are dissolution rates of crystalline material? *Geochim. Cosmochim. Acta* **2012**, *98*, 177–185. [CrossRef]

35. Tkáčová, K. *Mechanical Activation of Minerals*; Elsevier: Amsterdam, The Netherlands, 1989.

Article

Edge Structure of Montmorillonite from Atomistic Simulations

Aric G. Newton [1,2], Kideok D. Kwon [1] and Dae-Kyo Cheong [1,*]

[1]   Department of Geology, Kangwon National University, Chuncheon 24341, Korea;
       agnewton@kangwon.ac.kr (A.G.N.); kkwon@kangwon.ac.kr (K.D.K.)
[2]   Division of Energy and Environmental Systems, Faculty of Engineering, Hokkaido University, N13 W8,
       Kita-ku, Sapporo 060-8628, Japan
[*]   Correspondence: dkcheong@kangwon.ac.kr; Tel.: +82-33-250-8559

Abstract: Classical molecular dynamics (MD) simulations have been performed to investigate the effects of substitutions in the octahedral sheet (Mg for Al) and layer charge on an atomistic model of the montmorillonite edge. The edge models considered substitutions in both the solvent accessible and inaccessible octahedral positions of the edge bond chain for a representative edge surface. The MD simulations based on CLAYFF, a fully-flexible forcefield widely used in the MD simulations of bulk clay minerals, predicted Mg–O bond distances at the edge and in bulk that agreed with those of the density functional theory (DFT) geometry optimizations and available experimental data. The DFT results for the edge surfaces indicated that substitutions in the solvent inaccessible positions of the edge bond chain are energetically favorable and an increase in layer charge and local substitution density coincided with the occurrence of five-coordinate, square pyramidal Mg and Al edge structures. Both computational methods predicted these square pyramidal structures, which are stabilized by water bridging H-bonds between the unsaturated bridging oxygen [(Al or Mg)–O–Si] and other surface O atoms. The MD simulations predict that the presence of Mg substitutions in the edge bond chain results in increased disorder of the edge Al polyhedra relative to the unsubstituted edge. In addition to the square pyramidal Al, these disordered structures include trigonal bipyramidal and tetrahedral Al at the edge and inverted Si tetrahedra. These simulation results represent the first test of the fully-flexible CLAYFF forcefield for classical MD simulations of the Na-monmorillonite edge and demonstrate the potential of combined classical MD simulations and DFT geometry-optimizations to elucidate the edge structure of 2:1 phyllosilicate minerals.

Keywords: clay edge; mineral surfaces; Na-montmorillonite; nanoporous minerals; atomistic simulation; molecular dynamics; density functional theory

---

1. Introduction

Smectites are 2:1 dioctahedral phyllosilicates abundant in soils and sediments [1]. Smectites are natural nanominerals with layers ~1.0 nm thick composed of an octahedral sheet between two tetrahedral sheets. The basal surfaces of the tetrahedral sheets are inert, but isomorphic substitutions in the structure can impart a permanent negative charge to the layers. The hydration of interlayer cations that balance this permanent charge results in interlayer swelling and the creation of nanopores. This physical structure is responsible for the unique physicochemical properties of smectites that include high surface area, high cation exchange capacity, and low permeability. These microscopic properties affect a range of macroscopic geological and geochemical processes and have been exploited in engineered geologic barriers [2,3] and nanocomposite materials [4–6]. These applications have been developed based on the comprehensive experimental and theoretical investigations of the smectite

interlayers. The edges of these layer-type minerals, although they represent a much smaller fraction of the total surface area, are no less important to the reactivity of smectites.

The edges of 2:1 phyllosilicates are a source of pH dependent charge in soils. These highly-reactive edge sites exhibit a strong influence on cation and anion retention [7], the stabilization of soil organic matter [8–10], and colloidal and rheological properties [11–13]. In addition, the edge represents the boundary that diffusing solutes must cross between interlayer nanopores and neighboring meso- and micropores [14] and the dissolution of clay nanoparticles has been observed to proceed predominantly from the edge surfaces [15,16]. With a role in such an extensive list of clay surface reactions, a comprehensive understanding of 2:1 phyllosilicate structure and reactivity cannot be attained without a detailed atomistic characterization of the edge. This detailed characterization has remained elusive due to the experimental difficulties of isolating the edges. Careful manipulation of experimental variables such as pH and ionic strength [17–19] or the choice of non- or low-swelling 2:1 clay mineral phases such as pyrophyllite, K-mica, and beidellite [20–22] have been of some assistance in isolating the edge, but by far, the most insightful approach has been through atomistic simulations.

Numerous quantum mechanical (QM) simulations have provided valuable insights regarding the relaxation of the edge structure [23,24], surface energy of various facets [24,25], acid-base reactivity [23,24,26–28], and dynamical properties of the edge-water interface [29–31]. These simulations of the two dominant edge structures typically employ pyrophyllite as a model mineral as it is a non-swelling, 2:1 dioctahedral phyllosilicate with no structural charge; pyrophyllite possesses only a strongly reactive edge surface. Pyrophyllite is a useful analog for the study of the 2:1 dioctahedral phyllosilicate edge surfaces although it is somewhat rare in soils. Much more common in the environment is montmorillonite (MMT), a smectite mineral with a relatively low layer charge (x = 0.2 to 0.6 per chemical formula unit), wherein isomorphic substitutions in the octahedral sheet are in excess of those in the tetrahedral sheet [32]. Recent atomistic simulations using density functional theory (DFT) have sought to address the gap between the idealized atomistic models of the edge and the actual structure of smectites by introducing isomorphic substitutions into the models [26,27,30,31]. These simulations have demonstrated the effects of isomorphic substitutions on the coordination of the edge cations, the interfacial water structure, and the acid dissociation constants (pK_as) of the edge sites. Perhaps due to the computational costs of QM simulations, these previous studies have employed atomistic models that are small and considered only a single isomorphic substitution in isolation in the structure.

Molecular mechanical (MM) studies are rare for the edge surfaces compared to the QM studies and have typically employed a rigid clay structure [14,33,34]. MM simulations can address the limited length- and time-scales of QM methods, but the accuracy of MM simulations are strongly dependent on the choice of the potential-based forcefield that describes the interatomic interactions. No forcefield, however, has been extensively tested for the edge surfaces because of the absence of high-quality experimental data for the edge. The fully-flexible CLAYFF forcefield [35], which was derived from QM methods and spectroscopic data, has been used extensively in molecular mechanics simulations for clay mineral phases, particularly for the basal planes and interlayer nanopores. Recent classical molecular dynamics (MD) simulations [36] have demonstrated that CLAYFF predicts edge structures and surface energies consistent with those of QM studies of pyrophyllite. CLAYFF has also been used in simulations at the extended length- and time-scales that are currently inaccessible to QM methods to predict pyrophyllite nanoparticle structures and propose disordered edge structures [37,38]. Further investigation is required, but these studies have demonstrated that CLAYFF can be used in MM simulations of some clay edge surfaces. The validation of CLAYFF for atomistic simulations of more common 2:1 clay mineral edges that include isomorphic substitutions is a natural next step and would expand the already considerable list of model structures that can be simulated.

In this study, we report the results of MD simulations of a MMT edge with substitutions of Mg for Al in the octahedral sheet using the CLAYFF forcefield. The resultant MD edge structures are compared with those of DFT geometry-optimizations that examined the effects of layer charge and

the position of the edge substitution on the edge structures. We provide a quantitative description of the octahedral sheet edge structures and infer a relationship between layer charge and disordered edge structures.

2. Materials and Methods

2.1. Molecular Mechanics: Na-Montmorillonite Edge

The atomistic model of the Na-MMT edge was derived from a previous model of the pyrophyllite edge. The details of this previous model are described elsewhere [36], but the general characteristics of the model will be briefly summarized and differences that distinguish the Na-MMT model from the pyrophyllite model will be described in detail. Crystal growth theory [39] can be applied to 2:1 dioctahedral phyllosilicates [40] to identify three periodic bond chains (PBCs)—one is unique and two are symmetrically equivalent—that parallel the clay mineral edge faces. In this paper, we have chosen the nomenclature of White and Zelazny [40] and will refer to the symmetrically equivalent PBCs as the AC edge and the unique PBC as the B edge. These PBCs are composed of linked tetrahedron-octahedron-tetrahedron (TOT) units. Previous simulations identified the AC edge as the 2:1 dioctahedral edge with the lowest surface energy [24,36], and we have chosen the AC edge as the representative edge of Na-MMT. The atomistic models of the Na-MMT AC edge began from a $4 \times 4 \times 2$ ($a \times b \times c$) expansion of the pyrophyllite-1*Tc* unit cell of Lee and Guggenheim [41]. The octahedral sheet of this 2:1 dioctahedral phyllosilicate unit cell is *trans*-vacant (*i.e.*, the *trans*-site, where the anionic positions (OH^-) lie across the octahedron diagonal, is vacant; the two *cis*-sites, where the anionic positions are shared on an octahedral edge, are occupied; Figure 1). This triclinic supercell was cleaved along the (010) plane to create the AC edge face. A 60 Å vacuum space perpendicular to the AC edge was introduced to separate the surfaces across a macropore; the edge faces were also separated across the bulk mineral phase by approximately 30 Å. The unsaturated bonds of the edge surface were saturated in the manner of previous simulations of the pyrophyllite edge [36]—namely, through the dissociative chemisorption and physisorption of an integer number of water molecules to maintain the surface at the point of zero net proton charge (p.z.n.p.c.). Each solvent-accessible TOT unit at the edge surface requires two water molecules to be saturated. The simulation cell *c* dimension and relative clay layer position were adjusted to accommodate a hydrated bilayer. The simulation cell macropore and interlayer were hydrated with 1389 water molecules. The triclinic cell geometry was simplified to agree with the standard practice of using monoclinic simulation cells for Na-MMT. The initial simulation cell geometry was $a = 20.64$ Å, $b = 98.86$ Å, $c = 30.69$ Å, $\alpha = 90.00°$, $\beta = 100.46°$, and $\gamma = 90.00°$.

Isomorphic substitutions of Al^{3+} by Mg^{2+} in the octahedral layer were chosen at random and subject to two constraints. The random assignment of substitutions is consistent with previous solid-state nuclear magnetic resonance (NMR) experiments and QM simulations that demonstrated that Mg^{2+} substitutions are randomly distributed within the octahedral layer [42,43]. The first constraint follows from these experimental and theoretical investigations and requires that no $Mg–(OH)_2–Mg$ pairs exist within the octahedral sheet. The second constraint is informed by the properties of synthetic MMTs [44–47]. Synthetic MMTs with only octahedral substitutions produced via hydrothermal synthesis are limited to a layer charge, *x*, of 0.20 to 0.40. The units of *x* are the number of moles of excess electron charge per chemical formula. We define the reference chemical formula for MMT as $M_x[Al_{(2-x)}Mg_x]Si_4O_{10}(OH)_2$. Where *M* is the interlayer counter ion and the term in brackets represents the octahedral sheet. The octahedral substitution ratio (*i.e.*, the number of substitutions per total octahedral sites) is one-half of the layer charge. Synthetic MMTs with layer charges greater than 0.40 begin to exhibit trioctahedral character in the octahedral sheet and isomorphic substitutions in the tetrahedral layers [46]. Thus, the second constraint, derived from the layer charge, limits the substitution ratio of the edge PBC (*i.e.*, Mg edge substitutions: total no. of octahedral edge sites in the PBC) to less than 0.20. Random assignments of substitutions that violated either constraint

were ignored and a new random assignment was made. The random assignment of isomorphic substitutions in the octahedral layer created two distinct edge surfaces. One of the interfaces contains no isomorphic substitutions in the two bond chains that define the edge of the upper and lower layer (Figures 1 and 2 left edge surface); this interface and these edge bond chains are pyrophyllite-like. The second interface contains one isomorphic substitution in the edge PBC of each layer (*i.e.*, substitution ratio: 1:8; Figures 1 and 2 right edge surface). In the upper layer, this substitution is solvent inaccessible (*i.e.*, a linking position of the PBC; Figure 1, Mg^{PBC}). In the lower layer, the isomorphic substitution is in a solvent accessible position in the PBC (*i.e.*, a water molecule can sorb to the edge octahedra; Figure 1, Mg^{Sol}). These two interfaces can be further distinguished by the substitution ratio of the PBC that is adjacent to the edge bond chain. The bulk bond chains that are adjacent to the substituted edge have a higher substitution ratio (0.375) than the bond chains adjacent to the unsubstituted edge (0.125 and 0.25). A total of 26 Mg substitutions were introduced into the octahedral layer; an equal number of Na ions were placed in the hydrated interlayer space to balance this permanent structural charge. This atomistic model of Na-MMT had a layer charge of 0.40. The chemical formula for the MMT without sorbed water molecules was $(Mg_{26}Al_{102})Si_{256}O_{640}(OH)_{128}$.
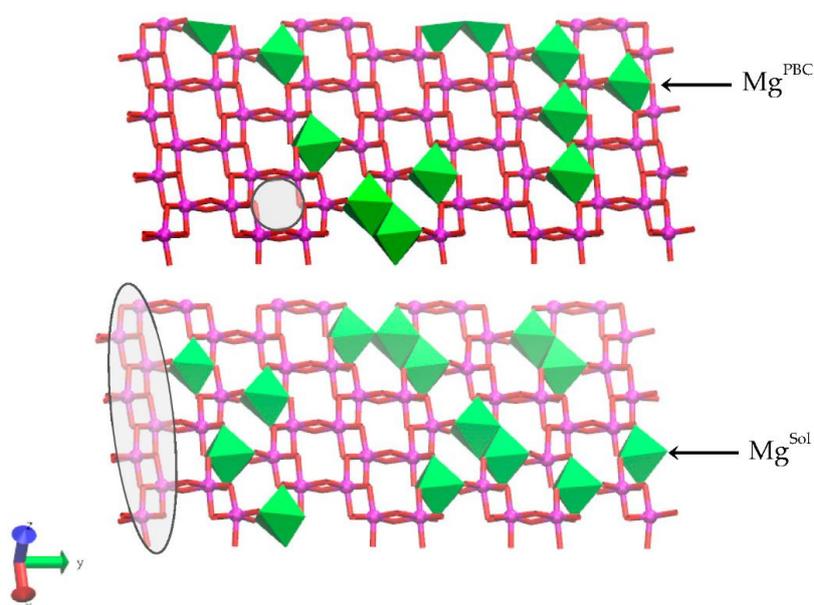
Figure 1. The upper and lower octahedral sheets of the Na-montmorillonite (Na-MMT) layers showing the locations of random Mg substitutions for Al. The solvent accessible Mg substitutions (Mg^{Sol}) are in the lower octahedral sheet at right; the solvent inaccessible Mg substitution in the linking PBC position is in the upper octahedral sheet at right. A representative *trans*-vacant site is shown in the shaded circle of the upper sheet. The octahedra of a periodic bond chain (PBC) that parallels the edge surface are highlighted in the shaded ellipse. The Al atoms are magenta spheres, the Mg atoms are green octahedra, and the O atoms in octahedral coordination with the Mg and Al are red.

The CLAYFF forcefield parameters [35] described the Coulomb and short-range interactions as well as the harmonic bonds of the hydroxyl groups in the atomistic model of Na-MMT. Minor adjustments were made to the partial Coulombic charges of the octahedral Mg atoms ($q_{mgo} = 1.3598$ e) and the bridging O atoms with double substitution ($q_{obss} = -1.3116$ e) to maintain the charge neutrality of the atomistic model. The aqueous phase was described by the extended simple point charge (SPC/E) water model [48] with harmonic bond stretching and angle bending terms [48,49]. Long-range electrostatic interactions and the attractive contribution to the van der Waals interaction were evaluated using the Ewald summation [50] with the repulsive contribution truncated at a distance of 9.0 Å. All Ewald summations were determined to an accuracy of 0.0001 kcal/mol.
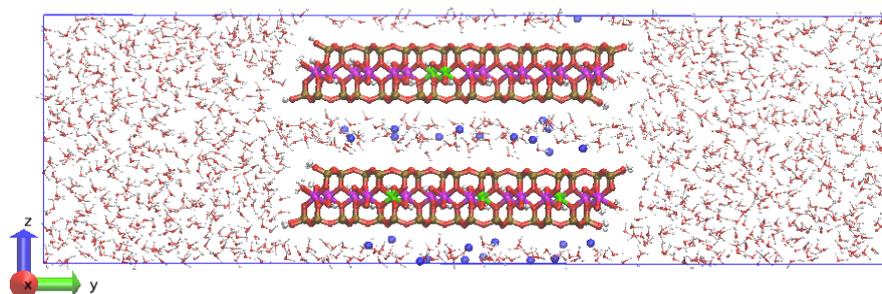
Figure 2. Simulation cell and initial atomic configuration of Na-MMT AC edge at *t* = 0. The Al atoms are magenta; Mg atoms are green; Si atoms are ochre, O atoms are red, H atoms are white, and Na atoms are blue.

All MD simulations were performed with the LAMMPS software package [51] installed on the supercomputer Hopper at the National Energy Research Scientific Computing Center (NERSC; Berkeley, CA, USA). The models were initiated with a series of short MD simulations in the microcanonical (NVE, *T* = 298.15 K) ensemble—where the number of atoms (*N*), simulation cell volume (*V*), and energy (*E*) were held constant. The temperature was controlled with a temperature-rescaling thermostat and the SHAKE algorithm for water molecule bonds and angles. The aqueous phase was equilibrated with a timestep progression of Δt = [0.001, 0.01, 0.2, 0.3, 0.4, 0.5 fs] for 40,000 steps each before the atoms of the MMT phase were relaxed from their rigid positions. The entire system was then simulated for an additional 10,000 steps with Δt = 0.25 and 0.5 fs. At this point, the ensemble was changed to isobaric-isothermal [NPT; (*P* = 1.0 atm, *T* = 298.15 K)]—where pressure (*P*) and temperature (*T*) were held constant. A chain of Nose-Hoover thermostats controlled the temperature and pressure for the next 100.0 ps of model equilibration with Δt = 0.5 fs. After these approximately 200 ps of equilibration, a production run of 3.5 ns was continued with this same simulation algorithm. The resultant edge structures from these 3.5 ns trajectories were assessed on the basis of the metal-oxygen pair distribution functions and the integral of these distribution functions that provides the metal-oxygen coordination number. The internal routines of the LAMMPS code were used to calculate these pair distribution functions. The charactersitic properties of the pair-distribution functions (*i.e.*, metal-oxygen distances, r_{MeO}; the first-shell minimum of the pair-distribution function, ρ; and the coordination numbers, CNs) were calculated from 10 time-averaged blocks of 200 ps duration. The hydrogen bonds (H-bonds) at the NaMMT edge-water interface were defined by the donor-acceptor separation distance and donor-hydrogen$\cdots$acceptor angle criteria developed by Kumar, *et al.* [52] for the SPC/E water model ($d_{H-bond} \leqslant$ 3.2 Å; $\angle$H-D$\cdots$A $\leqslant 40°$) and rendered with the open-source program, Visual Molecular Dynamics (VMD) [53].

2.2. Density Functional Theory (DFT) Computations

All DFT simulations were performed with the CASTEP code [54] using ultrasoft pseudopotentials [55] under the generalized gradient approximations [56]. The kinetic-energy cutoff for the planewave basis set was 600 eV. The primitive Brillouin zone was sampled using a 6 × 4 × 4 grid and one point in *k* space [57] for the pyrophyllite unit cell and supercells for the surface models, respectively. With the chosen kinetic-energy cutoff and *k*-point grid, the atomic forces converged to <<0.01 eV/Å. The geometry optimization permitted the coordinates of all ions to relax. Geometry optimizations were performed until the residual atomic force was ⩽0.03 eV/Å and the root-mean-square stress of the bulk structure was ⩽0.02 GPa.

A periodic slab model of the AC edge surface was created based on a 2 × 2 × 1 supercell of a geometry optimized pyrophyllite-1*Tc* unit cell from Lee and Guggenheim [41]. This slab model has two symmetric edge surfaces at the left and right of Figure 3. The AC edge structure was cleaved from the supercell in the same manner as the molecular mechanics simulations. The unsaturated

bonds were healed via the same dissociative chemisorption and physisorption reactions with water molecules to create an edge surface at the p.z.n.p.c. The Si edge tetrahedra each possess one silanol ($\equiv$SiOH) group and the solvent accessible octahedron has an amphoteric [$\equiv$(Al or Mg) ... OH$_2$] group. A total of four H$_2$O molecules per edge surface were used to saturate the solvent-accessible TOT units. The generic chemical formula for the surface slab models without sorbed water molecules was [Al$_{(16-n)}$Mg$_n$]Si$_{32}$O$_{80}$(OH)$_{16}$, where n = 2 or 3 in our DFT simulations, corresponding to a layer charge of 0.25 or 0.375. The slab model was comprised of four PBCs (~18 Å thickness). The vacuum space perpendicular to the edge surface slab model was ~20 Å. The supercell dimensions for the DFT edge surface model were: 10.40 × 38.05 × 10.12 Å ($a \times b \times c$) with each edge surface ~1.0 nm^2. The periodic images of the surface models were separated by a distance greater than 17.8 Å.
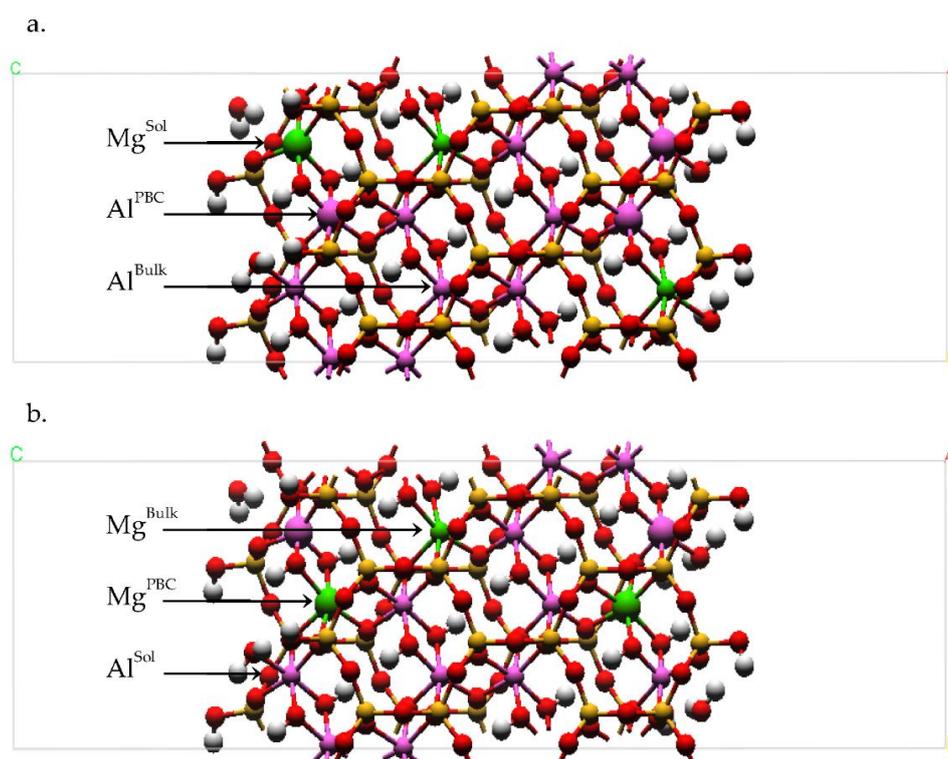
Figure 3. Plan view of the (**a**) solvent accessible Mg (Mg^{Sol}) and the (**b**) linking PBC Mg (Mg^{PBC}) models with a layer charge (x) of 0.375 from the DFT geometry optimizations. The solvent accessible (Mg^{Sol} and Al^{Sol}) and linking PBC cation positions (Mg^{PBC} and Al^{PBC}) in the edge bond chain are defined. The bulk Mg substitution (Mg^{Bulk}) is also defined. In models with x = 0.25, the Mg^{Bulk} atoms are replaced with an Al atom (Al^{Bulk}). Representative cation pairs for the hydroxyl sharing (Table 2: Al^{sol}-OH$_2$, oh) and bridging oxygen (Table 2: Al^{sol}-OH$_2$, ob) pairs are depicted as enlarged cations at left and right in the edge PBCs, respectively. Atom legend is the same as Figure 2.

Isomorphic substitutions of Mg for Al were introduced into the PBC of each edge surface and, in some models, the bulk of the octahedral sheet. The effect of the substitution location in the edge PBC was investigated by considering two different models. In the first model, the isomorphic substitution occupied a solvent accessible octahedron in the edge PBC (Figure 3a, Mg^{Sol}); the isomorphic substitution of the second model occupied a linking octahedral position in the PBC (Figure 3b, Mg^{PBC}). A single isomorphic substitution in each edge PBC results in a MMT with a layer charge of 0.25. The effect of layer charge was investigated by creating two additional models based on the originals. These two models introduced one additional isomorphic substitution in the bulk of the octahedral sheet (Figure 3b, Mg^{Bulk}). The additional Mg^{Bulk} substitution increased the layer charge of these models to 0.375, but the substitution ratio of the edge PBCs remained unchanged at 0.25.

Although in excess of our defined constraint, this edge substitution ratio is the lowest possible for our DFT model geometry. The small size of these atomistic models imposes limits on the substitution ratios and layer charges that can be considered. Thus, we have chosen models that most closely agree with those of the classical mechanical simulations described above and are within the range of the octahedral substitution ratios of synthetic MMT.

The isomorphic substitution of Mg for Al results in a net negative charge in the super cell that was compensated through the application of a uniform positive background [58]. Although errors may arise from unwanted Coulombic charge interactions between periodic images within the uniform background, this error can be eliminated through the use of simulations cells with infinitively large volumes. In this study, we compared the total energy of the two models with variations only in the position of the substituted Mg in a fixed supercell volume. As the error associated with interaction between the periodic images does not depend on the atomic positions, this error was cancelled in the energy comparison.

For the edge surfaces with solvent accessible Mg, the adsorption energy of a water molecule physisorbed to the octahedral site (H_{ads}) was calculated for the exposed Al and Mg sites (*i.e.*, six-fold *vs.* five-fold Al or Mg) by

$$H_{ads} = - \left[E_{4s} - E_{3s} - 2E_{H_2O} \right] / 2 \tag{1}$$

where E_{4s} and E_{3s} are the total energies of the surface with sorbed water coverage of 4 and 3 H_2O/nm^2, respectively, and E_{H_2O} is the total energy of an isolated H_2O molecule in a $25 \times 25 \times 25$ Å cell.

Table 1. Characteristic properties of the cation-oxygen (α-β) pair distribution functions of the octahedral sheet of the Na-MMT model from molecular dynamics (MD) simulations. The pair distribution functions are summarized by the distance to the first peak (r_{peak}), coordination number (CN), and the first minimum (ρ) of the cation-O pair distribution for the substituted edge PBC, unsubstituted edge PBC, and bulk positions within the model. The standard deviations for each property (+/−) are provided.

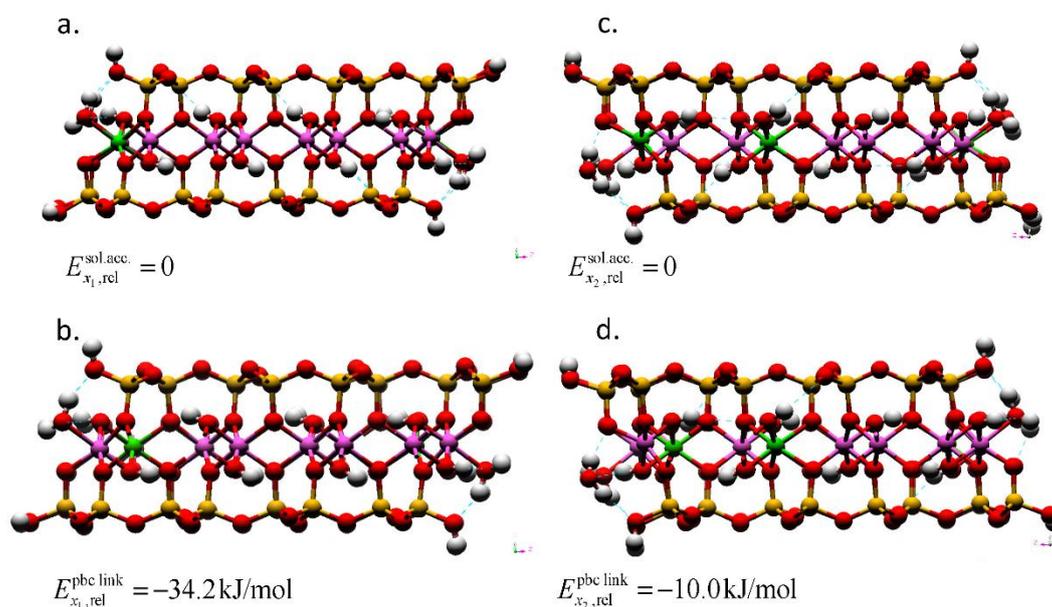| α-β **Pair**	r_{peak}, Å	+/−	CN	+/−	ρ, Å	+/−
Substituted Edge PBC						
Mg^{Sol}-O	2.10	0.003	5.72	0.054	2.88	0.033
Mg^{PBC}-O	2.12	0.002	5.99	0.004	2.60	0.038
Al^{Sol}-O	1.87	0.003	5.25	0.051	2.86	0.052
Al^{PBC}-O	1.90	0.004	5.85	0.006	2.91	0.017
Unsubstituted Edge PBC						
Al^{Sol}-O	1.92	0.005	5.81	0.040	2.89	0.083
Al^{PBC}-O	1.94	0.003	6.00	0.001	2.88	0.052
Bulk						
Mg^{Bulk}-O	2.10	0.001	5.98	0.001	2.34	0.002
Al^{Bulk}-O	1.93	0.002	5.98	0.001	2.47	0.004

3. Results

3.1. Surface Mg

The characteristic properties of the cation-O pair distribution functions of the octahedral sheet obtained by MD simulations are summarized in Table 1. The Mg–O coordination number (CN) for the solvent accessible Mg (Mg^{Sol}) was less than that of Mg in the linking PBC position (Mg^{PBC}) or bulk (Mg^{Bulk}). The Mg substitutions in the linked PBC position and bulk maintained octahedral coordination (CN $\approx$ 6) throughout the simulation. The physisorbed water of Mg^{Sol} was observed to exchange readily with the bulk water phase during the MD simulation. The ease with which water is exchanged from this site in the MD simulations is consistent with the low water adsorption energy for

the solvent accessible Mg sites (H_{ads}, -57 kJ/mol) calculated using DFT. This exchange resulted in a transient edge Mg that is in square pyramidal coordination with O.

The Mg substitutions can occur at two different locations within the edge bond chain (Mg^{Sol} and Mg^{PBC}). Using DFT, we compared the total energies of the different models to evaluate which substitution site is preferable (Figure 4). The Mg^{PBC} substitution possessed a lower total energy than the Mg^{Sol} substitution at both layer charges considered. The energy difference indicates that, in isolation, the solvent accessible sites are not preferable for Mg substitution at the edge surface. However, the relative difference in the total energies between the models with solvent accessible and linking PBC substitutions decreased with an increase in layer charge (-34.2 to -10.0 kJ/mol). At the higher layer charge, the Mg^{Sol} site that was closest to the Mg^{Bulk} assumed a square pyramidal coordination (left side of Figure 4c), whereas the Mg^{Sol} sites were in octahedral coordination at the edge most distant from the Mg^{Bulk} (right side of Figure 4c) and at the lower layer charge (Figure 4a). This change in the coordination number and reduction in the energy difference imply that solvent accessible sites could be substituted at higher layer charges with a tendency to assume five-fold coordination. In the MD simulations, the model possessed a higher layer-charge and included a Mg^{Sol} site. The CN of less than 6 at the Mg^{Sol} site is rationalized based on the energy difference in our DFT results.

a.

$E^{\text{sol.acc.}}_{x_1,\text{rel}} = 0$

c.

$E^{\text{sol.acc.}}_{x_2,\text{rel}} = 0$

b.

$E^{\text{pbc link}}_{x_1,\text{rel}} = -34.2\,\text{kJ/mol}$

d.

$E^{\text{pbc link}}_{x_2,\text{rel}} = -10.0\,\text{kJ/mol}$

Figure 4. Montmorillonite AC edge-surface models geometry-optimized by DFT with layer charges $x_1 = 0.25$ and $x_2 = 0.375$. The Mg substitutions for Al are in (**a**) solvent accessible and (**b**) the linking PBC positions for the models with a layer charge of $x = 0.25$. For the models with a layer charge of $x = 0.375$; the (**c**) solvent accessible and (**d**) linking PBC position models also show the location of the bulk isomorphic substitution. The total energies of the models with the solvent accessible substitution are taken as the reference ($E^{\text{sol,acc}}_{x,\text{rel}}$). The Mg substitutions at the right edge interfaces are obscured by the edge Al atom in these profiles. The hydrogen bonds are depicted as dotted blue lines. The atom legend is the same as Figure 2.

The MD-calculated average Mg-O distances (Table 1: r_{peak}) for the substitutions in the linked PBC position are slightly longer, but not significantly so, than the Mg-O distances of the solvent accessible and bulk mineral substitutions. The extent of the Mg-O first shell (ρ) is more compact in the bulk than at the edge surface. This difference is attributed to the greater crystallinity of the bulk phase and surface relaxation. The Mg-O distances obtained by MD simulations are within 0.04 Å ($\leqslant 2\%$) of the distances from our DFT geometry optimizations and both simulation results are in agreement with the experimental range (2.00–2.12 Å) reported for the bulk Mg-O distances in synthetic MMT [44]

and hydrotalcite [59] and for aqueous Mg ions [60]. In general agreement with the MD results, the DFT-calculated average Mg–O bond distances were relatively constant regardless of the position of the substitution (*i.e.*, Mg^{Sol}, Mg^{PBC}, or Mg^{Bulk}; Table 2) although an increase in the layer charge slightly decreased the Mg^{Sol}-O distance. This decrease is a result of a contraction of the Mg^{Sol}–O bonds associated with the mineral layer but the Mg^{Sol}-OH_2 distance that actually increased with increasing layer charge masks the extent of this contraction.

Table 2. Interatomic distances (in Å) of the octahedral sheets obtained by DFT for the Mg^{Sol} model and Mg^{PBC} model at each layer charge (x = 0.25 or 0.375). The model with x = 0.375 possesses two unique edges (Figure 3): one edge with an adjacent bond chain that is unsubstituted by Mg (unsub Mg^{Bulk}) and the other with the adjacent bond chain substituted by Mg (sub Mg^{Bulk}). The solvent accessible, linking PBC, and bulk sites are designated by Mg^{Sol} and Al^{Sol}; Mg^{PBC} and Al^{PBC}; and Mg^{Bulk}, and Al^{Bulk} respectively. The Al^{Sol}-OH_2 distances are delineated based on the connection to the Mg^{PBC} through a hydroxyl oxygen (oh) or bridging oxygen (ob).

α-β Pair	α-β Interatomic Distance, Å	
	Layer Charge, x = 0.25	Layer Charge, x = 0.375 Unsub/Sub Mg^{Bulk}
Mg^{Sol} Model		
Mg^{Sol}-O	2.09	2.06
Mg^{Sol}-OH_2	2.25	2.40/3.06
Mg^{Bulk}-O	-	2.07
Al^{Sol}-O	1.91	1.92
Al^{Sol}-OH_2	2.07	2.08/2.10
Al^{PBC}-O	1.92	1.92
Al^{Bulk}-O	1.92	1.92
Mg^{PBC} Model		
Mg^{PBC}-O	2.08	2.08
Mg^{Bulk}-O	-	2.07
Al^{Sol}-O	1.92	1.90
Al^{Sol}-OH_2, oh	2.17	2.28/3.20
Al^{Sol}-OH_2, ob	2.09	2.12/2.10
Al^{PBC}-O	1.92	1.92
Al^{Bulk}-O	1.92	1.92

3.2. Surface Al

The MD simulations also showed that the presence of isomorphic substitutions in the edge PBCs affects the structure of the edge Al. The average Al-O distances and CNs of the unsubstituted edge are nearly indistinguishable from one another by position (*i.e.*, Al^{Sol}, Al^{PBC}, and Al^{Bulk}). In contrast, the average Al-O distance and CN of the substituted edge differ by the Al position. The Al-O distance and CN decrease proceeding from the bulk to the edge in the substituted edge. A comparison of the two edges reveals that the average Al-O distances in the solvent accessible (Al^{Sol}) and linked PBC positions (Al^{PBC}) of the substituted edge (Table 1: substituted edge PBC) are less than the corresponding distances in the unsubstituted edge (Table 1: unsubstituted edge PBC). The decrease in the average Al-O distances in the substituted edge is a consequence of the greater number of edge Al in non-octahedral coordination with O, especially the solvent accessible Al. This interpretation of the Al-O CN can be confirmed visually in Figure 5 where square pyramidal, trigonal bipyramidal, and tetrahedral Al are present. These disordered edge Al structures have also been reported in previous MD simulations of pyrophyllite edges and nanoparticles [37,38].

The Al structural features shown by the MD simulations are consistent with our DFT results. In the DFT geometry optimizations, the effects of the Mg substitutions and increased layer charge on the Al-O distances are most evident when the Al^{Sol}-OH_2 distances are considered (Table 2). For

the pyrophyllite AC edge surfaces, which possess no isomorphic substitutions ($x = 0$), the Al^{Sol}-OH_2 distances were 2.02–2.06 Å [24,61]. When the edge PBC includes a Mg^{Sol} (Table 2: Mg^{Sol} models), the Al^{Sol}-OH_2 distance tends to increase with increasing layer charge. The greatest Al^{Sol}-OH_2 distance was 2.10 Å at $x = 0.375$, when the solvent accessible Al was nearest the bulk Mg substitution. When the edge PBC substitution is in the linking position (Table 2: Mg^{PBC} models), a dramatic increase in the Al^{Sol}-OH_2 distances occurred with increasing layer charge. The Al^{Sol} that share hydroxyl oxygens (oh) with the Mg^{PBC} have a greater Al^{Sol}-OH_2 distance than the Al^{Sol} that share bridging oxygens (ob) with the Mg^{PBC}. The greatest Al^{Sol}-OH_2 distance in the Mg^{PBC} models occurred at the Al^{Sol} that is nearest the bulk Mg substitution (3.20 Å), indicating non-octahedral coordination of edge Al as shown in the MD simulations.
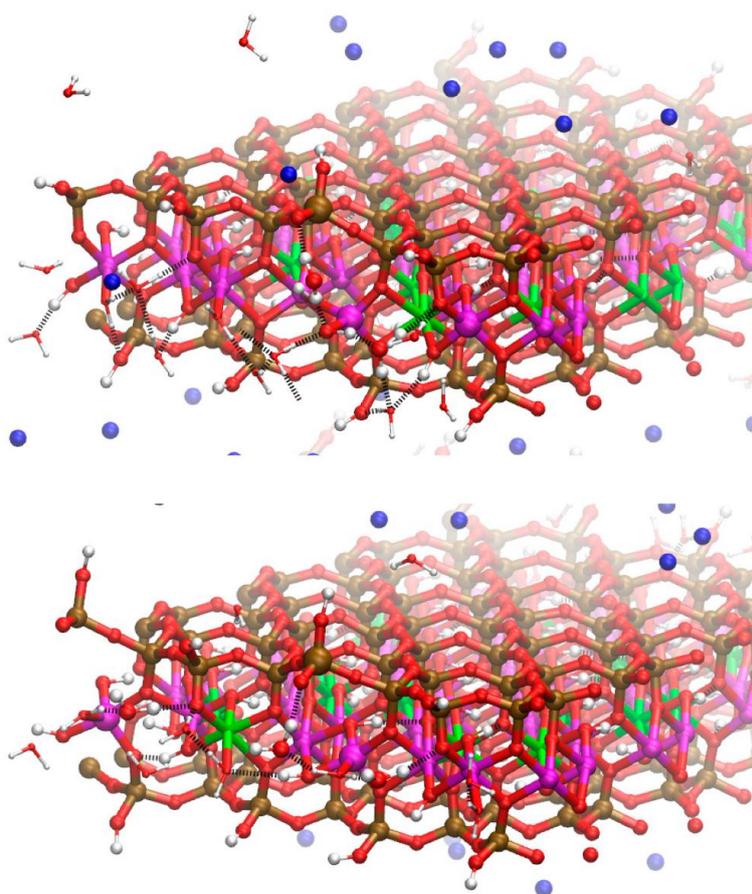

Figure 5. Snapshot of the molecular dynamics (MD) simulations showing disorder in the edge Al coordination on the Mg-substituted edges of the Na-MMT model. Non-octahedral edge Al are present in the top layer as a tetrahedron and square pyramid and, in the lower layer, as two trigonal bipyramids and a square pyramid. These non-octahedral Al are depicted as enlarged spheres. The bridging water molecules that stabilize these disordered edge structures through H-bonds are also enlarged. Near surface H-bonds shown as dashed black lines. Bulk water molecules removed for clarity. Atom legend is the same as Figure 2.

In our MD simulations, the coordination number of the Mg^{Sol} and Mg^{PBC} were 5.72 and 5.99—similar to the results of Al^{Sol} and Al^{PBC}. The reduced coordination of the Mg^{Sol} is attributed to the low water adsorption energy, H_{ads}, (−57 kJ/mol). When we calculated the H_{ads} for the solvent accessible Al sites using DFT, it was equivalent to that of the Mg sites (−57 kJ/mol). Thus, physisorbed water molecules associated with the solvent accessible octahedral sites of the AC edge are likely to be exchanged [29,30], regardless of whether the octahedral cation is Al or Mg.

3.3. Surface Si and H-Bonds

The MD simulations also predicted disorder in the Si tetrahedral sheet. The inverted Si tetrahedra of the AC edge (Figures 5 and 6) develop as a consequence of the trigonal bipyramidal Al at the edge. These inverted Si are a feature of a historic alternative model of montmorillonite first proposed by Edelman and Favejee [62]. Both the pyrophyllite-like and the Mg-substituted edge faces in the MD simulations of the Na-MMT model possessed these Si-inversions (Figure 6). The inverted Si and non-octahedral Al structures were stabilized by water bridging H-bonds as recently reported for the pyrophyllite edge surface [37,38]. Although experiments have not yet provided direct evidence of an inverted Si in 2:1 dioctahedral phyllosilicates, the alternative EF structure can, in principle, explain some inconsistencies in smectite reactivity [63–65]. A recent atomic thermodynamics study based on DFT has suggested that these inverted Si at the edge of pyrophyllite are possible defect structures at the AC edge of 2:1 phyllosilicates [61].
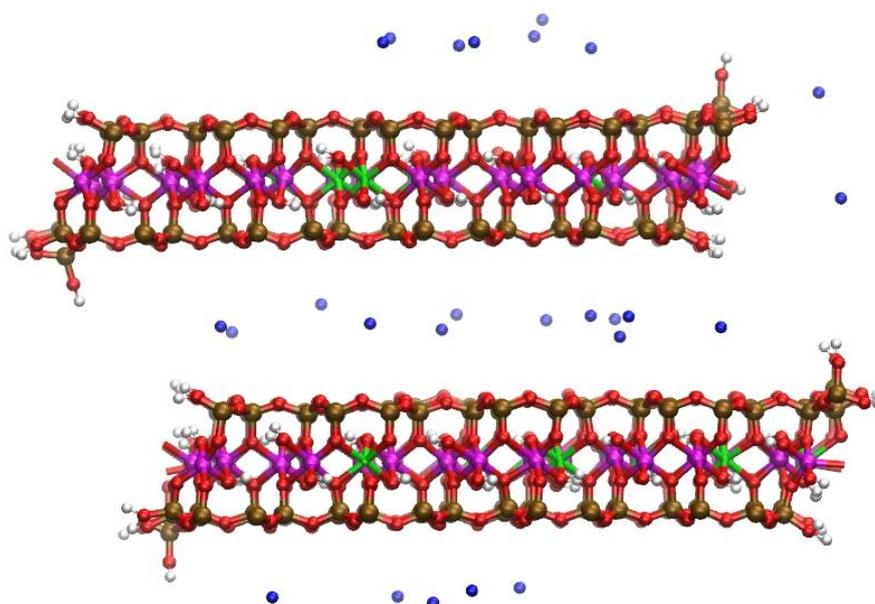
Figure 6. Snapshot of the Na-MMT MD simulations shown in profile at *t* ~3.5 ns; water molecules removed for clarity. Disordered structures have developed at the AC edge interfaces. The Al atoms are magenta; Mg atoms are green; Si atoms are ochre, O atoms are red, H atoms are white, and Na atoms are blue.

Our MD simulations further showed that the H-bonds associated with the unsaturated bridging oxygens at the edge (*i.e.*, ≡Al–O–Si≡ and ≡Mg–O–Si≡) differ depending on the identity of the edge cation. When the edge cation is Al, the average number of H-bonds between the bridging oxygen and water is 1.00. When a solvent accessible Mg is substituted at the edge, the average number of H-bonds between the water and the bridging oxygen was 1.64. This value should be interpreted carefully as only one bridging O bonded to Mg^{Sol} exists in the model in contrast to the 10 bridging O bonded to Al^{Sol}. The average number of H-bonds indicates that this bridging O, when bonded to Mg^{Sol}, is more likely to form two H-bonds with the water over the course of the MD trajectory than a single H-bond. This increase in the number of H-bonded water molecules at the site of the octahedral substitution agrees with that reported in a recent DFT MD simulation [31]. The square pyramidal Al and Mg observed in the geometry-optimized DFT models with layer charge *x* = 0.375 (Figure 4c,d) were also stabilized by water bridging H-bonds. The water bridge forms between the H atoms of water molecule and the unsaturated bridging O [≡(Al or Mg)–O–Si≡] and a silanol group (≡Si–OH).

The square pyramidal Al is further stabilized through an additional hydrogen bond between the O of the water bridge and the exposed structural hydroxyl ($\equiv$Al$_2$–OH).

4. Discussion

Previous QM simulations of a small 2:1 phyllosilicate edge model with Mg substitutions in the solvent accessible octahedral position have reported the existence of the square-pyramidal edge Mg in addition to octahedral Mg [30]. Our DFT geometry optimizations and classical MD simulations corroborate these previous findings and, contrary to the previous reports of the six-fold Al only being stable under the influence of an octahedral substitution, demonstrate that the solvent accessible Al can also take on a square pyramidal configuration. In the present DFT results, the square pyramidal Al develops when proximal to Mg substitutions in the linking PBC position and bulk mineral. Previous studies considered Mg substitutions only in one of the edge PBC and did not include bulk substitutions [30,31]; these edge PBC substitution ratios were less than or equal to the ratio in our models. Our larger slab model permitted us to consider substitutions both at interfaces and in bulk with a layer charge (x = 0.375) that more closely approaches the experimental layer charge constraint.

The five-coordinate Al and Mg surface structures developed in the model where the local charge deficit—due to isomorphic substitutions—would be greatest in the DFT model. These five-coordinate structures only developed at the solvent accessible cation closest to the bulk Mg substitution (Figure 4c); the solvent accessible cations isolated from the bulk substitution remained in octahedral coordination. Based on this co-occurrence, we infer that a relationship between disordered edge structures and local charge deficits exists. Our classical MD simulations qualitatively support this inference and predict that the presence of octahedral substitutions results in disordered Al edge structures. The disorder in the substituted edges of the MD model was more extensive than in the DFT geometry optimization. We attribute this increased disorder to the Mg in the edge PBC and the octahedral substitutions in the adjacent bulk-side bond chains. The substitution ratio of these adjacent bond chains is greater at the substituted edge (0.375) than at the pyrophyllite-like edges (0.25 and 0.125). Both the MD and DFT simulation results support the inference that disordered edge structures are related to excess negative charge at the edge.

Our classical MD simulations and DFT geometry optimization results provide a basis from which future atomistic simulations can be used to explore the structure and reactivity of the lateral edges of montmorillonite and to interpret experimental results. Synthetic MMTs with a permanent structural charge originating from only the octahedral sheet are limited to layer charges less than 0.4. When the edge substitution ratio of an atomistic model of the Na-MMT AC edge is similarly constrained, our results have demonstrated that the CLAYFF forcefield may be used in molecular mechanics investigations of the MMT AC edge-water interface at the p.z.n.p.c. The presence of octahedral edge substitutions have already been incorporated into some models of the acid-base chemistry of montmorillonite [66]. Acid dissociation constants that have been determined from DFT simulations indicate that solvent accessible Mg substitutions possess extremely high pK_as and increase the pK_a of neighboring silanol groups [26,27]. The effects of Mg substitutions on the pK_a of neighboring Al sites have not been reported but are worthy of consideration based on our present findings that Mg substitutions in the linking PBC position are energetically favored and increased layer charge can result in disordered edge structures. Our models of the Mg-substituted smectite edge also hold promise for future molecular mechanics simulations that examine surface phenomena such as cation complexation and diffusion across the boundary between meso- and nano-pores.

Conflicts of Interest: The authors declare no conflict of interest. The funding sponsors had no role in the design of the study; in the collection, analyses, or interpretation of data; in the writing of the manuscript, and in the decision to publish the results.

References

1. Sposito, G.; Skipper, N.T.; Sutton, R.; Park, S.H.; Soper, A.K.; Greathouse, J.A. Surface geochemistry of the clay minerals. *Proc. Natl. Acad. Sci. USA* **1999**, *96*, 3358–3364. [CrossRef] [PubMed]

2. Miller, A.W.; Wang, Y. Radionuclide interaction with clays in dilute and heavily compacted systems: A critical review. *Environ. Sci. Technol.* **2012**, *46*, 1981–1994. [CrossRef] [PubMed]

3. Pusch, R.; Carlsson, T. The physical state of pore water of Na smectite used as barrier component. *Eng. Geol.* **1985**, *21*, 257–265. [CrossRef]

4. Boulet, P.; Coveney, P.V.; Stackhouse, S. Simulation of hydrated Li$^+$-, Na$^+$- and K$^+$-montmorillonite/polymer nanocomposites using large-scale molecular dynamics. *Chem. Phys. Lett.* **2004**, *389*, 261–267. [CrossRef]

5. Liu, X.D.; Lu, X.C.; Wang, R.C.; Zhou, H.Q.; Xu, S.J. Interlayer structure and dynamics of alkylammonium-intercalated smectites with and without water: A molecular dynamics study. *Clays Clay Miner.* **2007**, *55*, 554–564. [CrossRef]

6. Yu, Y.R.; Yang, X.N. Molecular simulation of swelling and interlayer structure for organoclay in supercritical CO_2. *Phys. Chem. Chem. Phys.* **2011**, *13*, 282–290. [CrossRef] [PubMed]

7. Sposito, G. *The Chemistry of Soils*, 2nd ed.; Oxford University Press: Oxford, UK; New York, NY, USA, 2008; p. 329.

8. Lal, R. Soil carbon sequestration impacts on global climate change and food security. *Science* **2004**, *304*, 1623–1627. [CrossRef] [PubMed]

9. Stevenson, F.J. *Humus Chemistry: Genesis, Composition, Reactions*, 2nd ed.; John Wiley & Sons, Inc.: New York, NY, USA, 1994.

10. Wan, J.; Tyliszczak, T.; Tokunaga, T.K. Organic carbon distribution, speciation, and elemental correlations within soil micro aggregates: Applications of STXM and NEXAFS spectroscopy. *Geochim. Cosmochim. Acta* **2007**, *71*, 5439–5449. [CrossRef]

11. Ramos-Tejada, M.D.; Ontiveros, A.; Plaza, R.D.C.; Delgado, A.V.; Duran, J.D.G. A rheological approach to the stability of humic acid/clay colloidal suspensions. *Rheol. Acta* **2003**, *42*, 148–157. [CrossRef]

12. Rand, B.; Pekenc, E.; Goodwin, J.W.; Smith, R.W. Investigation into the existence of edge-face coagulated structures in Na-montmorillonite suspensions. *J. Chem. Soc. Faraday Trans. 1 Phys. Chem. Condens. Ph.* **1980**, *76*, 225–235. [CrossRef]

13. Tombacz, E.; Szekeres, M. Colloidal behavior of aqueous montmorillonite suspensions: The specific role of pH in the presence of indifferent electrolytes. *Appl. Clay Sci.* **2004**, *27*, 75–94. [CrossRef]

14. Rotenberg, B.; Marry, V.; Dufreche, J.F.; Giffaut, E.; Turq, P. A multiscale approach to ion diffusion in clays: Building a two-state diffusion-reaction scheme from microscopic dynamics. *J. Colloid Interface Sci.* **2007**, *309*, 289–295. [CrossRef] [PubMed]

15. Bickmore, B.R.; Bosbach, D.; Hochella, M.F.; Charlet, L.; Rufe, E. *In situ* atomic force microscopy study of hectorite and nontronite dissolution: Implications for phyllosilicate edge surface structures and dissolution mechanisms. *Am. Mineral.* **2001**, *86*, 411–423. [CrossRef]

16. Bosbach, D.; Charlet, L.; Bickmore, B.; Hochella, M.F. The dissolution of hectorite: *In-situ*, real-time observations using atomic force microscopy. *Am. Mineral.* **2000**, *85*, 1209–1216. [CrossRef]

17. Morton, J.D.; Semrau, J.D.; Hayes, K.F. An X-ray absorption spectroscopy study of the structure and reversibility of copper adsorbed to montmorillonite clay. *Geochim. Cosmochim. Acta* **2001**, *65*, 2709–2722. [CrossRef]

18. Papelis, C.; Hayes, K.F. Distinguishing between interlayer and external sorption sites of clay minerals using X-ray absorption spectroscopy. *Colloids Surf. A* **1996**, *107*, 89–96. [CrossRef]

19. Strawn, D.G.; Palmer, N.E.; Furnare, L.J.; Goodell, C.; Amonette, J.E.; Kukkadapu, R.K. Copper sorption mechanisms on smectites. *Clays Clay Miner.* **2004**, *52*, 321–333. [CrossRef]

20. Brouwer, E.; Baeyens, B.; Maes, A.; Cremers, A. Cesium and rubidium ion equilibria in illite clay. *J. Phys. Chem.* **1983**, *87*, 1213–1219. [CrossRef]

21. Elzinga, E.J.; Sparks, D.L. Nickel sorption mechanisms in a pyrophyllite-montmorillonite mixture. *J. Colloid Interface Sci.* **1999**, *213*, 506–512. [CrossRef] [PubMed]

22. Zachara, J.M.; Smith, S.C.; Liu, C.X.; McKinley, J.P.; Serne, R.J.; Gassman, P.L. Sorption of Cs$^+$ to micaceous subsurface sediments from the Hanford site, USA. *Geochim. Cosmochim. Acta* **2002**, *66*, 193–211. [CrossRef]

23. Bickmore, B.R.; Rosso, K.M.; Nagy, K.L.; Cygan, R.T.; Tadanier, C.J. Ab initio determination of edge surface structures for dioctahedral 2:1 phyllosilicates: Implications for acid-base reactivity. *Clays Clay Miner.* **2003**, *51*, 359–371. [CrossRef]

24. Churakov, S.V. Ab initio study of sorption on pyrophyllite: Structure and acidity of the edge sites. *J. Phys. Chem. B* **2006**, *110*, 4135–4146. [CrossRef] [PubMed]

25. Lavikainen, L.P.; Tanskanen, J.T.; Schatz, T.; Kasa, S.; Pakkanen, T.A. Montmorillonite interlayer surface chemistry: Effect of magnesium ion substitution on cation adsorption. *Theor. Chem. Acc.* **2015**, *134*. [CrossRef]

26. Liu, X.; Lu, X.; Sprik, M.; Cheng, J.; Meijer, E.J.; Wang, R. Acidity of edge surface sites of montmorillonite and kaolinite. *Geochim. Cosmochim. Acta* **2013**, *117*, 180–190. [CrossRef]

27. Liu, X.D.; Cheng, J.; Sprik, M.; Lu, X.C.; Wang, R.C. Surface acidity of 2:1-type dioctahedral clay minerals from first principles molecular dynamics simulations. *Geochim. Cosmochim. Acta* **2014**, *140*, 410–417. [CrossRef]

28. Tazi, S.; Rotenberg, B.; Salanne, M.; Sprik, M.; Sulpizi, M. Absolute acidity of clay edge sites from ab-initio simulations. *Geochim. Cosmochim. Acta* **2012**, *94*, 1–11. [CrossRef]

29. Churakov, S.V. Structure and dynamics of the water films confined between edges of pyrophyllite: A first principle study. *Geochim. Cosmochim. Acta* **2007**, *71*, 1130–1144. [CrossRef]

30. Liu, X.; Lu, X.; Meijer, E.J.; Wang, R.; Zhou, H. Atomic-scale structures of interfaces between phyllosilicate edges and water. *Geochim. Cosmochim. Acta* **2012**, *81*, 56–68. [CrossRef]

31. Suter, J.L.; Kabalan, L.; Khader, M.; Coveney, P.V. Ab initio molecular dynamics study of the interlayer and micropore structure of aqueous montmorillonite clays. *Geochim. Cosmochim. Acta* **2015**, *169*, 17–29. [CrossRef]

32. Sposito, G. *The Surface Chemistry of Natural Particles*; Oxford University Press: Oxford, UK; New York, NY, USA, 2004; p. 242.

33. Churakov, S.V.; Dähn, R. Zinc adsorption on clays inferred from atomistic simulations and EXAFS spectroscopy. *Environ. Sci. Technol.* **2012**, *46*, 5713–5719. [CrossRef] [PubMed]

34. Hedstrom, M.; Karnland, O. Donnan equilibrium in Na-montmorillonite from a molecular dynamics perspective. *Geochim. Cosmochim. Acta* **2012**, *77*, 266–274. [CrossRef]

35. Cygan, R.T.; Liang, J.J.; Kalinichev, A.G. Molecular models of hydroxide, oxyhydroxide, and clay phases and the development of a general force field. *J. Phys. Chem. B* **2004**, *108*, 1255–1266. [CrossRef]

36. Newton, A.G.; Sposito, G. Molecular dynamics simulations of pyrophyllite edge surfaces: Structure, surface energies, and solvent accessibility. *Clays Clay Miner.* **2015**, *65*, 278–290. [CrossRef]

37. Newton, A.G.; Sposito, G. Molecular simulations of disordered edge structures on 2:1 clay mineral nanoparticles. *J. Colloid Interface Sci.* **2016**. under review.

38. Newton, A.G. Atomistic Simulations of the Dioctahedral 2:1 Phyllosilicate Edge—Water Interface: Structure, Dynamic Properties, and Cation Complexes. Ph.D. Thesis, University of California, Berkeley, Berkeley, CA, USA, 2012.

39. Hartman, P. *Crystal Growth: An Introduction*; North-Holland Pub. Co.: Amsterdam, The Netherlands; Elsevier: New York, NY, USA, 1973; p. 531.

40. White, G.N.; Zelazny, L.W. Analysis and implications of the edge structure of dioctahedral phyllosilicates. *Clays Clay Miner.* **1988**, *36*, 141–146. [CrossRef]

41. Lee, J.H.; Guggenheim, S. Single-crystal X-ray refinement of pyrophyllite-1*Tc*. *Am. Mineral.* **1981**, *66*, 350–357.

42. Sainz-Diaz, C.I.; Timon, V.; Botella, V.; Artacho, E.; Hernandez-Laguna, A. Quantum mechanical calculations of dioctahedral 2:1 phyllosilicates: Effect of octahedral cation distributions in pyrophyllite, illite, and smectite. *Am. Mineral.* **2002**, *87*, 958–965. [CrossRef]

43. Cadars, S.; Guegan, R.; Garaga, M.N.; Bourrat, X.; le Forestier, L.; Fayon, F.; Huynh, T.V.; Allier, T.; Nour, Z.; Massiot, D. New insights into the molecular structures, compositions, and cation distributions in synthetic and natural montmorillonite clays. *Chem. Mater.* **2012**, *24*, 4376–4389. [CrossRef]

44. Reinholdt, M.; Brendlé, J.; Tuilier, M.-H.; Kaliaguine, S.; Ambroise, E. Hydrothermal synthesis and characterization of Ni-Al montmorillonite-like phyllosilicates. *Nanomaterials* **2013**, *3*, 48–69. [CrossRef]

45. Reinholdt, M.; Miehe-Brendle, J.; Delmotte, L.; le Dred, R.; Tuilier, M.H. Synthesis and characterization of montmorillonite-type phyllosilicates in a fluoride medium. *Clay Miner.* **2005**, *40*, 177–190. [CrossRef]

46. Reinholdt, M.; Miehe-Brendle, J.; Delmotte, L.; Tuilier, M.H.; le Dred, R.; Cortes, R.; Flank, A.M. Fluorine route synthesis of montmorillonites containing Mg or Zn and characterization by XRD, thermal analysis, MAS NMR, and EXAFS spectroscopy. *Eur. J. Inorg. Chem.* **2001**, *11*, 2831–2841. [CrossRef]

47. Lantenois, S.; Champallier, R.; Bény, J.M.; Muller, F. Hydrothermal synthesis and characterization of dioctahedral smectites: A montmorillonites series. *Appl. Clay Sci.* **2008**, *38*, 165–178. [CrossRef]

48. Berendsen, H.J.C.; Grigera, J.R.; Straatsma, T.P. The missing term in effective pair potentials. *J. Phys. Chem.* **1987**, *91*, 6269–6271. [CrossRef]

49. Lopez-Lemus, J.; Chapela, G.A.; Alejandre, J. Effect of flexibility on surface tension and coexisting densities of water. *J. Chem. Phys.* **2008**, *128*. [CrossRef] [PubMed]

50. Karasawa, N.; Goddard, W.A. Acceleration of convergence for lattice sums. *J. Phys. Chem.* **1989**, *93*, 7320–7327. [CrossRef]

51. Plimpton, S.J. Fast parallel algorithms for short-range molecular dynamics. *J. Comput. Phys.* **1995**, *117*, 1–19. [CrossRef]

52. Kumar, R.; Schmidt, J.R.; Skinner, J.L. Hydrogen bonding definitions and dynamics in liquid water. *J. Chem. Phys.* **2007**, *126*. [CrossRef] [PubMed]

53. Humphrey, W.; Dalke, A.; Schulten, K. VMD: Visual molecular dynamics. *J. Mol. Graph.* **1996**, *14*, 33–38. [CrossRef]

54. Clark, S.J.; Segall, M.D.; Pickard, C.J.; Hasnip, P.J.; Probert, M.J.; Refson, K.; Payne, M.C. First principles methods using CASTEP. *Z. Kristallogr.* **2005**, *220*, 567–570. [CrossRef]

55. Vanderbilt, D. Soft self-consistent pseudopotentials in a generalized eigenvalue formalism. *Phys. Rev. B Condens. Matter Mater. Phys.* **1990**, *41*, 7892–7895. [CrossRef]

56. Perdew, J.P.; Burke, K.; Ernzerhof, M. Generalized gradient approximation made simple. *Phys. Rev. Lett.* **1996**, *77*, 3865–3868. [CrossRef] [PubMed]

57. Monkhorst, H.J.; Pack, J.D. Special points for brillouin-zone integrations. *Phys. Rev. B* **1976**, *13*, 5188–5192. [CrossRef]

58. Leslie, M.; Gillan, M.J. The energy and elastic dipole tensor of defects in ionic-crystals calculated by the supercell method. *J. Phys. C Solid State Phys.* **1985**, *18*, 973–982. [CrossRef]

59. Wedepohl, K.H. *Handbook of Geochemistry*; Springer-Verlag: Berlin, Germany; Heidelberg, Germany; New York, NY, USA, 1978.

60. Ohtaki, H.; Radnai, T. Structure and dynamics of hydrated ions. *Chem. Rev.* **1993**, *93*, 1157–1204. [CrossRef]

61. Kwon, K.; Newton, A.G. Structure and stability of pyrophyllite edge surfaces: Effect of temperature and water chemical potential. *Geochim. Cosmochim. Acta* **2016**. under review.

62. Edelman, C.H.; Favejee, J.C.L. On the crystal structure of montmorillonite and halloysite. *Z. Kristallogr.* **1940**, *102*, 417–431. [CrossRef]

63. Monasterio, F.E.; Dias, M.L.; Pita, V.J.R.R.; Erdmann, E.; Destefanis, H.A. Effect of the organic groups of difunctional silanes on the preparation of coated clays for olefin polymer modification. *Clay Miner.* **2010**, *45*, 489–502. [CrossRef]

64. Pusch, R.; Karnland, O. Physico chemical stability of smectite clays. *Eng. Geol.* **1996**, *41*, 73–85. [CrossRef]

65. Sterte, J.; Shabtai, J. Cross-linked smecites. V. Synthesis and properties of hydroxy-silicoaluminum cross-linked montmorillonites and fluorhectorites. *Clays Clay Miner.* **1987**, *35*, 429–439. [CrossRef]

66. Tournassat, C.; Ferrage, E.; Poinsignon, C.; Charlet, L. The titration of clay minerals: II. Structure-based model and implications for clay reactivity. *J. Colloid Interface Sci.* **2004**, *273*, 234–246. [CrossRef] [PubMed]

The Growth of Gypsum in the Presence of Hexavalent Chromium: A Multiscale Study

Juan Morales [1], José Manuel Astilleros [2,3,*], Emilio Matesanz [4] and Lurdes Fernández-Díaz [2,3]

[1] Laboratorio de Estudios Cristalográficos, Instituto Andaluz de Ciencias de la Tierra,
Consejo Superior de Investigaciones Científicas, Universidad de Granada (CSIC, UGR),
Avenida de las Palmeras 4, E-18100 Armilla, Granada, Spain; juan.morales@csic.es

[2] Departamento de Cristalografía y Mineralogía, Universidad Complutense de Madrid,
C/José Antonio Novais 2, E-28040 Madrid, Spain; lfdiaz@geo.ucm.es

[3] Instituto de Geociencias, Consejo Superior de Investigaciones Científicas,
Universidad Complutense de Madrid (CSIC, UCM), C/José Antonio Novais 2, E-28040 Madrid, Spain

[4] Centro de Asistencia a la Investigación de Difracción de Rayos X, Universidad Complutense de Madrid,
E-28040 Madrid, Spain; ematesanz@quim.ucm.es

* Correspondence: jmastill@ucm.es; Tel.: +34-913-944-876

Abstract: The sorption of dissolved inorganic pollutants into the structure of minerals is an important process that controls the mobility and fate of these pollutants in the Earth's crust. It also modifies the surface structure and composition of the host mineral, affecting its crystallization kinetics. Here, we investigate the effect of hexavalent chromium, Cr(VI), on the nucleation and growth of gypsum by conducting two types of experiments: (i) *in situ* atomic force microscopy (AFM) observations of the growth of gypsum {010} surfaces in the presence of Cr(VI) and (ii) gypsum precipitation experiments by mixing aqueous solutions containing variable amounts of Cr(VI). Gypsum precipitation is progressively delayed when occurring from solutions bearing increasing Cr(VI) concentrations. Chemical analyses of gypsum precipitates show that gypsum incorporates small Cr(VI) amounts that correlate with the content of this ion in the aqueous solution. Gypsum cell parameters variation reflects this incorporation. At the molecular scale, Cr(VI) induces a slowdown of step advance rates on gypsum {010} surfaces accompanied by the roughening of nanostep edges and the so-called "template effect". This effect involves the reproduction of the original nanotopography after the completion of individual advancing monolayers and appears as a general nanoscale phenomenon occurring during growth of solid solutions from aqueous solutions even in the case of compositionally-restricted solid solutions.

Keywords: hexavalent chromium; gypsum; atomic force microscopy; crystal growth; nucleation; mineral surfaces; template effect

1. Introduction

There are numerous examples of crystal surfaces undergoing changes of nanotopographic features during growth from aqueous solutions containing foreign ions [1–7]. One of the most remarkable phenomena is the so-called "template effect", which was first defined by Astilleros [8] to describe the reproduction of the original nanotopography of a crystal surface, including etch-pits and step edges, after successive completion of advancing monolayers. This effect has been interpreted as the result of the incorporation of the foreign ions in the growing layers during step advancement. The difference between the ionic radii of the substituted ions induces lattice mismatch between the new doped layer and the original substrate (free of impurities), which in turn causes elastic strain and stress.

Subsequently, relaxation of this elastic stress occurs perpendicular to the layer, thereby introducing local variations in bond lengths. This, in turn, results in the roughing of the surface of the monolayer. This phenomenon is reflected by the characteristics of the advancement of successive monolayers on the original cleaved surface. Since the surface of successive monolayers is progressively rougher, their advancement also occurs at a progressively lower rate and eventually stops after a certain number of monolayers have piled up [2,8].

The template effect has been reported in varied systems as $CaCO_3$-Me^{2+}-H_2O (Me = Sr, Mn, Mg, Co), $CaMg(CO_3)_2$-H_2O; $BaSO_4$-Sr^{2+}-H_2O or $BaSO_4$-CO_3^{2-}-H_2O. In all cases, a slight lattice misfit through the interface between the original surface and the first growing monolayer is assumed. Most examples of the template effect correspond to systems where the compositional variation involves the substitution of cations [8–12]. However, several examples of this phenomenon occurring during the growth of anionic solid solutions have also been reported [3,13,14].

Chromium (Cr) is a most strategic element due to its use in numerous and important industrial procedures [15]. These industrial applications have determined significant increases of the concentration of Cr in certain settlements with important environmental consequences. Indeed, the hexavalent form of this element, Cr(VI), is highly toxic and can poison most organisms even at low degrees of exposure [15]. Moreover, Cr(VI) also is very soluble and, consequently, highly mobile. Thus, it is not surprising that the pollution of soil and ground waters by Cr(VI) is an important public health concern. Because under circumneutral to basic pHs CrO_4^{2-} is the most stable anion of Cr(VI), in most cases the remediation of Cr(VI)-related contamination can be achieved through the removal CrO_4^{2-} anions. CrO_4^{2-}-sorption on mineral surfaces can be an efficient method for this removal. Since the similarity of CrO_4^{2-} and SO_4^{2-} in both size and geometry permits the isomorphic substitution of these oxyanions in mineral structures, sulfate minerals are especially suitable phases for uptaking CrO_4^{2-} and reducing its bioavailability in the environment through the formation of solid solutions.

Here, we study the nanoscale characteristics of gypsum {010} growth in the presence of different concentrations of Cr(VI), aiming to confirm the template effect as a nanoscale phenomenon inherent to crystal growth in solid solution-aqueous solution systems. We also aim to study the capacity of gypsum to sequester Cr(VI). In order to achieve these goals, we conducted *in situ* crystal growth observations using atomic force microscopy (AFM) and direct precipitation experiments. The samples obtained from direct precipitation experiments were characterized using inductively coupled plasma-optical emission spectrometry (ICP-OES, SPECTRO Analytical Instruments, Kleve, Germany), X-ray diffraction (XRD, Panalytical B.V., Almelo, The Netherlands) and scanning electron microscopy (SEM JEOL Ltd., Tokyo, Japan).

2. Material and Methods

In order to study the growth of gypsum in the presence of Cr(VI), we conducted (i) nanoscale experiments of the growth of {010} gypsum surfaces using a Digital Instrument Multimode IIIA AFM (Veeco, Santa Barbara, CA, USA) and (ii) precipitation experiments by mixing solutions. Stock solutions of $CaCl_2$, Na_2SO_4 and Na_2CrO_4 were prepared by the addition of reagent-grade compounds (Sigma Aldrich, St. Louis, MO, USA) to high-purity deionized water (resistivity = 18.2 MΩ·cm).

The supersaturation of the aqueous solutions with respect to gypsum was calculated by using the expression:

$$\beta_{Gp} = a(Ca^{2+}) \cdot a(SO_4^{2-}) \cdot [a(H_2O)]^2 / K_{sp,Gp} \tag{1}$$

where $a(Ca^{2+})$, $a(SO_4^{2-})$ and $a(H_2O)$ are the respective activities of calcium, sulfate and water in the aqueous solution and $K_{sp,Gp}$ is the thermodynamic solubility product of gypsum ($K_{sp,Gp} = 10^{-4.85}$ at 25 °C; "minteq" database [16]). The solution is in equilibrium with respect to gypsum when $\beta_{Gp} = 1$, while $\beta_{Gp} > 1$ and $\beta_{Gp} < 1$ indicate that the solution is supersaturated and undersaturated, respectively. In all cases, the activities and supersaturation degrees were calculated by using the numerical code PHREEQC [16].

Other possible solid phases, such as chromatite ($CaCrO_4$) or calcium chromate dihydrate ($CaCrO_4 \cdot 2H_2O$), were not taken into consideration due to the very high solubilities of these phases [17]. All the experiments were conducted at 25 °C and atmospheric pressure.

2.1. In Situ AFM Observations

In situ observations of the growth of gypsum {010} surfaces in contact with solutions supersaturated with respect to this phase and bearing different amounts of CrO_4^{2-} were conducted using a Digital Instrument Multimode AFM equipped with a fluid cell and working in contact mode. Silicon nitride tips (Veeco NP-S10, Bruker, Camarillo, CA, USA) with a nominal force constant k = 0.06–0.58 N/m were used.

Gypsum has perfect cleavage along {010}, which is the most common crystallographic form in its habit [18]. Freshly cleaved fragments of natural, optically clear gypsum from Toledo (Spain) (size ~ 3 × 3 × 2 mm^3) were placed within the fluid cell. In all the cases and prior to the experiment, a solution undersaturated with respect to gypsum ($\beta_{Gp} = 0.8$) was passed over the cleaved surface to ensure its cleaning and slight dissolution. Crystallographic directions on the gypsum surface were established on the basis of its dissolution features [19]. The aqueous solutions were prepared from stock solutions immediately before being injected in the fluid cell.

Kinetic information was obtained from measurements of advancement of [001] and [102] steps, which are the most stable ones on gypsum {010} surfaces. Table 1 list the concentration of reactants used in the experiments (Ca^{2+}, Na^+, Cl^-, SO_4^{2-} and CrO_4^{2-}) and the respective supersaturation values. In all cases, the experiments were carried out varying the concentration of chromate in solution and keeping a relatively constant supersaturation value ($\beta_{Gp} \approx 1.35$). In addition, some experiments using more concentrated and supersaturated solutions ($[CrO_4^{2-}] = 0.075$ M, $\beta_{Gp} \approx 2.4$) were specifically conducted in order to enhance the effect of Cr(VI) on the growth process and, in this way, to clearly elucidate the inhibitory mechanism operating in this system. Special attention was paid to changes in the growth rate and morphology of the first layers.

Table 1. Concentrations and supersaturation values of the solutions used in the AFM experiments.

Exp. Id.	$[CrO_4^{2-}]$ (mol/L)	$[SO_4^{2-}]$ (mol/L)	$[Ca^{2+}]$ (mol/L)	$[Cl^-]$ (mol/L)	$[Na^+]$ (mol/L)	β_{Gp}
AFM-1	0.000	0.024	0.024	0.049	0.049	1.363
AFM-2	0.005	0.025	0.025	0.050	0.060	1.356
AFM-3	0.010	0.026	0.026	0.052	0.072	1.357
AFM-4	0.015	0.027	0.027	0.053	0.083	1.364
AFM-5	0.020	0.027	0.027	0.054	0.094	1.362
AFM-6	0.025	0.028	0.028	0.055	0.105	1.364

2.2. Precipitation Experiments

In addition, sets of experiments were performed by mixing 50 mL of two equi-molar solutions, one of $CaCl_2$ and the other of Na_2SO_4 in 100 mL polypropylene vessels. The latter solution contained amounts of Na_2CrO_4 ranging from 0.01 to 1 M. The vessels were immediately sealed after mixing and the solutions were kept at 25 °C and constantly stirred (200 rpm). Each experiment took one hour. In all the cases, the initial supersaturation with respect to gypsum was adjusted to a similar value ($\beta_{Gp} \approx 47$), irrespective of the amount of Na_2CrO_4 in the solution. Three replicates of each experiment were conducted.

Once the solutions of $CaCl_2$ and Na_2SO_4 (+ Na_2CrO_4) were mixed, the induction period for nucleation (t_w) was determined. This parameter can be defined as the time elapsed between the onset of supersaturation and the first changes in the physical properties of the system due to the formation of a solid phase [20]. t_w was determined by visually detecting the appearance of turbidity in the bulk of the solution. Although this method commonly yields slightly longer t_w than more sophisticated

detection methods, such as conductivity measurements, its accuracy is sufficient for the purposes of this work. Indeed, early classical papers on nucleation kinetics concluded that in the case of nucleation in bulk solution, optical methods and conductivity methods yielded values not significantly different when t_w values were longer than 10 s (see, for example, [21]). After one hour, solid phases were collected by filtering the solution through a 0.45-μm Millipore membrane under reduced pressure with a vacuum filtration system, washed twice with Milli-Q water and dried at 40 °C. After 24 h, the solids were weighed and prepared for analysis.

In order to investigate the possible incorporation of chromate in the precipitates, they were dissolved in Milli-Q water and analyzed by ICP-OES, Model Spectro Arcos.

X-Ray diffraction (XRD) analyses were carried out in reflection mode by using a Panalytical X'Pert PRO MPD Alfa1 diffractometer (Panalytical B.V., Almelo, The Netherlands) with Cu Kα radiation (λ = 1.54056 Å) from a Ge (111) primary beam monochromator and a fast X'Celerator detector. Diffractograms were acquired in continuous-scan mode with 50-s preset time and steps of 0.0084°. X-ray source conditions were 45 kV and 40 mA with 2200 W of power. Phase identification was done by means of X'Pert HighScore Plus (Panalytical B.V. software) in combination with ICDD PDF-4 database (International Center for Diffraction Data, Swarthmore, PA, USA). In addition, profile-matching refinement of the profile was done to study the possible variation of cell parameters due to the incorporation of chromate into the crystal structure. The lattice parameters were refined as monoclinic by the Le Bail method [22] using FullProf software [23]. Refinements were started using the *A*2/*a* space group and structure parameters derived from Comodi *et al.* [24]. Calculations were firstly performed for blank samples (grown in the absence of chromate) and the resulting data were used as starting point for subsequent refinements. In all cases, the background was fitted with a polynomial function with 6 coefficients, and peak shapes were modeled by means of a standard Thompson-Cox-Hasting pseudo-Voigt function [25] modified to incorporate asymmetry from axial divergence [26]. After several cycles of least-squares minimizations, the profile fitting converged to $R_p < 14$, $R_{wp} < 24$ and $\chi^2 < 2.4$.

Selected samples of the precipitates were dried and coated with a thin Au layer for further observation by means of field emission scanning electron microscopy (FE-SEM; JSM-6335F, JEOL Ltd., Tokyo, Japan). Images of the gypsum particles were taken at 15 kV accelerating voltage.

3. Results

3.1. AFM Observations

The dissolution of gypsum {010} surfaces is characterized by the retreat of the pre-existing cleavage steps and by the rapid formation and coalescence of etch pits of ~7.5 Å height, corresponding to the dimensions of half the *b*-axis periodicity of gypsum. These etch pits show a characteristic shape, controlled by the retreat movement of [001] and [101] steps (Figure 1). The features and the orientation of the etch pits enable the definition of the main crystallographic directions on gypsum {010} surfaces.
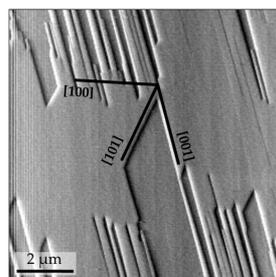

Figure 1. AFM image of a gypsum (010) surface dissolving in an undersaturated solution (β$_{Gp}$ = 0.8). Etch pits are oriented parallel to [001] and [101] and are ~7.5 Å in depth, which corresponds to the dimensions of half the *b*-axis periodicity of gypsum.

Figure 2 shows an AFM sequence obtained after first injecting a supersaturated (β_{Gp} = 1.36) chromate-free aqueous solution (Figure 2a) and then a chromate-bearing aqueous solution (Figure 2b,c). The growth on the {010} surface of gypsum from chromate-free aqueous solutions (AFM-1) is dominated by the straight advancement of steps [001] and [102] [27] and exhibits an anisotropic behavior, with steps parallel to [102] spreading much faster (76.2 ± 24.7 nm/s) than steps parallel to [001] (43.7 ± 12.5 nm/s). However, when small amounts of Na_2CrO_4 (0.025 mol/dm^{-3}) are added to the solution, (AFM-6) steps become rougher and their advancement rate speeds down. Step rate measurements as a function of ($[CrO_4^{2-}]_{aq}$) for a given supersaturation ($\beta_{Gp} \approx 1.35$) are shown in Figure 3. As can be observed, growth becomes less anisotropic and the step advancement rate decreases as $[CrO_4^{2-}]_{aq}$ increases. However, a complete stoppage of the growth is never attained.
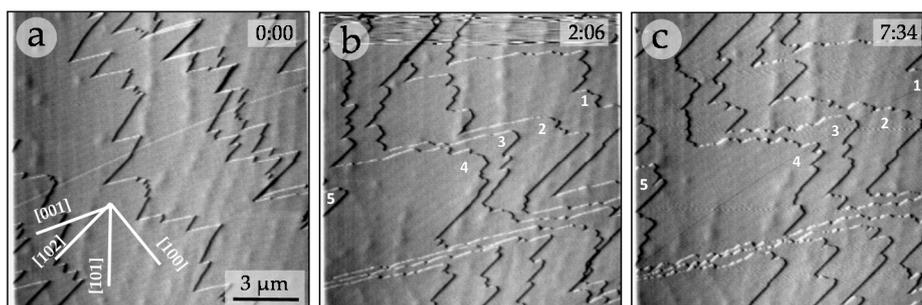
Figure 2. AFM sequence showing the growth of gypsum (0$\bar{1}$0) surface in the presence of CrO_4^{2-} ($[CrO_4^{2-}]$ = 0.025 M; β_{Gp} = 1.35). Elapsed times (minutes and seconds) are shown in the upper right-hand corner of each image. It becomes evident that the presence of CrO_4^{2-} in the aqueous solution (**b**–**c**) inhibits the step advancement, whereas those steps that can be distinguished in (**a**) are gone in (**b**) with about 2 min elapsed between these two images; those steps marked 1–5 in (**b**) can still be easily distinguished in (**c**), which elapses over 5 min with respect to (**b**).
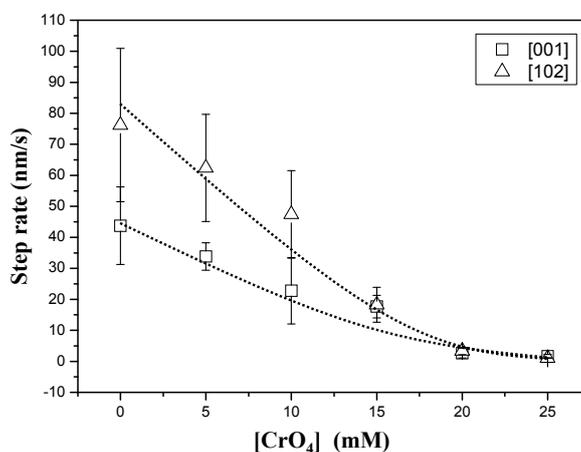
Figure 3. Step advancement rate measurements as a function of $[CrO_4^{2-}]_{aq}$ for a constant supersaturation value ($\beta_{Gp} \approx 1.35$).

In order to elucidate the possible effect on the growth process of the new surfaces generated during the experiments, we observed the behavior of the first steps seconds after injecting the solution using more supersaturated and concentrated aqueous solutions (β_{Gp} = 2.36; $[CrO_4^{2-}]_{aq}$ = 0.075 M). Figure 4 shows the surface of gypsum in contact with an undersaturated aqueous solution (Figure 4a) and just after injecting the growing solution (Figure 4b–d). When the step advancement occurs on the original pure-gypsum substrate, [001] and [101] step edges formed as a result of the initial dissolution of the surface remain straight. However, these steps roughen and become jagged when

their advancement occurs on a surface formed during the experiment. Moreover, steps growing on the original surfaces grow much faster than those growing on the newly formed layers. Thus, as can be seen by comparing images 4a and 4b. The first monolayer (labeled 1) rapidly spreads on the original substrate (labeled 0) to reach a macro-step (step edge marked by a white solid line) in less than 45 s (compare images 4a and 4b). Images in Figure 4b–d show that the second monolayer (labeled 2) spreads on the first monolayer (1). However, this second monolayer moves at a much lower rate than the first monolayer did on the original substrate. As a result, after over 11 min, monolayer 2 still has not reached the macro-step. Similarly, the distance between subsequent step edges, which bound successive monolayers (marked by black numbers 1'–3'), becomes progressively larger. This can only be explained by a progressive reduction of the rate at which successive monolayers spread. Moreover, the inhibitory effect of chromate on gypsum growth results in the reproduction of some features of the original microtopography (see black dashed lines in Figure 4a,c).
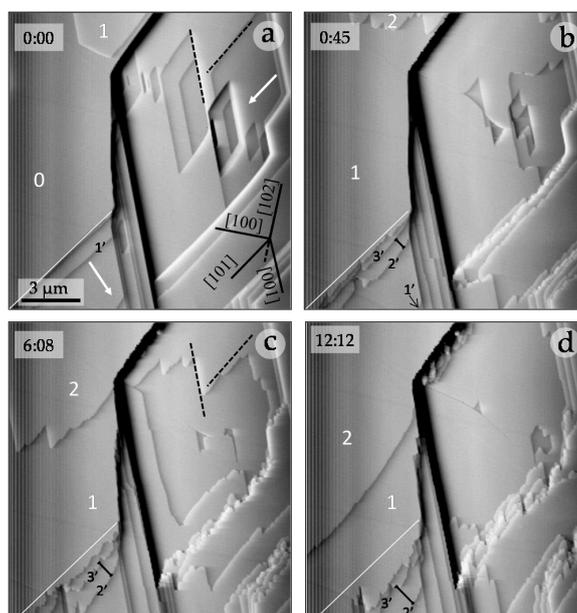
Figure 4. Growth sequence on gypsum (010) surface in the presence of chromate ($[CrO_4^{2-}]_{aq}$ = 0.075 M; β_{Gp} = 2.36). Elapsed times are shown in the upper left-hand corner of each image. Black-dashed lines (in pictures **a** and **c**) indicate step edges of the original topography and its reproduction by the advancement of the subsequent monolayer. White arrows (in picture **a**) indicate the movement directions of some steps. White numbers correspond to the original substrate (0) and the first (1) and the second (2) monolayers. The solid white line in a-d indicates the original position of a macro-step. The black numbers mark the edge of steps that bound the first (1'), second (2') and third (3') monolayers. Steps growing on the original substrate remain straight during their advancement and grow faster than those growing on layers formed during the experiment, which become jagged. The first monolayer (1) reaches the macrostep in less than 45 s (see (**a**,**b**)). The slower advance of monolayer 2 determines that it still has to reach this macro-step after advancing during 11 min (see images (**b**–**d**)). Note how the distance between steps 2' and 3' (lower left-hand corner in images **b**–**d**) progressively increases. This indicates that the third monolayer advances at a slower rate than the second monolayer, evidencing a cumulative inhibitory effect on the growth of successive monolayers.

## 3.2. Precipitation of Gypsum in the Presence of CrO_4^{2-}

Precipitation experiments have shown that t_w strongly depends on $[CrO_4^{2-}]_{aq}$. In the absence of chromate (blank experiment) the bulk solution becomes whitish very rapidly after the mixing of the reactive solutions ($t_w \approx 10$ s). In contrast, in those experiments conducted in the presence of CrO_4^{2-}, the turbidity appears later as $[CrO_4^{2-}]_{aq}$ increases ($t_w \approx 150$ s for $[CrO_4^{2-}]_{aq}$ = 1 M)

and follows an exponential trend (see Table 2). Moreover, the amount of precipitate recovered from the vessels progressively decreases as $[CrO_4^{2-}]_{aq}$ increases. For instance, the precipitate recovered in the experiments conducted under the higher $[CrO_4^{2-}]_{aq}$ (1.0 M) weighs approximately half the weight of the precipitate recovered in the blank experiments. The color of the precipitate also changes with the $[CrO_4^{2-}]_{aq}$, evolving from white in the blank experiment to progressively darker yellow as $[CrO_4^{2-}]_{aq}$ increases.

Table 2. Concentrations, supersaturation values, induction time for nucleation (t_w) and weight of the recovered solids in the direct precipitation (DP) experiments.

| Exp. Id.	$[CrO_4^{2-}]$ (mol/L)	$[SO_4^{2-}]$ (mol/L)	$[Ca^{2+}]$ (mol/L)	$[Cl^-]$ (mol/L)	$[Na^+]$ (mol/L)	β_{Gp}	t_w (s)	Weight (g)
DP-1	0.00	0.26	0.26	0.52	0.52	47.6	8.7 ± 2.3	4.08 ± 0.02
DP-2	0.01	0.26	0.26	0.52	0.54	47.6	9.3 ± 2.5	4.04 ± 0.05
DP-3	0.03	0.26	0.26	0.52	0.58	47.6	10.3 ± 3.2	4.05 ± 0.03
DP-4	0.06	0.26	0.26	0.52	0.64	47.6	12.0 ± 2.6	4.03 ± 0.07
DP-5	0.10	0.26	0.26	0.52	0.72	47.3	16.3 ± 3.0	3.99 ± 0.07
DP-6	0.20	0.26	0.26	0.52	0.92	47.3	25.0 ± 3.6	3.81 ± 0.04
DP-7	0.40	0.25	0.25	0.51	1.31	46.2	40.7 ± 6.0	3.47 ± 0.05
DP-8	0.60	0.25	0.25	0.50	1.70	47.3	60.0 ± 5.0	3.27 ± 0.04
DP-9	0.80	0.25	0.25	0.49	2.09	47.6	92.0 ± 3.0	2.85 ± 0.13
DP-10	1.00	0.24	0.24	0.48	2.48	47.6	150.0 ± 8.2	2.44 ± 0.08

Selected precipitates were chemically analyzed by ICP-OES. Figure 5 shows the molar concentration of Ca, S and Cr in the solid samples ($[Ca]_s$, $[S]_s$ and $[Cr]_s$). These results show that: (a) all the precipitates analyzed contain Cr and; (b) a direct correlation between $[CrO_4^{2-}]_{aq}$ and $[Cr]_s$ can be established. Moreover, it is interesting to note that whereas $[Ca]_s$ keeps an approximately constant value, $[S]_s$ and $[Cr]_s$ follow an opposite trend: *i.e.*, $[S]_s$ decreases by the same amount as $[Cr]_s$ increases ($[S]_s + [Cr]_s$ = constant).
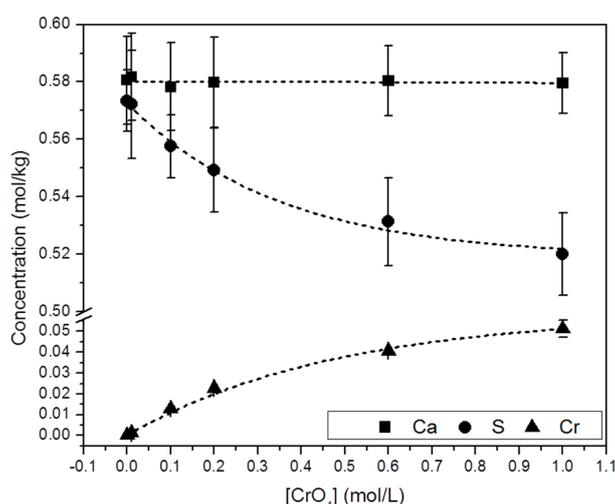
Figure 5. Chemical composition (from ICP-OES analyses) of solid samples collected from the precipitation experiments as a function of $[CrO_4^{2-}]_{aq}$. An increase of $[Cr]_s$ is closely followed by a decrease in $[S]_s$. Analyses yielded similar $[Ca]_s$ in all the solids.

XRD analyses confirm that precipitates exclusively consist of gypsum (Figure 6a), independent of $[CrO_4^{2-}]_{aq}$ and $[Cr]_s$ (Powder Diffraction File, Inorganic, #033-0311, International Center for Diffraction Data, Swarthmore, PA, USA). Moreover, a detailed study of the X-ray diffraction patterns of the precipitates reveals the existence of a clear and continuous shift of the most relevant gypsum diffraction peaks towards lower 2θ values as $[Cr]_s$ increases (see Table S1), as can be seen in Figure 6b for the

(020) reflection. Moreover, the relative intensities of the most important reflections also exhibit a continuous variation with respect to the amount of Cr in the solids (see values within parenthesis in Table S1). For instance, whereas the relative intensity of the (031) reflection gradually increases, the ($\bar{1}$22) reflection intensity clearly decreases as $[Cr]_s$ increases.
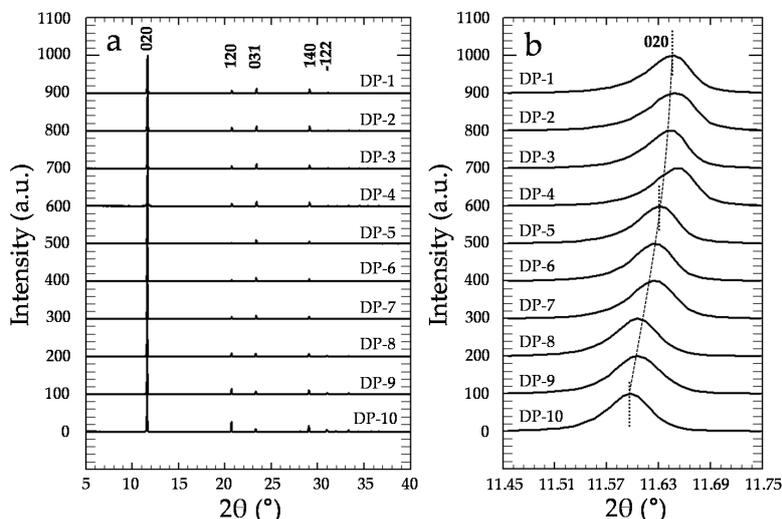

Figure 6. (**a**) Powder X-ray diffraction patterns of the precipitates. For the sake of clarity, all of the diffractograms have been normalized to the (010) peak, which is the most intense reflection; (**b**) Magnification of the (020) reflection, where a clear shift of this reflection towards lower 2θ values as $[Cr]_{aq}$ increases can be observed.

The incorporation of small amounts of chromate in the solids causes a small but perceptible change in the cell parameters (a_0, b_0, c_0) and the volume of the cell. As can be observed in Figure 7, a linear and positive correlation between $[Cr]_s$ and these parameters can be established.
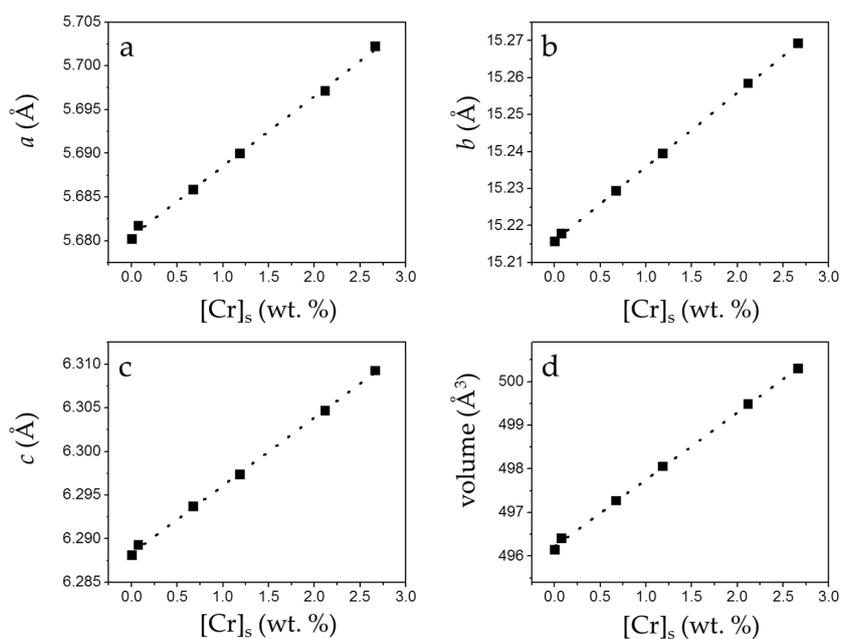
Figure 7. Unit cell parameters and cell volume (from the refinement of XRD patterns) of the precipitates plotted against $[Cr]_s$. Cell parameters (**a**–**c**) and cell volume (**d**) of gypsum increase as $[Cr]_s$ increases.

Figure 8 shows the morphological characteristics of the precipitates grown in the absence and presence of different $[CrO_4{}^{2-}]_{aq}$. Gypsum crystals precipitated in the absence of chromate exhibit the typical needle-like habit and are elongated along the c-axis (15–30 μm) (Figure 8a). However, those precipitates obtained from solutions containing higher amounts of chromate consist of less elongated needle-like crystals (5–15 μm) and show a greater abundance of larger plate-like crystals with {010} as the dominant form (Figure 8b,c).
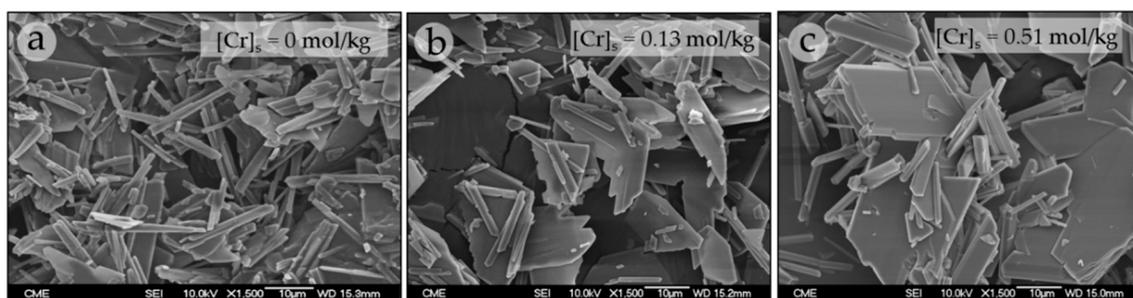
Figure 8. SEM micrographs of crystals collected in the precipitation experiments in the absence (**a**) and presence of different $[CrO_4{}^{2-}]_{aq}$: 0.1 M (**b**); and 1 M (**c**).

4. Discussion

In situ AFM observations of the growth of gypsum {010} surfaces in the presence of chromate unequivocally show that this anion inhibits the growth of gypsum {010} surfaces, affecting not only the step advancement rate but also the morphology of the growing steps. These observations can be interpreted in terms of the so-called "template effect", as defined by Astilleros *et al.* [2,8–11], who observed a similar inhibition-incorporation phenomenon during the growth of calcite surfaces in contact with supersaturated solutions bearing additives like Mn, Ba, Mg or Sr. The anomalous growth behavior of gypsum {010} surfaces and the inhibiting effect on gypsum growth caused by the presence of chromate can only be satisfactorily explained by assuming the incorporation of this pollutant into the structure of this mineral phase. Indeed, the subtle variation of the color shade of the solids obtained from precipitation experiments can be regarded as a first indication that chromate is probably incorporated into the crystal structure of gypsum.

In the experiments carried out, such a sorption mechanism involves the trapping of chromate ions into the structure of gypsum during the precipitation of this phase, according to the reaction:

$$SO_4{}^{2-}(aq) + CrO_4{}^{2-}(aq) + Ca^{2+}(aq) + nH_2O \rightarrow Ca(SO_4, CrO_4) \cdot 2H_2O + (n-2)H_2O \qquad (2)$$
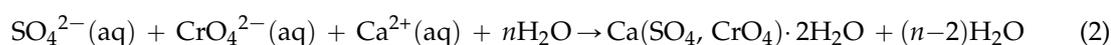
As highlighted in Figure 5, the net increase of $[Cr]_s$ (~0.51 mol/kg) virtually equals the net decrease in $[S]_s$ (~0.53 mol/kg). Moreover, the total molalities of calcium and sulfate plus chromate are similar, clearly pointing to the existence of a substitutional solid solution between two end-members, $CaSO_4 \cdot 2H_2O$ and a hypothetical, isostructural with gypsum $CaCrO_4 \cdot 2H_2O$. In such a solid solution, $CrO_4{}^{2-}$ would substitute $SO_4{}^{2-}$ in the layered structure of gypsum. This assumption is additionally supported by the results of the XRD analysis. In all isomorphic substitutions, the difference in size between the substituting ions leads to an increase of the unit cell parameters as the concentration of the larger ion (chromate in the present case) increases in the crystal structure [28,29]. This is indirectly reflected by the shift towards lower 2θ values observed in specific, relevant peaks in the diffraction diagrams of the precipitates as $[Cr]_s$ in the solid increases (Figure 6b and Table S1). Le Bail refinements also reveal the enlargement of the unit cell parameters and the expansion of the unit cell volume, which are most probably a consequence of the substitution of $SO_4{}^{2-}$ by $CrO_4{}^{2-}$. The plot of the refined cell parameters (Figure 7) shows a linear correlation between cell parameters and the amount of chromium present in the crystal lattice, in agreement with Vegard's Law [30].

When one anion substitutes another in a crystal structure, the amount of substitution depends to a great extent on the size and shape of the involved anionic groups. CrO_4^{2-} and SO_4^{2-} share a tetrahedron-like geometry and show a similar size. The isomorphic substitution of sulfate and chromate is not uncommon in mineral phases. For instance, the solid solution between barite ($BaSO_4$) and $BaCrO_4$ is assumed to be ideal [31], which means that both phases are end-members of a complete solid solution [32]. Other sulfate minerals like ettringite [17,33] or jarosite [34] can also incorporate small amounts of CrO_4^{2-} substituting SO_4^{2-}.

Although the similarity in the size and shape of two anions points to their isomorphic subtitution in a mineral structure as being possible, the degree of substitution and, therefore, the ability of a certain mineral to trap a foreign element via coprecipitation is the result of a variety of physico-chemical factors. One key factor is the difference of solubility between the end-members of the solid solution. In solid solution-aqueous solution (SS-AS) systems, distribution coefficients, D, are frequently used to express the partitioning of an ion between an aqueous solution and a solid phase. In the system considered here, the partition coefficient of (CrO_4^{2-}) between the aqueous solution and the solid phase $Ca(SO_{4(1-x)}CrO_{4(x)})\cdot 2H_2O$ can be defined by:

$$D_{CrO_4^{2-}} = \frac{X_{CaCrO_4\cdot 2H_2O}}{X_{CaSO_4\cdot 2H_2O}} \left/ \frac{a\left(CrO_4^{2-}\right)}{a\left(SO_4^{2-}\right)} \right. \tag{3}$$

where $X_{CaCrO_4\cdot 2H_2O}$ and $X_{CaSO_4\cdot 2H_2O}$ are the mole fractions of the end-members in the solid phase and $a(CrO_4^{2-})$ is the activity of chromate in the aqueous solution.

At thermodynamic equilibrium and assuming an ideal solid solution, the partition coefficient (D_{eq}) is defined by the ratio between the solubility product of gypsum and a calcium chromate dihydrate phase, isoestructural with the gypsum structure. Although the solubility of this phase is unknown, it should be necessarily higher than that of the stable form of the calcium chromate dihydrate, which is orthorhombic and over three orders of magnitude more soluble than gypsum. By considering this solubility, a maximum distribution coefficient $D_{eq} < 0.001$ can be estimated. Such a small partition coefficient means that the tendency of the CrO_4^{2-} ion to incorporate into the solid phase during the precipitation of a $Ca(SO_{4(1-x)}CrO_{4(x)})\cdot 2H_2O$ solid solution is extremely low.

On the other hand, experimental studies have shown that the distribution coefficient also depends on kinetic factors, such as supersaturation levels, and that the "effective" distribution coefficients can largely differ from the equilibrium values. As has been profusely shown by Prieto *et al.* [35–37], at high supersaturations there is less chance for thermodynamically based selectivity effects to be exerted. For instance, Fernández-González *et al.* [32] studied the formation of the solid solution between $BaSO_4$ and $BaCrO_4$, showing that at high levels of supersaturation with respect to the less soluble end-member $BaSO_4$, the effective distribution coefficients (D_{eff}) for CrO_4^{2-} reached values very close to 1, even though the $D_{eq} = 0.42$. In the system under consideration here the D_{eff} for CrO_4^{2-} has a value < 0.05. Although in this case this parameter is increased due to the effect of the high supersaturations used, a very marked preferential partitioning of SO_4^{2-} towards the solid phase still occurs.

The results obtained in the precipitation experiments indicate that the presence of chromate in the aqueous solution exerts an important role in the precipitation process of gypsum. This effect is revealed by both the lengthening of t_w and a decrease of the amount of recovered precipitate as $[CrO_4^{2-}]_{aq}$ increases. These results clearly point to an inhibitory effect of chromate on the nucleation of gypsum. This effect is also supported by the SEM images, which clearly reveal changes in both size and habit of the gypsum crystals. The larger size of the crystals formed in the presence of increasing amounts of chromate is consistent with moderate kinetics of nucleation which, in turn, can only be ascribed to an inhibitory effect of this anion, since the supersaturation with respect to gypsum was similar in all the experiments. Indeed, according to the nucleation theory ([20], and references therein), smaller and numerous crystals are frequently the result of catastrophic nucleation events, whereas scarcer and larger crystals are formed under nucleation-restricted conditions. On the other hand, changes in

crystal habit are also frequently explained by a selective sorption of the additive on certain faces of a crystal. When this is the case, the inhibitory effect is more intense on those specific faces, which will grow more slowly. The resulting effect is the modification of the crystal habit. In the gypsum crystals, the transition from crystals with a needle-like habit elongated along the c-axis to plate-like crystals with {010} as the dominant form could be tentatively explained by a selective sorption of CrO_4^{2-} on specific gypsum surfaces.

Finally, the results demonstrate that although gypsum can incorporate chromate into its structure, the substitution of SO_4^{2-} by CrO_4^{2-} in the gypsum structure detected in the precipitates reaches a maximum value as low as ~8%, even under the most favorable physicochemical conditions for CrO_4^{2-} incorporation (high supersaturation with respect to gypsum and high concentration of chromate in the solution). Such conditions are far from those prevailing in natural environments and, consequently, coprecipitation with gypsum cannot be regarded as an effective method for the removal of chromate from soil and groundwaters. Other sulfate minerals like barite have proved to be much more effective at chromate sequestration. This said, it is important to keep in mind that gypsum is a very abundant a mineral, at any rate much more abundant than barite, and as pointed out by Prieto *et al.* (2013) [37] for aqueous solution-solid solution reactions, the equilibrium end-point depends on the specific initial amounts of solid and liquid as well as the solubility of the respective end-members and the degree of ideality of the solid solution.

Author Contributions: Juan Morales, José Manuel Astilleros and Lurdes Fernández-Díaz contributed to the conception of the study; Juan Morales and José Manuel Astilleros performed the laboratory experiments; Juan Morales and Emilio Matesanz were responsible for the XRD analyses; all authors analyzed the data; Juan Morales, José Manuel Astilleros and Lurdes Fernández-Díaz were involved in the manuscript preparation. All authors read and approved the manuscript.

Conflicts of Interest: The authors declare no conflict of interest.

References

1. Davis, K.J.; Dove, P.M.; de Yoreo, J.J. The role of Mg^{2+} as an impurity in calcite growth. *Science* **2000**, *290*, 1134–1137. [CrossRef] [PubMed]
2. Astilleros, J.M.; Pina, M.; Fernández-Díaz, L.; Putnis, A. Nanoscale growth of solids crystallising from multicomponent aqueous solutions. *Surf. Sci.* **2003**, *545*, L767–L773. [CrossRef]
3. Shtukenberg, A.G.; Astilleros, J.M.; Putnis, A. Nanoscale observations of epitaxial growth of hashemite on barite (001). *Surf. Sci.* **2005**, *590*, 212–223. [CrossRef]
4. Astilleros, J.M.; Pina, M.; Fernández-Díaz, L.; Prieto, M.; Putnis, A. Nanoscale phenomena during the growth of solid solutions on calcite {10$\bar{1}$4} surfaces. *Chem. Geol.* **2006**, *225*, 322–335. [CrossRef]
5. Vavouraki, A.I.; Putnis, C.V.; Putnis, A.; Koutsoukos, P.G. An Atomic Force Microscopy study of the growth of calcite in the presence of sodium sulfate. *Chem. Geol.* **2008**, *253*, 243–251. [CrossRef]
6. Sethmann, I.; Wang, J.; Becker, U.; Putnis, A. Strain-induced segmentation of magnesian calcite thin films growing on a calcite substrate. *Cryst. Growth Des.* **2010**, *10*, 4319–4326. [CrossRef]
7. Nielsen, L.C.; de Yoreo, J.J.; de Paolo, D.J. General model for calcite growth kinetics in the presence of impurity ions. *Geochim. Cosmochim. Acta* **2013**, *115*, 100–114. [CrossRef]
8. Astilleros, J.M. Estudio Integrado de la Cristalización de Soluciones Sólidas no Ideales: (Ca,M)CO$_3$ (M = Ba, Sr, Mn). Ph.D. Thesis, Universidad Complutense de Madrid, Madrid, Spain, 2001. (In Spanish)
9. Astilleros, J.M.; Pina, C.M.; Fernández-Díaz, L.; Putnis, A. Molecular scale surface processes during the growth of calcite in the presence of manganese. *Geochim. Cosmochim. Acta* **2002**, *66*, 3177–3189. [CrossRef]

10. Astilleros, J.M.; Pina, C.M.; Fernández-Díaz, L.; Putnis, A. Metastable phenomena on calcite {10$\bar{1}$4} surfaces growing from Sr^{2+}-Ca^{2+}-CO_3^{2-} aqueous solutions. *Chem. Geol.* **2003**, *193*, 93–107. [CrossRef]

11. Astilleros, J.M.; Fernández-Díaz, L.; Putnis, A. The role of magnesium in the growth of calcite: An AFM study. *Chem. Geol.* **2010**, *271*, 52–58. [CrossRef]

12. Freij, S.J.; Putnis, A.; Astilleros, J.M. Nanoscale observations of the effect of cobalt on calcite growth and dissolution. *J. Cryst. Growth* **2004**, *267*, 288–300. [CrossRef]

13. Sánchez-Pastor, N.; Pina, C.M.; Fernández-Díaz, L.; Astilleros, J.M. The effect of CO_3^{2-} on the growth of barite {001} and {210} surfaces: An AFM study. *Surf. Sci.* **2006**, *600*, 1369–1381. [CrossRef]

14. Ruiz-Agudo, E.; Putnis, C.V.; Kowacz, M.; Ortega-Huertas, M.; Putnis, A. Boron incorporation into calcite during growth: Implications for the use of boron in carbonates as a pH proxy. *Earth Planet. Sci. Lett.* **2012**, *345–348*, 9–17. [CrossRef]

15. Nriagu, J.O.; Nieboer, E. *Chromium in the Natural and Human Environments*; John Wiley & Sons: New York, NY, USA, 1988.

16. Parkhurst, D.L.; Appelo, C.A.J. *User's Guide to PHREEQC (Version 2): A Computer Program for Speciation, Batch-Reaction, One-Dimensional Transport and Inverse Geochemical Calculations: U.S. Geological Survey Water Resources Investigations Report 99-4259*; U.S. Geological Survey: Denver, CO, USA, 1999.

17. Perkins, R.B.; Palmer, C.D. Solubility of $Ca_6[Al(OH)_6]_2(CrO_4)_3 \cdot 26H_2O$, the chromate analogue of ettringite; 5–75 °C. *Appl. Geochem.* **2000**, *15*, 1203–1218. [CrossRef]

18. Kostov, L.; Kostov, R.I. *Crystal Habits of Minerals*; Bulgarian Academic Monographs; Pensoft Publishers: Sofia, Bulgaria, 1999; pp. 308–310.

19. Morales, J.; Astilleros, J.M.; Fernández-Díaz, L. Nanoscopic characteristics of anhydrite (100) growth. *Cryst. Growth Des.* **2012**, *12*, 414–421. [CrossRef]

20. Söhnel, O.; Mullin, J.W. Interpretation of crystallization induction periods. *J. Colloid Interface Sci.* **1988**, *123*, 43–50. [CrossRef]

21. Söhnel, O.; Mullin, J.W. A method for the determination of precipitation induction periods. *J. Cryst. Growth* **1978**, *44*, 377–382. [CrossRef]

22. Le Bail, A.; Duroy, H.; Fourquet, J.L. *Ab initio* structure determination of $LiSbWO_6$ by X-ray powder diffraction. *Mater. Res. Bull.* **1988**, *23*, 447–452. [CrossRef]

23. Rodríguez-Carvajal, J. Recent advances in magnetic structure determination by neutron powder diffraction. *Phys. B Condens. Matter* **1993**, *192*, 55–69. [CrossRef]

24. Comodi, P.; Nazzareni, S.; Zanazzi, P.F.; Speziale, S. High-pressure behavior of gypsum: A single-crystal X-ray study. *Am. Mineral.* **2008**, *93*, 1530–1537. [CrossRef]

25. Thompson, P.; Cox, D.E.; Hastings, J.B. Rietveld refinement of Debye-Scherrer synchrotron X-ray data from Al_2O_3. *J. Appl. Crystallogr.* **1987**, *20*, 79–83. [CrossRef]

26. Finger, L.W.; Cox, D.E.; Jephcoat, A.P. A correction for powder diffraction peak asymmetry due to axial divergence. *J. Appl. Cryst.* **1994**, *27*, 892–900. [CrossRef]

27. Van Driessche, A.E.S.; García-Ruiz, J.M.; Delgado-López, J.M.; Sazaki, G. *In situ* observation of step dynamics on gypsum crystals. *Cryst. Growth Des.* **2010**, *10*, 3909–3916. [CrossRef]

28. Hawthorne, F.C.; Krivovichev, S.V.; Burns, P.C. The crystal chemistry of sulfate minerals. In *Sulfate Minerals Crystallography, Geochemistry, and Environmental Significance. Reviews in Mineralogy & Geochemistry*; Alpers, C.N., Jambor, J.L., Nordstrom, D.K., Eds.; Mineralogical Society of America and Geochemical Society: Washington, DC, USA, 2000; Volume 40, pp. 1–112.

29. Casari, B.M.; Eriksson, A.K.; Langer, V. Synthesis methods for $Ce(CrO_4)_2 \cdot xH_2O$ and crystal structures of K_2CrSO_7, $(NH_4)_2Cr_2O_7$ and $Na_2Cr_2O_7 \cdot 2H_2O$. *Z. Naturforsch. B* **2007**, *62*, 771–777. [CrossRef]

30. Vegard, L. Die Konstitution der Mischkristalle und die Raumfüllung der Atome. *Z. Phys.* **1921**, *5*, 17–26. (In German) [CrossRef]

31. Glynn, P.D.; Reardon, E.J.; Plummer, L.N.; Busenberg, E. Reaction paths and equilibrium end-points in solid-solution aqueous-solution systems. *Geochim. Cosmochim. Acta* **1990**, *54*, 267–282. [CrossRef]

32. Fernández-González, A.; Martín-Díaz, R.; Prieto, M. Crystallisation of $Ba(SO_4, CrO_4)$ solid solutions from aqueous solutions. *J. Crys. Growth* **1999**, *200*, 227–235. [CrossRef]

33. Leisinger, S.M.; Lothenbach, B.; Saout, G.L.; Kägi, R.; Wehrli, B.; Johnson, C.A. Solid solutions between CrO_4- and SO_4-ettringite $Ca_6(Al(OH)_6)_2[(CrO_4)_x(SO_4)_{1-x}]_3 \cdot 26H_2O$. *Environ. Sci. Technol.* **2010**, *44*, 8983–8988. [CrossRef] [PubMed]

34. Baron, D.; Palmer, C.D. Solid-solution aqueous-solution reactions between jarosite (KFe$_3$(SO$_4$)$_2$(OH)$_6$) and its chromate analogue. *Geochim. Cosmochim. Acta* **2002**, *66*, 2841–2853. [CrossRef]

35. Prieto, M.; Fernández-González, A.; Putnis, A.; Fernández-Díaz, L. Nucleation, growth, and zoning phenomena in crystallizing (Ba,Sr)CO$_3$, Ba(SO$_4$,CrO$_4$), (Ba,Sr)SO$_4$, and (Cd,Ca)CO$_3$ solid solutions from aqueous solutions. *Geochim. Cosmochim. Acta* **1997**, *61*, 3383–3397. [CrossRef]

36. Prieto, M.; Fernández-González, A.; Martín-Díaz, R. Sorption of chromate ions diffusing through barite-hydrogel composites: Implications for the fate and transport of chromium in the environment. *Geochim. Cosmochim. Acta* **2002**, *66*, 783–795. [CrossRef]

37. Prieto, M.; Astilleros, J.M.; Fernández-Díaz, L. Environmental remediation by crystallization of solid solutions. *Elements* **2013**, *9*, 195–201. [CrossRef]

Ab initio Studies of O$_2$ Adsorption on (110) Nickel-Rich Pentlandite (Fe$_4$Ni$_5$S$_8$) Mineral Surface

Peace P. Mkhonto, Hasani R. Chauke * and Phuti E. Ngoepe

Materials Modelling Centre, University of Limpopo, Private Bag X1106, Sovenga 0727, South Africa;
peace.mkhonto@gmail.com (P.P.M.); phuti.ngoepe@ul.ac.za (P.E.N.)
*   Correspondence: hr.chauke@ul.ac.za; Tel.: +27-015-268-2206; Fax: +27-015-268-3268

Abstract: *Ab initio* density functional theory was used to investigate the adsorption of oxygen molecule on the nickel-rich pentlandite (110) surface, which is important for mineral extraction. The three most reactive adsorption sites: Fe-top, Ni-top, and fcc-hollow have been considered. Firstly, the non-adsorbed pentlandite surface reflects the Ni atoms relaxing inwards. Consequently, their electronic structure showed high Fe 3d-orbital contribution than the Ni 3d-orbitals at the E$_F$ (indicating that the Fe atoms are more reactive than Ni). Secondly, the O$_2$-adsorbed surface predicted lowest adsorption energy for Fe-top (-1.902 eV), as a more spontaneous reaction is likely to occur than on fcc-hollow (-1.891 eV) and Ni-top (-0.040 eV) sites, suggesting Fe preferential oxidation. The density of states indicates that the O$_2$ show prevalence of electrons in the π_p* antibonding orbitals, and are reduced to zero states at the valence band on metal-bonded oxygen (O1). The σ_p* orbital is observed to reside just above the E$_F$ for Fe-top and fcc-hollow site, while on Ni-top is half-occupied for both metal-bonded oxygen (O1) and terminal oxygen (O2). Finally, the isosurface charge density difference showed electron (charge) depletion on Ni/Fe metals and accumulation on the O$_2$ molecule. Bader analysis indicated that the oxidized Fe and Ni atoms adopt more positive charge, while O$_2$ on Fe-top atoms possesses more negative charge than on Ni-top, resulting with O1 possessing a smaller charge than O2 atom.

Keywords: nickel-rich pentlandite (Fe$_4$Ni$_5$S$_8$); (110) surface; oxidation; adsorption energies; density of states; Bader analysis; electronic properties; isosurface charge density

1. Introduction

Transition metal sulphides are an important group of minerals and have found application in the mining industry to meet the ever growing demand of nickel [1]. Minerals such as pyrites and pentlandite have been under investigation recently, as pentlandites are regarded a principal source of nickel [2]. Amongst others, oxygen interactions on pentlandite surface both by natural means and during flotation is an important process in mineral ore extraction. A previous investigation has reported that oxidation tends to depress the sulphide minerals [3–6] and had shown iron preferential oxidation [7]. Naturally, minerals in atmospheric contact are exposed to gaseous oxygen and this results in oxide formation. As such, oxidation of sulphide mineral surfaces is of outstanding practical importance and requires theoretical fundamental understanding of surface chemistry during mineral flotation.

The study of surface reaction on pentlandite, in particular the disordered (Fe, Ni)$_9$S$_8$ is not amenable using density functional theory (DFT) methods. The Fe and Ni atoms occupy a site at a certain occupancy ratio, with Fe atoms preferentially occupying the octahedral sites [8]. However, simulation of cobalt pentlandite, Co$_9$S$_8$ is relatively easier but computationally demanding since the same metal (Co) is present in all 36 metal sites in the crystal structure.

The oxidation of sulphide mineral surfaces has been investigated previously [3,4,9]. It has been indicated that the atmospheric oxidation of these minerals either by weathering or aging involves physical and chemical adsorption of oxygen on the surface and thus forms various peroxides and hydroxides. Furthermore, the oxidation products of synthetic pentlandite were found to be similar to the natural pentlandite, and are independent of the composition [3,4]. Richardson and Vaughan observed that oxidation of synthetic pentlandite under various oxidation conditions could lead to the formation of violarite ($FeNi_2S_4$) and a thin iron oxyhydroxide overlayer [9]. On the other hand, Buckley and Woods revealed that oxidation of natural pentlandite from a pyrrhotite matrix using XPS resolution, showed two doublets in the S $2p$ spectra. Furthermore, rapid oxidation of pentlandite to form thin FeOOH overlayers was also observed [4]. Again, oxidation of sulphide mineral in the presence of water has been investigated and showed the significant of oxide/hydroxide and sulphate species formation; and the formation of a sulphur-rich and nickel-rich subsurface layers [4,9,10]. As it is well known that the discharge acid mine drainage results from the oxidation of pyrite due to the formation of FeOOH species. This often causes serious environmental problems [11,12]. In order to reduce the unwanted oxidation of sulphide, it is necessary to ascertain the interaction mechanism of sulphide surfaces with O_2 in the absence of H_2O.

In this paper a computational simulation method is used to investigate the surface configurations and electronic properties of nickel-rich pentlandite mineral. The adsorption of pure oxygen molecule on the (110) $Fe_4Ni_5S_8$ surface is studied using DFT method to observe formation of reactant species and metal preferential bonding. It was found that the surface reaction between oxygen molecule and pentlandite mineral gave reasonable Fe–O and Ni–O bond distance. The oxygens (O1 and O2) show directional bonding leading to formation of superoxo species. Furthermore, Bader charge analysis of Fe and Ni metals show that the charges increase suggesting charge transfer to the oxygen molecule. This study provides the computational explanation to the mechanism of oxygen reaction with nickel-rich pentlandite mineral. Such information is important for enhancing the efficiency of mineral extraction during froth flotation, which depends mainly on the selective adhesion of air bubbles to mineral surfaces in a mineral.

## 2. Computational Model and Methods

2.1. Computational Model

Our simulation model is based on the geometry of the pentlandite structure with a space group of *Fm-3m* (225) [13]. An important aspect of the pentlandite structure is the presence of three metal-metal bond extending from each tetrahedral cation to form essential isolated cube cluster of tetrahedral cation, Rajamani and Prewitt [14] and Vaughan and Craig [15]. In order to simulate the surface properties precisely, different possible arrangements of the Ni and Fe atoms were considered to construct the desired $Fe_4Ni_5S_8$ pentlandite structure (Figure 1), with four octahedral metal sites occupied by Ni(O), while the 32 tetrahedral metal sites are evenly occupied by Fe(T) and Ni(T). The Ni(O) are coordinated to the face-capping sulphurs, while the Fe(T) and Ni(T) are coordinated to the linked and face-capping sulphurs. The S(l) are 4-coordinated while the S(f) are 5-coordinated.

We used the stable bulk nickel-rich pentlandite structure to cleave (110) surface. Note that different surface terminations have been considered since these display different reactivity and surface energies. Furthermore, this has an effect during adsorption, as a very reactive surface may not give a reasonable thermodynamic behaviour of the mineral surface. As such we have tested different terminations and considered the most stable surface termination (Term. 3) with lowest positive surface energy (less reactive), represented in Figure 1b. This is also based on the previous report that during the first stage of flotation where mineral particles are crushed, the minerals will mainly cleave along surfaces that have large inter-planar spacing and few inter-planar bonds, usually low-index surfaces with low surface energies under dry conditions [16]. Due to the high computational demand of the pentlandite structure, we considered a stoichiometric surface slab composed of four-layered

of atoms separated by a vacuum slab of 20 Å, which was tested and found to be sufficient to avoid interaction between slabs. The two top-most atomic layers of the substrate were allowed to relax and the bottom-most atomic layers of the substrate were fixed to the bulk coordinates in the adsorption calculations (see Figure 2). The energy required to cleave the bulk crystal exposing the surface is the surface energy and this is obtained by:

$$E_{surface} = \left(\frac{1}{2A}\right) [E_{slab} - nE_{bulk}] \tag{1}$$

where E_{slab} is the total energy of the cell containing the surface slab, E_{bulk} is the total energy of the bulk per atom, n is the number of atoms in the slab and A is the area of the cell containing the surface slab. A low positive value of $E_{surface}$ indicates stability of the surface.
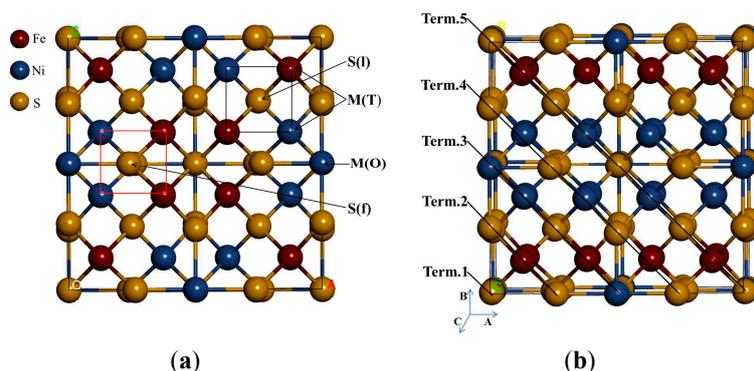
Figure 1. The crystal structure of nickel-rich pentlandite: (**a**) conventional $4(Fe_4Ni_5S_8)$ and (**b**) different terminations considered. M(O) and M(T) represent the octahedral and tetrahedral metals, respectively, with S(f) and S(l) representing the face-capping and the linked sulphurs, respectively.
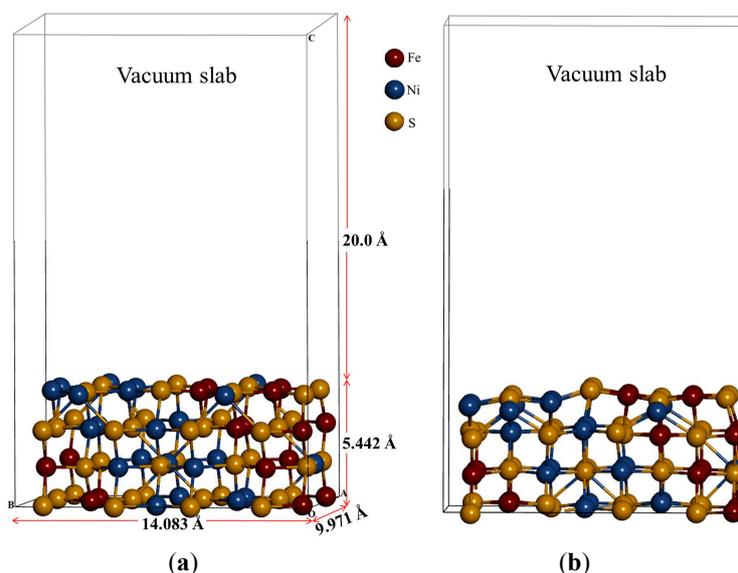
Figure 2. The side view of (110) surface: (**a**) un-relaxed and (**b**) relaxed surfaces.

2.2. Computational Methods

Ab initio quantum-mechanical density functional theory [17,18] calculations are used to investigate the surface-O_2 reaction on nickel-rich pentlandite mineral, employing VASP (Vienna Ab-initio Simulation Package) code [19]. The plane-wave (PW) pseudopotential method with

generalized gradient approximation of Perdew-Burke-Ernzerhof (GGA-PBE) exchange-correlation functional [20] was used to model surface properties of $Fe_4Ni_5S_8$ (110) surface. The ultrasoft pseudopotential is used with a plane-wave basis set truncated at a kinetic energy of 400 eV, since this was sufficient to converge the total energy of the bulk and surface systems. The equilibrium cell parameters for the bulk nickel-rich pentlandite were obtained using k-point mesh of $5 \times 5 \times 5$ to be sampled in the Brillouin zone integrations. The resulting cell parameters was 9.977 Å, which agrees well with the previously calculated value of 9.991 Å by Chauke *et al.* [21], also with the experimental value of 10.100 Å, Lindqvist *et al.* [22]. Structural optimization of the surface model were then performed using a conjugate gradients technique with an iterative relaxation of the atomic positions until the forces on the atoms were all less than 0.01 eV/Å. For all geometry optimization of the surface, a $5 \times 5 \times 1$ k-point mesh was used. This is chosen according to the scheme proposed by Monkhorst and Pack [23]. These are also employed at the final single-point runs for the calculation of the electronic spin-polarized density of states, where the spin down and spin up of the electrons are considered.

Now, in order to calculate reaction energies, the energy of the free O_2 molecule was evaluated using a $10 \times 10 \times 10$ cubic cell with similar oxygen PAW potential, cut-off energy and other equivalent precision parameters as in the surface calculations. The O_2 molecule was calculated as a spin triplet and we obtained an equilibrium bond distance d[O–O] of 1.211 Å, which correlates well with experimental bond length of 1.21 Å [24].

The charge states of the ions at the surface were discussed on the basis of a Bader analysis, which consists of integrating the electron density in a region defined for each atom in such a way that the density gradient flux through the dividing surfaces is zero [25]. An algorithm and a program developed for this purpose by Henkelman *et al.* have been employed [26,27]. The charge density difference upon adsorption was determined by calculating the charge density for the adsorbed system first and then for the (110) clean surface and finally for the O_2 molecule alone, each in the optimized geometry obtained for the adsorbed system. The difference between the charge density distribution of the adsorption system and the sum of the distribution for the (110) substrate and the O_2 adsorbate,

$$\rho\,(Surface + O_2) - \rho\,(Surface) - \rho\,(O_2) \tag{2}$$

reveals the distribution of charge upon adsorption. We have used the VESTA software [28], to visualize the charge density difference between the oxidized surface system and the clean surface plus the oxygen molecule.

3. Results and Discussions

3.1. Relaxations of the (110) Surface

Based on the stable surface geometry (Figure 3), we noted that the S(l) and S(f) atoms change from four-coordinated and five-coordinated as in the bulk to three-coordinated and four-coordinated on the surface slab, respectively. The Fe(T) and Ni(T) atoms change from four-coordinated as in the bulk to three-coordinated on the surface slab. After the surface relaxation we noted that the top layer 1 relaxes into three layers. The surface results in sulphur termination as the sulphur (S2) atoms relaxes outwards forming layer 1. The Fe atoms and S1, S3 and S4 atoms form layer 2, while Ni atoms form layer 3.

The vertical displacement of these atoms results in S1 and S3 relaxing inwards as S4 relaxes outwards. The Fe atoms are noted to have the Fe1 and Fe4 relaxing outwards minimally, as Fe2 and Fe3 remain un-displaced. Figure 3c clearly shows that the top bond length between the Ni atoms is weakened (stretches to 3.693 and 3.433 Å). The Ni atoms are observed to relax deep compared to the Fe atoms, indicating that the surface layer is composed of mainly Fe atoms. This suggests the Fe preferential oxidation character of the pentlandite [8].
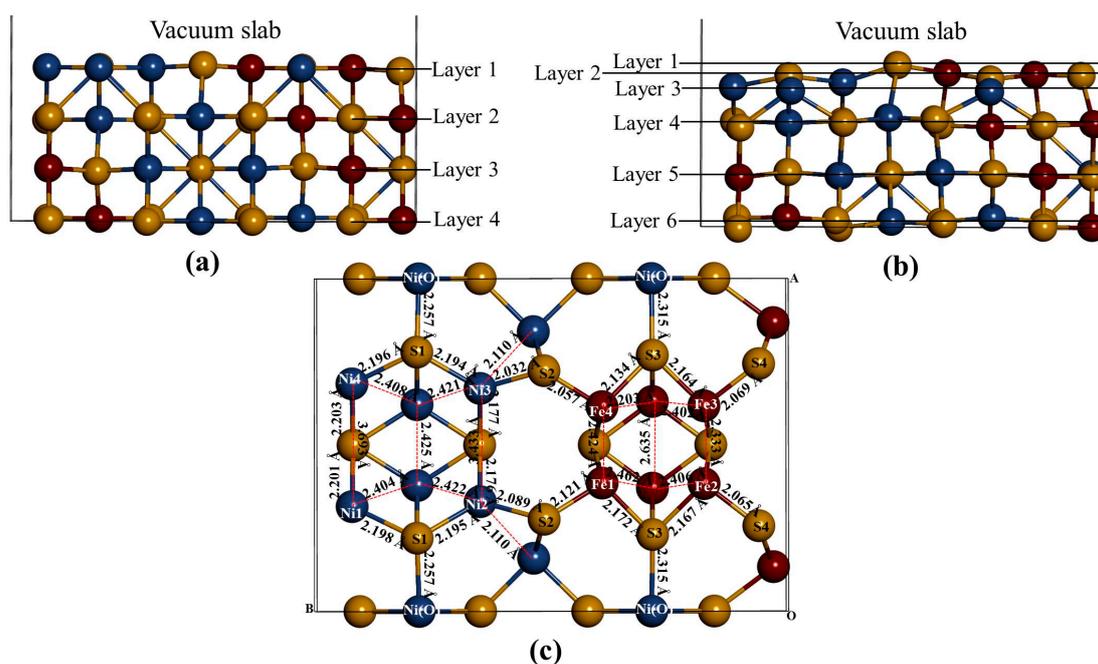
Figure 3. The (110) surface: Show side view of the layers, (**a**) before relaxation and (**b**) after relaxation and (**c**) top view after relaxation with bond distances between the top four layers.

Table 1 shows the vertical displacement of the top atoms on the surface after relaxation (negative and positive sign indicate inwards and outwards displacement, respectively). Only S2 and Fe1 have a higher outwards displacement, and Fe2 and Fe3 remains un-displaced, significantly changes the bond distances. The Ni atoms are noted to have the highest inwards displacement.

Table 1. Atomic vertical displacements (Å) of the relaxed top three layers on slab model.

Atom	Displacement
S1	−0.003
S2	+0.009
S3	−0.006
S4	+0.002
Ni1–Ni4	−0.018
N2–Ni3	−0.012
Fe1	+0.008
Fe2	0.000
Fe3	0.000
Fe4	+0.003

*3.2. Electronic Structures of the Bulk and Non-Adsorbed Surface*

The density of state for the bulk convectional nickel-rich pentlandite is presented in Figure 4. We noted from the total density of states (TDOS) that the spin up/down peaks are equally occupied and appear as mirror images suggesting a non-magnetic behavior, this confirms the character of the pentlandite mineral [29]. The partial density of states (PDOS) clearly shows that the *d*-orbital for Fe(T) are predominant and those of Ni(O) are lowest at the Fermi energy (E_F). We note that the octahedral Ni(O) *d*-orbital form a sharp peak at about −2.0 eV. The Fe(T) *d*-orbital peaks reside just below the E_F at the valence band (VB), while the Ni(T) *d*-orbital contribution is very low at the E_F. At the conduction band (CB), the Ni atoms have very little contribution while the Fe atoms show a peak at around 2.0 eV.
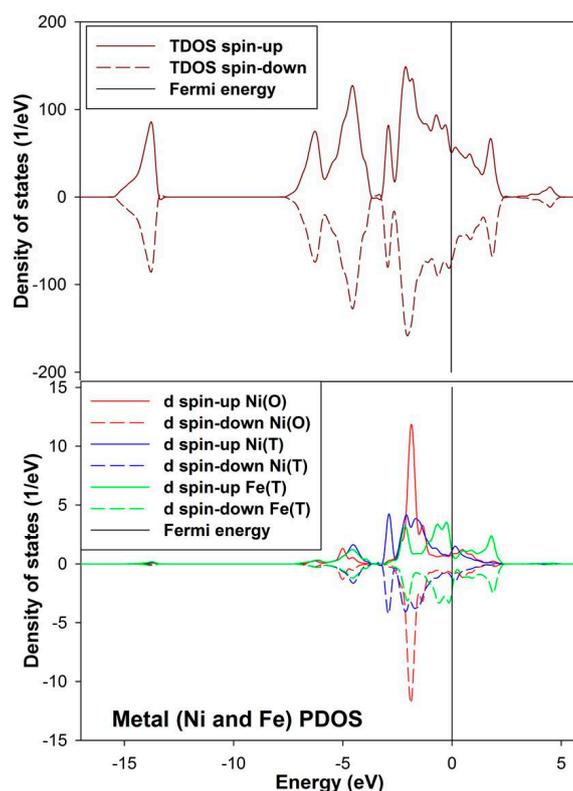
Figure 4. Projection total and partial density of states for the tetrahedral metals (Ni(T) and Fe(T)) and octahedral metals (Ni(O)) in the bulk conventional 4(Fe$_4$Ni$_5$S$_8$) nickel-rich pentlandite.

Figure 5a show density of states (DOS) of (110) surface and it is evident from the total density of states (TDOS) that the *d*-orbital of the metals (M) are the centre of reactivity on the surface as they highly dominate more at the E$_F$. Moreover, the TDOS shows that the surface has a metallic behavior characteristic as there is no band gap at the E$_F$ and still shows a non-magnetic character. Note that the partial density of states (PDOS) is plotted only for the top metals (*i.e.*, Fe and Ni) atoms adsorbed. The PDOS demonstrates that both the Ni and Fe atoms provide accessible bands at the E$_F$. This indicates that the electrons are delocalized, and that the Ni atoms contribute considerably to this delocalization.

Now considering the PDOS (Figure 5a), we note different feature with respect to both top Ni and Fe atoms. Note that we show the PDOS of the Ni and Fe atoms where adsorption will take place. Firstly, the behavior of Ni2–Ni3 *d*-orbital is observed to move closer to the E$_F$ and its contribution is characterized by a sharp *d*-orbital peak near E$_F$ at the (VB) (compared to the Ni(O) in the bulk) with very little contribution at the E$_F$ and at the (CB). Secondly, the Fe1–Fe4 PDOS are noted to have five *d*-orbital peaks, three at the VB and two at the CB. We observed that the *d*-orbital moves across the E$_F$, where the E$_F$ cuts the highest states peak, and we also noted two broad peaks, *i.e.*, the highest states peak (at about 0.05 eV) and the second highest states peak (at about 2.0 eV). It is clear that the bulk *d*-orbital contribution for both tetrahedral and octahedral metals is different than the surface metals. The bulk tetrahedral coordinated metals show predominance of states in the VB, while states are shifted towards the E$_F$ for the surface metals.
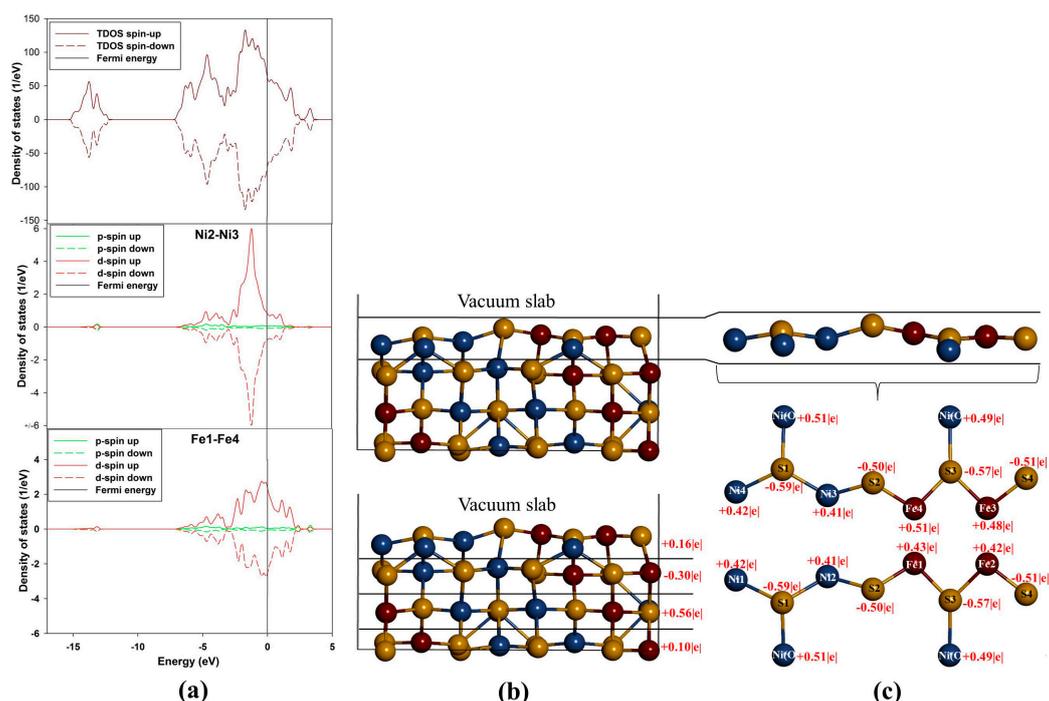
Figure 5. Projection density of states and Bader charges for the top adsorbed Ni and Fe atoms: (**a**) total and partial density of states; (**b**) Bader charges for each layer and (**c**) Bader charges for the top layer atoms.

The Fe atoms on (110) surface are observed to have different Bader charges (Figure 5c). This difference indicates that the Fe atoms are not charge ordered and there is alternation of the charges on the Fe atoms. Furthermore, this suggests that the presence of Ni atoms breaks the charge symmetry of the Fe atoms to a small degree, such that the Fe atoms with $Fe^{+0.42|e|}$ have $0.09|e|$ less than the $Fe^{+0.51|e|}$. Such observations of the charge symmetry breakage have been observed on doping of FeS with Ni by Devey *et al.* [30]. Now, for the case of Ni atoms, we observed that Ni1–Ni4 have the same charges and so are Ni2–Ni3 atoms. Thus, by analogy it can be deduced that there is a high level of covalent nature predicted for the Ni–S and Fe–S bonds in $Fe_4Ni_5S_8$ pentlandite. The Bader charges of the metals shown in Figure 5c indicate that the Fe atoms carry more positive charges than the Ni atoms. The three outermost layers are positively charged, while the second layer is electronegative (Figure 5b).

3.3. Free O_2 Molecule

The ground state of free O_2 molecule is experimentally found to be a spin triplet state, and the equilibrium bond length is 1.21 Å [24], this compares well with our predicted value 1.211 Å. In order to get more information about the electronic structure of the oxygen molecule, we analyze the density of states (DOS) of free O_2 molecule in Figure 6. The energy level of the occupied orbitals of free oxygen molecule shows a band gap between the highest occupied molecular orbitals (HOMO) and the lowest unoccupied molecular orbitals (LUMO), referred to as HOMO-LUMO (H-L) gap. Our predicted H-L gap is 1.3 eV, this is low compared to the H-L gap of 2.27 eV using PBE [31]. However, it has been reported that HSEO6 and PBEO hybrid functionals widen the H-L gap [31]. The current H-L gap suggests that the small value is significant and may suggest that the O_2 will react strongly with the surface. This correlates with previous literature that the chemical reactivity of a molecule is dependent on the H-L gap [32].
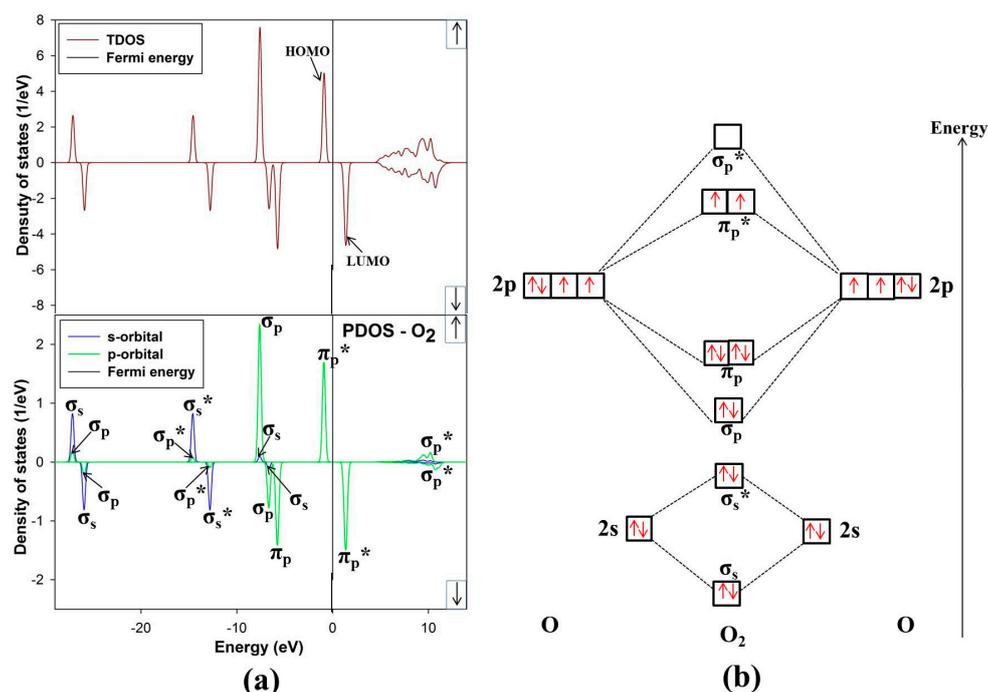
Figure 6. (**a**) Total and partial density of states and (**b**) molecular electron configuration of free O_2 molecule.

The energy levels of the molecular orbitals for O_2 especially that of the *p*-orbital LUMO peak, play an important role in the initial adsorption for O_2 on the nickel-rich pentlandite surface. This is so because O_2 accepts electrons from the mineral surface through the LUMO π_p^* antibonding [26]. Figure 6 of free-O_2 clearly illustrates the versatility of O_2. We note that not only σ and π orbitals; bonding and antibonding orbitals are present but also a significant spin splitting of the levels. This clearly shows the significance of Hund's first rule, since the antibonding spin-up π_p^* orbitals are occupied and the spin-down ones are empty reflecting that O_2 molecule in its ground state is a spin triplet. We also noted some *s-p* hybridization, particularly for the 2*s* derived σ_s and σ_s^* orbitals, these observations have been previously reported [33].
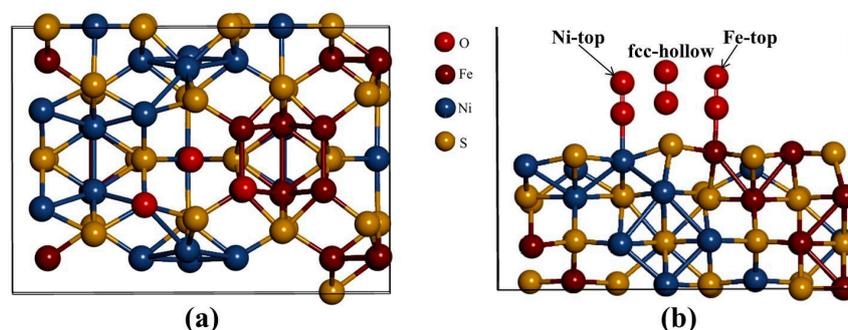
3.4. O_2 Adsorption

Now we evaluate the effect of O_2 molecule adsorbed on the (110) surface, considering three distinct adsorption trajectories as shown in Figure 7. The three sites fcc-hollow, Ni-top, and Fe-top are the possible active adsorption sites. The oxygen molecule is positioned vertical on the surface and the O–O bond length is optimized at each height. In this case the reaction co-ordinate is the height from surface to oxygen molecule. The adsorption strength on interaction of O_2 and the substrate is calculated as,

$$E_{adsorption} = E_{system} - (E_{slab} + E_{adsorbate}) \qquad (3)$$

where E_{system} is the energy of the surface slab with adsorbate, E_{slab} is the energy of the slab and $E_{adsorbate}$ is the energy of the free O_2 molecule. Note that a negative value shows a spontaneous exothermic reaction between the oxygen molecule and the surface, whereas a positive value reveals the opposite.

In considering the adsorption of O_2 at fcc-hollow site (Figure 8a); we noted that the oxygen molecule forms a bridging bond with Fe atoms (Fe1–O_2–Fe4). This observation suggests the preferential oxidation of Fe atoms, and similar results have been previously reported by Merape *et al.* [8]. A bond angle of 84.68° was noted on the bridge bond and compares well with the previous studies of Wang *et al.* [34], where a bond angle of 81.9° was reported. The difference of 2.78

between these two bond angles may be due to the fact that unlike in the current study an oxygen atom was adsorbed instead of the oxygen molecule. This also had an effect on the Fe1–Fe4 bond length, which increased from 2.292 to 2.449 Å. The bond lengths of Fe1–O1 and Fe4–O1 are similar (1.818 Å), which is smaller than the radius between Fe–O of 1.920 Å. This indicated a strong electron overlap across Fe1–O1 and Fe4–O1.

Figure 7. (**a**) Top view and (**b**) side view of the three different adsorption geometries investigated: fcc-hollow, Fe-top, and Ni-top.

The adsorption of O_2 on Fe-top site (Figure 8a) showed similar behavior as observed for fcc-hollow site. However, the resulting bond lengths of Fe1–O1 and Fe4–O1 are different with 1.815 Å and 1.817 Å, respectively (Table 2). Again these values are smaller than the radius between Fe–O of 1.920 Å, suggesting a strong electron overlap across Fe1–O1 and Fe4–O1. The bond angle of Fe1–O1–Fe4 was found to be 84.96° slightly higher than that of fcc-hollow. The oxygen bond length (O1–O2) for both fcc-hollow site and Fe-top site is found to increase to 1.316 Å, which indicates weakening of the O_2 bond. This corresponds to the report that the back donation of an electron from Fe *d*-orbital to oxygen $\pi_p{}^*$ antibonding molecular orbitals generates the diminishing of the O–O bond and lowers the bond strength of oxygen molecule [35].
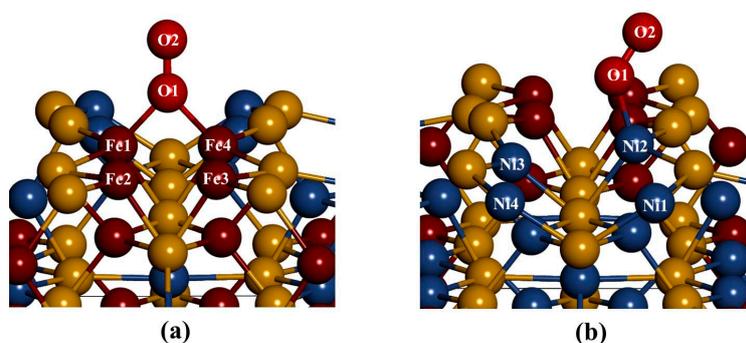
Figure 8. The relaxed geometries of O_2 molecule on the surface: (**a**) fcc-hallow site and Fe-top site and (**b**) Ni-top site.

Table 2. Variation of bond distances between O and metal (M) atoms of the mineral (110) surfaces after adsorption.

Bond Distances	**Fcc-Hollow**	**Fe-Top**	**Ni-Top**
Bonds	Fe–O	Fe–O	Ni–O
$d_o = r_o + r_{metal}$ (Å)	1.920	1.920	1.840
d_{ads} (Å)	1.818	1.815 and 1.817	1.801
$\Delta d = d_{ads} - d_o$ (Å)	−0.102	−0.105 and −0.103	−0.039

d_o is the theoretical value, r_o is the radius of O for O_2; r_{metal} is atomic radius of metal for sulphide, d_{ads} is the distance between O atom for O_2 and metal atom of mineral surface after adsorption.

The adsorption on Ni-top (Figure 8b) shows that the oxygen molecule bends and forms an orientation of a superoxo. Furthermore, we observed that O_2 moves the Ni atom to the outermost layer, forming a Ni2–O1 bond distance of 1.801 Å, which is smaller than the radius between Ni–O of 1.840 Å. This suggested a strong electron overlap across Ni2–O1. We also found an O1–O2 bond distance of 1.284 Å and a Ni2–O1–O2 bond angle of 128.78°. This observation is in line with the previous studies by Gutsev *at al.* [36]. A Ni superoxo isomer, Ni-O bond lengths of 1.728 Å and O–O of 1.284 Å and a Ni–O–O bond angle of 125.3° were reported. Similarly, Citra *et al.* [37], found Ni–O (1.721 Å), O–O (1.302 Å) and Ni–O–O (123.0°). Also Uzunova *et al.* [38], found Ni–O and O–O of 1.722 Å and 1.272 Å, respectively and a Ni–O–O bond angle of 126.3°. These findings compared well with the current results and confirm a neutral superoxo isomer species forming on the surface.

Table 2 present the change in distances (Δd) between O atom (of O_2 molecule) and adsorbed-metal atom of the mineral surface (d_{ads}) compared with the sum of the atomic radius of O atom and adsorbed-metal atom (d_o). We noted that the distance between O and Fe atoms decrease (−0.102 Å), indicating strong interaction between O_2 molecule and top layer Fe atoms. The distance between O atom and Ni atom also slightly changes (−0.039 Å). These results indicate that Fe oxidize rapidly than Ni atoms.

Table 3 list the surface and adsorption energies of the nickel-rich pentlandite (110) surface. Adsorption of O_2 is found to be an exothermic process (the reaction happens spontaneously). The adsorption strength of O_2 on the surface is found to be stronger on the Fe-top (−1.902 eV) than fcc-hollow site (−1.891 eV) and Ni-top (−0.040 eV). Clearly the Fe-top is more exothermic than fcc-hollow by 0.011 eV, suggesting that some energy is lost in the chemisorption process on fcc-hollow site. It is thus evident that the adsorption energy of Fe atoms is more spontaneous than on Ni atoms, confirming the preferential oxidation of Fe.

Table 3. Calculated surface and adsorption energies.

| Surface	Surface Energy	Adsorption (Ads.) Energies		
	$E_{(surface)}$ (eV/Å^2)	$E_{(Ads.)}$ (eV)		
(110)	0.061	fcc-hollow −1.891	Ni-top −0.040	Fe-top −1.902

3.5. Electronic Structure of O_2 Adsorbed Surface

The density of states has been calculated to describe the interaction between the O_2 molecule and the nickel-rich pentlandite mineral (110) surface (Figure 9a,b). Note that we only discuss the DOS for adsorption on Fe-top and Ni-top, since the fcc-hollow showed similar behavior as the Fe-top site. The TDOS is characterized by three spin up/down broad peaks at the VB at −2.0, −5.0 and −14.0 eV, where the −2.0 eV peaks clearly emanate from 3*d* hybridization with O_2 π_p* orbital. A clear distinction is noticed on the PDOS depicting effects of O_2 adsorption on metal atoms. The LUMO π_p* moves to the VB, clearly illustrated that the adsorption of O_2 on the surface is initiated by accepting electrons from the mineral surface into the LUMO π_p* antibonding orbital. This charge transfer is in the form of back-donation of electrons from the mineral surface *d*-orbital to the π_p* anti-bonding orbital, confirming report by Blyholder *et al.* [39].

In Figure 9a, the PDOS for Fe display three dominant spin up/down peaks near E_F at the VB, while only one peak for Ni2 *d*-orbital contribution is observed in Figure 9b. This may suggest strong hybridization of Fe 3*d* with O 2*p* orbital and less for Ni 3*d*. It is also clear that the M-bonded oxygen (O1) and terminal oxygen (O2) PDOS are different for Fe and Ni interaction. The Fe–O_2 interaction shows a single peak of σ_p-orbital (equal states for both O1 and O2) and double degenerate π_p-orbital. The Ni–O_2 interaction shows a single peak of σ_p-orbital and a single degenerate π_p-orbital. More importantly for Fe–O_2, the O1 π_p-orbital peak is two degenerate and becomes reduced for the case of O2 π_p-orbital peak. The single σ_p-orbital peak becomes dominant for O2 PDOS. This behavior is

different for Ni and O interaction (Figure 9b), displaying singlet degenerate π_p and σ_p peaks in the VB. However, σ_p and π_p orbital shows strong overlap for O1.

The other contribution peaks are noticed at energies -25.0 and -16.0 eV for Fe-top and -25.0 and -15.0 for Ni-top, which are of σ_s and σ_s* character, respectively. Furthermore, O2 contribution for both case are also distinct, a sharp π_p* peak and broad π_p* (reduced states) peak are observed at about -2.0 eV for Fe and Ni, respectively. The PDOS on O1 is observed to have the π_p* peaks reduced to zero states at -2.0 eV, while the σ_p* peaks reside just above the E_F and is half-occupied at the E_F for Fe–O_2 and Ni–O_2, respectively. The half occupancy of the σ_p* orbital have been observed previously on O_2 adsorption on Al(111) surface [40].
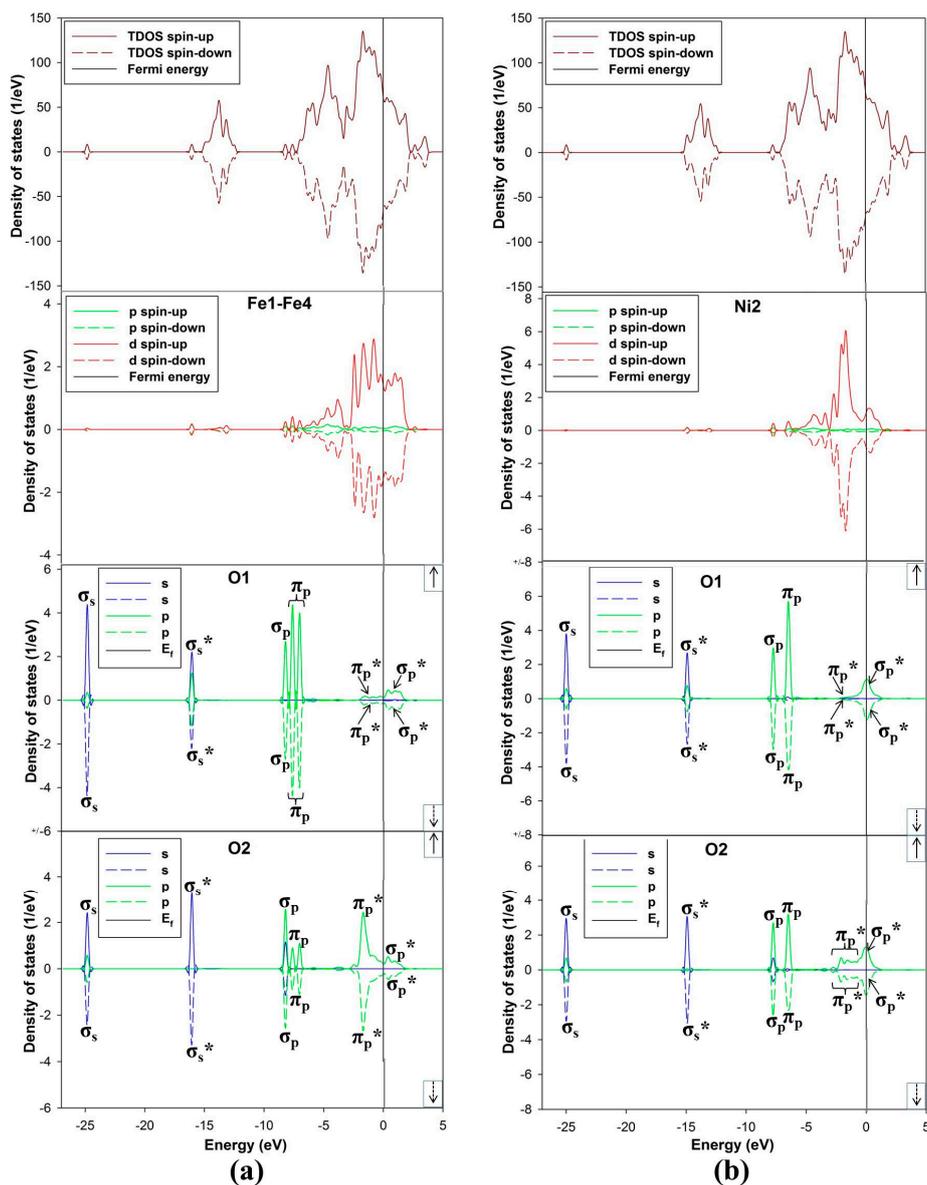
Figure 9. The density of states (DOS) TDOS and PDOS: (**a**) adsorption on Fe-top site and (**b**) adsorption on Ni-top site.

Figure 10a,b display the charge density difference, for the Fe-top and Ni-top adsorption sites. We observed that the Fe and Ni atoms donate electrons while O_2 accept. This is due to a formation of negative electronic cloud (charge depletion) while the O_2 has a positive electronic cloud (charge accumulation). The cylindrical shape around O2 atom represents the π_p* orbital, as observed from the

PDOS and it signifies a superoxo bonding mode. Similar observation has been formed in the studies by Yoon *et al.* [41].
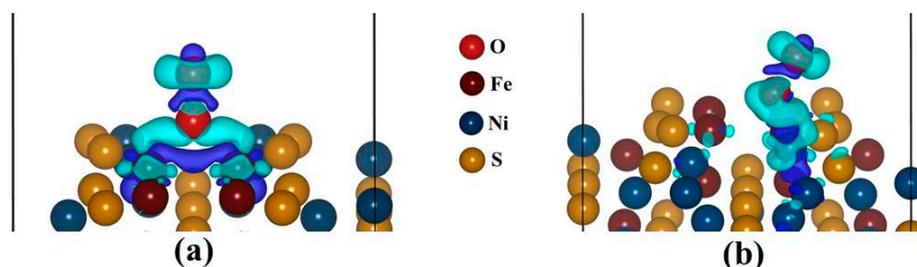
Figure 10. The sketch of isosurface charge density difference: (**a**) Fe-top site (isosurface level = 0.004 eÅ^{-3}) and (**b**) Ni-top site (isosurface level = 0.003 eÅ^{-3}). Cyan represents positive electronic clouds which accept electrons and blue stands for negative electronic clouds which donate electrons.

Now, we use Bader analysis to examine the electron transfer from the surface Fe and Ni atoms to the oxygen molecule, in the fcc-hollow, Fe-top and Ni-top sites. Interestingly, we found that in all cases the oxidized Fe and Ni atoms adopts more positive charge. For fcc-hollow: Fe1 = Fe4 = +0.72|e|, Fe-top: Fe1 = +0.72|e| and Fe4 = +0.71|e| and for Ni-top: Ni2 = +0.64|e|, which indicates that an electron has been donated to the O_2 molecule. This is due to a negative electronic cloud (charge depletion) on the Fe and Ni atoms while the O_2 has a positive electronic cloud (charge accumulation), as observed from the charge density difference in Figure 10a,b. The cylindrical shape around O2 atom, represent the π_p^* orbital and this signifies a superoxo bonding mode, similarly to the PDOS observation (Figure 9a,b). The oxygen molecule possesses negative charges: for fcc-hollow (O1 = −0.48|e| and O2 = −0.18|e|), Fe-top (O1 = −0.48|e| and O2 = −0.15|e|) and for Ni-top (O1 = −0.25|e| and O2 = −0.12|e|). It is clear that the terminal oxygen (O2) has a smaller charge than the M-bonded oxygen atom (O1). This charge distribution behavior for superoxide has been previously reported [38]. The charge on O_2 (*i.e.*, charge sum of O1 and O2), for lowest ground state are as: for fcc-hollow (−0.66|e|), for Fe-top (−0.63|e|) and for Ni-top (−0.37|e|). It clearly shows that O_2 on Fe atoms possesses more negative charge than on Ni atom. The negative charge on the oxygen atoms is also confirmed by experiment for superoxo or end-bonded O_2 [42].

4. Summary and Conclusions

The O_2 adsorption on nickel-rich pentlandite (110) surface has been investigated using DFT for three adsorption sites: fcc-hollow, Fe-top and Ni-top. Firstly, the optimized non-adsorbed surface was observed to have Ni atoms relaxing inward into the surface. As a result their DOS showed less contribution of Ni 3*d*-orbital contribution at E_F, while the Fe atoms contribute more, indicating that the Fe atoms are more reactive than the Ni. Secondly, the O_2 adsorption for all cases is spontaneous reaction (exothermic), with Fe-top being more favorable with adsorption energy of −1.902 eV, compared to fcc-hollow (−1.891 eV) and Ni-top (−0.040 eV). This suggested a preferential oxidation of Fe than Ni.

The DOS, Bader analysis and isosurface charge density difference were computed for the O_2 adsorbed surface. The DOS for fcc-hollow and Fe-top showed similar trend, displayed two degenerate π_p orbital peaks, while for Ni-top a single degenerate π_p peak was observed at the VB. In all three adsorption sites cases, their π_p^* peak at −2.0 eV reduced to zero state for O1 atom, while the σ_p^* peaks reside just above the E_F for fcc-hollow and Fe-top and is half-occupied for Ni-top on both O1 and O2. The O_2 interaction with Fe1 and Fe4 atoms on the top surface, showed three sharp 3*d*-orbital peaks at the VB and a broad peak at the CB (between −2.5 and 1.5 eV), while Ni2 is observed to have a sharp peak at the VB (at around −2.0 eV) and a small peak at the E_F. The isosurface charge density

difference and Bader analysis showed the difference in electron (charge) depletion and accumulation between the top surface (Fe and Ni) and the O_2. In particular, the charge density difference showed directional bonding, a cylindrical shape cloud on O2 was observed, suggesting a superoxo bonding. Finally, Bader analysis, in all cases indicated that the oxidized Fe and Ni atoms adopts more positive charge, while O_2 on Fe atoms possesses more negative charge than on Ni atom. Interestingly, the M-bonded oxygen (O1) has smaller charge than the terminal oxygen (O2).

Author Contributions: P.E.N. and H.R.C. conceived and designed the computational approaches used in the paper; P.P.M. performed the calculations towards his thesis project. All authors, P.P.M., H.R.C. and P.E.N. contributed to the writing and analysis of the paper.

Conflicts of Interest: The authors declare no conflict of interest.

References

1. Ngobeni, W.A.; Hangone, G. The effect of using sodium di-methyl-dithiocarbamate as a co-collector with xanthates in the froth flotation of pentlandite containing ore from Nkomati mine in South Africa. *Miner. Eng.* **2013**, *54*, 94–99. [CrossRef]

2. Cabri, L.J. Platinum-group elements: Mineralogy, geology and recovery. *Can. Inst. Min. Metall. CIM Spec.* **1989**, *23*, 199–217.

3. Legrand, D.L.; Bancroft, G.M.; Nesbitt, H.W. Oxidation/alteration of pentlandite and pyrrhotite surface at pH 9.3: Part 1. Assignment of XPS spectra and chemical trends. *Am. Miner.* **2005**, *90*, 1042–1054. [CrossRef]

4. Buckley, A.N.; Woods, R. Surface composition of pentlandite under flotation related condition. *Surf. Interface Anal.* **1991**, *17*, 675–680. [CrossRef]

5. Heiskanen, K.; Kirjavainen, V.; Laapas, H. Possibilities of collectorless flotation in the treatment of pentlandite ores. *Int. J. Miner. Process.* **1991**, *33*, 263–274. [CrossRef]

6. Kelebek, S.; Nanthakamar, B. Characterrization of stockpile oxidation of pentlandite and pyrrhotite through kinetic analysis of their flotation. *Int. J. Miner. Process.* **2007**, *84*, 69–80. [CrossRef]

7. Merape, G. Fundamental Electrochemical Behaviour of Pentlandite. Master's Thesis, University of Pretoria, Pretoria, South Africa, August 2010.

8. Knop, O.; Huang, C.H.; Woodhams, F.W.D. Chalcogenides of transition elements. VII. A mossbauer study of pentlandite. *Am. Miner.* **1970**, *55*, 1115–1130.

9. Richardson, S.; Vaughan, D.J. Surface alteration of pentlandite and spectroscopic evidence for secondary violarite formation. *Mineral. Mag.* **1989**, *53*, 213–222. [CrossRef]

10. Sit, H.L.P.; Cohen, M.H.; Selloni, A. Interaction of oxygen and water with the (100) surface of pyrite: Mechanism of sulphur oxidation. *J. Phys. Chem. Lett.* **2012**, *3*, 2409–2414. [CrossRef] [PubMed]

11. Rimstidt, J.D.; Vaughan, D.J. Pyrite oxidation: A state-of-the-art assesment of the reaction machanism. *Geochim. Cosmochim. Acta* **2003**, *67*, 873–880. [CrossRef]

12. Evangelou, V.P. *Pyrite Oxidation and Its Control*, 1st ed.; CRC Press: New York, NY, USA, 1995; pp. 1–295.

13. Geller, S. Refinement of the crystal structure of Co_9S_8. *Acta Crystallogr.* **1962**, *15*, 1195–1198. [CrossRef]

14. Rajamani, V.; Prewitt, C.T. Crystal chemistry of natural pentlandites. *Can. Miner.* **1973**, *12*, 178–187.

15. Vaughan, D.J.; Craig, J.R. *Mineral Chemistry of Metal Sulphides*; Cambridge University Press: Cambridge, UK, 1978.

16. Mkhonto, D.; Ngoepe, P.E.; Cooper, T.G.; de Leeuw, N.H. A computer modelling study of the interaction of organic adsorbates with fluorapatite surfaces. *Phys. Chem. Miner.* **2006**, *33*, 314–331.

17. Hohenberg, P.; Kohn, W. Inhomogeneous electron gas. *Phys. Rev. B* **1965**, *136*, 864–871. [CrossRef]

18. Hohenberg, P.; Kohn, W. Density functional theory. *Phys. Rev. B* **1964**, *136*, 864–876. [CrossRef]

19. Kresse, G.; Furthermüller, J. Efficient iterative schemes for ab-initio total-energy calculations using a plane-wave basis set. *Phys. Rev. B* **1996**, *54*, 11169–11186. [CrossRef]

20. Perdew, J.; Burke, K.; Ernzerhof, M. Generalized gradient approximation made simple. *Phys. Rev. Lett.* **1996**, *118*, 3865–3868. [CrossRef]

21. Chauke, H.R.; Nguyen-Manh, D.; Ngoepe, P.E.; Pettifor, D.G.; Fries, S.G. Electronic structure and stability of the pentlandites Co_9S_8 and $(Fe,Ni)_9S_8$. *Phys. Rev. B* **2002**, *66*, 1–5. [CrossRef]

22. Lindqvist, M.; Lundqvist, D.; Westgren, A. Crystal structure of Co_9S_8 and of pentlandite $(Ni,Fe)_9S_8$. *Svensk Kemisk Tidskrift* **1936**, *48*, 60–156.

23. Monkhorst, H.F.; Park, J.D. Special points for Brillouin-Zone integrations. *Phys. Rev. B* **1976**, *13*, 5188–5192. [CrossRef]

24. Weast, R. *CRC Handbook of Chemistry and Physics*, 86th ed.; CRC Press Inc.: Boca Raton, FL, USA, 1985; pp. 1098–4178.

25. Bader, R.F.W. *Atoms in Molecules: A Quantum Theory*; Oxford University Press: London, UK, 1994.

26. Sanville, E.; Kenny, S.D.; Smith, R.; Henkelman, G. An improved grid-based algorithm for Bader charge allocation. *J. Comput. Chem.* **2007**, *28*, 899–908. [PubMed]

27. Henkelman, G.; Arnaldsson, A.; Jonsson, H. A fast and robust algorithm for Bader decomposition of charge density. *Comput. Mater. Sci.* **2006**, *36*, 354–360. [CrossRef]

28. Momma, K.; Izumi, F. VESTA: A Three-Dimensional Visualization System for Electronic and Structural Analysis. *J. Appl. Crystallogr.* **2008**, *41*, 653–658. [CrossRef]

29. Pentlandite Wikipedia. Available online: http://en.wikipedia.org/wiki/Pentlandite (accessed on 25 May 2015).

30. Devey, A.J.; de Leeuw, N.H. Computer Modelling Studies of Mackinawite, Greigite and Cubic FeS. Ph.D. Thesis, University College London, London, UK, October 2009.

31. Liu, H.; Xiang, H.; Gong, X.G. First principles study of adsorption of O_2 on Al surface with hybrid functionals. *J. Chem. Phys.* **2011**, *135*, 1–5. [CrossRef] [PubMed]

32. Periyasamy, G.E.; Durgun, R.J.Y.; Remacle, F. DFT studies of solvation effects on the nanosize bare, thiolated and redox active ligated Au55 cluster. *J. Phys. Chem.* **2010**, *38*, 15941–15950.

33. Yourdshahyan, Y.; Razaznejad, B.; Lundqvist, B.I. Adiabatic potential-energy surface for oxygen on Al(111). *Phys. Rev. B* **2001**, *65*, 1–17. [CrossRef]

34. Wang, L. Photodetachment photoelectron spectroscopy of transition oxide species. *Adv. Ser. Phys. Chem.* **2000**, *10*, 854–957.

35. Rosso, K.M.; Becker, U.; Hochella, M.F. The interaction of pyrite (100) surfaces with O_2 and H_2O: Fundamental oxidation mechanisms. *Am. Miner.* **1999**, *84*, 1549–1561.

36. Gutsev, G.L.; Rao, B.K.; Jena, P. Systematic study of oxo, peroxo, and superoxo isomers of 3d-metal dioxides and their anions. *J. Phys. Chem. A* **2000**, *104*, 11961–11971. [CrossRef]

37. Citra, A.; Chertihin, G.V.; Andrews, L. Reactions of laser-ablated nickel atoms with dioxygen. Infrared spectra and density functional calculations of nickel oxides NiO, ONiO, Ni_2O_2, and Ni_2O_3, superoxide NiOO, peroxide $Ni(O_2)$, and higher complexes in solid argon. *J. Phys. Chem. A* **1997**, *101*, 3109–3118. [CrossRef]

38. Uzunova, E.L.; Mikosch, H.; Nikolov, G.S. Electronic structure of oxide, peroxide, and superoxide clusters of the 3d elements: A comparative functional study. *J. Chem. Phys.* **2008**, *128*, 094307. [CrossRef] [PubMed]

39. Blyholder, G.; Head, J.; Ruette, F. Semi empirical Calculation of Iron-Oxygen Interactions. *Inorg. Chem.* **1982**, *21*, 1539–1545. [CrossRef]

40. Yourdshahyan, Y.; Razaznejad, B.; Lundqvist, B.I. Adiabatic potential-energy surface of O_2/Al(111): Rare entrance-channel barriers but molecularly chemisorbed state apt for abstraction. *Solid State Commun.* **2001**, *117*, 531–535. [CrossRef]

41. Yoon, B.; Hakkinen, H.; Landman, U. Interation of O_2 with Gold Cluster: Molecular and Dissociative Adsorption. *J. Phys. Chem. A* **2003**, *107*, 4066–4071. [CrossRef]

42. Lever, A.B.P.; Ozin, G.A.; Gray, H.B. Electron transfer in metal–dioxygen adducts. *Inorg. Chem.* **1980**, *19*, 1823–1824. [CrossRef]